
Photoionisation detection of single ^{87}Rb -atoms using channel electron multipliers

Florian Alexander Henkel



München 2011

Photoionisation detection of single ⁸⁷Rb-atoms using channel electron multipliers

Florian Alexander Henkel

Dissertation
an der Fakultät für Physik
der Ludwig-Maximilians-Universität
München

vorgelegt von
Florian Alexander Henkel
aus München

München, den 02.09.2011

Erstgutachter: Prof. Dr. Harald Weinfurter
Zweitgutachter: Dr. Jörg Schreiber
Tag der mündlichen Prüfung: 08.11.2011

Abstract

Fast and efficient detection of single atoms is a universal requirement concerning modern experiments in atom physics, quantum optics, and precision spectroscopy. In particular for future quantum information and quantum communication technologies, the efficient readout of qubit states encoded in single atoms or ions is an elementary prerequisite. The rapid development in the field of quantum optics and atom optics in the recent years has enabled to prepare individual atoms as quantum memories or arrays of single atoms as qubit registers. With such systems, the implementation of quantum computation or quantum communication protocols seems feasible.

This thesis describes a novel detection scheme which enables fast and efficient state analysis of single neutral atoms. The detection scheme is based on photoionisation and consists of two parts: the hyperfine-state selective photoionisation of single atoms and the registration of the generated photoion-electron pairs via two channel electron multipliers (CEMs). In this work, both parts were investigated in two separate experiments. For the first step, a photoionisation probability of $p_{\text{ion}} = 0.991$ within an ionisation time of $t_{\text{ion}} = 386$ ns is achieved for a single ^{87}Rb -atom in an optical dipole trap. For the second part, a compact detection system for the ionisation fragments was developed consisting of two opposing CEM detectors. Measurements show that single neutral atoms can be detected via their ionisation fragments with a detection efficiency of $\eta_{\text{atom}} = 0.991$ within a detection time of $t_{\text{det}} = 415.5$ ns. In a future combined setup, this will allow the state-selective readout of optically trapped, single neutral ^{87}Rb -atoms via photoionisation detection with an estimated detection efficiency $\eta = 0.982$ and a detection time of $t_{\text{tot}} = 802$ ns.

Although initially developed for single ^{87}Rb -atoms, the concept of photoionisation detection is in principle generally applicable to any atomic or molecular species. As efficient readout unit for single atoms or even ions, it might represent a considerable alternative to conventional detection methods due to the high optical access and the large sensitive volume of the CEM detection system. Additionally, its spatial selectivity makes it particularly suited for the readout of single atomic qubit sites in arrays of neutral atoms as required in future applications such as the quantum-repeater or quantum computation with neutral atoms.

The obtained high detection efficiency η and fast detection time t_{tot} of the new detection method fulfill the demanding detector requirements for a future loophole-free test of Bell's inequality under strict Einstein locality conditions using two optically trapped, entangled ^{87}Rb -atoms at remote locations. In such a configuration, the locality and the detection loophole can be simultaneously closed in one experiment.

Zusammenfassung

Ein schneller und effizienter Nachweis von Einzelatomen ist eine universelle Voraussetzung für aktuelle Experimente in den Gebieten der Atomphysik, der Quantenoptik und der Präzisions-Spektroskopie. Die effiziente Auslese von einzelnen Qubit-Zuständen, die in Einzelatomen oder -ionen kodiert sind, ist darüber hinaus eine Grundbedingung für zukünftige Technologien im Rahmen der Quanteninformation oder der Quantenkommunikation. In den letzten Jahren ermöglicht die rapide fortschreitende, technische Entwicklung im Bereich der Quanten- und Atomoptik, individuelle Atome als Quantenspeicher zu präparieren, beziehungsweise ganze Anordnungen von Einzelatomen als Quantenregister zusammenzufassen. Mit diesen Systemen scheint eine experimentelle Umsetzung von neuartigen Anwendungen in der Quanteninformationsverarbeitung und der Quantenkommunikation möglich.

Im Rahmen dieser Arbeit wird ein neuartiges Nachweisschema beschrieben, das ein schnelles und effizientes Auslesen von internen Zuständen einzelner Atome ermöglicht. Das vorgestellte Nachweisschema basiert auf Photoionisation und besteht aus zwei Teilen: der selektiven Photoionisation von Einzelatomen abhängig vom Hyperfein-Zustand und der Detektion der erzeugten Photoelektron-Ionen Paare mittels zweier Sekundärelektronen-Vervielfacher (Channeltrons). In dieser Arbeit wurden beide Teile des Nachweisschemas in zwei getrennten, experimentellen Aufbauten untersucht. Für den ersten Schritt wurden einzelne ^{87}Rb -Atome in einem optischen Einzelatomfallen-Aufbau zustandsselektiv ionisiert. Innerhalb von $t_{\text{ion}} = 386 \text{ ns}$ wurde eine Photoionisationswahrscheinlichkeit von $p_{\text{ion}} = 0.991$ erreicht. Für den zweiten Teil wurde ein eigenständiger, kompakter Detektor für den Nachweis der Ionisationsfragmente entwickelt, der aus zwei entgegengesetzt angeordneten Channeltrons besteht. Messungen bestätigen, dass einzelne Neutralatome mittels ihrer Photoionisations-Fragmente mit einer Detektionseffizienz von $\eta_{\text{atom}} = 0.991$ innerhalb von $t_{\text{det}} = 415.5 \text{ ns}$ nachgewiesen werden können. In einer zukünftigen, kombinierten Anordnung dieser beiden Systeme könnten demnach optisch gefangene ^{87}Rb -Atome über Photoionisation zustandsselektiv mit einer voraussichtlichen Detektionseffizienz von $\eta = 0.982$ in einer Gesamtzeit von $t_{\text{tot}} = 802 \text{ ns}$ nachgewiesen werden.

Obwohl der Photoionisations-Nachweis ursprünglich für einzelne ^{87}Rb -Atome entwickelt wurde, eignet er sich für beliebige Isotope oder Moleküle. Als effizienten Ausleseeinheit für einzelne Atome oder Ionen könnte sich der neuartige Nachweis durch den hohen optischen Zugang und das große, räumliche Detektionsvolumen des Channeltron-Detektors als eine mögliche Alternative zu bestehenden Nachweis-Methoden erweisen. Seine räumliche Selektivität macht ihn zusätzlich besonders geeignet für die Auslese von einzelnen, atomaren Qubits in Anordnungen mit Neutralatomen. Er könnte daher speziell in zukünftigen Anwendungen wie dem 'Quanten-Repeater' oder einem Quantencomputer basierend auf Neutralatomen verwendet werden.

Die hohe Detektionseffizienz η und die schnelle Detektionszeit t_{tot} der neuen Nachweismethode erfüllen die anspruchsvollen Voraussetzungen an einen Detektor, um ihn innerhalb eines schlupflochfreien Tests einer Bell-Ungleichung mit zwei optisch gefangenen, miteinander verschränkten und raumartig getrennten ^{87}Rb -Atomen zu verwenden. Mit einem solchen Aufbau kann das Lokalitäts-Schlupfloch und das Nachweis-Schlupfloch gleichzeitig in einem Experiment geschlossen werden.

Contents

1. Introduction	1
2. Channel Electron Multiplier as Charged Particle Detectors	5
2.1. Theory of operation	6
2.1.1. CEM detector operation	6
2.1.2. Generalised cascaded dynode model	8
2.2. Detector quantum yield	11
2.2.1. Finite discriminator level and detector quantum yield	12
2.3. General design and operation criteria	13
2.3.1. Compound loss probability	13
2.3.2. Conversion dynodes	17
2.3.3. Obtaining a high quantum yield	18
2.4. Absolute detection efficiency	19
2.4.1. Collection efficiency and detector quantum yield	19
2.4.2. Kinetic impact energy	21
2.4.3. Angle of incidence	25
2.5. Detector efficiency performance	26
2.5.1. Theoretical CEM efficiency response	27
3. Basic Operation of Channel Electron Multiplier Detectors	31
3.1. Basic CEM operation parameters	32
3.1.1. Theoretical CEM gain	33
3.1.2. Experimental CEM gain	34
3.1.3. Optimum operating point	38
3.2. Associated CEM operation parameters	39
3.2.1. Transit time	40
3.2.2. Maximum count rate and resolution of two consecutive pulses	41
3.2.3. Detector dark current and background counts	42
3.3. Single CEM detector performance	43
3.3.1. Experimental data acquisition	45
3.3.2. Single pulse parameters	46
3.3.3. Pulse height distribution histogram	48
3.3.4. Experimental modal CEM gain	50
3.3.5. Characteristic knee curve	51
3.4. Particle counting and CEM operation	52
3.4.1. Single pulse counting and trigger level	53
3.4.2. Background cable noise and spurious counts	54
3.4.3. Signal cable ringing and impedance matching	54
3.4.4. Maximum count rate and resolution of two consecutive pulses	56
3.4.5. Pulse height distribution and detector quantum yield	57

4. Joint Channel Electron Multiplier Detector	59
4.1. Concept of photoionisation detection	61
4.1.1. Alternative charged particle detection systems	64
4.2. Joint CEM detector	66
4.2.1. Channel electron multipliers	66
4.2.2. Vacuum system setup	68
4.2.3. Glass cell setup	70
4.2.4. Joint CEM detection system	72
4.3. Charged particle optics	75
4.3.1. Numerical simulation of the electric field configuration	76
4.3.2. Basic FemLab model for $\Delta U_{\text{acc}} = 3800 \text{ V}$	77
4.3.3. Effect of CEM cone apertures	77
4.3.4. Determination of the kinetic energy at primary particle impact	80
4.3.5. Cone entrance energy versus particle impact energy	84
4.4. Photoionisation fragment flight time model	85
4.4.1. Time-of-flight capacitor model	85
4.4.2. Detection time	88
4.4.3. Collection efficiency	88
4.5. Beam overlap and photoionisation fragment imaging	91
4.5.1. Calibration measurement setup	91
4.5.2. Spatial beam overlap and ionisation volume	93
4.5.3. Photoionisation fragment imaging	96
5. Fast and Efficient Photoionisation Detection of Single Atoms	101
5.1. Detector efficiency calibration and absolute detection efficiency	103
5.1.1. Conventional, relative detection efficiency	104
5.1.2. Absolute detection efficiency via counting coincidences	106
5.1.3. Photoionisation as unique calibration pair source	107
5.2. Electron-ion correlation measurements	109
5.2.1. Single coincidence pulse trace	110
5.2.2. Electron-ion correlation histograms	111
5.2.3. Accidental coincidences	114
5.2.4. Analysis of background counts	115
5.3. Photoionisation fragment detection time	118
5.3.1. Photoelectron-ion arrival time difference Δt	119
5.3.2. Neutral atom detection time	121
5.4. Absolute detection efficiencies	122
5.4.1. CEM calibration to absolute detection efficiencies	122
5.4.2. Neutral atom detection efficiency	124
5.4.3. Kinetic energy at primary particle impact	125
5.4.4. Absolute detection efficiency versus impact energy	126
5.4.5. Obtaining high CEM efficiencies	129
5.5. Spatial efficiency dependence and particle impact position in the CEMs	130
5.5.1. Spatial dependence of detection efficiency	131
5.5.2. Sensitive detection area and sensitive volume	134
5.5.3. ^{87}Rb -ion impact position in the ion-CEM	135

6. Summary and Outlook	139
6.1. Short term prospects with the current CEM detection system	140
6.2. Long term options using photoionisation detection	142
A. Appendix	145
A.1. Natural constants	145
A.2. Atomic properties	145
A.3. Channel electron multiplier data	146
A.4. Joint CEM detector data	146
B. Compound Poisson distribution	147
C. Three alternative CEM detector configurations	149
C.1. Two CEMs, individual acceleration of the ionisation fragments	149
C.2. Two CEMs, and conversion dynodes	150
C.3. Single CEM detector, and photoion conversion dynode	150
D. Possible CEM detection system applications	153
D.1. Photoionisation as calibration source for charged particle detectors	153
D.2. Mass spectroscopy below the current detection limit	153
D.3. Readout of neutral atom qubits and of ultracold heteronuclear molecules	154
E. Publications	155
Bibliography	157

1. Introduction

Fast and efficient detection of single qubit states is a universal requirement regarding future applications in quantum communication, quantum metrology, and quantum information processing. In such qubit-based quantum systems, entanglement and superposition represent key properties, allowing to entangle single qubits of few or many-body systems, or at spatially remote locations. As quantum memories or quantum registers, these entangled qubits are the basis for applications in quantum computing, and quantum communication protocols. Moreover, entanglement between two spatially separated qubit systems enables a fundamental test on quantum mechanics itself. However, for such a test highly efficient qubit state analysers are required which simultaneously provide short detection times.

For a fundamental test of quantum mechanics, John Bell derived a certain class of inequalities [1] which are based on a gedankenexperiment of Einstein, Podolsky, and Rosen [2]. The derived inequalities allow to experimentally discriminate local realistic theories from quantum mechanics. In an experiment, the inequalities can explicitly be probed by measuring correlated events between two or more entangled particles. Since that time, many experiments have attained to violate the fundamental limit imposed by the Bell inequalities [3–14]. Remarkably, all these experiments have exclusively confirmed quantum mechanics. However, for a strict violation of a Bell inequality, two important conceptual assumptions have additionally to be considered. These fundamental considerations have opened the so-called detection loophole and the locality loophole [15, 16]. Until today, no concise loophole-free test of a Bell inequality has been performed which closes the two loopholes simultaneously in a single experiment.

Conceptionally, the two loopholes affect an experimental test of a Bell inequality thoroughly. For a system of two entangled particles, closing the locality loophole demands the strictly independent measurement of the two detection events. In the context of special relativity, this is realised only by a strict *spatial* separation of the two entangled particles. The locality loophole further includes the completely random choice of two independent sets of measurement bases for the correlation measurements at the two particles sites. Closing the detection loophole requires that a large contribution of the entangled pairs has to be detected with certainty. Otherwise a subensemble of the possible measurement outcomes could agree with quantum mechanics, while the overall set of measurement outcomes including the undetected events might not [15].

In recent years, a loophole-free test of a Bell inequality has come into experimental reach. As the most promising approach, atomic qubits have turned out to be particularly suited for such a test [17, 18]. The proposal schematically starts with two spatially separated atomic qubits, each entangled with an emitted photon, respectively. The two photons are then propagated to an intermediate location where a Bell state analysis on the two photons is performed. By entanglement swapping [19], the entangled state of the two photons is heralded onto the two remote atomic qubits, resulting in atom-atom entanglement. The violation of a Bell inequality is then subsequently verified by the individual local readout of the stationary atom qubits with an efficient qubit state detector. In our group, substantial effort has been undertaken in the last years towards the realisation of such an experiment [18, 20–24]. The present results seem promising for a final test of a Bell inequality with two remote ^{87}Rb -atoms in the future.

However, the simultaneous closing of both loopholes in one experiment imposes huge prerequisites on the detection efficiency and the detection time of a possible readout unit. In a system of two maximally entangled particles, the minimum detection efficiency for a single qubit is $\eta \geq 2/(1 + \sqrt{2}) \approx 0.8284$ [15, 25–27] for a CHSH-type Bell inequality [28]. Moreover, reasonable experimental distances between the two measurement setups in the range of several hundred meters will demand sub-microsecond measurement times to close the locality loophole. Therefore, a possible readout unit has to provide detection efficiencies of $\eta > 0.828$ within sub-microsecond time for a loophole-free test of a Bell inequality with two remote particles. To our knowledge, such a highly-efficient detection unit does presently not exist for any system.

For single atom qubits, shelving techniques [29] have proven to yield the highest readout efficiencies for atomic qubits within considerably short detection times. For single ions in Paul traps, this method has been successfully applied [30–33] with a maximum reported readout fidelity exceeding 99.99 % for a single trapped ^{43}Ca -ion within a detection time of 145 μs [34]. In comparison with single neutral atom systems, experimental readout fidelities of 98.6 % within 1.5 ms time are observed¹ [35, 36]. Moreover, using fluorescence collection enhancement via sophisticated collection optics [37–39] or optical cavities [40–43], maximum readout fidelities of 99.4 % within 85 μs are reported for optical cavity systems [41]. However, the *single-shot* readout efficiency of all these systems is still comparatively low. For a single photon scattering, single photon detection efficiencies of approximately only 20 % have been estimated [41], with a calculated maximum attainable efficiency of 41 % in these systems [43].

The previous fluorescence detection schemes are all based on repetitive scattering of single photons on the probed atom or ion. For conventional fluorescence detection, this leads to comparably long detection times in the order of several scattering transitions due to the small collection efficiency in these systems. Even more, also the most sophisticated fluorescence collection setups like cavity structures hardly achieve detection times below one microsecond [44] for typical atomic lifetimes of $\tau = 25 - 30 \text{ ns}$ with current state of the art technologies. Additionally, these readout systems seem difficult to be scaled up to larger arrays or samples of atomic qubits due to the typically small mode volume and the reduced optical access in such systems [40–42]. Therefore, a completely different detection approach seems to be required.

The novel detection scheme developed in this thesis applies photoionisation detection. It allows fast, efficient, and state selective detection of single atom qubits in a single-shot readout operation and might represent a considerable alternative to fluorescence detection in future experiments.

The concept of photoionisation detection is based on the hyperfine-state selective photoionisation of single atoms and the subsequent detection of the ionisation fragments using two channel electron multiplier detectors (CEMs). For the atomic qubit readout, photoionisation detection appears to be particularly promising as the photoionisation probability of single atoms and the detection efficiency of the photoionisation fragments with the single CEM detectors is expected to be high. The new detection method will therefore theoretically provide the detection efficiency necessary to serve as an atomic qubit readout unit in a future loophole-free test of a Bell inequality [18, 21]. Due to acceleration of the generated photoionisation fragments by considerable electric fields and the close configuration of the two CEM

¹The difference in fidelity and readout time mainly results from the by magnitude smaller trapping potential of optical tweezers compared to common potential depths of ion trap configurations. This requires a continuous re-cooling of the probed neutral atoms in relation to the trapped ions to prevent any atom loss by heating the atom out of the trap.

detectors in the CEM detection system, sub-microsecond detection times are anticipated for such a readout.

Photoionisation detection of single neutral atoms with channel electron multipliers. The CEM detection system of this thesis is primarily developed with the goal to serve as highly-efficient and hyperfine-state selective readout unit for a loophole-free test of a Bell inequality with two remote, entangled ^{87}Rb -atoms [18, 21]. In the current single atom experiment, it will substitute the comparably slow and inefficient fluorescence detection readout. By comparison, the detection time of the fluorescence readout in the actual single atom trap is in the range of 10 ms for detection efficiencies greater 95% [45]. An implementation of the novel CEM photoionisation detection unit in the actual setup will thus boost the detection time by a factor of 10^4 at comparable detection accuracies. However, the concept of photoionisation detection intrinsically provides a single-shot readout operation only as the photoionisation process is inherently destructive for the neutral ^{87}Rb -atom to be detected.

For an integration into the actual single atom trap setup, the strategy to implement and optimise the novel detection scheme is twofold. On the one hand, the ionisation probability p_{ion} and the ionisation time t_{ion} of the photoionisation process itself have to be optimised. On the other hand, the detection efficiency of the photoionisation fragments with the CEM detection system has to be maximised. Although the first component represented a considerable part of this work too, the comprehensive description of the single atom trap setup will be subject of a future contribution by my colleague Michael Krug [46]. In this thesis, the design, the implementation, and the optimisation of the CEM detection system for the fast and efficient photoionisation fragment detection are reported in detail.

To avoid disturbance of the current atom-photon entanglement experiments, the CEM detection system for the photoionisation detection is initially implemented in a second glass cell UHV chamber *identical* to the current single atom trap system (see section 4.2). A future integration of the CEM detection system is thus possible by simply interchanging the two identical vacuum systems while preserving the MOT optics and single atom trap components of the actual setup. This modular design will provide a fast and easy integration of the novel photoionisation detection readout in the current single atom trap system. However, in order to experimentally realise the CEM detection system, severe technical challenges had to be overcome to successfully implement an entire charged particle imaging system in the compact glass cell UHV environment of the single atom trap.

From a detector point of view, the measurements of this thesis further may resemble a major contribution concerning charged particle detector calibration. This follows as the photoionisation of single neutral atoms serves as a unique source to generate correlated charged particle pairs. The registration of coincidence detections of these correlated pairs enables to calibrate the single CEM detectors to *absolute* detection efficiencies. It further allows to estimate the impact parameters of the primary ^{87}Rb -ions for the impact in the CEM detector. As such a calibration source for charged particle detectors was previously not available, the calibration measurements therefore presumably represent one of the first characterisations of CEM detector efficiency response to absolute values. Moreover, they admit a direct comparison with cascaded dynode detector theory, and with reported relative detector efficiencies in the literature. The comparison with theory will allow to push the performance of a conventional CEM detector as used in the experiment to its limiting extremes.

Thesis outline This thesis is organised as follows. In chapter 2, an introduction is given into the basic principles underlying the cascaded amplification process for the secondary electron avalanche buildup in cascaded dynode detectors. The theory provides the theoretical framework for optimising the efficiency of a single CEM detector or a given CEM detection system. Additionally, an explicit model for the efficiency response of a CEM detector is deduced and related to experimentally accessible parameters.

Chapter 3 specifies the relevant operational parameters for a single CEM detector in pulse counting mode. The CEM parameters are first theoretically introduced. A detailed analysis of the parameters yields the theoretical estimate of the ultimate CEM detector limits. In the second part of the chapter, the performance of the two CEM detectors used in the CEM detection system is experimentally analysed. Accordingly, their operational parameters are individually characterised by separate measurements. By this, a stable and reproducible operation of the single CEM detectors in the CEM detection system is provided.

The concept of photoionisation detection and the experimental implementation of the CEM detection system are introduced in chapter 4. In this chapter, the main components of the detection system are discussed along with their technical realisation. In accordance with the particular geometry, the modelling of the electric potential distribution between the CEM detectors enables to derive a theoretical flight time model for the photoionisation fragments. The chapter closes with measurements on the calibrating beam optics and on the CEM detection system in the glass cell UHV chamber. The CEM detection system introduced in this chapter has been built from scratch. The development and successful realisation of this system therefore constitutes a significant part of the work presented here.

In chapter 5, the fundamental principles to calibrate the efficiency response of charged particle detectors to absolute values are introduced. In this context, resonant photoionisation of single neutral atoms evolves as a unique calibration source for charged particle detectors. By using this source, the raw quantum yield of the CEM detectors and the absolute efficiency of the CEM detection system are obtained. The measurement of correlated events from photoionisation with the two CEM detectors allows to experimentally determine the detection time for the ionisation fragments. In combination with the ionisation probability and ionisation time of the photoionisation process, the single atom detection efficiency and the detection time for the photoionisation detection of single, optically trapped ^{87}Rb -atoms can be estimated.

The strong temporal correlation of the photoionisation fragments additionally enables to determine the impact position of the photoions in the corresponding CEM detector. This allows to directly relate the observed CEM detection efficiencies to the theoretical estimations of chapter 2. Two dimensional calibration scans using photoionisation as calibration source further permit to determine the sensitive detection area of the CEM detection system, and its sensitive volume. Parts of chapter 4 & 5 are published in Ref. [24].

2. Channel Electron Multiplier as Charged Particle Detectors

In this chapter, the detection of a single primary particle by its conversion into secondary electrons and its amplification via a secondary electron avalanche in the continuous dynode structure of a channel electron multiplier (CEM) detector is theoretically introduced. For this purpose, a basic model is presented which describes the cascaded multiplication process in the continuous CEM dynode structure by quasi-discrete stages $g_{1..m}$ in perfect analogy to discrete dynode multipliers. Relying only on a few fundamental parameters and Poisson statistics, the model reduces the cascaded amplification of the secondary electron avalanche in the CEM until the generation of a macroscopic pulse at the output of the detector to the two secondary emission yield parameters δ_0 and δ .

By means of the model, several key parameters for CEM operation can therefore be theoretically quantified. In particular, it allows to determine the compound Poisson distribution $P_m(n)$ which enables to define the calculated quantum yield $\eta_{\text{detector}} = 1 - P_m(0)$ of any conventional dynode detector via its attributed overall loss probability $P_m(0)$. Additionally, the first moment of the distribution $P_m(n)$ will yield the modal gain G_0 of the CEM (see chapter 3). In the context of CEM detector theory, the basic model therefore enables to explicitly parametrize the key quantities for CEM operation which have previously remained comparably undefined in the literature, and further allows a distinct comparison to experimentally obtained values in this thesis, and in the general literature.

Moreover, the theoretical investigation of the influence of the individual yield parameters δ_0 and δ on the model will yield fundamental design and operation characteristics for a given CEM detector. Used as an instructive instance, the model will therefore reveal a general strategy to improve and optimize the amplification cascade process, and thus the quantum yield η_{detector} of a discrete or continuous dynode detector. In this context, the primary impact of the incident particle at the first amplification stage g_1 represents the *key* stage for achieving a high quantum yield. This results as the primary particle emission yield δ_0 resembles the initiating 'seed' of the developing, secondary electron avalanche in the dynode detector.

In contrast to the fundamental considerations of the initial sections, the absolute detection efficiency η_{det} of a given CEM detection system is then introduced and explicitly defined. The analysis of the single components contributing to η_{det} relates it to experimentally accessible parameters and allows to derive an explicit relation for η_{detector} based on these quantities. For single CEM detectors, the two relevant parameters are the kinetic energy E_{kin} and the corresponding incident angle θ at primary particle impact. Accordingly, an explicit model for the dependence of the quantum yield of a CEM detector on these parameters, the so-called reduced yield curve model, is subsequently deduced. Moreover, the collection efficiency η_{col} of the CEM detection system of this work can be assumed as unity. This leaves the raw quantum yield $\eta_{\text{detector}}(\delta_0, \delta)$ as the only parameter to determine the absolute detection efficiency η_{det} of a single CEM detector in the CEM detection system.

Finally, exemplary theoretical curves display the calculated quantum yield $\eta_{\text{detector}}(\delta_0, \delta)$ of a conventional CEM detector according to the two relevant, experimentally accessible param-

eters E_{kin} and θ . In particular, the calculations show the explicit influence of the secondary emission yield values $\delta_0(E_{\text{kin}}, E_{\delta_0, \text{max}}, \delta_{0, \text{max}})$ and $\delta(E_{\text{kin}}, E_{\delta, \text{max}}, \delta_{\text{max}})$ on the reduced yield curve model in contrast to the more general considerations of section 2.3. As a result of the calculations, the maximum attainable quantum yield η_{detector} of any given dynode detector in a single particle detection system can be theoretically estimated, provided that the impact position of the incident primary particle in the dynode detector with its associated properties E_{kin} and θ is known.

Generally speaking, the basic theoretical model introduced in this chapter is universally applicable to any cascaded dynode multiplier, or even to any particle amplification process where subsequent cascading amplification stages are involved. From a model point of view, it therefore resembles a genuine testing ground for the application of discrete dynode multiplier theory onto continuous channel electron multipliers. Moreover, in combination with the absolute efficiency calibration measurements of chapter 5, it will allow, possibly for the first time¹ in the literature, to compare experimentally measured quantum yield values η_{detector} of a given CEM detector with the theoretical quantities based on δ_0 and δ , respectively.

2.1. Theory of operation

In the following, the theory for the basic operation of a CEM detector is introduced. Identical to discrete dynode detectors as, e.g., photomultipliers, the detection of an incident primary particle relies on the conversion of the particle into secondary electrons and the subsequent cascaded multiplication of these secondary electrons in the continuous dynode structure of the CEM. By means of Poisson statistics, and the two secondary emission yield parameters δ_0 and δ , a model is illustrated which will allow to theoretically derive and quantify some of the key parameters of CEM operation as, e.g., the compound Poisson distribution $P_m(n)$ represented by the observed pulse height distribution at the dynode detector anode, or the quantum yield η_{detector} of a particular CEM detector via its associated compound loss probability $P_m(0)$ (see subsection 2.1.2 and section 2.2). It will further enable to derive the modal gain G_0 of any cascaded dynode detector based on the number m of cascaded amplification stages (see section 3.1.2) and therefore admit to explicitly relate the determined key parameters of a given dynode detector to experimentally obtained quantities.

2.1.1. CEM detector operation

The detection of an incident primary particle with a CEM detector is based on the development and amplification of the secondary electron avalanche in the continuous dynode structure of the CEM channel tube. In general, it can be reduced to the secondary electron emission of m quasi-discrete dynode stages g_m in cascade after the impact of a primary particle at the first stage g_1 (fig. 2.1). By means of this approximation, the secondary electron avalanche buildup in the CEM channel, and thus the overall secondary emission characteristics of the CEM detector in response to an incident primary particle can be modelled [47, 48]. In conceptual correspondence to the discrete dynode model introduced by [49], the cascaded electron avalanche in the CEM can therefore be described by a compound Poisson distribution (see subsection 2.1.2).

¹This follows as in previous calibration measurements of the CEM detector efficiency in the literature, only relative calibration methods have been employed (see section 5.1).

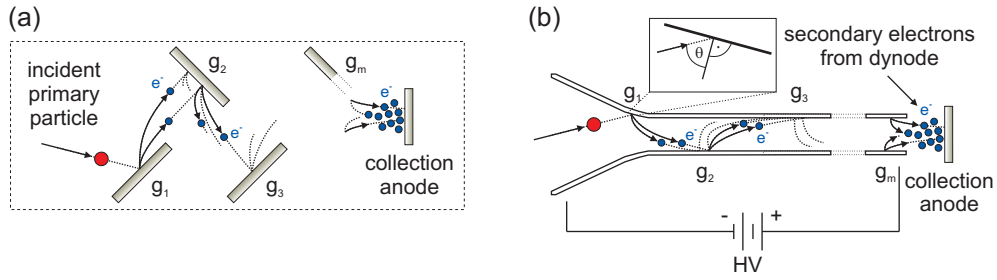


Figure 2.1: (a) Secondary electron cascade in a discrete dynode multiplier. Each dynode corresponds to a single amplification stage g_i . (b) Amplification of an incident primary particle due to the generation of a secondary electron avalanche down the CEM dynode structure. Inset-zoom: Incident particle angle θ to secondary electron emitting CEM surface normal at primary particle impact.

From a model point of view, the application of a compound Poisson distribution on CEM detectors is in perfect analogy to calculations for discrete dynode multipliers with m stages of multiplication [49–54]. The same model is also used to determine similar operating characteristics and parameters in multi channel plates (e.g., [55–57]). In general, theoretical models based on compound probability distributions are extensively used in the description of cascade processes as, e.g., cosmic rain showers [52] or nuclear chain reactions [58]. Moreover, besides fundamental applications in probability theory itself, compound probability distributions are further frequently applied for common cascade models in biology, seismology, risk theory, meteorology, and health science.

In detail, the detection of a primary particle via a CEM detector relies on the conversion of the incident primary particle into secondary electrons, and the subsequent cascaded amplification of these secondary electrons. Figure 2.1 illustrates the generation of the secondary electron avalanche down the CEM dynode structure due to the impact of an incident primary particle. At the first amplification stage g_1 , the incident primary particle (charged particle, neutral particle, or photon) is converted into the initial secondary electrons (primary particle impact; fig. 2.1, inset). These initial secondary electrons therefore resemble the ‘seed’ of the secondary electron avalanche in the dynode detector. Consequently, the emitted secondary electrons at stage g_1 represent the incident primary electrons at the next subsequent stage g_2 (fig. 2.1). In consecutive stages $g_{2..m}$, each single emitted secondary electron itself initiates a new secondary electron cascade. In order to accelerate the generated secondary electrons down the continuous dynode structure of the CEM for multiplication, a potential gradient U_{CEM} (CEM gain voltage) is applied over the full length of the CEM between the CEM input and the output end (fig. 2.1). Finally, the cascade of all generated secondary electrons is gathered by a galvanically isolated collection anode, and further processed.

More specifically, the secondary emission of a particular dynode surface at an amplification stage $g_{1..m}$ can be described by the secondary emission yield $\delta_{1..m}$. It is defined as the number of secondary electrons n emitted from the active surface after a single particle impact in the surface. The secondary emission yield $\delta_{1..m}$ generally depends on a variety of experimentally accessible parameters (section 2.4). However, the secondary electron emission conditions for each incidence at all consecutive amplification stages $g_{2..m}$ in the multiplier but the first one are approximately identical [47]. The secondary electron emission yield $\delta_{2..m}$ of these stages $g_{2..m}$

can therefore be generalized² to an overall secondary emission yield $\delta = \delta_2 = \delta_3 = \dots = \delta_m$. Nevertheless, the primary emission yield δ_1 of the first stage g_1 is generally different to all consecutive amplification stages $g_{2..m}$. The primary emission yield is thus denoted as $\delta_0 \equiv \delta_1$ in the following to emphasize the difference to the generalised secondary emission yield δ .

2.1.2. Generalised cascaded dynode model

According to the model of [49–52, 54], in the CEM the emission of secondary electrons out of the active CEM surface at a single incidence obeys a Poissonian probability distribution. This genuine assumption holds for each single stage of amplification $g_{1..m}$. Moreover, as the secondary electron avalanche cascades down the CEM channel tube in several, quasi-discrete amplification stages (fig. 2.1), the emission of consecutive secondary electrons is dependent on the number of incident secondary electrons at a particular stage g_i . It thus strongly depends on the number of secondary electron emissions at the *previous* stage g_{i-1} , and from the therewith associated emission probabilities.

In order to obtain the probability distribution for the whole secondary electron cascade process down the channel tube, the statistics for compound Poisson distributions has therefore to be applied. It admits to incorporate the dependence of the emission probabilities of all consecutive amplification stages g_i from their corresponding previous stages g_{i-1} . By this, a compound probability distribution for the number of electrons n in the secondary electron avalanche at the dynode detector end is generated. This allows to theoretically determine some of the key parameters of CEM operation as, e.g., the pulse height distribution of the CEM detector with its associated detector gain G_0 (see subsection 3.1.2), or the maximum attainable quantum yield of a particular detector defined by its compound loss probability (see section 2.2).

The probability that n secondary electrons are emitted for a single incident primary particle is given by the Poissonian [49, 51, 52]

$$P(n, \delta_a) = \frac{\delta_a^n}{n!} e^{-\delta_a}, \quad (2.1)$$

where δ_a denotes the secondary emission yield of the single incidence. Correspondingly, the probability that *no* secondary electrons are emitted for an incident primary particle is $P(0, \delta_a) = e^{-\delta_a}$. There is therefore a nonvanishing probability for any cascaded dynode detector that *no* electrons ($n = 0$) are emitted at a particular stage³ g_i of amplification in the multiplier. The latter fact results in a finite probability that the secondary electron avalanche will cease in the dynode detector, not producing any secondary electron current at the detector end (see section 2.2). However, the subsequent development of the secondary electron

²Note that the generalised secondary electron yield $\delta = \delta_2 = \delta_3 = \dots = \delta_m$ results from considerations of [47, 59–61] in analogy to the discrete dynode model as illustrated in fig. 2.1(a). It assumes that all secondary electrons at a stage g_i have an identical acquired kinetic energy $\overline{E}_{\text{kin},i}$ at re-impact in the active CEM surface at the subsequent amplification stage g_{i+1} . This is inferred as their initial kinetic energy $\overline{E}_{\text{ini},i}$ at emission out of the active surface is negligible ($\overline{E}_{\text{ini},i} = 2 - 5 \text{ eV}$, [47, 60–63]), and generally independent of the previous incident primary particle type or even kind of emitting surface (e.g., reviews by [64, 65]). Correspondingly, as these secondary electrons represent the incident primary particles for the next amplification stage g_{i+1} (fig. 2.1), they all yield identical properties at re-impact in the active surface, allowing a generalization of the parameter $\delta = \delta_{2..m}$ for all consecutive stages of amplification $g_{2..m}$.

³This assumes that all single emission events $P(n, \delta_a)$ at this particular stage g_i produce no emitted secondary electron ($n = 0$).

avalanche at a particular stage g_i strongly depends on the number of incident primary electrons at this stage, and therefore on the probability of already generated secondary electrons at previous stages g_{i-1} . The secondary avalanche die-out probability will thus become smaller and smaller for each additional consecutive stage of amplification g_i in the dynode multiplier, assuming secondary electron yield values $\delta_a > 1$.

As the secondary emission at an actual stage g_i depends on the secondary emission of previous stage g_{i-1} , the buildup of the secondary electron avalanche in a dynode multiplier of m stages by cascaded secondary electron emission can most generally be described by means of a generating function [49, 52, 53], being given by the compound function

$$\mathcal{F}_m(s) = \underbrace{\mathcal{F}[\mathcal{F}\{\dots\mathcal{F}(s)\}]}_m = \mathcal{F}[\mathcal{F}_{m-1}(s)].$$

where the value s is a generating function parameter [58]. Assuming a single incident primary particle at the stage g_1 (fig. 2.1), and Poisson statistics for all consecutive stages of multiplication $g_{1..m}$, the generating function for the compound Poisson distribution $P_m(n)$ of a cascaded dynode detector reads according to [51],

$$\mathcal{F}_m(s) = \sum_{n=0}^{\infty} P_m(n) s^n = \exp[\delta_1(-1 + \exp[\delta_2(-1 + \exp[\delta_3(-1 + \dots + \exp[\delta_m(s-1)]])])\dots)], \quad (2.2)$$

where δ_m is the generalized⁴ secondary electron yield for each individual amplification stage g_m , and $P_m(n)$ is the expected frequency distribution for the emission of exactly n secondary electrons at a stage g_m . For an explicit calculation of the compound Poisson distribution and its single components $P_m(n)$ at each single stage g_m , the coefficients of s^n can be expressed as a Maclaurin series in $P_m(n)$ [51]. By this, the single probabilities $P_m(n)$ can be evaluated as initially derived by [49], and computed numerically for different values of $\delta_{1..m}$.

In this work however, the explicit calculation of the compound Poisson distribution $P_m(n)$ according to eq. 2.2 up to n secondary electrons, and for m stages of amplification follows a more general formulation. In this representation [52, 53], the compound distributions are calculated from a Polya statistical model, which includes the compound Poisson distribution and the exponential distribution as limiting cases. This more general approach by Ref. [53] avoids the repetitive differentiation of the $\mathcal{F}_m(s)$ as stated by [49, 51], and thus seems, by recursion, easier to be implemented with standard computer programming⁵. In the Polya representation, the probability $P(n; k, l)$ of producing n electrons after k subsequent amplification stages g_k within a cascaded device of m amplification stages is [53]

$$P(n; k, l) = (\delta_l/n)[P(0; k, l)]^{b_l} \sum_{i=0}^{n-1} [n + i(b_l - 1)] \times P(i; k, l) \times P(n - i; k - 1, l - 1) \quad (2.3)$$

for $n \geq 1$, $1 \leq k \leq m$ and $1 \leq l \leq m$. The probability of producing zero electrons is

⁴Note that in this generalization, the individual secondary emission yield δ_a (eq. 2.1) of all incidences at a single amplification stage g_m is already averaged to a uniform, stage specific secondary emission yield $\delta_{1..m}$ per stage $g_{1..m}$, as suggested by [52].

⁵See Appendix B for the explicit source code of the programming.

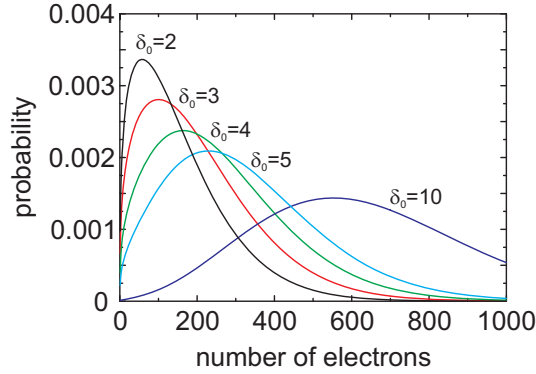


Figure 2.2: Calculated, compound Poisson distribution $P_m(n)$ of detecting n secondary electrons after $m = 7$ stages of amplification for different primary particle yield values δ_0 , and at a fixed secondary electron yield $\delta = 2$. For sufficient high primary particle yield values δ_0 , the compound probability distribution will readily evolve from a negative exponential into a quasi-Gaussian shape. Note that the calculated probabilities correspond experimentally to the observed pulse height distribution at the dynode detector end.

$$P(0; k, l) = \{1 + b_l \delta_l [1 - P(0; k - 1, l + 1)]\}^{-1/b_l} \quad (2.4)$$

where $n = 0$, $1 \leq k \leq m$ and $1 \leq l \leq m$. In eq. 2.3 and eq 2.4, the parameter b_l is the Polya parameter, with the limiting case of $b_l \rightarrow 0$ for a compound Poisson distribution, and the exponential distribution with $b_l \rightarrow 1$, accordingly. The parameter δ_l is the secondary emission yield at the stage g_l while l is a stage index running from $1 \leq l \leq m$. In eq. 2.3 and eq 2.4, the initial condition for a *single* primary particle (ion or electron) incident at the entrance of the cascaded dynode detector is further defined as $P(n; 0, l) = 1$ for $n = 1$, and $P(n; 0, l) = 0$, otherwise [53].

For the calculation of the compound Poisson distribution $P_m(n)$ according to eq. 2.3 and eq 2.4, parameters of $\mu_1 \equiv \delta_0 = 2, 3, \dots, 10$, $\mu_{2..l} \equiv \delta = 2$, $n_{\max} = 1000$, $k \equiv m = 7$, and $b_l = .0000001$ (corresponding to $b \rightarrow 0$; Poisson limit) are chosen. The corresponding programming source code⁶ for the explicit calculation of the distributions displayed in fig. 2.2 is given in Appendix B.

Figure 2.2 shows the calculated, compound Poisson distribution $P_m(n)$ of detecting n secondary electrons after $m = 7$ stages of amplification. The probability distribution $P_m(n)$ is displayed for different δ_0 at stage g_1 , and using a secondary emission yield of $\delta = 2$ for all subsequent stages of amplification $g_{2..m}$ as recommended by respective experiments on single CEM detectors [48, 66, 67]. For sufficient high primary particle yield values δ_0 at the initial stage g_1 , the distribution will readily evolve into a quasi-Gaussian shape as illustrated in fig. 2.2. In comparison, the contribution of single probabilities $P_m(n)$ generating only a few or even no secondary electrons ($n = 0$) after m consecutive stages of amplification will therefore significantly decrease for considerable high primary particle yield values of δ_0 at stage g_1 . This decrease for a high initial yield δ_0 will become particularly important for the experimental choice of a discriminator level of any subsequent current or pulse processing electronics (see subsection 2.2.1).

⁶*Mathematica 7*, Wolfram Research.

The calculated compound Poisson distribution $P_m(n)$ in fig. 2.2 agrees with similar simulations for the first few stages up to $m = 5$ [50–54]. Moreover, the calculations additionally match with experimentally observed pulse height distributions of discrete dynode multipliers [68] and of conventional CEM detectors (e.g., [69, 70]). By theory, the calculated Poisson distribution $P_m(n)$ therefore determines the expected distribution of observed pulse heights at the dynode detector end. From the first moment of the distribution, the average gain G_0 of a given dynode detector will be determined (see subsection 3.1.2).

Although the numerical computation of the compound Poisson distribution $P_m(n)$ as illustrated in fig. 2.2 seems to be rather unchallenging for just a few stages of m with current computing resources, the final number of amplification stages m can easily exceed values of $m = 25$ for long CEM dynode tubes. Additionally, the expected average electron numbers will be in the order of $n_0 = 10^7 - 10^8$ (see subsection 3.1.1). The explicit calculation effort of the probability distribution via its recursive coefficients $P_m(n)$ will increase approximately polynomially. For practical purposes however, the compound Poisson distribution fortunately reaches its quasi-final shape already after a small number of amplification stages (i.e., 4 – 5 stages, [49]).

2.2. Detector quantum yield

Even more important, from the cascaded dynode model of the preceding section and the associated compound Poisson distribution $P_m(n)$ (eq. 2.2), the compound Poisson probability $P_m(0)$ of collecting *zero* electrons at the multiplier anode can be deduced. In this context, the compound Poisson probability $P_m(0)$ is in the following denoted as the ‘compound loss probability’. As a genuine result of the calculation of the probability $P_m(0)$, it allows to derive the quantum yield $\eta_{\text{detector}} = 1 - P_m(0)$ of a particular dynode detector [51, 53].

In detail, the compound loss probability $P_m(0)$ thus represents the accumulated probability that not a single electron ($n = 0$) is emitted after m consecutive stages of amplification in the dynode detector. In the particular case of CEMs, it hence corresponds to a secondary avalanche die-out in the CEM channel before reaching the channel end, resulting in no observable pulse of secondary electrons at the CEM anode. As a consequence, an incident primary particle on the detector will not be detected. Assuming $\delta_1 = \delta_0$ for the first amplification stage g_1 , and $\delta_{2..m} \approx \delta$ for all consecutive stages $g_{2..m}$, the compound loss probability⁷ is [51]

$$P_m(0) = \mathcal{F}_m(s = 0) = \exp[\delta_0(-1 + \underbrace{\exp[\delta(-1 + \dots + \exp[-\delta])]}_{m-1})]. \quad (2.5)$$

In the following, this particular formula will be used for the estimation of the maximum attainable quantum yield of a given dynode detector. Further note that the loss $P_1(0)$ of only the first stage g_1 compared to the whole compound loss probability $P_m(0)$ contributes with the fraction $P_1(0) = \exp[-\delta_0]$. The latter fraction therefore represents a measure for the unsuccessful conversion of the incident primary particle into the initial seed of the secondary electron avalanche in the detector. The efficiency of this first conversion stage g_1 becomes especially important if, e.g., the quantum yield of a CEM detector in combination with a conversion dynode is estimated (see subsection 2.3.2).

⁷From a detector point of view, this particular value resembles the probability of a non-detection of the incident primary particle at the dynode detector.

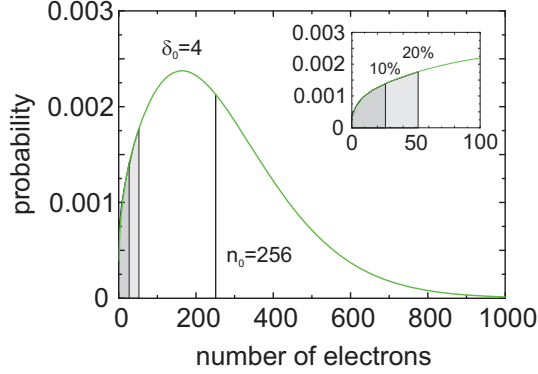


Figure 2.3: Calculated, compound probability distribution $P_m(n)$ of detecting n secondary electrons after $m = 7$ stages of amplification. For the calculation, $\delta_0 = 4$ and a fixed $\delta = 2$ are used (fig. 2.2). Inset: Zoom for the corresponding discriminator levels of 10% of n_0 ($n = 26$) and 20% ($n = 52$).

Following eq. 2.5, the maximum attainable quantum yield η_{detector} of a cascaded dynode⁸ detector is given by [51, 53]

$$\eta_{\text{detector}} = 1 - P_m(0) = \sum_{n=1}^{\infty} P_m(n) = 1 - \exp[\delta_0(-1 + \underbrace{\exp[\delta(-1 + \dots + \exp[-\delta])]}_{m-1})]. \quad (2.6)$$

Remarkably, in the preceding equation, the quantum yield η_{detector} is expressed only by means of the two secondary electron emission coefficients δ_0 and δ . As a result, the quantum yield of any given detector can in principle be determined from eq. 2.6, assuming that the two key emission parameters δ_0 and δ can be quantified, or even measured for the particular detector.

2.2.1. Finite discriminator level and detector quantum yield

Although the distribution in eq. 2.6 represents the theoretically attainable, maximum quantum yield of a detector, in the experiment the finite discriminator level of any subsequent current or pulse processing electronics will reduce η_{detector} of the corresponding detector by a certain amount [51]. However, from eq. 2.2 and eq. 2.5 the additional loss of pulses in pulse counting mode due to a finite discriminator level can be evaluated. The loss is, in terms of a reduced, maximum attainable quantum yield for the detector, defined as the additionally missed electrons $n > 0$ in the probability distribution $P_m(n)$ up to the applied discriminator level of f electrons per pulse [51],

$$\eta_{\text{disc}} = 1 - P_m(0) - \sum_{n=1}^f P_m(n) = \eta_{\text{detector}} - \sum_{n=1}^f P_m(n) = \sum_{n=f+1}^{\infty} P_m(n). \quad (2.7)$$

For experimental values of $\delta_0 = 4$ and $\delta = 2$, calculating for $m = 7$ stages of amplification, an average gain $G_0 \sim n_0 = 256$ is determined (n_0 denotes the mean value of n for the distribution

⁸CEMs, MCPs, or other discrete dynode multiplier detectors as, e.g., photomultiplier.

$P_m(n)$), for G_0 see subsection 3.1.1). As illustrated in fig. 2.3 and calculated by eq. 2.7, the maximum attainable quantum yield η_{detector} will be reduced by only 2.7% efficiency using a discriminator level⁹ of 10% (eq. 2.7; $f = 26$). For a discriminator level of 20%, this will rise to 6.8% efficiency ($f = 52$). As the shape of the probability distribution exhibits similar behavior for different $\delta_0 > 2$, a discriminator setting of 10% of the detector gain level will therefore not significantly reduce the maximum quantum yield of a given detector.

In pulse counting mode, the effect of space charge saturation will effectively compress and shift the pulse height probability distribution with fewer probabilities at lower gain voltages (see subsection 3.1.2). As a result, the contribution of missed pulses due to a reasonable discriminator level will become rather insignificant.

2.3. General design and operation criteria

In the following, general design and operation characteristics for a given dynode¹⁰ multiplier are investigated according to the two secondary electron emission yield values δ_0 and δ . The optimization of these two parameters will allow to produce a high quantum yield $\eta_{\text{detector}}(\delta_0, \delta)$ with the detector. As a result of these calculations, some fundamental predictions can be derived in the aspect of the general design and construction of a single dynode detector, or of an integrated dynode detection system, if a high quantum yield η_{detector} is to be obtained with these systems.

In this context, an important subject of investigation is especially the dependence of a high secondary emission yield δ_0 or δ for the subsequent development of the secondary electron avalanche in a given dynode detector. As it will turn out, the first stage g_1 of amplification resembles the *key* stage for the subsequent secondary electron development in the dynode detector, and for the therewith associated parameters like the compound loss probability $P_m(0)$ and the maximum attainable quantum yield η_{detector} . Moreover, the explicit impact of a high primary emission yield δ_0 on the quantum yield $\eta_{\text{detector}}(\delta_0, \delta)$ of the dynode detector is further studied.

As the analysis of this section remains on a more fundamental level of dynode detector theory, we will primarily continue with the generalized formulation of the secondary electron emission yield values δ_0 and δ . The use of this generalized yield values enables to qualify some basic predictions for a given dynode detector without further knowledge of any particular dependence of the two quantities δ_0 and δ on experimentally accessible parameters as particularly stated in section 2.4, and as measured in section 5.4.

However, the specific evaluation of more explicit relations on some of the experimentally accessible parameters for the single yield values δ_0 or δ with their associated quantum yield $\eta_{\text{detector}}(\delta_0, \delta)$ will be object of inquiry of section 2.4.

2.3.1. Compound loss probability

Figure 2.4(a) shows the calculated compound loss probability $P_m(0)$ to obtain *zero* electrons ($n = 0$) after m consecutive stages of amplification in the CEM detector in discrete steps up to $m = 30$. For the calculation according to eq. 2.5, the secondary emission yield for the second

⁹In the experiments, a discriminator level of up to 10% is commonly used for pulse counting applications.

¹⁰Although the considerations of this section are primarily applied to CEM detectors in the context of this thesis, they generally hold for any cascaded dynode detector or multiplier detection system where cascaded amplification stages g_m are involved.

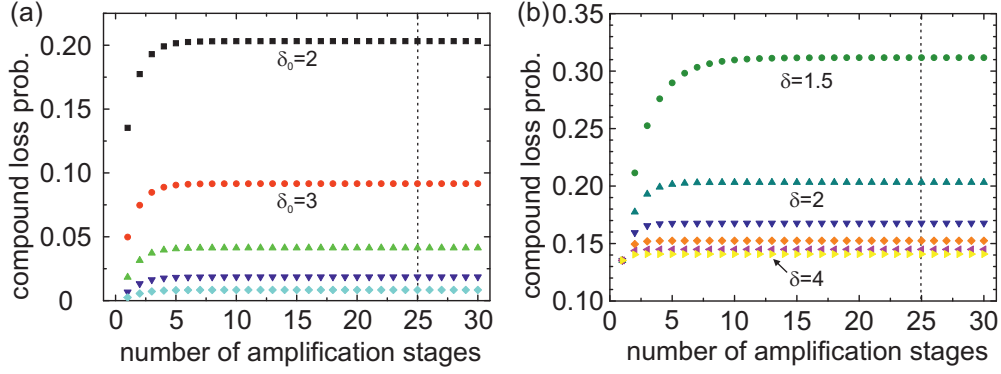


Figure 2.4: Calculated, compound loss probabilities $P_m(0)$ to obtain zero electrons ($n = 0$) after m consecutive stages of amplification in the CEM detector according to eq. 2.5. The dashed lines indicate $m = 25$ stages as used for the upcoming calculations as common CEM parameter. (a) Compound loss probability for different secondary electron emission yield values δ_0 at the first stage g_1 ($\delta_0 = 2, 3, \dots, 6$), using a generalised, secondary emission yield $\delta = 2$ for the consecutive stages $g_{2..m}$ [48]. (b) Compound loss probability after m amplification stages according to different secondary emission yield values δ ($\delta = 1.5, 2, \dots, 4$) for the consecutive stages $g_{2..m}$. For the calculations, the primary emission yield δ_0 at stage g_1 is set to a value of two.

to the m th stage is set to a common experimental value of $\delta_{2..m} = 2$ for conventional CEMs as suggested by [48, 66, 67]. Moreover, the calculated probabilities $P_m(0)$ are displayed for five different primary emission yield values $\delta_0 = 2, 3, \dots, 6$ for the first stage g_1 of amplification.

As illustrated in fig. 2.4(a), the calculated compound loss probability $P_m(0)$ converges already after a few amplification stages m to a finite, maximum loss probability $\lim_{m \rightarrow \infty} P_m(0)$ in accordance with calculations by [49, 51–54]. For primary emission yield values from $\delta_0 = 2–4$ (fig. 2.4(a)), the corresponding, maximum compound loss probabilities are $P_\infty(0) = 0.203$ for $\delta_0 = 2$, $P_\infty(0) = 0.092$ for $\delta_0 = 3$, $P_\infty(0) = 0.042$ for $\delta_0 = 4$, and $P_\infty(0) = 0.019$ for $\delta_0 = 5$. In the aspect of convergence, a compound loss probability of $P_m(0) \geq 0.99 P_\infty(0)$ is reached only after $m = 4–7$ stages of amplification for each of the values of δ_0 , similar to simulations by [51]. Consequently, the first few stages $g_{1..m}$ (i.e., $m \leq 10$) of amplification in the multiplier resemble the *key* stages for the development of the secondary electron avalanche in the CEM. This results as later amplification stages g_m do not contribute macroscopically to the compound loss probability $P_m(0)$ once a sufficient secondary electron avalanche is started at the initial stages.

In addition to fig. 2.4(a), also the influence of the variation of the generalized secondary emission yield $\delta = \delta_{2..m}$ on the compound loss probability $P_m(0)$ for the second to the m th stage is analyzed. For the calculations, in this case the primary emission yield δ_0 is set to a fixed value of $\delta_0 = 2$. Accordingly, in fig. 2.4(b) the calculated compound loss probability $P_m(0)$ is displayed for different values of δ , and for $m = 30$ consecutive stages of amplification (eq. 2.5). Similar to the variation of the primary emission yield δ_0 in fig. 2.4(a), the calculated probabilities converge after a few stages m of amplification. The corresponding, maximum compound loss probabilities are $P_\infty(0) = 0.311$ for $\delta = 1.5$, $P_\infty(0) = 0.203$ for $\delta = 2$, $P_\infty(0) = 0.168$ for $\delta = 2.5$, $P_\infty(0) = 0.152$ for $\delta = 3$, and $P_\infty(0) = 0.141$ for $\delta = 4$. In comparison to the preceding calculations of a variation in δ_0 , there is a slightly reduced maximum loss probability for higher values of δ . This leaves the initial conversion of the

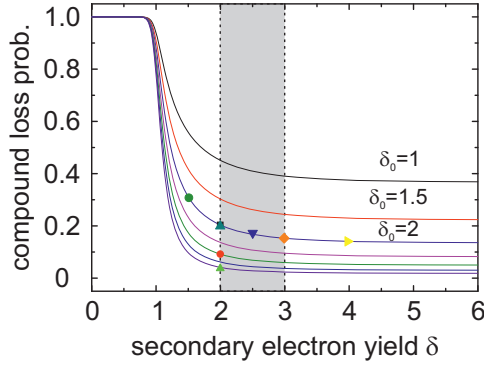


Figure 2.5: Calculated, maximum loss probability $P_m(0)$ after $m = 30$ stages of multiplication, according to different secondary emission yield values δ , and for different primary emission yield values of δ_0 ($\delta_0 = 1, 1.5, \dots, 4$). The shaded area indicates common experimental values of $\delta = 2 - 3$ for CEM detectors [48, 66, 67], old/fatigued detectors will range at values of $\delta < 2$. The parameter of the corresponding calculated curves of fig. 2.4(a,b) are indicated by coloured symbols.

incident primary particle at the first stage g_1 with its associated primary emission yield δ_0 as the crucial stage for an efficient amplification of an incident particle in the CEM detector.

To demonstrate the importance of the primary emission yield δ_0 at the first stage g_1 in contrast to the secondary emission yield δ at the consecutive stages $g_{2..m}$ of amplification, in fig. 2.5 the calculated compound loss probability $P_m(0)$ after $m = 30$ stages according to eq. 2.5 is shown. Here, the loss probability $P_m(0)$ is computed for different primary emission yield values δ_0 , according to a variation in the generalized secondary electron yield value δ for the consecutive amplification stages $g_{2..m}$ in the detector. The shaded area in fig. 2.5 indicates typically observed, secondary electron yield values of $\delta = 2 - 3$ for conventional CEMs after burn-in phase [48, 66, 67]. Note that old or fatigued CEM detectors will range at values of $\delta < 2$ [48].

As illustrated in fig. 2.5, for any given primary emission yield δ_0 , an increase of the secondary emission yield δ above values of $\delta > 3$ will produce no significant reduction in the maximum loss probability $P_m(0)$, and likewise an increase in the quantum yield of the corresponding detector as stated by eq. 2.6. From a point of view of conventional CEM design, the obtained secondary electron yield values of $\delta \approx 2 - 3$ are thus already almost optimized for commercially manufactured CEMs, if one considers the secondary emission yield δ of the active secondary emitting surface for the consecutive amplification stages $g_{2..m}$. On the contrary, an increase of the primary particle yield δ_0 will macroscopically reduce the calculated maximum loss probability $P_m(0)$ for high values, as already illustrated in fig. 2.4(a). As a result, an increase in the primary particle yield δ_0 will still significantly enhance the associated maximum attainable quantum yield η_{detector} of a given CEM detector as expressed by eq. 2.6.

To further illustrate the influence of the primary emission yield δ_0 on the whole secondary avalanche buildup process, in fig. 2.6 the probability $P_1(0, \delta_0) = e^{-\delta_0}$ of generating *zero* secondary electrons at primary particle impact is shown. Consequently, this will create an early secondary avalanche die-out in the CEM channel as no secondary electrons are propagated to the second stage g_2 of amplification in the CEM. For the determination of the preceding probability $P_1(0, \delta_0)$, only the first stage of amplification g_1 in the detector is used in eq. 2.1, correspondingly. Further note that the conversion efficiency $\eta_{\text{prm}} = 1 - P_1(0, \delta_0) = 1 - e^{-\delta_0}$

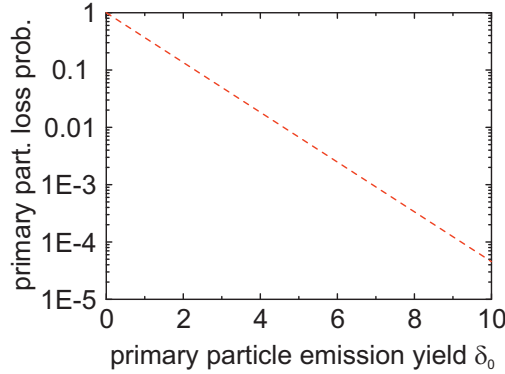


Figure 2.6: Primary particle loss probability according to δ_0 at the first stage of amplification g_1 (primary particle impact; fig. 2.1). The calculated probability represents the possibility that the incident primary particle is not converted, and therefore no secondary electron avalanche is initiated in the dynode detector.

of an incident primary particle at primary particle impact (fig. 2.1) can be derived from the probability $P_1(0, \delta_0)$.

For values of $\delta_0 = 4$ as typically observed for new CEMs [48], there is a calculated probability of only $P_1(0, 4) \simeq 0.018$ that, e.g., an incident electron as primary particle will not be converted into any secondary electrons, and thus *not* start a secondary electron avalanche within the detector. For old or fatigued CEMs with $\delta_0 = 2$ [48], this probability will rise to $P_1(0, 2) \simeq 0.135$, revealing already a significant loss of incident primary particles at first stage g_1 which are not converted and amplified, and thus remain undetected. The conversion of the primary particle at first impact becomes especially important, if a conversion dynode is used in front of the CEM detector to enhance the quantum yield $\eta_{\text{detector}}(\delta_0, \delta)$ of the particular detector (see subsection 2.3.2).

Finally, the maximum attainable quantum yield $\eta_{\text{detector}} = \eta_{\text{detector}}(\delta_0, \delta)$ according to eq. 2.6 is calculated for $m = 30$ stages of amplification. The quantum yield is displayed in fig. 2.7 for different secondary emission yield values δ according to the primary particle yield δ_0 . For common experimental, primary emission yield values of $\delta_0 = 2 - 4$, and a secondary yield value of $\delta = 2$, a maximum attainable quantum yield η_{detector} ranging from $\eta_{\text{detector}}(\delta_0 = 2, \delta = 2) = 0.797$, $\eta_{\text{detector}}(3, 2) = 0.908$, and $\eta_{\text{detector}}(4, 2) = 0.959$ is determined. In comparison to this, for a fixed primary emission yield value of $\delta_0 = 2$, and a corresponding variation in the secondary emission yield $\delta = 2 - 4$, a calculated quantum yield of $\eta_{\text{detector}}(2, 2) = 0.797$, $\eta_{\text{detector}}(2, 3) = 0.848$, and $\eta_{\text{detector}}(2, 4) = 0.859$ will be obtained. Consequently, the maximum attainable quantum yield $\eta_{\text{detector}}(\delta_0, \delta)$ as stated by eq. 2.6 will be influenced more by an increased value δ_0 compared to a similar increase in δ . Note that for the previous calculations, the particular choice of the two emission parameter δ_0 and δ corresponds to common experimental secondary emission yield values obtained by [48, 66, 67], and indicated by the shaded area in fig. 2.7. Additionally note that similar values are observed in the efficiency calibration measurements (see subsection 5.4.1).

In addition to that, in the particular case of considerable high quantum efficiencies with a given CEM detector, an increase in the quantum yield $\eta_{\text{detector}}(\delta_0, \delta)$ will almost only be obtained by further raising the primary emission yield δ_0 . For example, a detector with a maximum attainable quantum yield $\eta_{\text{detector}}(\delta_0, \delta)$ exceeding 99% will need a primary particle

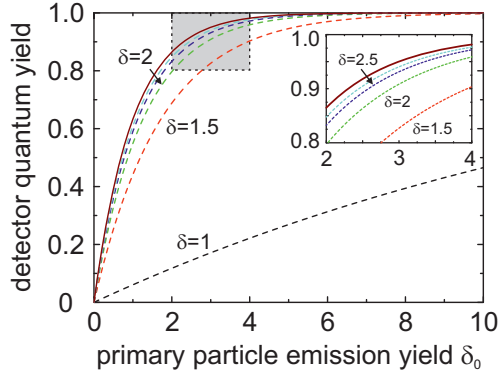


Figure 2.7: Maximum attainable quantum yield η_{detector} according to eq. 2.6 for different values of the primary particle emission yield δ_0 . For comparison, various values of the secondary yield $\delta = 1, 1.5, \dots, 3$ of the consecutive stages $g_{2..m}$ are depicted (dashed lines; solid black line for $\delta \gg 1$). Common CEM values range from $\delta = 2 - 3$. Inset: Zoom of the shaded area, showing the maximum attainable quantum yield for primary particle emission yield values of $\delta_0 = 2 - 4$ as measured in our experiments.

yield of $\delta_0 > 5.8$. A quantum yield $\eta_{\text{detector}}(\delta_0, \delta)$ exceeding 99.9% will demand a primary particle yield value of $\delta_0 > 8.7$. Note that in the previous calculations a value of $\delta = 2$ is employed in both cases. However, using an even more emissive dynode material for the CEM channel with, e.g., a secondary emission yield¹¹ of $\delta = 10$ will only lower the demanded, primary emission yield δ_0 to values of $\delta_0 > 4.6$, and to $\delta_0 > 6.9$, respectively, if similar quantum yield values $\eta_{\text{detector}}(\delta_0, \delta)$ as in the previous example are to be generated.

2.3.2. Conversion dynodes

Although sometimes underestimated, the use of conversion dynodes can yield a huge benefit to further increase the secondary electron yield δ_0 of an incident particle at primary particle impact, and on the quantum yield η_{detector} of a subsequent CEM detector (eq. 2.7). In the literature, several dynode materials have been evaluated according to different incident particles: (a) ions [51, 62, 66, 71–75], (b) electrons [62, 68, 75–78], or (c) photons [79, 80]. By incorporation of a dynode into a CEM detection system as primary conversion stage g_1 for the incident primary particle *before* the actual CEM detector, a dynode will effectively substitute a probably inefficient particle conversion at primary impact in the CEM (fig. 2.1), serving as an efficient seed of the subsequent secondary avalanche in the CEM.

Considering the primary emission yield δ_0 at primary particle impact, metal surfaces typically display secondary emission yield values δ_0 of up to two [62, 76, 81–84], whereas specifically emissive materials as BeO or Al₂O₃ will exhibit $\delta_0 > 5$ even for incident angles of $\theta = 0^\circ$ [51, 62, 71, 73, 76, 82]¹². In comparison, the secondary emission yield δ_0 of an active CEM lead glass surface will yield substantially less [66, 67, 75]. By proper choice of the dynode material and conversion of the incident particle, a secondary electron yield of up to $\delta_0 = 20$

¹¹This value is rather theoretical as common experimental values usually range only between $\delta = 2 - 4$ [48, 66, 67].

¹²Interestingly, corresponding values for several different, singly charged alkali species are explicitly stated in [72].

can be reached for, e.g., the primary impact of incident ^{85}Rb -ions, as measured by Ref. [72]¹³. For such particular high values of δ_0 , approximately only the conversion loss of the primary particle determines the quantum yield η_{detector} of a given CEM detector.

As an illustrating example therefore, one can estimate the quantum yield $\eta_{\text{detector}}(\delta_0)$ for a secondary emission parameter of $\delta_0 = 20$ at primary particle impact. Assuming that, e.g., only 50% (i.e., $\eta_{\text{col}} = 0.5$) of all secondary electrons emitted by the primary emission out of the conversion dynode are collected¹⁴ in the CEM, and are subsequently amplified, one will still end up with an estimated quantum yield of $\eta_{\text{detector}}(\delta_{10}) \sim 1 - e^{-\delta_{10}} \sim 0.99995$ for this yield value by the use of an efficient dynode.

2.3.3. Obtaining a high quantum yield

In summary of the considerations of the preceding subsections, the first few stages $g_{1..m}$ of amplification in any dynode multiplier generally resemble the important stages for the development of the secondary electron avalanche in the detector [49, 51–54]. This results as later amplification stages g_m do not contribute macroscopically to the compound loss probability $P_m(0)$ once a sufficient secondary electron avalanche is started at the initial stages (fig. 2.4). However, an already low primary particle yield δ_0 at the initial conversion stage g_1 will lead to a substantial loss of incident primary particles (fig. 2.6). This initial loss cannot be compensated by any high secondary emission yield δ of the consecutive amplification stages $g_{2..m}$. The latter observation leaves the initial conversion of the incident primary particle at the first stage g_1 with its associated primary emission yield δ_0 as the *key* stage for an efficient conversion and amplification of the particle in the CEM detector.

In consequence, if one intends to obtain a high quantum yield η_{detector} for incident single particles using a commercial CEM detector, in any case one is essentially bound in improving the primary emission yield δ_0 at primary particle impact in the detector. This follows as for conventional CEM detectors the secondary emission yield δ is already considerably predefined by the shape, material, and fabrication of the particular CEM. However, the generalized secondary electron yield δ of the subsequent amplification stages $g_{2..m}$ is comparably optimized in conventional CEM detectors (fig. 2.5). The latter conclusion is further supported by experimentally observed values for the secondary emission yield in CEMs of $\delta = 2 - 3$ by [48, 66, 67].

Moreover, the use of conversion dynodes can produce a huge increase in the primary particle yield δ_0 of an incident particle at primary particle impact, and thus on the quantum yield η_{detector} of a subsequent CEM detector (see subsection 2.3.2). As multiple secondary electrons are generated at primary particle impact by an adequate choice of an efficient conversion dynode, a probably inefficient primary particle conversion in the CEM detector can thus be compensated. The installation of an additional conversion dynode in front of a CEM detector may thereby significantly increase the quantum yield $\eta_{\text{detector}}(\delta_0, \delta)$ of the corresponding detector.

In conclusion, one has to optimize the primary emission yield δ_0 at primary particle impact in the CEM detector, if a detection of single particles with a high quantum yield $\eta_{\text{detector}}(\delta_0, \delta)$ is required, and conventional CEMs as detecting units are to be used.

¹³Using a dynode material of Al_2O_3 , with the primary ^{85}Rb -ions being under grazing incidences ($\theta = 70^\circ$) and at kinetic impact energies of $E_{\text{kin}} = 29.6$ keV.

¹⁴A collection and amplification of only 50% of the secondary electrons emitted from the dynode by the CEM will simply correspond to $\delta_{10} = \frac{1}{2} \cdot 20 = 10$.

2.4. Absolute detection efficiency

This section defines and describes important parameters for the absolute detection efficiency η_{det} of an integrated dynode detector within a single particle detection system. Based on the theoretical definition of section 2.2, it specifically investigates the quantum yield η_{detector} of a dynode detector according to the primary emission yield δ_0 , and the generalized secondary emission yield δ . In particular, it relates the quantum yield $\eta_{\text{detector}} = \eta_{\text{detector}}(\delta_0, \delta)$ of a given CEM detection system to two experimentally accessible parameters, which are the kinetic energy E_{kin} at primary particle impact, and the incident angle θ at particle impact. As both quantities are comparably defined by the impact position of the incident primary particle in the corresponding dynode detector, an explicit relation for $\delta_0 = \delta_0(E_{\text{kin}}, \theta)$ according to the parameters E_{kin} and θ can be derived. As a genuine result, the maximum attainable quantum yield $\eta_{\text{detector}} = \eta_{\text{detector}}(\delta_0, \delta)$ of any given detector in a single particle detection system can thus be estimated, provided that the impact position of the incident primary particle in the dynode detector with its associated parameters E_{kin} and θ is known.

2.4.1. Collection efficiency and detector quantum yield

The absolute detection efficiency η_{det} of any particle detection system is defined as the probability for an incident particle (charged or neutral particle, or a photon) at the input of the detection system to produce an observable output pulse. Based on this definition, η_{det} can be separated into two components,

$$\eta_{\text{det}} = \eta_{\text{col}} \eta_{\text{detector}}, \quad (2.8)$$

where η_{col} is the collection efficiency, and η_{detector} is the quantum yield of the bare detector¹⁵. Consequently, the absolute detection efficiency includes all possible sources of eventual particle losses at every stage of the detection process.

In the case of a reduced collection efficiency $\eta_{\text{col}} < 1$, possible particle losses generally result from: (a) collecting only a fraction of the incident primary particles due to, e.g., a reduced solid angle ($\Omega < 4\pi$) of the imaging system, (b) transmission losses as, e.g., caused from an applied biased grid¹⁶ attached to the bare detector, or (c) conversion losses at supplementary primary particle conversion elements as, e.g., scintillation crystals or conversion dynodes. However, the collection efficiency η_{col} for the charged photoionisation fragments of the joint CEM detection system in this thesis is assumed to be unity. This results from the particular arrangement of the CEM detection system as investigated in subsection 4.4.3. Therefore, for a qualitative description of the detection efficiency η_{det} of the entire detection system only the respective quantum yield η_{detector} of the used CEM detectors has to be calibrated. Nevertheless, the absolute detection efficiency in conventional detection systems usually corresponds to eq. 2.8, with a reduced collection efficiency $\eta_{\text{col}} < 1$ (see subsection 2.4.2).

In the case of the quantum yield η_{detector} , the particular quantum yield of a CEM detector as stated by eq. 2.6 can generally be associated with two fundamental quantities (see section 2.1). These quantities are the primary emission yield δ_0 of the first emission stage g_1 in the CEM

¹⁵In general, this parameter has to be substituted by η_{disc} in the experiments as the discriminator level of any subsequent current or pulse processing electronics will be finite (see subsection 2.2.1).

¹⁶In common CEM detection systems, a biased grid is attached to the front of the CEM detector. The grid ensures a high homogeneity of the internal CEM fields in the cone, and prevents entrance from stray charges (e.g., [85]).

detector, and the generalized secondary emission yield δ of the subsequent stages $g_{2..m}$ of amplification. As a result, the absolute detection efficiency η_{det} of the used CEM detection system of this thesis work can be reduced to the secondary emission yield of the individual CEMs with their corresponding parameters δ_0 and δ .

Detector quantum yield and emission yield parameters δ_0 and δ

In the experiment, the primary emission yield δ_0 in a CEM detector generally depends on: (a) the incident primary particle type (charged or a neutral particle, or photon), and the associated particle parameters as, e.g., the mass, or the mass to charge ratio, (b) the kinetic energy E_{kin} of the primary particle at impact in the active CEM surface (primary particle impact; fig. 2.1), (c) the incident angle θ of the primary particle to the surface normal at the impact position (fig. 2.8), and (d) the particular material, layer thickness, or doped constituents of the active surface layer (hydrogen reduced lead glass (SiO or SiO₂) [66, 67, 86], or additionally coated with, e.g., MgO [75]).

Although almost all of these parameters substantially influence the primary emission yield δ_0 of a given CEM detector, the *key* quantities are the kinetic energy E_{kin} , and the incident angle θ of the primary particle at impact are the essential parameters. Note that for a given CEM detector, these are the only experimentally accessible quantities which can effectively be altered to improve the parameter δ_0 , leading to an optimized quantum yield η_{detector} .

Correspondingly to δ_0 , the generalized secondary emission yield δ for the subsequent amplification stages $g_{2..m}$ in the CEM depends on: (a) the particular material, layer thickness, or doped constituents of the active surface layer in the CEM detector, (b) the individual CEM detector geometry (curved or straight channel structure), and (c) the applied CEM gain voltage U_{CEM} over the CEM detector (fig. 2.1).

Although the secondary emission parameter δ individually depends on all these different properties, it can usually be assumed to be uniform for all consecutive secondary emission stages $g_{2..m}$ along the entire CEM channel for a fixed gain voltage U_{CEM} [47, 48]. For a conventional CEM detector therefore, a variation in gain voltage U_{CEM} remains as the only free parameter if one wants to experimentally influence¹⁷ δ . Accordingly, an increase in gain voltage U_{CEM} , and thus in δ , results in enhanced CEM detection efficiencies (e.g., [87, 88]). Particularly this effect will be used later on to achieve uniform detection efficiencies over the entire sensitive area $A_{i,e}$ of both CEM detectors (see section 5.5.1).

However, reconsidering the influence of both emission parameters δ_0 and δ , for reasonable high values of δ_0 even large values of $\delta > 2$ will not affect the quantum yield η_{detector} of a CEM detector (see section 2.3). At the end, the primary particle emission yield δ_0 with its two associated dependencies $\delta_0(E_{\text{kin}})$ and $\delta_0(\theta)$ at primary particle impact is thus the parameter of choice, if an optimization in the absolute detection efficiency η_{det} of a given CEM detector system is intended. Further note that both parameters strongly depend on the

¹⁷Note that the generalised secondary electron yield δ assumes that all secondary electrons at a stage g_m have an identical acquired kinetic energy $\bar{E}_{\text{kin},m}$ at re-impact in the active CEM surface at the subsequent amplification stage g_{m+1} (fig. 2.1) [47, 60, 61]. However, these kinetic energies $\bar{E}_{\text{kin},m}$ generally depend on the CEM gain voltage U_{CEM} , and on the number m of subsequent amplification stages g_m in the CEM. For the CEMs used in the context of this thesis, calculated values are $\bar{E}_{\text{kin},m} = 80 \text{ eV}$ for $U_{\text{CEM}} = 2 \text{ keV}$, and $\bar{E}_{\text{kin},m} = 120 \text{ eV}$ for $U_{\text{CEM}} = 3 \text{ keV}$ ($\bar{E}_{\text{kin},m} \approx U_{\text{CEM}}/m$; assuming $m = 25$ [48]). Thus, by raising the CEM gain U_{CEM} , this allows to some extent to increase the secondary emission yield δ in the CEM corresponding to higher kinetic energies $\bar{E}_{\text{kin},m}$, as suggested by [60, 61] and explicitly measured by [66].

impact position of the primary particle in the particular CEM, whether it be a cone hit or a channel hit in the CEM detector.

As a result, in the experiment an optimization of $\delta_0(E_{\text{kin}}, \theta)$ at primary particle impact will maximize the quantum yield η_{detector} of a given CEM detector, and therefore push the absolute detection efficiency η_{det} of the entire detection system to its limiting extremes. In the following, we will therefore focus on the individual dependency and optimization of the primary particle yield δ_0 according to the impact energy E_{kin} and the incident angle θ at primary particle impact.

2.4.2. Kinetic impact energy

In the past, there has been a considerable effort to measure the quantum yield η_{detector} of a given CEM detector, and to calibrate a particular CEM detector within a detection system with absolute efficiency values. Nevertheless, until today there is still no generally agreed response function for the quantum yield $\eta_{\text{detector}} = \eta_{\text{detector}}(E_{\text{kin}})$ of a CEM detector to the kinetic energy E_{kin} of an incident primary particle. In the literature, there are numerous efficiency calibrations of CEM detectors in pulse counting mode for the detection of incident electrons [48, 89–94], various species of positive ions (for low energy ions $E_{\text{kin}} < 10$ keV [89, 91, 95–106], for highly-energetic ions $E_{\text{kin}} > 10$ keV [95, 107]), for negative ions [101, 104, 108], photons [80, 109–115], and for neutral atoms [116, 117]. However, all these individual calibration attempts display at least partially huge discrepancies in the observed efficiency values [48]. Moreover, even as identical CEM models are used in several of the calibration measurements, the particular experiments still show a large variety in the observed quantum yield values of the individual CEM detectors (see, e.g., compilation by [48] for identical CEM models).

Although the individual experimental systems differ significantly from each other, the observed deviations in η_{detector} can basically be attributed to two possible error sources in the calibration measurements: (a) the accidental simultaneous influence of η_{col} in addition to the actual quantum yield η_{detector} of the bare CEM detector (eq. 2.8), i.e., unintentionally measuring the varying product $\eta_{\text{col}}\eta_{\text{detector}}$ instead of the isolated raw quantum yield η_{detector} of the CEM detector as stated by eq. 2.6, (b) the efficiency determination methodology used itself, i.e., in most cases the accuracy of a *relative* calibration of the unknown detector to a specific precalibrated source or detector (see section 5.1).

Concerning the collection efficiency η_{col} for the calibration measurements, in many of the above systems a *reduced* collection efficiency $\eta_{\text{col}} < 1$ is accidentally introduced in the calibration measurements. Such a reduced collection efficiency is given, e.g., by the application of a biased grid¹⁸ in front of the CEM detector. Additionally, in many experimental systems the parameters η_{col} and η_{detector} are often not even properly specified or generally ill defined. Consequently, in particular the impact position of the primary particle in the CEM and the therewith attributed kinetic energy E_{kin} at primary particle impact remain comparably undefined in many systems. In addition, for low kinetic particle energies E_{kin} at cone entrance¹⁹, the internal field of the CEM caused by the gain voltage U_{CEM} will macroscopically affect the kinetic energy E_{kin} of the primary particle at impact in the CEM surface (see subsec-

¹⁸For the transmission of a metal grid structure, the technically maximum attainable open surface area peaks at approximately 95%, correspondingly reducing the collection efficiency down to this value.

¹⁹In the literature, for the quantum yield response $\eta_{\text{detector}} = \eta_{\text{detector}}(E_{\text{kin}})$ of a CEM detector, the kinetic energy E_{kin} of the incident primary particle is usually stated only to the cone entrance of the CEM detector.

tion 4.3.4). A comparison of the efficiency values of any such system is therefore generally difficult, even for identical CEM models [48].

Referring to the second of the above mentioned error sources, one should note that almost all published calibration measurements are based on *relative* measurements only, not on an absolute measurement method (see section 5.1). As a consequence, many of the above systems are referenced only relatively to a precalibrated particle source, or a second precalibrated detector (see subsection 5.1.1). Strictly speaking therefore, in all these calibration measurements no absolute efficiency values or an explicit quantum yield η_{detector} as expressed by eq. 2.6 can be stated. On the contrary, the described CEM detection system of this thesis will rely on an absolute efficiency calibration method based on coincident counting of two simultaneously generated ionisation fragments (see section 5.1). As the collection efficiency η_{col} of this detection system is assumed to be one (see subsection 4.4.3), the CEM detectors can be calibrated to absolute efficiency values.

Linear approach and reduced yield curve approach

Although there is no generally agreed response function of the quantum yield $\eta_{\text{detector}} = \eta_{\text{detector}}(E_{\text{kin}})$ of a CEM detector, in the literature there are two phenomenological approaches for η_{detector} in correspondence to the kinetic energy of the incident primary particle. Both approaches are based on fundamental considerations²⁰ of the subsequent kinetic emission of secondary electrons out of a surface after the impact of an incident primary particle [64, 65, 118–120]. As a result, both approaches relate the CEM quantum yield η_{detector} to the primary emission yield δ_0 of the incident primary particle at primary particle impact in the CEM (fig. 2.1, primary particle hit).

The first approach is associated to the potential and kinetic emission of secondary electrons depending on the impact velocity of the primary particle, and the incident primary particle type. This initial approach is based on calculations of [121], and results in a linear increase of the secondary electron emission yield $\delta_0(v_{\text{kin}}, v_{\text{thres}}) \sim k \cdot (v_{\text{kin}} - v_{\text{thres}})$ with increasing impact velocity v_{kin} of the incident particle (e.g., reviews by [62, 122]). The secondary electron emission starts at a minimum threshold velocity v_{thres} under which no secondary electrons are emitted from the active CEM surface. The quantum yield of the CEM is then stated to be linearly proportional to the velocity of the incident particle as [122]

$$\eta_{\text{detector}}(v_{\text{kin}}, v_{\text{thres}}) \sim \delta_0(v_{\text{kin}}, v_{\text{thres}}) \cdot Z = k \cdot (v_{\text{kin}} - v_{\text{thres}}) \cdot Z, \quad (2.9)$$

where Z is the atomic number of the incident particle, δ_0 is the primary emission yield, and k denotes a constant.

Although this approach is successful for the description of the quantum yield η_{detector} and its associated primary emission yield δ_0 within a certain range of velocities v_{kin} , the response of $\delta_0(v_{\text{kin}})$ is significantly different to a linear increase for considerable low values next to the threshold velocity v_{thres} [62]. Moreover, for high values of v_{kin} , saturation of the primary emission yield δ_0 is observed experimentally [62, 81–83, 118], but cannot be described by this

²⁰In the secondary emission theory, after interaction with the incident primary particle there is a certain probability for a secondary electron to leave the bulk material without being re-adsorbed by the solid. By theory, the emission probability of a secondary electron is generally associated with the skin depth l_λ of the primary particle in the solid, i.e. the depth in the solid where the secondary electron is liberated by the primary particle.

particular approach. Consequently, the linear approximation²¹ of the quantum yield of the CEM detector as stated by eq. 2.9 is only applicable to a certain, reduced range of kinetic energies for the incident primary particle. Although used in the literature [122, 124], it seems that the linear approach is only a limiting special case relating to a more general description of the quantum yield of a CEM detector. In the following, we will therefore focus on the second approach only.

The second approach for the CEM efficiency response goes back to theoretical work of [119, 125]. It introduces a universal reduced secondary emission yield curve for the primary emission yield $\delta_0(E_{\text{kin}})$, and to $\delta(E_{\text{kin}})$, according to the kinetic energy of the incident particle. Remarkably, the global shape of this universal reduced yield curve is assumed to be applicable to any type of incident primary particle, and for any secondary emitting surface [125]. Furthermore, the reduced yield curve characteristic describes quantitatively the global shape of many different primary emission yield measurements for different materials, and different incident primary particles [62, 81, 82, 118]. With respect to the CEM efficiency response of this approach, the second approach is based on two parts [48, 92]. The first part consists of the cascaded continuous dynode CEM model as introduced in section 2.1. The second part incorporates the global characteristic of the universal reduced yield curve of the secondary emission yield $\delta_0(E_{\text{kin}}, E_{\delta_0, \text{max}}, \delta_{0, \text{max}})$, and $\delta(E_{\text{kin}}, E_{\delta, \text{max}}, \delta_{\text{max}})$, respectively, into the quantum yield $\eta_{\text{detector}} = \eta_{\text{detector}}(\delta_0, \delta)$ of the CEM detector, as stated by eq. 2.6.

In more detail, the first part of the CEM efficiency response approach is associated with the maximum attainable quantum yield $\eta_{\text{detector}} = 1 - P_m(0)$, where the compound loss probability $P_m(0)$ of all subsequent stages $g_{1..m}$ for the secondary electron avalanche in the CEM is defined by eq. 2.5. Note that the loss probability $P_m(0)$ and therefore the associated quantum yield $\eta_{\text{detector}} = \eta_{\text{detector}}(\delta_0, \delta)$ is expressed only in terms of the emission parameters δ_0 and δ [92]. In the second part of the CEM efficiency response approach, the two secondary emission parameters δ_0 and δ at any cascade stage g_m are now individually characterised by the reduced yield curve according to the kinetic particle energy E_{kin} of the incident primary particle at impact [48].

Although the *global* shape of the universal reduced yield curve is independent on surface or incident particle type [125], to obtain explicit yield values δ_0 and δ , the individual emission properties for a particular surface are specified by two material associated parameters $\delta_{0, \text{max}}$ and $E_{\delta_{0, \text{max}}}$. Accordingly, the parameter $\delta_{0, \text{max}}$ is the maximum primary particle emission yield $\delta_{0, \text{max}} \approx \delta_0(E_{\delta_{0, \text{max}}})$ with the corresponding kinetic energy value $E_{\text{kin}} \approx E_{\delta_{0, \text{max}}}$ at primary particle impact. For kinetic particle energies E_{kin} lower or higher than the latter energy, the primary emission yield δ_0 will generally decrease with respect to the maximum attainable value at $E_{\delta_{0, \text{max}}}$ as observed in various primary emission experiments (see, e.g., compilation by [62], or [76, 81, 82, 118, 120, 126]). Although extensively measured for electrons as incident primary particles, for incident ions it appears that both parameters $E_{\delta_{0, \text{max}}}$ and $\delta_{0, \text{max}}$ are shifted to considerably higher values [62, 127], respectively.

Combining both previously introduced parts of the second approach, the response of the quantum yield $\eta_{\text{detector}} = \eta_{\text{detector}}(\delta_0, \delta)$ according to the kinetic energy E_{kin} of the primary particle at primary impact in the representation of [48, 66] reads

²¹In the past, there have been attempts to expand the linear approach by a Taylor series in the velocity component into a polynomial description of the primary emission yield $\delta_0(v_{\text{kin}}, v_{\text{kin}}^2, \dots)$ [73, 105, 123]. Although some observations are quantitatively well described by the individual fittings, the polynomial approach lacks a universal description of the observed phenomena, with the obtained parameters more or less referring only to the individual characteristic of the particularly measured data set.

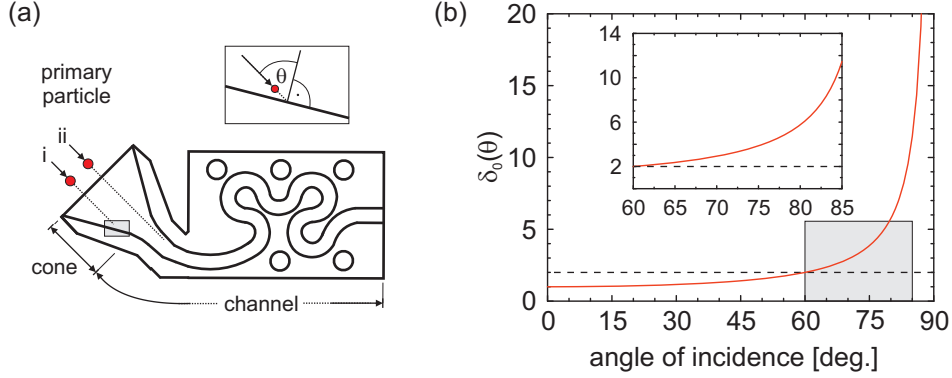


Figure 2.8: (a) CEM cone hit i in contrast to a channel hit ii at grazing incident angle θ of the primary particle at surface impact (primary particle hit, stage g_1 , fig. 2.1). Inset: Zoom of shaded area displaying the definition of the incident angle θ . (b) Relative dependency of the primary emission yield $\delta_0(0^\circ)$ according to the angle of incidence θ to the surface normal as stated by eq. 2.12. For comparison, a common CEM cone impact under an angle of $\theta = 60^\circ$ is indicated by the dashed line. Inset: Zoom for relative values from $\theta = 60^\circ - 85^\circ$.

$$\eta_{\text{detector}}(\delta_0, \delta) = 1 - \exp[\delta_0(-1 + \underbrace{\exp[\delta(-1 + \dots + \exp[-\delta])]}_{m-1})\dots], \quad (2.10)$$

where

$$\delta_0 = \delta_0(E_{\text{kin}}, E_{\delta_0, \text{max}}, \delta_{0, \text{max}}) = \frac{1 - \exp[-z^{1.35}]}{0.725 z^{0.35}} \cdot \delta_{0, \text{max}}, \quad (2.11)$$

and $\delta = \delta(E_{\text{kin}}, E_{\delta, \text{max}}, \delta_{\text{max}})$, correspondingly. In eq. 2.10, the parameter δ_0 is the primary emission yield, δ denotes the generalized secondary emission yield of all subsequent stages $g_{2..m}$ of amplification, and m is the number of amplification stages in the CEM until the generation of a macroscopic pulse at the CEM end. In eq. 2.11, the parameter E_{kin} represents the kinetic energy of the primary particle at impact in the secondary emitting surface of the CEM, and $\delta_{0, \text{max}}$ is the maximum emission yield $\delta_{0, \text{max}} = \delta_0(E_{\delta_0, \text{max}})$ with the energy value $E_{\text{kin}} = E_{\delta_0, \text{max}}$ (correspondingly, $\delta_{\text{max}} = \delta(E_{\delta, \text{max}})$ where $E_{\text{kin}} = E_{\delta, \text{max}}$). Note that the explicit value in the parameter $z = 1.8431 E_{\text{kin}}/E_{\delta_0, \text{max}}$ in eq. 2.11 represents a generally accepted, experimental fit parameter for the global reduced yield curve characteristic from various independent emission experiments [48, 125]. Nevertheless, although the obtained parameter quantitatively describes the universal emission yield properties of many metal, semiconducting, and isolating surfaces, this introduced parameter leaves the second approach of the CEM efficiency response as stated by eq. 2.10 still basically phenomenological. Further note that for calculations, the parameter m in eq. 2.10 is chosen to be $m = 25$ [48]. Moreover, assuming that the collection efficiency η_{col} attains unity as introduced in subsection 2.4.1, the absolute detection efficiency η_{det} of the individual CEM detector in the joint CEM detection system of this thesis is given by $\eta_{\text{det}} \equiv \eta_{\text{detector}}(\delta_0, \delta)$ (eq. 2.8).

2.4.3. Angle of incidence

In the aspect to optimize the quantum yield η_{detector} of a given CEM detector, the incident angle θ of the primary particle offers a huge potential to increase the primary emission yield δ_0 of the corresponding CEM detector. As the primary emission yield $\delta_0 = \delta_0(\theta)$ macroscopically influences the quantum yield η_{detector} of the CEM (see section 2.3), a grazing incident angle θ of the primary particle at impact will significantly increase the maximum attainable quantum yield $\eta_{\text{detector}}(\delta_0(\theta))$ of the corresponding CEM detector.

To obtain an enhanced primary emission yield δ_0 at the first stage g_1 and a corresponding, higher quantum yield η_{detector} of a given CEM detector according to eq. 2.6, grazing incidences to surface normal ($\theta > 80^\circ$) at primary particle impact are highly advantageous. In conventional CEMs, such grazing incident angles will usually correspond to an impact position of the primary particle at the CEM channel tube wall only (fig. 2.8(a), *i*), in contrast to an ordinary, average cone impact (fig. 2.8(a), *ii*) [87, 88]. Note that for conventional CEM detectors, a CEM cone impact is commonly designed for the incident primary particle, with a typical surface normal to incident particle angle of $\theta = 60^\circ$ for particles entering the CEM cone perpendicular to the cone opening [88, 128].

As a result of above considerations, the actual impact position of the primary particle in the CEM becomes an important parameter. In detail, it specifies the incident angle θ to surface normal and therefore likewise the attributed quantum yield $\eta_{\text{detector}}(\delta_0(\theta))$ of the given CEM detector at this particular position as stated by eq. 2.6. However, the actual impact position of the primary particle for common CEM detectors integrated in most conventional charged particle detection systems is rather unknown. Moreover, the general stated detection efficiency of commercially available CEMs is simply averaged using CEM cone hits only under a fixed angle. This results as CEM channel impacts usually do not contribute significantly to the detection efficiency of the CEM and therefore play a negligible role in conventional detector calibration [88]. Consequently, the efficiency calibration curves found in standard CEM operating manuals (e.g., [85]) usually refer to averaged CEM cone hits under corresponding incident angles of $\theta = 60^\circ$.

Primary particle yield versus incident angle

In the aspect of the incident angle θ to the surface normal, the primary particle yield $\delta_0(\theta)$ of a surface material underlies a general characteristic dependency observed by various different emission experiments [62, 66, 73, 77, 81–83, 118, 126, 129, 130]. In the literature, there are generally two similar secondary emission models for the incident angle. Although either model is still a quasi-phenomenological approach, they are both founded on fundamental assumptions in relation to the skin depth λ_l of the incident primary particles at intrusion in the secondary emitting surface and the corresponding emission of secondary electrons as introduced by [81, 82, 118, 120, 125]. In reference to the literature [62, 111], the shape of the secondary emission yield dependence $\delta_0(\theta)$ according to the angle of incidence θ to the surface normal of the secondary electron emitting surface is described by

$$\delta_0(\theta) = k \cdot \delta_0(0^\circ) \sec(\theta), \quad (2.12)$$

where k is a material associated constant, $\delta_0(0^\circ)$ is the secondary emission yield of the active secondary emitting layer under perpendicular particle incidence, and θ is the corresponding

incident angle of the primary particle to the surface normal (fig. 2.8(a), inset). However, the alternative description of the secondary emission yield dependence $\delta_0(\theta)$ as stated by eq. 2.12 is given by $\delta_0(\theta) = \delta_0(0^\circ) \cdot \exp[p(1 - \cos(\theta))]$, with p representing a specific, material associated parameter [66, 75, 81, 87, 131]. Nevertheless, similar results are achieved by either approach for corresponding angles of $\theta \leq 85^\circ$ as considered in the context of this thesis.

In eq. 2.12, the particular value $\delta_0(\theta)$ substantially varies for distinct emission surface materials and incident particles [62, 66, 75, 77, 81, 126]. Moreover, an incident primary particle angle $\theta > 0^\circ$ to the surface normal generally results in an enhanced primary particle yield $\delta_0(\theta)$. Assuming identical impact energies E_{kin} , of the primary particles, it approximately varies by a fixed, relative factor as stated eq. 2.12, and measured by [62, 66, 72, 73, 81, 118]. In the particular case of hydrogen reduced lead glass [48, 66, 67, 132], CEM channel impacts will thus have a higher quantum yield $\eta_{\text{detector}}(\delta_0(\theta))$ compared to CEM cone hits due to the higher primary yield $\delta_0(\theta)$ caused by the grazing incidence θ of the primary particle to the active surface of the CEM at a channel impact (fig. 2.8). In the literature, there are several references which explicitly confirm this increased quantum yield η_{detector} in comparison of channel to cone impacts [87, 88, 133, 134]. Furthermore, for grazing incident angles θ also the general response of the reduced yield curve (eq. 2.11) will be shifted to higher values of $E_{\delta_0, \text{max}}$ and $\delta_{0, \text{max}}$ as measured by [63, 66, 81, 87, 118].

Influence of grazing particle impact

As stated in eq. 2.12, a grazing incident angle θ of the primary particle at impact thus macroscopically increases the maximum attainable quantum yield $\eta_{\text{detector}} = \eta_{\text{detector}}(\delta_0(\theta))$ of the corresponding CEM detector. For example, if one assumes a primary emission yield²² of $\delta_0(60^\circ) = 2$ as typically observed for active CEM surfaces [48, 63, 66, 67], and using a fixed value of $\delta = 2$ for the consecutive stages $g_{2..m}$ in the CEM [48, 66], the corresponding quantum yield according to eq. 2.6 is $\eta_{\text{detector}}(\delta_0(60^\circ)) = 0.79681$ at an incident angle of $\theta = 60^\circ$. However, if one increases the incident angle of the primary particle from $\theta = 60^\circ$ to 85° , the primary particle yield $\delta_0(85^\circ)$ will rise according to eq. 2.12 by a relative factor of $\delta_0(85^\circ)/\delta_0(60^\circ) \sim 5.7$ compared to the common value of $\delta_0(60^\circ)$ of typical CEM detectors (fig. 2.8(b), inset). Consequently, a calculated primary emission yield of $\delta(85^\circ) \approx 11.4$ is determined at an incident angle of $\theta = 85^\circ$. The latter value results in a dramatically increased, estimated quantum yield of $\eta_{\text{detector}}(\delta_0(85^\circ)) = 0.99989$ (eq. 2.6).

In the literature, such a characteristic increase in the quantum yield of a CEM detector according to the incident angle θ of the primary particle is explicitly measured by [131]. In the current detector setup of this thesis, the actual impact position of the primary particle is designed to reside at the CEM channel wall, and not in the CEM cone. This will allow to achieve a grazing angle of $\theta > 80^\circ$ in the CEM. Experimentally, the grazing incidence θ is implemented by focusing and deflecting the incident charged particles with copper plate apertures in front of the CEM cone entrances (fig. 4.7; see subsection 4.2.4).

2.5. Detector efficiency performance

In the following, sample theoretical curves are generated which will describe and specify the theoretical quantum yield η_{detector} of a CEM detector. The generated curves will display the ef-

²²For simplification, this will correspond to estimated values of $k = 1$ and $\delta_0(0^\circ) = 1$ in eq. 2.12.

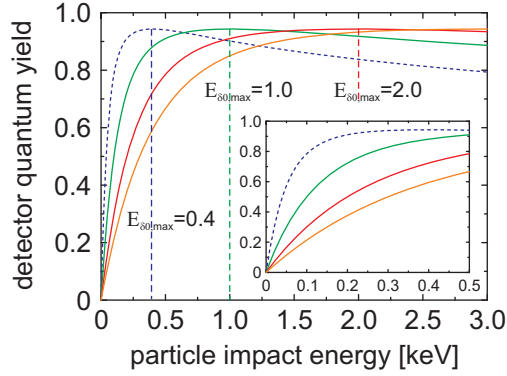


Figure 2.9: Calculated quantum yield $\eta_{\text{detector}}(\delta_0, \delta)$ of a CEM detector according to eq. 2.10 and eq. 2.11 for varying kinetic energies E_{kin} at primary particle impact in the CEM. Additionally, different maximum primary yield energies $E_{\delta_0, \max} = 0.4, 1.0, 2.0, 3.0$ keV are displayed, using $\delta_{0, \max} = 3.6$ [66], and $\delta = 2$ [48]. The dashed curve ($E_{\delta_0, \max} = 0.4$ keV) resembles the CEM efficiency response for incident electrons as displayed in standard CEM operating manuals (e.g., [85]). Inset: Zoom for energies from $E_{\text{kin}} = 0 - 500$ eV.

efficiency performance $\eta_{\text{detector}} = \eta_{\text{detector}}(\delta_0, \delta)$ of the detector as stated by eq. 2.10 and eq. 2.11 according to the associated parameters $\delta_0(E_{\text{kin}}, E_{\delta_0, \max}, \delta_{0, \max})$, and $\delta(E_{\text{kin}}, E_{\delta, \max}, \delta_{\max})$. In particular, the calculations will show the influence of the reduced yield curve characteristic in the emission yield values $\delta_0 = \delta_0(E_{\text{kin}}, E_{\delta_0, \max}, \delta_{0, \max})$, and $\delta = \delta(E_{\text{kin}}, E_{\delta, \max}, \delta_{\max})$ as introduced in subsection 2.4.2.

In contrast to the more general considerations for the operation characteristics and the quantum yield of a dynode detector in section 2.3, the following calculations explicitly state the efficiency response of a given CEM detector according to two experimentally accessible parameters. These two parameters primarily influence δ_0 and are the kinetic energy E_{kin} at impact of the primary particle in the CEM surface (subsection 2.4.2), and the incident angle θ at impact (subsection 2.4.3). However, the latter parameter only modifies the corresponding primary particle emission yield δ_0 by a constant factor as illustrated in subsection 2.4.3. Therefore, in this section the quantum yield $\eta_{\text{detector}}(\delta_0, \delta)$ is investigated only according to the kinetic energy E_{kin} at primary particle impact and displayed in the following subsection. Furthermore, one has to emphasise that in the context of this thesis, the quantum yield $\eta_{\text{detector}}(\delta_0, \delta)$ of the CEM detector as stated by eq. 2.10 is identical with the absolute detection efficiency η_{det} of the detector in the joint CEM detection system (eq. 2.8; $\eta_{\text{det}} \equiv \eta_{\text{detector}}(\delta_0, \delta)$, as $\eta_{\text{col}} = 1$).

2.5.1. Theoretical CEM efficiency response

In fig. 2.9, the calculated quantum yield η_{detector} of a CEM detector according to eq. 2.10 and eq. 2.11 is illustrated for different kinetic energies E_{kin} at primary particle impact in the CEM, and for different maximum primary yield energies $E_{\delta_0, \max} = 0.4, 1.0, 2.0, 3.0$ keV. In the figure, the influence of the maximum primary yield energy $E_{\delta_0, \max}$ on the characteristic of the quantum yield η_{detector} of a CEM detector according to eq. 2.10 and eq. 2.11 is particularly investigated. For the calculations, common parameters of conventional CEM detectors are chosen, using a fixed maximum primary yield value of $\delta_{0, \max} = 3.6$ as measured by [66], and a generalised secondary emission yield of $\delta = 2$ for the consecutive amplification stages $g_{2..m}$

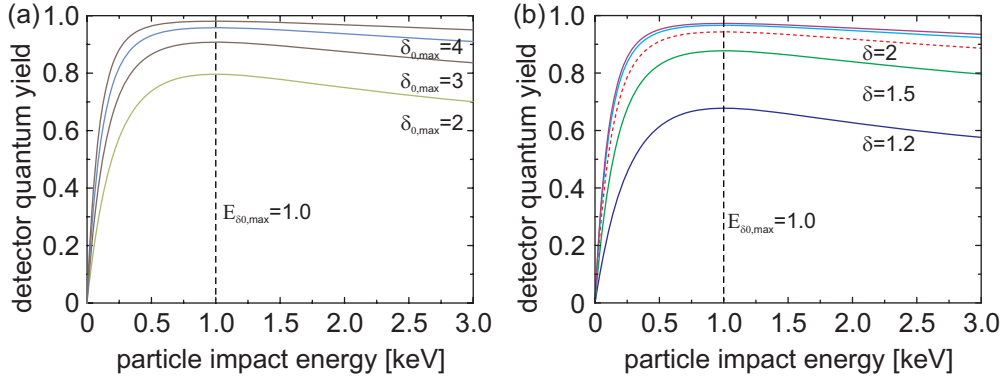


Figure 2.10: CEM detector quantum yield $\eta_{\text{detector}}(\delta_0, \delta)$ according to eq. 2.10 and eq. 2.11 at a fixed maximum yield energy $E_{\delta_0, \max} = 1.0$ keV (fig. 2.9). (a) Quantum yield $\eta_{\text{detector}}(\delta_0, \delta)$ for different maximum primary particle yield values $\delta_{0, \max} = 2, 3, 4, 5$, using $\delta = 2$ [48]. (b) Similar to (a), but for different secondary emission yield values $\delta = 1.2, 1.5, 2.0, 3.0, 10.0$, and assuming $\delta_{0, \max} = 3.6$ [66]. For used or old CEMs, common secondary yield values of $\delta = 2$ (fig. 2.5) are indicated by the dashed curve.

[48]. The inset in fig. 2.9 shows a zoom of the calculated quantum yield η_{detector} for kinetic particle impact energies of up to $E_{\text{kin}} = 0.5$ keV. The shape of the curves in the zoom display η_{detector} for comparable low kinetic energies, corresponding to the assumed linear increase of the primary emission yield δ_0 as stated by eq. 2.9 (e.g., [121, 122]).

For a maximum primary yield energy of $E_{\delta_0, \max} = 0.4$ keV, the calculated quantum yield $\eta_{\text{detector}}(\delta_0, \delta)$ according to eq. 2.10 and eq. 2.11 already shows a significant decrease in efficiency for values $E_{\text{kin}} > 1.5$ keV related to the peak value at $E_{\text{kin}} = E_{\delta_0, \max} = 0.4$ keV. In comparison to that, for high maximum primary yield energy of $E_{\delta_0, \max} > 2$ keV, this decrease in efficiency will occur at considerably higher kinetic energy values E_{kin} . However, the quantum yield $\eta_{\text{detector}}(\delta_0, \delta)$ of a CEM detector as stated by eq. 2.10 and eq. 2.11 will generally decrease again after surpassing a maximum efficiency value for sufficient high energies of E_{kin} . In particular the latter property is explicitly observed for incident electrons and kinetic energy values $E_{\text{kin}} > 1$ keV (compilation by [48]), and for incident ions for considerable high energy values E_{kin} [95]. However, these observations and above calculations are in contrast to still frequently assumed saturating models in the literature [97, 123], and in CEM operating manuals (e.g., [85]; ion efficiency response).

In comparison to the literature, the dashed curve in fig. 2.9 with $E_{\delta_0, \max} = 0.4$ keV represents the commonly assumed CEM efficiency response for incident electrons, and assuming a CEM cone hit. This particular curve is usually displayed for the CEM quantum yield of incident electrons in standard CEM operating manuals (e.g., [85]), in accordance with the observations of several authors [48, 66, 87, 92]. However, as fewer experimental data exists on incident ions, only a phenomenological saturation of the CEM efficiency response at considerable high kinetic energies is stated in most common CEM operating manuals for the ions, with a quasi-linear increase of the quantum yield for low kinetic energies E_{kin} . Nevertheless, in comparison to the above calculations, this linear increase up to the onset of saturation simply corresponds to the low kinetic energy regime of the calculated quantum yield curves with $E_{\delta_0, \max} \geq 2.0$ keV as shown in fig. 2.9, and as further experimentally observed by [88, 105, 106, 123, 135].

In fig. 2.10, the calculated quantum yield $\eta_{\text{detector}}(\delta_0, \delta)$ according to eq. 2.10 and eq. 2.11 at a fixed maximum yield energy $E_{\delta_0, \text{max}} = 1.0 \text{ keV}$ (fig. 2.9) is further investigated. In fig. 2.10(a), it is displayed for different maximum primary yield values $\delta_{0, \text{max}} = 2, 3, 4, 5$ using a generalised secondary electron yield $\delta = 2$ [48]. In contrast to that, in fig. 2.10(b) the calculated quantum yield $\eta_{\text{detector}}(\delta_0, \delta)$ is depicted for different secondary emission yield values $\delta = 1.2, 1.5, 2.0, 3.0, 10.0$, and assuming $\delta_{0, \text{max}} = 3.6$. The latter value is deliberately chosen in accordance with [66], as it will correspond to an average CEM cone impact of the primary particle for conventional CEM detectors.

In more detail, fig. 2.10(a) depicts the influence of the maximum primary yield value $\delta_{0, \text{max}}$ on the calculated quantum yield $\eta_{\text{detector}}(\delta_0, \delta)$. For example, at a maximum primary yield value $\delta_{0, \text{max}} = 2$, a calculated quantum yield of $\eta_{\text{detector}}(\delta_0(1 \text{ keV}, 1 \text{ keV}, 2), \delta = 2) = 0.797$ is obtained for a kinetic energy of $E_{\text{kin}} = 1 \text{ keV}$ at primary particle impact (eq. 2.10 and eq. 2.11). In comparison to that, a primary yield value of $\delta_{0, \text{max}} = 4$ will correspond to $\eta_{\text{detector}}(\delta_0(1 \text{ keV}, 1 \text{ keV}, 4), \delta = 2) = 0.959$ at $E_{\text{kin}} = 1 \text{ keV}$. Consequently, higher CEM detector efficiencies are achieved at identical impact energies E_{kin} for increased maximum primary yield values $\delta_{0, \text{max}}$ (fig. 2.10(a)). This results as an increased maximum primary yield $\delta_{0, \text{max}}$ simply corresponds to an increased primary particle yield δ_0 for identical maximum yield energies $E_{\delta_0, \text{max}}$. Experimentally, such higher primary yield values are realised, e.g., by a CEM channel impact under grazing incident angle $\theta > 80^\circ$, compared to a CEM cone hit at $\theta \approx 60^\circ$ (see subsection 2.4.3). Further note that similar values for $\delta_{0, \text{max}}$ and $E_{\delta_0, \text{max}}$ are derived from the measured quantum yield $\eta_{\text{detector}} = \eta_e(E_{\text{kin}})$ of the e^- -CEM used in the context of this thesis (see subsection 5.4.3).

Figure 2.10(b) illustrates the influence of the secondary electron yield δ of the consecutive stages $g_{2..m}$ of amplification on the calculated quantum yield $\eta_{\text{detector}}(\delta_0, \delta)$ of a CEM detector. For example, at a generalised secondary electron yield value of $\delta = 3$, a calculated quantum yield of $\eta_{\text{detector}}(\delta_0(1 \text{ keV}, 1 \text{ keV}, 3.6), \delta = 3) = 0.966$ can be derived. In comparison, a yield value of, e.g., $\delta = 1.5$ will result in a calculated quantum yield of $\eta_{\text{detector}}(\delta_0(1 \text{ keV}, 1 \text{ keV}, 3.6), \delta = 1.5) = 0.877$, whereas a value of $\delta = 2$ will already yield $\eta_{\text{detector}}(\delta_0(1 \text{ keV}, 1 \text{ keV}, 3.6), \delta = 2) = 0.943$. Therefore, already considerable secondary electron yield values of $\delta > 2$ will produce an almost optimised quantum yield $\eta_{\text{detector}}(\delta_0, \delta)$ in the aspect of δ (compare to $\delta = 10$; fig. 2.10(b)). Experimentally, common secondary electron yield values δ for conventional CEM detectors will range from $\delta = 2 - 3$ (see section 2.3). However, for 'old' or heavily used CEMs, the secondary emission yield δ will drop below two [48]. In contrast to values of $\delta > 2$, such low secondary emission yield values will significantly reduce the overall efficiency performance of the CEM detector (fig. 2.10(b)). Fortunately, an increase in the CEM gain voltage U_{CEM} will to some extent temporally restore the initial secondary electron yield $\delta > 2$ (see subsection 2.4.1).

As overall result of the previous calculations, in comparison of fig. 2.10(a) and fig. 2.10(b), the primary emission yield δ_0 generally resembles the *key* parameter for an efficiency optimisation in $\eta_{\text{detector}} = \eta_{\text{detector}}(\delta_0, \delta)$ if a high quantum yield of a given CEM detector is to be obtained. This particular result is in perfect agreement with the more general considerations of section 2.3. Moreover, the influence of the secondary emission yield δ of the consecutive amplification stages $g_{2..m}$ on the quantum yield η_{detector} will be comparably insignificant for considerable high secondary emission yield values of $\delta > 2$.

3. Basic Operation of Channel Electron Multiplier Detectors

The following chapter describes the basic and associated CEM parameters which resemble the experimental key quantities for conventional CEM detector operation. The subsequent analysis and optimization of these parameters permits to produce stable count rates and a reproducible quantum yield with the corresponding detector. In the context of CEM detector operation, it further enables to explicitly parametrize the key quantities for CEM operation which have previously been comparably undefined in the literature, and allows an extensive comparison to experimentally obtained values in this thesis, and to the general literature.

The theoretical considerations of this chapter are based on the cascaded dynode multiplier model introduced in chapter 2. As a remarkable property of the model, it specifically allows to calculate the compound probability distribution $P_m(n)$ for a given dynode detector and further enables to determine the compound loss probability $P_m(0)$ of the generated secondary electron avalanche in the detector. In the aspect of detector operation parameters, the compound Poisson distribution $P_m(n)$ admits to theoretically quantify some of the experimental key parameters for CEM operation as, e.g., the modal gain G_0 of a given CEM detector. Accordingly, the compound loss probability will in turn determine the raw quantum yield $\eta_{\text{detector}} = 1 - P_m(0)$ of a given CEM detector.

In addition to that, the cascaded dynode multiplier theory of chapter 2 will also provide a general model for the number of cascaded amplification stages g_m in the CEM detector. This modelling of the cascaded amplification process in the CEM will macroscopically affect the theoretical modal gain G_0 of a detector, the transit time t_{transit} of the secondary electron avalanche in the CEM, and define to some extent the expected shape of a single pulse incidence at the CEM anode. The definition of the common CEM operation parameters by the model therefore represents a genuine testing ground for the performance of any particular dynode detector. It further enables to relate the theoretical considerations of this chapter and of chapter 2 to experimentally observable quantities as, e.g., the particular shape of a single pulse incidence at the CEM detector anode, or the experimental modal gain G_0 of a CEM detector. More importantly, the optimization of these experimentally accessible parameters allows to push a conventional dynode detector to its limiting extremes.

In the first part of this chapter (section 3.1 and section 3.2), the common CEM operation parameters of a single CEM detector are theoretically introduced and defined according to experimentally accessible quantities. Consequently, these operation parameters will substantially influence and characterize the particular performance of the corresponding detector in linear amplification or pulse counting mode. In the context of experimentally accessible quantities, the operation of a CEM detector will primarily depend on the CEM gain voltage U_{CEM} applied over the detector. A variation of this parameter according to the obtained gain value G_0 , or the observed count rate, will exhibit if the corresponding CEM detector is operated in linear amplification or in so-called space charge saturation (see subsection 3.1.2). However, in particular the latter operation condition will provide a specifically suited, highly non-linear amplification mode of the CEM detector which results in a transformed and shifted pulse

height distribution produced by the corresponding CEM detector. As a unique property of CEM detectors in pulse counting mode, this transformed distribution enables a rather defined discrimination of the single pulses at the CEM detector anode from the signal background, requiring only comparably few and inelaborate pulse processing circuitry for the detection of single pulse incidences. A careful examination of the applied CEM gain voltage U_{CEM} with respect of the individual CEM detector response will thus lead to operation characteristics of the used multiplier which will allow to maintain stable event counting and an invariable, reproducible quantum yield with the detector.

In the second part of this chapter (section 3.3 and section 3.4), the common CEM operation parameters of the single CEM detectors used in the context of this thesis are experimentally investigated. In particular, in section 3.3 single pulse traces at the CEM anode resulting from primary particle incidences in the CEM detector entrance are explicitly measured. From these obtained single pulse traces, the accumulated pulse parameter histograms are then subsequently derived and investigated. Experimentally, the calibration measurements at each individual CEM detector allow to determine the specific CEM operation parameters of the corresponding CEM detector as introduced in section 3.1 and section 3.2. These individually obtained CEM operation parameters further permit a general comparison to precalibrated values provided by the supplier, and to commonly observed operation parameters for similar CEM models stated in the literature. In addition to that, the influence of possible counting errors on the observed count rate N' with the CEM detectors compared to the true count rate N defined by the incident flux of primary particles at the CEM entrance is investigated in section 3.4. Here, eventual counting errors with a given CEM detection system are analyzed, which are not the result of the detection of an incident primary particle with the CEM detector, but are introduced, e.g., by the subsequent pulse processing electronics attached to the CEM.

As a genuine result from the CEM calibration measurements and the corresponding counting error considerations of this chapter, the observed quantum yield η_{detector} of the single CEM detectors will only suffer from detector-related properties as, e.g., an inefficient conversion of the incident primary particle at primary particle impact in the CEM, or an early secondary electron avalanche die-out in the CEM channel. Remarkably, this leaves the count rate measurements and the corresponding absolute detector efficiency calibrations of this thesis unencumbered by any non-detector based counting errors. In combination with the absolute efficiency calibration introduced in chapter 5, this allows to calibrate the quantum yield η_{detector} of the respective CEM detectors to absolute values¹. As a unique property of the joint CEM detection system of this thesis therefore, the raw quantum yield η_{detector} of a CEM detector is measured and can be compared to the theoretical quantum yield η_{detector} of the cascaded dynode detector model in the previous chapter, and to the general literature.

3.1. Basic CEM operation parameters

In this section, basic operation parameters of a single CEM detector are introduced which primarily influence and determine the performance of the corresponding detector. The following considerations will lead to operation characteristics of the used multiplier which will allow to produce stable count rates and an invariable, reproducible quantum yield. In this context,

¹Without any accidental admixture of the collection efficiency η_{col} of the CEM detection system (see section 2.4), or of any non-detector based counting errors.

particularly the modal gain G_0 of the CEM detector represents an integral parameter. Therefore, in subsection 3.1.1 initially the theoretical modal gain G_0 of a given dynode detector is deduced based on the calculations of the cascaded dynode model introduced in chapter 2. As a result from the model, the calculated compound Poisson distribution $P_m(n)$ represents the theoretical prediction for the expected pulse height distribution of a given CEM detector observed at the CEM detector anode. It further turns out that the theoretical modal gain G_0 corresponds to the first moment of the compound Poisson distribution $P_m(n)$. Remarkably, the definition of the modal gain G_0 enables to theoretically specify the basic parameters for CEM operation in reference to the considerations of the cascaded dynode detector model and to compare them to experimentally accessible quantities.

In subsection 3.1.2, the experimental modal gain G_0 is introduced and subsequently defined according to experimentally observable quantities. However, the operation of any CEM detector and the particular CEM gain are heavily dependent on the applied CEM gain voltage U_{CEM} . By measurement, in particular a variation in the gain voltage U_{CEM} allows therefore to investigate the actual operation properties of a given CEM detector. Accordingly, the basic CEM operation parameters will subsequently be specified from the detector gain curve G corresponding to the respective pulse height distribution, the modal gain G_0 versus the gain voltage U_{CEM} characteristic, and the count rate response of a CEM detector to the gain voltage U_{CEM} .

Moreover, for considerable values of U_{CEM} , the CEM detector will operate in space charge saturation (see subsection 3.1.2). This highly non-linear amplification mode transforms the initial compound Poisson distribution $P_m(n)$ of the CEM detector (see section 2.2) into a narrow quasi-Gaussian distribution of pulse heights. Due to the particular shape of the transformed distribution, the corresponding pulse heights at the CEM detector anode are easily discriminated against low background signals, signal feedback, or spurious background noise in the signal cable. This genuine property of continuous dynode detectors generally enables to employ only comparably simple current or pulse processing circuitry for the registration of single particle incidences.

Finally, some experimentally related comments on the operation of any conventional CEM detector are stated. In particular, the optimum operation point of a given CEM according to the CEM gain voltage U_{CEM} is proposed. However, this operation point has to be monitored frequently and probably readjusted to ensure stable event counting, and to sustain a reproducible operation of the corresponding detector over a certain time period. Nevertheless, an eventual readjustment of a CEM detector will generally occur from time to time as the detector gradually degrades due to extensive use of the detector.

3.1.1. Theoretical CEM gain

The gain of any cascaded dynode particle detector is generally defined as the ratio of the number of generated output electrons to the number of incident particles. According to the theoretical considerations of section 2.2, the number n of output electrons in a secondary electron avalanche respectively the corresponding distribution is determined by the compound Poisson distribution $P_m(n)$ as illustrated in fig. 2.2. Remarkably, the latter distribution $P_m(n)$ therefore immediately represents the theoretical prediction of the pulse height distribution for a CEM detector. This results as the number of electrons in a CEM pulse is linearly proportional to the observed charge at the CEM anode, and thus to the obtained pulse amplitude in a CEM pulse.

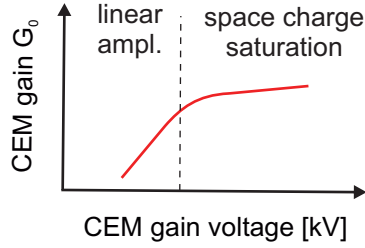


Figure 3.1: Illustrated characteristic of the modal CEM gain G_0 versus the CEM gain voltage U_{CEM} . At considerable CEM gain voltages U_{CEM} , the effect of space charge saturation significantly changes the initial linear amplification response of the detector.

The average number of electrons emitted per pulse can be derived from the first moment of the compound Poisson distribution $P_m(n)$, thereby defining the modal gain G_0 of the detector. As a unique property of compound Poisson distributions and their associated generating functions $\mathcal{F}_m(s)$ [52, 58], the first moment of the compound distribution is the product of the first moments of the single distributions at all amplification stages g_m , respectively. Consequently, the modal gain of the multiplier thus depends on the number m of subsequent amplification stages g_m in the CEM detector (fig. 2.1), and is defined after [49, 51, 52] as

$$G_0(\delta_0, \delta, m) = \delta_0 \delta^{m-1}, \quad (3.1)$$

where δ_0 is the primary emission yield at primary particle impact at stage g_1 , and δ is generalized for all consecutive multiplication stages $g_{2..m}$ (see section 2.1). Note that the gain of eq. 3.1 is conceptually identical to the definition for any discrete dynode multiplier as, e.g., photomultipliers.

With the gain defined in this way and secondary emission yield values of $\delta_0 = 4$ and $\delta = 2$ (new detector and incident particles are electrons, [48, 66, 67]), an average of $m = 25$ stages of multiplication (see dashed vertical lines, fig. 2.4(a,b)) is calculated for common, experimental modal gain values of $G_0 = 1 \times 10^8$ (fig. 3.7(a)). However, in the preceding calculation the impact position of the primary particle is situated in the center region of the CEM cone (fig. 4.4(d)). The theoretical gain G_0 for a primary particle hit lying in the CEM channel section will be reduced by a factor of up to $\sim \delta^5$ as the generated secondary electron avalanche of a CEM channel hit “misses” up to five amplification stages g_m compared to a CEM cone hit [87, 107]. This reduced pulse height will possibly become restrictive for single pulse counting (see section 3.4), if an enhanced detector quantum yield η_{detector} via a grazing particle incidence θ at primary particle impact is intended, where the impact position corresponds to a CEM channel hit (see section 5.4). Nevertheless, as the impact in the channel is most probable under grazing incidence the loss in gain will be compensated to some extent by the expected higher primary particle emission yield $\delta_0 > 4$ under grazing incidences ([87]; or subsection 2.4.3).

3.1.2. Experimental CEM gain

The experimental gain G of a dynode detector is given by the average ratio of the output current at the detector end to the input current at the detector entrance ($G_0 = I_{\text{out}}/I_{\text{in}}$). In pulse counting mode, this reduces to the number of generated secondary electrons in a

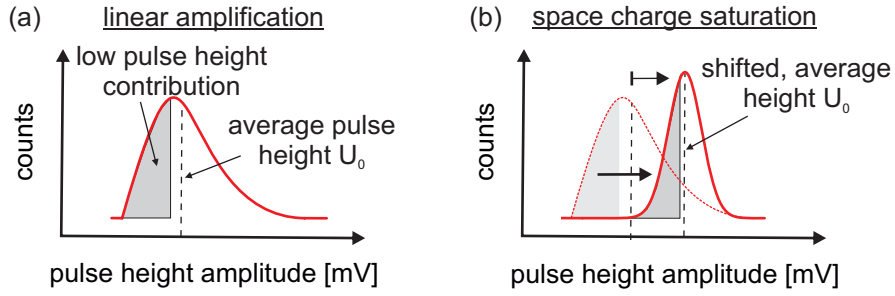


Figure 3.2: (a) Illustrated pulse height distribution in the CEM corresponding to the calculated compound Poisson distribution $P_m(n)$ as shown in fig. 2.2. Derived pulse height distribution prior to the last stages of amplification up in the CEM from, e.g., g_{m-5} . Due to the effect of space charge saturation, at the last stages only lower pulse heights are still further amplified. (b) Resulting final, compressed pulse height amplitude distribution after g_m . By space charge saturation, the initial compound Poisson distribution $P_m(n)$ evolves into a narrow quasi-Gaussian distribution of pulse amplitudes.

single output pulse per incident primary particle at the detector entrance. In the particular case of CEMs, the experimental gain G_0 is a function of the applied CEM gain voltage U_{CEM} over the detector (fig. 2.1), and the length-to-diameter ratio l/d of the CEM tube [47]. Experimentally, these two parameters will significantly affect the secondary emission properties in the CEM and therewith associated secondary electron yield $\delta_{1..m}$ in the dynode detector (see subsection 2.4.1). However, the length to diameter ratio l/d is intrinsically given by the spatial dimensions and the design of the particular CEM model. Therefore, for a given detector especially the applied CEM gain voltage U_{CEM} is an important parameter which influences the gain of a CEM detector.

In fig. 3.1(a), a commonly measured, experimental CEM gain G_0 versus gain voltage U_{CEM} characteristic is illustrated (e.g. [85]). For comparably low values of U_{CEM} , the CEM detector stays in analogue mode acting as a perfect linear amplifier for incident primary particles as stated by eq. 3.1. The observed pulse height distribution at the CEM detector end strictly corresponds to the calculated compound Poisson distribution $P_m(n)$ as illustrated in fig. 2.2 (see subsection 3.1.1). However, for considerable high values of U_{CEM} , the CEM gain G_0 evolves into highly non-linear amplification mode due to the effect of space charge saturation at the CEM channel end [47, 53, 59, 136–138]. With the onset of space charge saturation, the CEM detector still amplifies incident primary particles but the pulse height distribution at the CEM output is significantly changed in shape with only the low pulse height contribution of the overall pulse height distribution being further amplified (fig. 3.2). Note that this non-linear amplification behaviour is particularly exploited for the pulse counting mode of CEM detectors.

Space charge saturation

To illustrate the effect of space charge saturation on the observed pulse height amplitude distribution², in fig. 3.2 the pulse height distribution prior to the last stages of amplification in the CEM from, e.g., g_{m-5} is shown (fig. 2.1). In space charge saturation, the initially

²Note that according to subsection 3.1.1, the pulse height distribution at the CEM anode will directly correspond to the calculated compound Poisson distribution $P_m(n)$ as depicted in fig. 2.2.

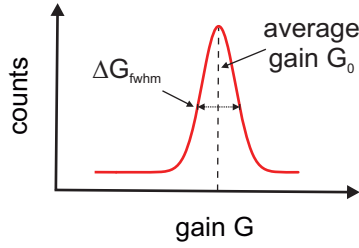


Figure 3.3: Illustrated distribution of gain values G of a CEM detector operating in space charge saturation, showing the modal gain G_0 of a CEM. In the experiment, the gain curve G simply corresponds to the respective pulse height distribution as depicted in fig. 3.2 as stated by eq. 3.4.

uniform secondary emission yield value $\delta = 2$ decreases to $\delta \leq 1$ for the last few stages g_m of amplification due to positive wall charging of the channel tube [47, 137] (eq. 2.3 and eq. 2.4; subsection 2.1.2). The accumulated secondary electron avalanche in the CEM detector will thus experience no further amplification above a certain maximum value at the end of the CEM for macroscopic charge values. More specific, at the last multiplication stages g_m only lower pulse heights (fig. 3.2(a); shaded area) are still amplified whereas already higher pulse heights are only maintained in charge [53, 59, 136, 137]. This results in CEM output pulses which all exhibit nearly the *same* amplitude. It further leads to a shifted and compressed pulse height amplitude distribution compared to the initial compound Poisson distribution $P_m(n)$ (fig. 3.2(b)).

Therefore, by the effect of space charge saturation the initial compound Poisson distribution $P_m(n)$ evolves into a narrow quasi-Gaussian distribution of pulse amplitudes centered at the average pulse height U_0 (fig. 3.2(b)). Moreover, by the particular Gaussian shape, a rather defined pulse height distribution of signal pulses is obtained which is easily discriminated against any low spurious background signals, feedback pulses, or any background noise in the signal cable. This results as for the Gaussian pulse height distribution, the discriminator level for any successive current or pulse processing electronics can be adjusted to a much higher threshold level without losing any significant distribution of pulses which will otherwise remain undetected (see subsection 2.2.1; fig. 2.3).

Experimental CEM gain

Interpreted in experimentally measurable quantities, the modal gain G_0 of a CEM detector is defined as the average number of electrons per pulse at the anode of the CEM. In pulse counting mode, it therefore represents the integrated charge in an output pulse with respect to an incident primary particle. As the CEM gain G is proportional to the electric charge in the output pulse (see subsection 3.1.1), the modal gain G_0 is thus given by the corresponding average pulse height value U_0 in the observed pulse height distribution (fig. 3.2).

By definition, the amplification factor for an incident primary particle in a CEM is denoted as the CEM gain G , and reads

$$G = Q_{\text{pulse}}/e_0 = \frac{1}{e_0 R} \int U(t) dt, \quad (3.2)$$

where $Q_{\text{pulse}} = e_0 \int n(t) dt$ is the integrated number of secondary electrons within the generated output pulse, $U(t)$ is the pulse height amplitude at the time t , and R denotes

the ohmic output resistance at the CEM anode (50 Ω ; fig. 4.8(b), see section 4.2). Due to the Poissonian nature of the secondary emission processes in the CEM and the Maxwellian velocity distribution of the emitted secondary electrons at any stage g_m within the cascade [47, 60, 61], the temporal amplitude shape $U(t)$ of the output pulse in eq. 3.2 arriving at the CEM anode is expected to be Gaussian [139], corresponding to

$$U(t) = U_0 \cdot \exp\left(-\frac{1}{2} \left(\frac{t-t_0}{\sigma}\right)^2\right), \quad (3.3)$$

where U_0 is the amplitude of the Gaussian pulse at the time t_0 (fig. 3.3), and $\sigma = t_{\text{fwhm}}/(2\sqrt{2\ln 2})$ represents a single standard deviation of the Gaussian. Assuming $t_0 = 0$, the gain G for a particular single primary particle incidence is then given by

$$G = \frac{U_0}{e_0 R} \int_{-\infty}^{\infty} \exp\left(-\frac{1}{2} \left(\frac{t}{\sigma}\right)^2\right) dt = \frac{\sqrt{2\pi}}{e_0 R} U_0 \sigma = \frac{\sqrt{\pi}}{2\sqrt{\ln 2}} \frac{U_0 t_{\text{fwhm}}}{e_0 R}. \quad (3.4)$$

As the CEM gain G is thus linearly proportional to the pulse height amplitude U_0 , the modal gain G_0 is given by the corresponding average pulse height value \bar{U}_0 in the observed pulse height distribution for several particle incidences (e.g., fig. 3.2). The modal gain G_0 of a CEM detector therefore yields the most probable gain value (fig. 3.3), and is correspondingly defined as

$$G_0 = \frac{\sqrt{\pi}}{2\sqrt{\ln 2}} \frac{\bar{U}_0 \bar{t}_{\text{fwhm}}}{e_0 R}, \quad (3.5)$$

where \bar{U}_0 represents the average pulse height of the observed pulse height distribution, and \bar{t}_{fwhm} denotes the average pulse width at half maximum, respectively. In contrast to eq. 3.5, in the literature often a simplifying rectangular approximation of the Gaussian pulse shape to determine the experimental CEM gain G_0 is used, with

$$G_{0,\text{linear}} = \frac{\bar{U}_0 \bar{t}_{\text{fwhm}}}{e_0 R}. \quad (3.6)$$

However, the linear approximation slightly underestimates the CEM gain compared to the observed Gaussian shaped pulses of eq. 3.5 by a factor of $G_0 \approx 1.06447 G_{0,\text{linear}}$.

CEM detector gain degradation and detector age

Intrinsically, CEM detectors display a stable operation only over a certain period of time. In particular, gradual degradation of the active surface of the secondary emitting layer in the CEM worsens the detector performance as the detector deteriorates by extensive use [48, 90, 139]. Therefore, if one considers the lifetime of stable operation for a CEM detector there are some potential sources and unfavourable operation conditions which will promote an enhanced detector degradation [139, 140]. Of these, high vacuum pressures $p > 10^{-6}$ mbar [89, 90, 141], multiple vacuum bakeout [142–146], extensive atmospheric/alkaline exposure, contamination with hydrocarbons presumably from vacuum pump oils [112, 140, 147], ultra-high vacuum fatigue [148–150], intensive particle bombardment [144], and accumulated counts greater than 10^{10} [90, 151] are the most prominent representatives. As a result, an aged or heavily used detector needs a higher gain voltage U_{CEM} to sustain the magnitude of the

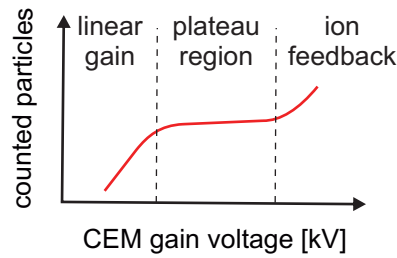


Figure 3.4: Illustrated, characteristic response of a CEM detector to the CEM gain voltage U_{CEM} assuming a constant flux of incident particles ('knee-curve', [85]). For optimum pulse counting in pulse counting mode, U_{CEM} is set to a value at the plateau region where the detector is operated in space charge saturation.

initially measured gain values G_0 for operation [152]. Moreover, also the knee curve (see subsection 3.1.3) of the corresponding detector is shifted to considerably higher gain voltages U_{CEM} (e.g., [85]). Consequently, as the CEM degrades and ages, the gain $G = G(U_{\text{CEM}})$ of the CEM has frequently to be monitored to ensure stable event counting. However, readjusting the CEM to the plateau region (fig. 3.4) will maintain a sufficient high pulse height distribution which can clearly be discriminated against the signal background.

3.1.3. Optimum operating point

The optimum operating point of a CEM detector according to the CEM gain voltage U_{CEM} is usually determined from the observed count rate versus CEM gain voltage characteristic. In fig. 3.4, the characteristic response of a CEM detector as a function of the CEM gain voltage U_{CEM} is depicted ('knee-curve', [85]). Note that for this characteristic a constant flux of incident primary particles at the CEM detector entrance is assumed (see section 5.1).

For low CEM gain voltages U_{CEM} , the CEM detector operates in analogue mode³ where it acts as a linear amplifier for incident primary particles (fig. 3.4; linear gain). At this stage, the CEM exhibits a pulse height distribution corresponding to fig. 2.2 with a modal gain G_0 as stated by eq. 3.1. By an increase in gain voltage U_{CEM} , the modal gain G_0 of the compound distribution moves to higher pulse height amplitudes allowing more and more incident particles to be detected. Therefore, raising the gain voltage U_{CEM} results in an almost linear increase in the observed count rate.

For increased CEM gain voltages U_{CEM} , the count rate versus gain voltage characteristic enters a flat plateau region where the observed count rate remains essentially constant (fig. 3.4; plateau region). In the plateau region, the CEM gain versus gain voltage characteristic of the CEM detector (fig. 3.1) becomes highly non-linear due to the onset of space charge saturation. The resulting shifted and compressed pulse height distribution allows a clear discrimination of the pulse signal compared to the background (fig. 3.2), considering that the incident primary particle is properly converted and amplified in the CEM. As a result, at this stage in space charge saturation an increase in gain voltage U_{CEM} still raises the gain G_0 of the CEM, but does not affect the observed count rate. Moreover, the advent of the plateau region in the count rate characteristic indicates that a fixed contribution of the constant incident flux of primary particles at the CEM entrance is converted, amplified, and subsequently counted.

³This operation mode is identical to the amplification in a discrete dynode multiplier as, e.g., a photomultiplier.

This particular contribution is defined by the quantum yield η_{detector} of the CEM detector. As the quantum yield of the CEM stays essentially constant during the entire plateau region, also the corresponding count rate will thus remain stable (see, e.g., [153]).

Raising the CEM gain voltage U_{CEM} beyond the plateau phase will create high electron densities which will exist within the CEM channel near the CEM output end. Residual gasses, which have prior been adsorbed on the active surface in the channel of the CEM detector, are eventually desorbed and ionised, forming positively charged ions. These feedback ions initiate additional secondary electron cascades in the CEM, which are identified by subsequent afterpulsing in the observed output pulse signals [59]. In pulse counting mode, ion feedback thus becomes visible in extra counts for very high CEM gain voltages U_{CEM} (fig. 3.4; ion feedback). However, feedback ions are highly undesired as they are produced within the CEM itself, and are not the result of a primary input particle. Moreover, the resulting high charge densities at the output end of the CEM detector in the ion feedback region will permanently damage and degrade the active layer of the CEM (e.g., [85]). Therefore, CEM detectors are commonly operated below the ion feedback region.

Thus, the optimum operating point to efficiently count single particles with a CEM detector is the plateau region of the characteristic CEM gain curve in space charge saturation (fig. 3.4). Operating the detector at this stage, the measured count rates are relatively insensitive to gain voltage shifts. Moreover, any signal pulses can be clearly discriminated against low background cable noise, or spurious feedback pulses. This results as the operation in space charge saturation yields a defined, narrow output pulse amplitude distribution requiring only simple pulse counting circuitry for the registration of single particle incidences.

3.2. Associated CEM operation parameters

In this section, some additionally important CEM parameters are introduced which further characterise and specify the operation of a single CEM detector. In contrast to the basic parameters described in section 3.1, these associated parameters become especially important for the performance of the CEM detector in a CEM based detection system where the corresponding requirements and restrictions of a particular application have to be met. Associated CEM operation parameters are the transit time t_{transit} of the secondary electron avalanche in the CEM detector, the temporal resolution of two consecutive single pulses, the maximum count rate of the CEM, and the dark count rate of the corresponding detector.

In the context of this thesis and the fast detection of single particles, e.g., the transit time t_{transit} of the secondary electron avalanche in the CEM detector is a key parameter. This results as it significantly influences the total detection time t_{det} of the ionisation fragments with the CEM detectors (see subsection 4.4.2) due to the comparable short flight time of the fragments until impact in the CEMs (see section 4.4). Moreover, for future readout applications of the joint CEM detector considering many particles as, e.g., single atoms in optical lattices via photoionisation detection, the temporal resolution of two consecutive pulses and the maximum count rate are essential parameters. As it turns out, the restrictive quantity for a subsequent readout of several single atoms will finally be the temporal pulse width of the single pulses arriving at the CEM anode (see subsection 3.2.2). With measured pulse widths of 8 – 15 ns (fig. 3.6), this will theoretically allow to resolve consecutive single pulses corresponding to count rates of up to 10^8 counts per second. Referring again to, e.g., the fast

detection of single atoms in optical lattices, this will equal to an estimated readout of up to 10×10 lattice sites in one microsecond.

On the contrary, for detection applications of only a few particle incidences over a considerable detection time, the dark and background count rate of the CEM detector will represent an ultimate constraint. Here, particularly spectroscopic precision measurements with only a few incidences per minute will suffer from an enhanced dark count or background rate in the CEM detector, if no proper additional shielding is applied. By magnitude however, in this thesis work mainly the background counts in the CEM detector are of considerable interest.

3.2.1. Transit time

The time for a transit of the secondary electron avalanche through the CEM detector is generally described by the transit of the secondary electrons through a segmented cascade of m stages [47, 60, 61]. The model assumes that the secondary avalanche electrons at any cascade stage g_m are accelerated by the local electric field $\vec{\mathcal{E}}(\vec{r}) = E_i(\vec{r})$ in the continuous dynode structure of the CEM tube, strongly depending on the CEM gain U_{CEM} over the CEM detector. As illustrated in section 2.1, the acceleration of the generated secondary electrons in the CEM tube in an amplification stage g_i continues until the electrons again hit the CEM channel wall, initiating a new cascade stage g_{i+1} (fig. 2.1). This 'cascaded acceleration' of the individual secondary electrons in the developing avalanche leads to an average drift velocity per channel length, similar to, e.g., the drift velocity of electrons in the valence band of a conductor. Thus, the average number m of amplification stages g_m , the channel length l , and the applied electric field U_{CEM}/l over the entire length of the CEM channel tube represent important parameters to characterise the transit time t_{transit} of the secondary electron avalanche through the CEM channel [47, 60, 61].

Experimentally, the transit time t_{transit} corresponds to the elapsed time from the conversion of an incident primary particle, initiating the secondary electron avalanche in the CEM detector, until the resulting generated secondary electron avalanche is terminated at the CEM anode (fig. 2.1(b)). Referring to [47, 61], the transit time t_{transit} is therefore defined with the length to diameter ratio l/d , and the normalized⁴ electric field intensity \bar{E}_i as key values. Common values for CEMs are $m \approx 25 - 30$, a CEM gain voltage of $U_{\text{CEM}} \approx 2 - 3$ kV, and a length to diameter ratio of $l/d \approx 40 - 80$. For the CEM model used in the context of this thesis, calculated transit times according to [61] yield times of $t_{\text{transit}} \approx 9.4$ ns and $t_{\text{t-spread}} < 0.9$ ns (at $U_{\text{CEM}} = 3$ kV, an effective channel length of $l = 45$ mm, for $d = 1.4$ mm, and assuming $m = 25$ stages of amplification). Note that the obtained temporal spread t_{spread} of the avalanche cascade is owed to the Maxwellian distribution of initial velocities and to the variation of emission angles of the emitted secondary electrons at each subsequent emission stage g_i , respectively [61].

Common measured experimental transit times t_{transit} for different CEMs range from 5–50 ns [139]. The transit time specified by the manufacturer for our CEM model (see appendix A.3) is $t_{\text{transit}} = 26$ ns with a corresponding transit time spread of $t_{\text{t-spread}} < 2.4$ ns (at $U_{\text{CEM}} = 2.3$ kV). Accordingly, this deviation in contrast to the above calculated value presumably results from the elaborated curved structure of the used CEM model as depicted in fig. 4.4.

⁴The parameter \bar{E}_m denotes the average electric field for one amplification stage g_m from the emission of a secondary electron until the re-impact into the CEM channel wall (fig. 2.1(b)).

3.2.2. Maximum count rate and resolution of two consecutive pulses

In pulse counting mode, the minimal pulse resolution⁵ of two consecutive pulses represents an important parameter for, e.g., the maximum count rate a CEM detector can still resolve, or to discriminate single particle events from each other in an incident particle cascade arriving within a small time window. Generally, one has to distinguish between continuous high count rates associated with a constant incident particle flux, and a sudden burst of few incident particles within a small defined time window [154–157].

For continuous operation at elevated count rates, the modal gain G_0 of a CEM detector will generally decrease [48, 85]. More specific, a significant contribution of surface charges will be drawn out of the active secondary emitting layer of the CEM detector, and be replenished again. Therefore, a macroscopic gain current flux from the high voltage power supplies to the conduction layer of the CEM will continuously be reached [158], leaving the CEM detector unable to sustain the required current in the active layer for further pulse amplification while recharging. Additionally, the CEM channel will heat up due to ohmic heating. Likewise, the decreasing ohmic resistance of the CEM will also affect the overall CEM response and recharge characteristic of the entire CEM detector. In contrast to that, the lead oxide glass tube of the CEM will not be significantly heated from a particle burst as a considerable number of surface charges will only be drawn from time to time from the detector. This enables the CEM detector to retain the basic detector resistance and parameters corresponding to low count rates of incident particles.

To determine the temporal limit of two subsequent single pulses to be properly resolved, one can use a model of [155] which describes the observed phenomena reasonably well. According to this model, the charge, which is instantaneously removed from the active CEM surface after the generation of a secondary electron avalanche, is exponentially replenished in the active CEM surface in conceptual correspondence to an RC -circuit with a characteristic recharge time

$$\tau_{\text{CEM}} = R_{\text{CEM}}C_{\text{CEM}}, \quad (3.7)$$

where R_{CEM} is the overall ohmic CEM resistance (see appendix A.3), and the parameter $C_{\text{CEM}} = Q_{\text{pulse}}/U_{\text{CEM}}$ denotes the CEM capacitance, where $Q_{\text{pulse}} = G_0e_0$ represents the accumulated charge in a single pulse (eq. 3.2) which depends on the actual CEM gain G_0 . Consequently, the gain of a CEM detector is restored exponentially in time as

$$G_0(t) = G_0(1 - e^{-t/\tau_{\text{CEM}}}), \quad (3.8)$$

with G_0 being the modal gain of the CEM (see subsection 3.1.2). Experimentally, the calculated recharge constant according to eq. 3.7 is on the order of $\tau_{\text{CEM}} \approx 200 \text{ ns}$ ⁶. This results for measured gain values of $G_0 = 2 \times 10^7$, corresponding CEM gain voltages of $U_{\text{CEM}} = 3000 \text{ V}$ for heavily used CEM detectors (see chapter 5), and a primary particle impact in the CEM channel. On such time scales therefore, if two consecutive pulses arrive within, e.g., $t = 50 \text{ ns} \equiv \tau_{\text{CEM}}/4$, the charge in the active CEM surface is still not fully replenished in the

⁵Here, the temporal response and resolution of the CEM detector itself is discussed, not of any consecutive pulse processing electronics or additional circuitry.

⁶Alternatively, the CEM capacitance $C_{\text{CEM}} = \epsilon_0\epsilon_r A/d$ can be calculated similar to the capacitance of MPCs but with a single channel only. Here, for the lead glass a dielectric constant ϵ_r , between 7.8–8.3 is assumed [155]. With a channel area of $A = \pi/4 (1.3 \text{ mm})^2$ and a channel length of $l = 54 \text{ mm}$, the capacitance of the used CEMs is calculated to $C_{\text{CEM}} = 1.8 \times 10^{-15} \text{ F}$, yielding a recharge time constant of $\tau_{\text{CEM}} = 361 \text{ ns}$.

conduction layer by the gain current of the CEM. At this point in time, a subsequent second pulse arriving at the CEM detector will therefore be able to maximally draw only a pulse charge of $Q_{\text{second}} = (1 - e^{-1/4}) Q_{\text{pulse}} \approx 0.22 Q_{\text{pulse}}$ for its corresponding pulse amplification from the CEM (eq. 3.8). This leads to a *reduced* maximum CEM gain $G_0(t)$ the detector can supply for two or more subsequent pulses in a burst, or at elevated count rates. While the CEM is still recharging, a second or further consecutive pulse will therefore not experience the full amplification by the detector.

Consequently, if the resolved detection of such fast pulse trains is demanded, the discriminator level of the corresponding detection electronics has to be adjusted to a lower threshold setting (fig. 3.5(b) and fig. 3.6(a)) according to the reduced gain $G_0(t)$ of the CEM as calculated from eq. 3.8. Such an adjustment thus enables to count fast pulses with a lower amplitude as long as the pulse signal compared to the background noise can still be discriminated. By this, assuming a properly adjusted discriminator level and appropriate highspeed electronic circuits, pulse count rates exceeding 5×10^7 counts per second can be recorded [80].

At the very end, the final limit for fast pulse recording will naturally be given by the temporal resolution of the two consecutive pulses as imposed by the temporal pulse width of the individual single pulse [154]. Therefore, for common pulse widths of 8–12 ns (fig. 3.6(d)), two consecutive single pulses corresponding to bursts and count rates of up to 10^8 counts per second can ultimately be resolved (see also [85]).

3.2.3. Detector dark current and background counts

The dark count rate of a CEM detector is defined as the resulting output current or count rate when no input signal is present⁷. Generally, the dark count rate characteristic for CEMs is extremely low, ranging from values of 0.01–0.05 counts per second in pulse counting mode [85, 159] if proper shielding is applied and no parasitary leakage currents are present. Consequently, such low dark count rates enable to use CEM detectors in single particle detection applications where the expected count rate to be observed is very low (i.e., down to a single event per second only).

Experimentally, there are three different contributions to the dark count rate in a CEM detector [160]. From these three contributions, one is due to external nature, while the other two contributions are generated by the CEM detector itself. The external contribution results from cosmic rays and radiation interacting with the bulk material of the CEM detector, where the generated scattering products eventually initiate a secondary electron avalanche in the CEM. From the two detector specific interactions, the first one accidentally creates secondary electron avalanches at surface defects or mismatches at the active secondary emitting layer under the influence of the high electric fields in the corresponding detector. The other contribution originates from traces of radioactive constituents in the detector itself which likewise produce secondary avalanches in the CEM by spontaneous decay. As a result, all three processes generate additional counts in the CEM which do not originate to an incident primary particle.

⁷Note that in the context of this subsection, one has to discriminate background counts in the CEM detector (i.e., stray particles from the residual vacuum background directly entering the CEM detector via the cone) against dark counts.

Additionally, there will be a considerable influence⁸ of current leakages and parasitary currents from the ambient vacuum environment as a further error source [161]. This is in conceptual correspondence to, e.g., macroscopic leakage currents affecting the current measurement of ion gauges or ion getter pump systems at extremely low vacuum pressures. Such currents will result due to improper decoupling of the electronic circuitry from the ambient environment of the detection system by, e.g., using unshielded cables, or due to elaborate ground loops. In this case, appropriate galvanic decoupling and shielding of the electrical circuitry in the UHV inhibits such undesired current flow [104].

Nevertheless, the contribution of the dark count rate in a CEM is still comparably low in relation to the residual background count rate of most systems. Additionally, although cosmic radiation is, e.g., insignificant at sea level for conventional detector operation, it can be of relevance for precision measurements or for space applications, while it will consequently be reduced using appropriate additional shielding of the detection system [160, 162, 163].

Background counts

In contrast to the dark count considerations of the preceding subsection, in this thesis especially the influence of incident stray particles on the observed count rate of a CEM detector is very important (background counts). In general, such stray particles entering the CEM cone stem from the residual vacuum background, components of the UHV system itself, or as photons from stray light in the detection system. In the case of massive particles and electrons, a distinct dependency between the background pressure and the background count rate is observed at least for vacuum background pressures ranging from $p > 10^{-6}$ mbar [164]. In the aspect of stray light, electromagnetic radiation of the visible or invisible spectrum, i.e. photons entering the CEM cone, will initiate additional background counts in the detector. This kind of background noise results from the nonvanishing detection efficiency of CEMs for photons in the visible or UV/IR-range [80, 109, 114, 115]. Moreover, in the particular case of photoionisation in the UHV, additional spurious events will eventually arise due to photoionisation fragments from constituents of the residual vacuum background as, e.g., N₂, H₂O, and O₂, or from any traces of pump oils from the forevacuum backing.

At the end, the accidental entrance of any stray particles can effectively be reduced by proper shielding the CEM cone using solid apertures (neutral particles), or biased grids (charged particles). In the context of this thesis, this is realized by the application of a solid circular copper plate on the entrance of the CEM cone with an opening aperture of 2 mm (fig. 4.4).

3.3. Single CEM detector performance

For the general performance of the single CEMs used in this thesis, in the following section single pulse traces and accumulated pulse histograms of these single traces are recorded and evaluated. The analysis of the measurements allows to experimentally derive the common operation parameters of conventional CEM detectors (see section 3.1 and section 3.2). Even more important, it enables to relate these parameters to the general cascaded dynode detector theory introduced in chapter 2. Experimentally, the investigation of the individual character-

⁸This will become particularly important in the case of increased spurious noise in the signal cable, or in the analogue mode of the CEM detector,

istic of the CEM performance parameters will further ensure an efficient and stable operation of the corresponding CEM detector in pulse counting mode. Moreover, as the particular CEM model of this thesis work represents a typical CEM detector, the measured quantities of this section will therefore display common CEM detector operation parameters for any CEM based particle detection system.

Accordingly, from the measured data of the individual pulse traces at the CEM anode the basic operation quantities and associated operation parameters for the single CEMs of this thesis are deduced. For this, the CEM detector calibration setup and the acquisition of the experimental data from the calibration measurements of the single CEMs in this section are introduced in subsection 3.3.1. The corresponding setup simply resembles the joint CEM detection system introduced in chapter 4, although specific operation parameters are chosen for the individual CEM detectors, the laser beams, and the associated vacuum setup. In order to experimentally illustrate several of the CEM operation parameters of the particular CEM detectors, a sample trace of a single pulse incidence is shown in subsection 3.3.2 which is typically observed during common pulse counting measurements. Correspondingly, the particular shape and characteristic of such individual pulse traces defines to a considerable extent the initial pulse detection and the subsequent pulse procession electronics for the CEM detectors in pulse counting mode.

From the measured single pulse traces, accumulated histograms of the observed pulse height distribution and the corresponding pulse width distribution are further generated (see subsection 3.3.3). In this context, particularly the obtained pulse height distribution (fig. 3.6) will represent a key CEM operation parameter, allowing an explicit comparison to the calculated compound Poisson distribution $P_m(n)$ introduced in chapter 2. In addition to that, the observed pulse height distribution also defines the trigger level of any subsequent pulse processing electronics attached to the CEM detector. The derived pulse height and pulse width parameters of the histograms further enable to calculate the experimental modal gain G_0 of a CEM detector (see subsection 3.3.4). As the modal gain G_0 resembles the first moment of the observed pulse height distribution (see subsection 3.1.1), this permits to relate the experimentally obtained modal gain G_0 to the calculated values of the cascaded dynode detector model of chapter 2. In subsection 3.3.5, the count rate versus CEM gain voltage U_{CEM} characteristic of the particular CEM detectors is examined. Here, the particular position of the operation point of the CEM ensures that the respective detector is continuously operated in space charge saturation (see subsection 3.1.3). However, the observed count rate versus CEM gain voltage U_{CEM} characteristic of this section already includes the simultaneous calibration of the CEM detector efficiencies due to the particular measurement configuration (see section 5.1) in contrast to conventionally observed knee-curves in the literature. As a result, the count rate characteristic of an individual CEM detector can thus be directly related to the observed quantum yield $\eta_{\text{detector}} = \eta_{\text{detector}}(U_{\text{CEM}})$ of the detector, with the associated quantum yield η_{detector} being calibrated to absolute values.

The detailed analysis of the observed single pulse traces of the individual CEM detectors and their accumulated pulse parameter histograms in this section allows a direct comparison to theory. Additionally, they also enable to derive associated CEM operation parameters (see section 3.2), which further characterise the individual operation and performance of a particular CEM detector. For example, the specific shape of the observed pulse height distribution at the CEM anode (fig. 3.6) will explicitly determine if the CEM detector is

operated in space charge saturation or in linear amplification mode⁹ (see subsection 3.1.2). Moreover, the observed count rate versus CEM gain voltage U_{CEM} characteristic will define the optimum point of operation for the CEM detector (see subsection 3.1.3). On the other hand, e.g., the individual shape of the single pulse traces will allow to model the amplification process in the CEM according to the cascaded dynode detector theory (see subsection 3.2.1), yielding the obtained Gaussian shaped pulses at the CEM detector anode. Considering the associated CEM parameters derived from the key quantities (see section 3.2), for example the average pulse width \bar{t}_{fwhm} from the observed pulse width distribution (fig. 3.6(d)) will yield the temporal resolution limit of multiple consecutive pulse incidences (see subsection 3.2.2). Moreover, the observed modal gain G_0 will allow, e.g., to determine the maximum count rate per second with the CEM detector using an adequate trigger level (see subsection 3.2.2).

The two key CEM operation parameters¹⁰ observed in this section are in general agreement with the cascaded dynode detector theory introduced in chapter 2. Moreover, they are also consistent with precalibrated values provided by the supplier [159], and with obtained values for similar CEM models the literature. As the used CEM model represents a standard CEM model with common CEM operation parameters, the single CEM detector measurements and calibrations of this section thus resemble a genuine testing ground for the application of the cascaded dynode detector model of chapter 2 on continuous dynode detectors. Moreover, in combination with the count rate considerations of section 3.4, it will provide the experimental calibration of the raw quantum yield η_{detector} of a CEM detector to absolute values (see subsection 3.4.5), where the efficiency calibration is not encumbered with any eventual counting errors associated with the subsequent pulse processing electronics of the detector (see subsection 3.4.5).

3.3.1. Experimental data acquisition

The entire data of this section and the next section 3.4 is recorded with the two single CEM detectors of the joint CEM detection system introduced in chapter 4. However, distinct operation parameters and conditions are chosen for the basic calibration experiments of this section in comparison to the corresponding measurements of chapter 4 and chapter 5. Additionally, in this section only the individual performance of each single CEM detector is characterized. This corresponds to standard calibration measurements for single CEM detectors as accomplished by common CEM detector suppliers (e.g., [85, 159]). However, in contrast to these standard calibration measurements, the corresponding measurements of this section can also be performed in coincident mode (see section 5.1) using photoionisation in a small overlap volume as a perfect charged particle pair source (see section 4.5). As a unique property of the CEM detection system of this thesis therefore, this additionally allows to relate all measured operation parameters of the CEM detectors to absolute efficiency values in contrast to the standard detector calibrations in the literature (see subsection 3.3.5).

The experimental calibration data of each individual CEM detector in this section is recorded from particle events out of the residual background in the UHV setup of the joint

⁹According to the cascaded dynode detector model of chapter 2, in linear amplification mode a pulse height distribution corresponding to fig. 2.2 is proposed. In contrast to that, a Gaussian distribution is predicted in space charge saturation as illustrated in section 3.1 (fig. 3.2).

¹⁰The corresponding CEM operation parameters are: (a) the observed pulse height distribution with the calculated experimental modal gain G_0 , and (b) the particular shape of the single pulse incidences at the CEM detector anode.

CEM detection system (see section 4.2). To ensure collecting only positively charged ions or neutral atoms from the background, during calibration measurements each single CEM is held at a negative potential with the CEM cone at $U_{\text{cone}} = -2.3 \text{ kV}$, and a CEM gain voltage of $U_{\text{CEM}} = 2.3 \text{ kV}$ (fig. 4.8). The corresponding opposite CEM is held on ground potential ($U_{\text{cone}} = 0 \text{ V}$) with an applied gain voltage of $U_{\text{CEM}} = 0.1 \text{ kV}$. This minor voltage offset in the opposite CEM prevents positively charged particles leaving the detector, thus inhibiting eventual charged particle crosstalk between both CEM detectors.

During the single CEM calibration measurements, both laser beams and the ^{87}Rb -atom dispenser source are switched off¹¹ (see section 4.5). Typical background pressures are in the range of $p = 1 \times 10^{-8} \text{ mbar}$. Additionally, the ion gauge, the ion getter pump, and the backing TMP pump are kept operating during measurements (see section 4.2). For the collection of the measurement data, a commercial oscilloscope¹² is used with the CEM signal cable being galvanically decoupled via a standard high-voltage capacitor¹³, and the decoupled signal cable terminated at the oscilloscope with 50Ω (fig. 4.8(b)). If not otherwise stated, the discriminator level at the oscilloscope is adjusted to -20 mV (fig. 3.5(b)). This chosen value corresponds to the trigger level of the discriminator unit¹⁴ used in the single pulse counting measurements of chapter 4 and chapter 5.

3.3.2. Single pulse parameters

To illustrate the experimental CEM operation parameters for the detectors¹⁵ used in the context of this thesis, in fig. 3.5 a sample single pulse trace is shown which is typically observed at the anode of the CEM detector. Accordingly, the derived pulse parameters of the measurements are compared to conventional CEM operation parameters in the literature, or as listed in common CEM supplier manuals (e.g., [85]).

Figure 3.5(a) displays a common single pulse trace at the CEM anode caused by a positive ion or neutral atom incidence out of the residual background vapor. The depicted pulse trace yields a pulse height amplitude of $U_0 = -84.5 \text{ mV}$, and a corresponding pulse width of $t_{\text{fwhm}} = 4.6 \text{ ns}$ (see subsection 3.1.2). However, typically observed pulse height amplitudes range from values of $U_0 = -60 \text{ mV}$ up to -150 mV (see subsection 3.3.3), with typical pulse width values between $t_{\text{fwhm}} = 8 - 15 \text{ ns}$, respectively. To illustrate the difference between these commonly observed pulse height amplitudes of primary particle incidences and the spurious noise in the signal cable, in fig. 3.5(a) the fluctuations of the noise in the cable are shown in advance of the pulse incidence (red box, fig. 3.5(a)). However, in comparison to the observed pulse signal amplitudes of $U_0 = -60 \text{ mV}$ to -150 mV , typical background noise fluctuations yield amplitude heights of only up to -2 mV (see subsection 3.4.2). By amplitude, this leaves the background noise in the cable comparably insignificant to the commonly observed single pulse heights.

Figure 3.5(b) shows a zoom of fig. 3.5(a) where the trigger level of the oscilloscope is additionally displayed (dashed line). The chosen threshold value of -20 mV corresponds to the trigger level of the discriminator unit used in the single pulse counting applications of

¹¹Note that the ambient laboratory illumination (fluorescent lamps) is left on during calibration measurements. Further, the UHV chamber is not additionally shielded against any external radiation as, e.g., stray light or cosmic background radiation.

¹²LeCroy, Waverunner 204Xi.

¹³ $C = 100 \text{ pF}$, breakthrough voltage $\geq 15 \text{ kV}$.

¹⁴Preamplifier/discriminator unit WMT PAD 01A, Dr. Sjuts Optotechnik GmbH.

¹⁵Channel electron multiplier model KBL10RS45V2, Dr. Sjuts Optotechnik GmbH.

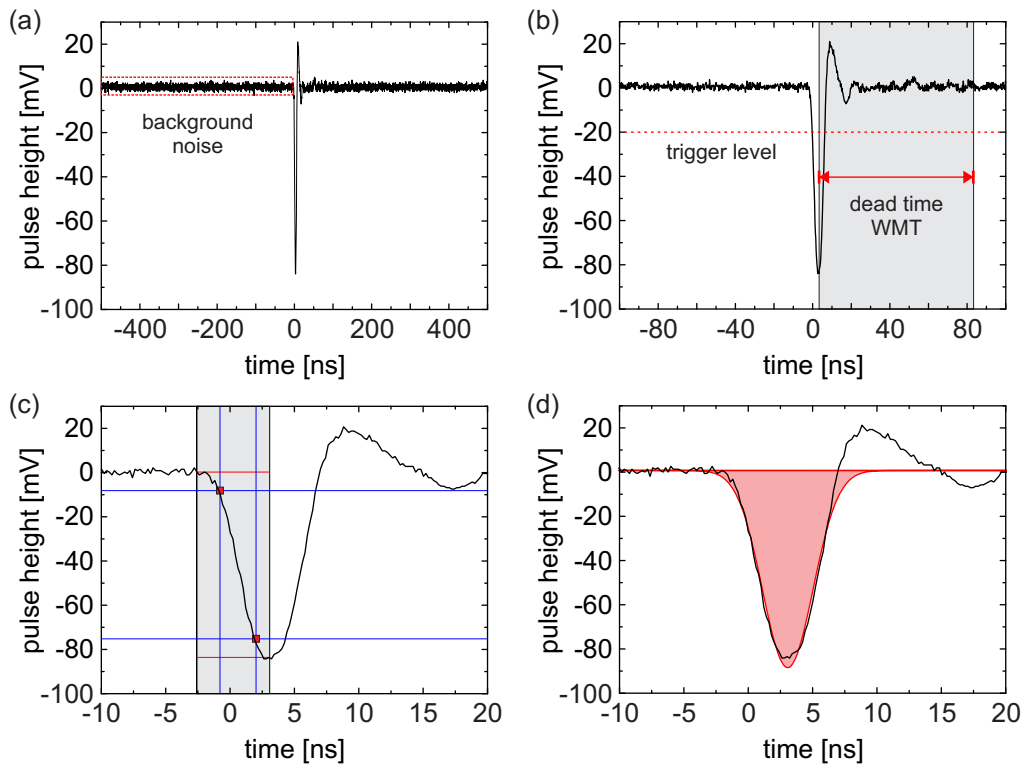


Figure 3.5: Single CEM pulse. (a) Measured sample CEM pulse trace, displaying the spurious noise in the signal cable in comparison to a single pulse incidence. (b) Zoom of (a), showing the trigger level of the discriminator unit of the subsequent pulse processing electronics. The corresponding dead time t_{wmt} of the discriminator unit is indicated by the shaded area with $t_{\text{wmt}} = 80 \pm 20$ ns. (c) Further zoom of (b), depicting the 10% - 90% pulse edge fall time $t_{\text{fall}} = 2.8$ ns. (d) Identical zoom to (c), showing a Gaussian fit of the pulse area (eq. 3.3).

chapter 4 and chapter 5. In addition to that, also the dead time of the respective discriminator unit is depicted (shaded area), with a given dead time of $t_{\text{wmt}} = 80 \pm 20 \text{ ns}$ as stated by the supplier. This dead time ensures that no second consecutive pulse is counted within the corresponding dead time window of t_{wmt} (see subsection 3.4.4). Additionally, also minor pulse ringing is observed in fig. 3.5(b) succeeding the single pulse incidence (see subsection 3.4.3).

In fig. 3.5(c), the 10% – 90% pulse edge fall time t_{fall} of the single pulse trace is depicted. The observed pulse edge fall time yields a value of $t_{\text{fall}} = 2.8 \text{ ns}$, comparable to commonly obtained pulse edge fall times of $t_{\text{fall}} = 2 - 5 \text{ ns}$ in the literature [153, 165]. However, the observed pulse edge fall (rise) time will mainly be of relevance in the particular case of determining the performance requirements of the subsequent pulse processing circuitry, and for the temporal resolution limit of two consecutive pulses (see subsection 3.4.4).

Finally, in fig. 3.5(d) the identical pulse to (c) is displayed, showing the Gaussian approximation (shaded area) of the temporal shape of the single CEM pulse (eq. 3.3). From the integrated area of the pulse, the individual pulse gain G can be derived (see subsection 3.1.2). For the single pulse of the trace, a Gaussian fit yields a pulse area of 0.434 V ns , with a full width at half maximum of $t_{\text{fwhm}} = 4.6 \text{ ns}$ of the Gaussian pulse peak. This results in a calculated single gain value of $G = 5.42 \times 10^7$ (eq. 3.2; $R = 50 \Omega$). In comparison to that, numerical integration of the respective pulse area in fig. 3.5(d) does not show any significant difference to the Gaussian fit, leaving eq. 3.3 a considerable approximation of the observed pulse shapes at the CEM anode.

3.3.3. Pulse height distribution histogram

From the individually measured single pulse traces as depicted in fig. 3.5, accumulated histograms of the measured pulse height distribution and the corresponding pulse width distribution can be generated. In fig. 3.6(a), a sample histogram of the observed pulse height distribution at a CEM gain value of $U_{\text{CEM}} = 2.3 \text{ kV}$ is displayed in logarithmic representation. For single pulse counting, the trigger level of the subsequent pulse processing electronics is indicated by a dashed line (fig. 3.5(b)). In the histogram, the obtained pulse height distribution exhibits a quasi-Gaussian shape. Accordingly, a Gaussian fit of the distribution (fig. 3.6(c)) yields an average pulse height $\bar{U}_0 = -94.5 \text{ mV}$, and a standard deviation of $1\sigma(\bar{U}_0) = 2.0 \text{ mV}$. The Gaussian shape of the observed pulse height distribution is in perfect agreement with the theoretical considerations of section 3.1. It further indicates that the corresponding CEM detector is operated in space charge saturation (fig. 3.2). In the literature, similar histograms of a Gaussian pulse height distribution of a CEM detector in space charge saturation are observed by, e.g., [106, 107, 131].

In correspondence to the observed pulse height distribution, the pulse width distribution of the measured single pulse traces is displayed in fig. 3.6(b). Note that the pulse width distribution is recorded simultaneously with the respective pulse height data. Similar to the pulse height distribution in fig. 3.6(a), also the pulse width distribution exhibits a Gaussian shape with an average pulse width of $\bar{t}_{\text{fwhm}} = 12.0 \text{ ns}$, and a standard deviation of $1\sigma(\bar{t}_{\text{fwhm}}) = 1.1 \text{ ns}$. As the product of both determined, average pulse parameters is linearly proportional to the modal gain G_0 (eq. 3.5), the calculated modal gain G_0 of this CEM detector at a particular gain voltage of $U_{\text{CEM}} = 2.3 \text{ kV}$ is $G_0 = 1.51 \times 10^8$ (fig. 3.7).

In the aspect of the trigger level for any subsequent pulse processing electronics in pulse counting mode, the observed effect of space charge saturation (see subsection 3.1.2) will yield a huge benefit on the choice of an appropriate trigger level for single pulse detection. In space

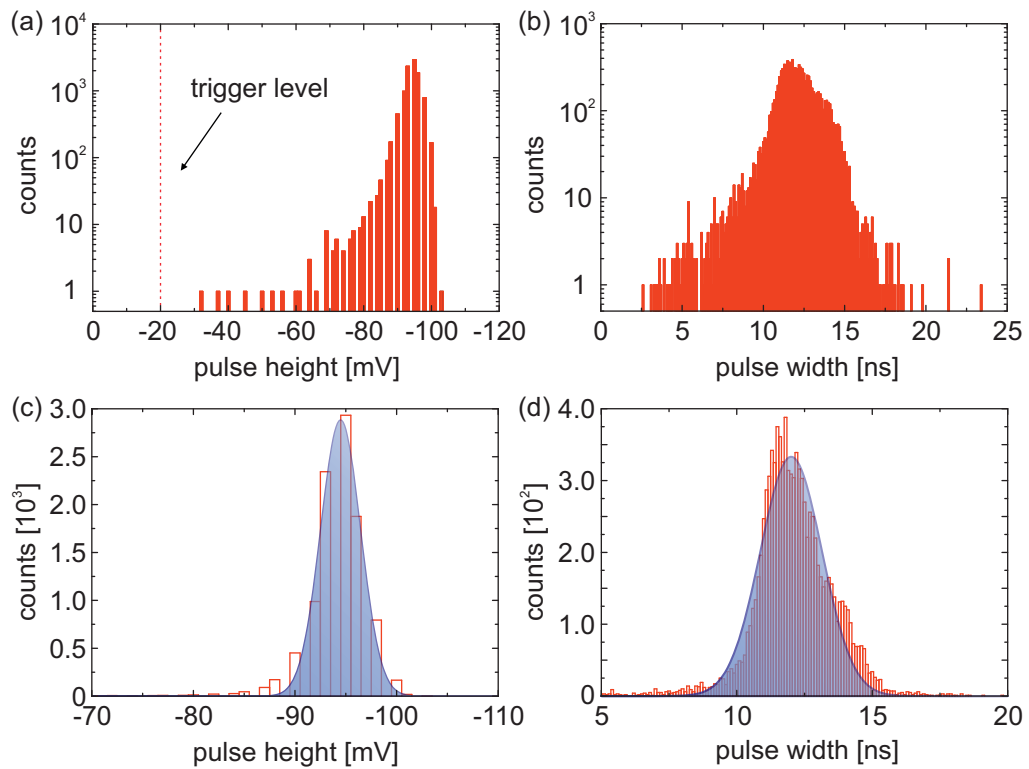


Figure 3.6: (a) Sample logarithmic histogram of the observed pulse height distribution at the CEM anode of a single CEM. The dashed line denotes the trigger level of the subsequent pulse processing electronics (fig. 3.5(b)). (b) Corresponding pulse width histogram to (a), recorded simultaneously with the pulse height data. (c) Linear zoom of (a) for pulse height values of -70 mV to -110 mV . The fit indicates the Gaussian shape of the pulse height distribution (fig. 3.2), while the detector is operated in space charge saturation. (d) Corresponding linear zoom of (b) for pulse width values of $5 - 20\text{ ns}$, with Gaussian fit, accordingly.

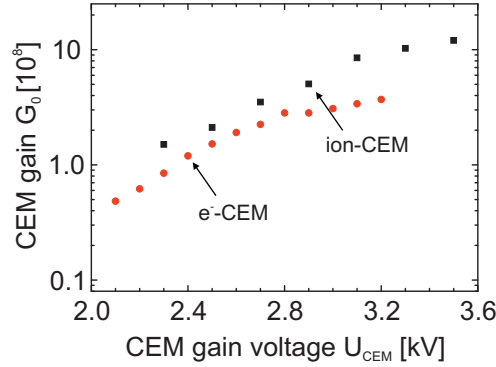


Figure 3.7: Measured CEM gain curve for two comparably new/unused CEM detectors for CEM gain values exceeding the linear amplification mode (fig. 3.1). The observed gain values $G_0(U_{\text{CEM}})$ are consistent with the calibrated gain values provided by the supplier, and common CEM detectors [47, 85, 139].

charge saturation, the pulse height distribution is expected to be quasi-Gaussian shaped and shifted to higher pulse height amplitudes (fig. 3.2). Therefore, not the initial compound Poisson distribution $P_m(n)$ will be subject to an eventual pulse loss due to an elevated trigger level (see subsection 2.2.1), but the resulting shifted quasi-Gaussian pulse height distribution. In fig. 3.6(a), the Gaussian fit of the observed pulse height amplitudes yields an average value of $\bar{U}_0 = -94.5$ mV, with a standard deviation of $1\sigma(\bar{U}_0) = 2.0$ mV (fig. 3.6(c)). In comparison to this, a chosen trigger level at -20 mV will correspond to more than 37 standard deviations (37σ) of the Gaussian pulse height distribution (fig. 3.6(a)). This results in literally no single pulse being lost by the particular choice of the trigger level for the subsequent pulse processing electronics.

3.3.4. Experimental modal CEM gain

From the individually measured parameters of single pulse traces (fig. 3.5) and their generated pulse histograms (fig. 3.6), the average pulse height \bar{U}_0 and pulse width \bar{t}_{fwhm} at the CEM anode for a corresponding gain voltage U_{CEM} can be determined. With these parameters, the experimental modal gain G_0 of a CEM detector can be calculated (eq. 3.5).

Figure 3.7 shows the measured sample gain curve for two comparably new/unused CEM detectors (ion-CEM, e⁻-CEM). Note that the experimental modal gain value G_0 of the e⁻-CEM at a CEM gain voltage of $U_{\text{CEM}} = 2.3$ kV explicitly corresponds to the pulse parameters illustrated in fig. 3.6. In general, both CEM gain voltage curves display to a considerable extent the expected gain characteristic as described in subsection 3.1.2. However by magnitude of the gain, the displayed gain values $G_0(U_{\text{CEM}})$ for these new detectors will already correspond mainly to the non-linear amplification mode of the CEM detector in space charge saturation (fig. 3.1), while the linear mode will presumably end at CEM gain voltages of $U_{\text{CEM}} < 2.4$ kV. The obtained modal gain values $G_0(U_{\text{CEM}})$ are further consistent to calibrated modal gain values provided by the supplier [159], and correspond to common experimental CEM gain values in the literature of $G_0 = 10^7 - 10^8$ for new, 'burned-in' detectors operating in pulse counting mode (e.g. [47, 85, 139]).

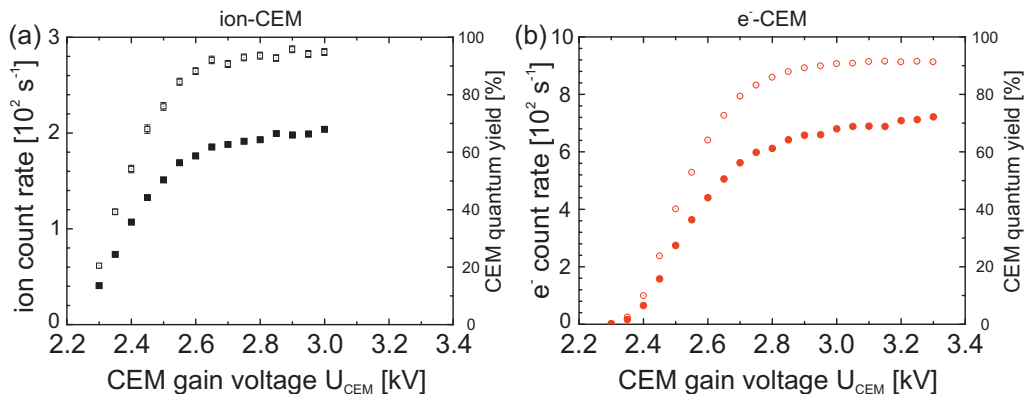


Figure 3.8: Characteristic knee curve (solid symbols), and corresponding CEM quantum yield (open symbols). Observed count rates according to the applied CEM gain voltage U_{CEM} for the ion-CEM (a), and the e⁻-CEM (b), respectively. In particular for the e⁻-CEM, the measured quantum yield shows the expected constant characteristic of the detector efficiency for considerable CEM gain values of U_{CEM} as illustrated in subsection 3.1.3.

3.3.5. Characteristic knee curve

In pulse counting mode, an important criterion of CEM detector operation is the continuous operation in space charge saturation which ensures the particular Gaussian shape of the pulse height amplitude distribution (see subsection 3.3.3). Accordingly, the specific shape of the distribution enables to count single incidences with literally no incidence loss, yielding the maximum attainable quantum yield η_{detector} with the CEM (see subsection 3.4.5). To routinely check that both CEM detectors are still operated in space charge saturation (see subsection 3.1.3), two sample count rate versus CEM gain voltage characteristics ('knee-curves') are displayed (fig. 3.8). Such knee curves are produced standardwise for CEM detector calibration to check the individual CEM detector operation parameters (e.g., [68, 166], or standard manuals as [85]). However, in contrast to the previous calibration measurements of this section, the CEMs are not calibrated out of random, spurious background incidences but from a well defined, constant particle flux of ionisation fragments (⁸⁷Rb-ions, e⁻) from photoionisation of neutral atoms in a defined ionisation volume (see chapter 4). In the aspect of any knee curve calibration measurement, such a defined particle flux is an integral parameter and important prerequisite (see subsection 5.1.3). Moreover, the simultaneously measured quantum yield η_{detector} of the individual CEM detector is determined to absolute values using photoionisation as correlated charged particle pair source (see section 5.1) and the two CEM detector arrangement of chapter 4. The absolute calibration measurements are then performed with a constant flux of correlated charged particle pairs at a chosen spatial position of the sensitive detection area $A_c(x, y)$ of the joint CEM detection system (fig. 5.13; $x = 1.2 \text{ mm}$, $y = -0.4 \text{ mm}$).

In fig. 3.8, the resulting characteristic knee curves¹⁶ (solid symbols) for the used CEM detectors are displayed. The sample knee curves are stated for the two CEM detectors calibrated in fig. 3.7, but after one and a half years of extensive use in the experiment. The observed count rate characteristics in fig. 3.8 show the linear gain and the plateau region of the knee curve as illustrated in fig. 3.4. Remarkably, no significant ion feedback is observed for these

¹⁶The displayed count rates are background corrected.

detectors for high CEM gain voltages U_{CEM} . Additionally, as both CEM detectors have to be considered 'old' at these measurements due to extensive use (see subsection 3.1.2), the knee curves of both detectors are already shifted to considerable higher gain voltages U_{CEM} compared to new CEM detectors¹⁷.

Moreover, also the observed quantum yield η_{detector} of the individual CEM detectors corresponding to the count rate response is illustrated in fig. 3.8 (open symbols). As previously proposed by several sources in the literature but *not* explicitly measured (e.g., [85, 139]), the quantum yield η_{detector} of a CEM detector follows the corresponding count rate characteristic (see subsection 3.1.3), and saturates at a constant efficiency, respectively (e.g., e^- -CEM; fig. 3.8(b)). However, a small increase in efficiency in the plateau phase of the knee curve observed for high values of U_{CEM} is owed to the enhanced secondary electron emission δ for increased CEM gain values (see section 2.4).

3.4. Particle counting and CEM operation

In this section, the influence of possible counting errors on the observed count rate N' compared to the true count rate N incident at the CEM detector entrance is investigated. In particular, eventual counting errors with a given CEM detection system are analyzed, which are not the result of the detection of an incident primary particle with the CEM detector, but are introduced, e.g., by the subsequent pulse processing electronics attached to the CEM.

For this, the possible sources for counting errors in pulse counting mode with a given CEM detection system are generally stated in subsection 3.4.1. Additionally, the particular choice of the trigger level of the subsequent pulse processing electronics is discussed in accordance to the observed single pulse traces and the associated pulse height distribution of section 3.3. In subsection 3.4.2, the influence of noise fluctuations in the signal cable in combination with a low trigger level of the subsequent pulse processing electronics is analysed. Accordingly, in subsection 3.4.3 accidental multiple counting of single particle incidences due to afterpulse ringing in the signal cable is illustrated. In this context, the beneficial influence of a dead time window associated with the subsequent pulse processing electronics in pulse counting mode is further stated. In subsection 3.4.4, an eventual loss of counting incidences at elevated count rates due to a reduced gain G_0 in a CEM detector is analyzed. Moreover, also the loss of incidences due to dead time corrections associated with the dead time of the CEM detector or any subsequent pulse processing electronics is examined. In this context, also the detailed resolution of two or more consecutive pulse incidences within a certain time period is specifically investigated.

Remarkably, from this detailed analysis it turns out that all these possible sources for additional spurious counts or an eventual counting loss of an incident particle can be disregarded in the context of this thesis. This results due to the particular shape of the observed pulse height distribution of the CEM detectors operating in space charge saturation, and the respective trigger level of the subsequent pulse processing electronics (see section 3.3). Moreover, this leaves the count rate measurements and the corresponding absolute detector efficiency calibrations of this thesis (see chapter 5) unencumbered by any counting errors or spurious counts associated with the subsequent pulse processing electronics (see subsection 3.4.5). As a unique property of this particular system, it therefore enables to determine

¹⁷Here, the corresponding 'knee' of the count rate characteristic approximately starts at CEM gain voltages of $U_{\text{CEM}} = 1.7 \text{ kV}$, in comparison to, e.g., the knee curve of the ion-CEM at $U_{\text{CEM}} = 2.6 \text{ kV}$ (fig. 3.8).

the raw quantum yield η_{detector} of a CEM detector to absolute values and compare the observed yield η_{detector} to the cascaded dynode detector theory of chapter 2. Finally note that the detailed counting error considerations of this section are universally applicable to any detection system based on single pulse counting, and are not particular specific for CEM detectors or cascaded dynode detectors only.

3.4.1. Single pulse counting and trigger level

For particle counting applications in general, the accurate determination of the observed count rate N' compared to the true count rate N is an important prerequisite. In the following subsections, possible error sources for additional spurious counts¹⁸ or an eventual pulse loss during single particle detection are therefore investigated. In pulse counting mode, such corrections will possibly affect the observed count rate N' at the corresponding detector in comparison to the true count rate N incident on the detector entrance. On one hand, additional spurious counts or multiple counting of a single primary particle incidence will enhance N' compared to N . On the other hand, an eventual counting loss due to, e.g., a non-vanishing contribution of observed small pulse heights below the chosen trigger level (see subsection 2.2.1), will lower the observed count rate N' compared to the true count rate N .

In pulse counting mode, the trigger level (i.e., the threshold value) of a subsequent discriminator unit is thus an important quantity for the counting of incident primary particles. If the trigger level is adjusted too high, single CEM pulses arriving at the CEM anode with a low pulse height amplitude will eventually fall below the particular trigger level of the corresponding counting unit. The incident primary particles will thus remain uncounted, accordingly. On the contrary, if the trigger level is adjusted too low, e.g., amplitude fluctuations of the noise background in the signal cable will produce additional spurious counts. However, such additional counts are not initiated by the impact of an incident primary particle in the CEM detector, but are introduced by the associated pulse processing circuitry and electronics of the CEM detection system. For an efficient and reliable particle counting ($N' = N$), the careful adjustment of the trigger level for each individual CEM detector is thus a prime requisite.

In this thesis context, assuming pulse counting mode and the case of a trigger level adjusted to comparably low pulse heights, eventual additional counts (spurious counts) will possibly result due to: (a) spurious counts initiated from amplitude fluctuations of the background noise in the signal cable (see subsection 3.4.2), or (b) accidental multiple counting of a single particle incidence due to afterpulse ringing in the signal cable (see subsection 3.4.3). In contrast to that, in the case of a comparably high adjusted trigger level, a possible loss of counting incidences will occur due to: (i) a considerable contribution of pulse heights distributed at small amplitudes below the trigger level in linear amplification mode (see subsection 2.2.1), in contrast to the expected pulse height distribution in space charge saturation (fig. 3.2), (ii) low pulse height amplitudes due to a reduced CEM gain G_0 at elevated count rates in the CEM detector, with the respective amplitudes situated below the trigger level (see subsection 3.4.4), and (iii) loss of incidences due to dead time corrections associated with a possible dead time of the CEM detector or the corresponding dead time of any subsequent pulse processing electronics (see subsection 3.4.4). In the following therefore, these possible error sources and counting corrections will be specifically investigated.

¹⁸By definition, spurious counts are not the result of a primary particle incidence at the CEM detector entrance, but are produced by the detector itself or the subsequent pulse processing electronics.

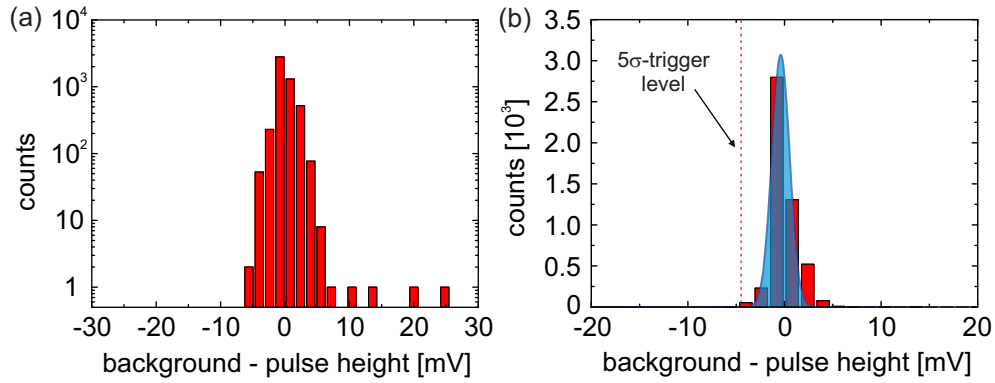


Figure 3.9: Sample histogram of observed noise fluctuations in the CEM signal cable. (a) Logarithmic histogram illustrating the pulse height distribution of the background noise prior to the single pulse incidence at $t = 0$ (red box; fig. 3.5(a)). (b) Zoom of (a) in linear representation, showing a Gaussian fit of the background noise (shaded peak), and an assumed trigger level at $5\sigma = -4.6$ mV (dashed line).

3.4.2. Background cable noise and spurious counts

In this subsection, eventual additional counts due to a low trigger level of the subsequent pulse processing electronics are analysed. These false trigger events will provoke spurious counts, altering the observed count rate N' at the CEM detector in comparison to the true count rate N (see subsection 3.4.4). The proportion of eventual false trigger events initiated from the fluctuations of the background noise in the signal cable can be calculated from the trigger level of the subsequent pulse processing electronics. In fig. 3.9, a pulse height distribution histogram of the noise fluctuations in the signal cable is displayed, with the fluctuation data taken in advance of the pulse incidence at $t = 0$ (red box; fig. 3.5(a)). A Gaussian fit of the background noise yields a Normal distribution of the fluctuations centered at $\bar{U}_{\text{noise}} = -0.39$ mV with a width of $1\sigma(\bar{U}_{\text{noise}}) = 0.92$ mV.

For a given trigger level of a subsequent discriminator unit, the proportion of false trigger events from the background noise is deduced from the determined width $1\sigma(\bar{U}_{\text{noise}})$ of the Normal distribution. However, in fig. 3.9(b) the observed width of the distributed background noise is remarkably small. For example, an imaginary trigger level of, e.g. five standard deviations ($5\sigma = -4.6$ mV; fig. 3.9(b)) of the Gaussian approximation of the background noise, will already be low enough to only get a false trigger event in the order of 1.744×10^6 fluctuation events from the background noise. However, in the experiments a trigger level of -20 mV is used for the measurements with the CEM detectors in this work (fig. 3.6(a)). In comparison, this will equal to an estimated trigger level of approximately more than 20σ of the observed background noise. Therefore, any eventual false trigger events caused by the fluctuations of the background noise in the signal cable can be disregarded for the current setup.

3.4.3. Signal cable ringing and impedance matching

In pulse counting mode, prominent afterpulse ringing in the pulse signal will possibly lead to the unfavorable situation of double or multiple counting a single primary particle incidence in the CEM detector. Similar to the considerations of subsection 3.4.2, this will result in ad-

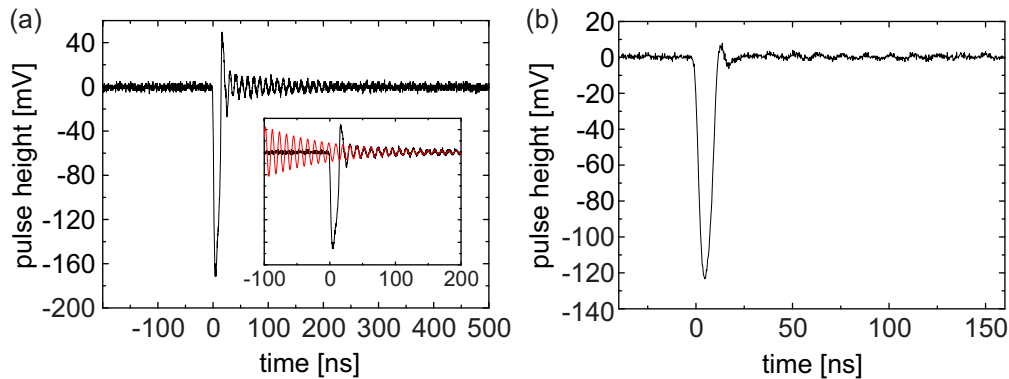


Figure 3.10: (a) Measured single CEM pulse trace of a CEM detector, displaying significant afterpulse ringing in the CEM signal cable caused by an unmatched cable impedance. Inset: Damped Sine fit of the afterpulse ringing. (b) Single pulse trace of a similar CEM detector arrangement with only minor afterpulse ringing due to improved impedance matching.

ditional spurious counts with the corresponding CEM detector. However, the observed afterpulse ringing even for comparably unmatched signal cables is generally small. Figure 3.10(a) shows a sample single CEM pulse trace of a previous CEM detector setup, displaying significant afterpulse ringing presumably caused by an unmatched cable impedance. The depicted trace is obtained with a comparably long signal cable in the UHV, with a cable length of $l > 50$ cm up to the connections of the electrical UHV-feedthrough (see section 4.2). As illustrated in fig. 3.10(a), the ringing indicates internal cable backreflections caused by an unmatched cable impedance. The inset in fig. 3.10(a) shows a damped Sine fit of the corresponding afterpulse ringing. The fit enables to determine a defined central frequency f , and a corresponding $1/e$ -decay parameter, which likewise allows improved impedance matching of the unmatched signal cable via additional electronic circuitry [167, 168]. In the contrast to that, fig. 3.10(b) displays the single pulse trace of an already quasi-matched signal cable of another CEM detector arrangement, only yielding minor afterpulse ringing. In this case, a comparably short signal cable ($l < 5$ cm) is used, leading to much faster ringing oscillations with lower amplitude.

In the case of accidental multiple counting of a single primary particle incidence in the CEM detector, some of the first ringing oscillations succeeding the main pulse will eventually still surpass the trigger level of the subsequent discriminator unit (fig. 3.10(a)). However, in pulse counting mode the integral dead time¹⁹ $t_{\text{wmt}} = 80 \pm 20$ ns of the discriminator unit prevents possible multiple counting of a single pulse incidence (shaded area; fig. 3.5(b)). This follows as even for primary particle incidences with large pulse amplitudes - after a dead time of 80 ns - most pulse ringing oscillation amplitudes will be well below the trigger level of -20 mV (dashed line; fig. 3.5(b)). Therefore, by using a discriminator unit with a considerable integral dead time and a correspondingly adjusted trigger level, no double or multiple counting of single primary particle incidences should be observed. This will result in no additional spurious counts due to an eventual afterpulse ringing for counting applications with the current setup.

¹⁹In general, any dead time t_{wmt} of the subsequent pulse processing electronics will inhibit the counting of consecutive pulses in pulse counting mode for the duration of t_{wmt} following an initial first pulse [169, 170].

3.4.4. Maximum count rate and resolution of two consecutive pulses

For several single particle counting applications, the efficient and reproducible counting of continuous high count rates resembles an important quantity. This follows as particularly an eventual loss of a considerable number of counting incidences at elevated count rates will significantly affect the observed count rate N' compared to the true count rate N . Additionally, also the detailed resolution of two or more consecutive pulse incidences within a certain time period is a relevant parameter for single particle counting applications.

Non-extendable dead time correction

In the aspect of high count rates, there is intrinsically no detector-based²⁰ dead time for the CEM detector itself (see subsection 3.2.2), but the CEM amplifies two or more temporally close, incident primary particles only by a reduced gain value (eq. 3.8). Accordingly, an eventual counting loss of incident primary particles can be prevented by adjusting the trigger level of the subsequent pulse processing electronics to lower pulse height amplitudes, correspondingly.

In pulse counting mode, the counting of consecutive pulses at elevated count rates is thus in principle not constrained by the amplification response of the CEM detector itself. Consequently, the relevant parameter for any possible dead time correction in pulse counting mode is only the dead time τ of any subsequent pulse processing electronics as, e.g., the integral dead time of an associated discriminator unit. Therefore, a possible correction of the true count rate N at the CEM detector due to the dead time of any subsequent pulse processing electronics can be calculated. Accordingly, for the registration of elevated count rates in pulse counting mode, the dead time correction of the observed count rate N' is defined as

$$N' = N/(1 + N\tau) \quad (3.9)$$

for a discriminator unit with an non-extendable dead time [169, 170]. In the previous equation, N represents the true count rate, while the quantity N' denotes the observed count rate, and the parameter τ yields the corresponding dead time of the subsequent pulse processing electronics. In the context of this thesis, the constraining time τ is the dead time of the discriminator unit $\tau \equiv t_{\text{wmt}} = 80 \text{ ns}$ (fig. 3.5(b)). At elevated count rates ($N_{i,e} \leq 10^4 \text{ s}^{-1}$) as typically obtained from photoionisation (see, e.g., section 5.4), this will correspond to a dead time correction ratio of $N'/N = 0.9992$, i.e., theoretically leaving only eight out of 10000 events eventually uncounted. However, applying faster pulse processing electronics with shorter dead times of, e.g., $\tau \sim 10 \text{ ns}$, will result in a dead time correction ratio of $N'/N = 0.9999$ for count rates of ($N_{i,e} \leq 10^4 \text{ s}^{-1}$), although at the cost of increased eventual afterpulsing due to the shorter dead time (see subsection 3.4.3).

Resolution of two consecutive pulses

The resolution limit of two consecutive pulses is derived from the temporal pulse width of the respective single pulses (see subsection 3.2.2). Correspondingly, the average pulse width of several single pulses can be deduced from the pulse width histogram (fig. 3.6(b)), yielding an average pulse width of $\bar{t}_{\text{fwhm}} = 12.0 \text{ ns}$ for the respective CEM detector (fig. 3.6(d)). Note

²⁰This implies that the CEM detector is at no point in time 'blind' to an incident primary particle at the CEM entrance.

that in the latter histogram, a Gaussian shape of the individual single pulses is assumed (fig. 3.5(d)). According to their average temporal width \bar{t}_{fwhm} , consecutive single incidences corresponding to count rates exceeding 80 MHz should therefore theoretically be resolved. In comparison, in the experiment sample traces of two or more pulses within, e.g., a time window below 100 ns, are occasionally observed²¹ (ion-CEM; fig. 5.3(a)). This indicates that the CEM detector is principally able to operate on count rates of at least 10 MHz. Moreover, similar temporal pulse resolutions of multiple consecutive CEM pulses are stated by, e.g. [85, 139, 154].

3.4.5. Pulse height distribution and detector quantum yield

In pulse counting mode, the particular shape of the observed pulse height distribution further enables to experimentally obtain the maximum attainable quantum yield η_{detector} with a given CEM detector as stated by eq. 2.6. In space charge saturation, this results due to the shifted and compressed quasi-Gaussian pulse height distribution at the CEM anode (see subsection 3.1.2). In pulse counting mode with the pulse height distribution shifted to higher pulse height amplitudes (see subsection 3.3.3), the trigger level of any subsequent pulse processing circuitry can thus be adjusted to considerably high pulse height amplitudes. Moreover, this additionally prevents the eventual counting of any spurious counts usually associated with a low trigger level (see subsection 3.4.2, subsection 3.4.3, and subsection 3.4.4). In space charge saturation therefore, the particular shape and position of the pulse height distribution assures that literally no pulses are lost by counting, or are additionally introduced by a low trigger level.

From a calibration measurement point of view, the observed CEM quantum yield will thus only suffer from detector-related properties as, e.g., an inefficient conversion of the incident primary particle at primary particle impact, or an early secondary electron avalanche die-out in the CEM channel. As a result from the measurements of this section and the previous section 3.3, the observed quantum yield η_{detector} of this thesis will therefore not be associated with any pulse loss or with additional spurious counts induced by the subsequent pulse processing electronics²². Remarkably, this leaves the count rate measurements and the corresponding absolute detector efficiency calibrations of this thesis work unencumbered by any non-detector based counting errors. By this, the raw quantum yield η_{detector} of a CEM detector can be calibrated to absolute values²³, and compared to the cascaded dynode detector theory of chapter 2.

²¹If single pulse traces are recorded as displayed in fig. 4.4, there is no associated pulse processing dead time within the time window of the observed trace. In contrast to the pulse counting mode with a discriminator unit, this allows to measure single pulse trains consisting of two or more consecutive pulses within a short time window of $t < 100$ ns.

²²This implies that the observed count rate N' will be identical to the true count rate N ($N' = N$), where N corresponds to the incident flux of primary particles at the CEM detector entrance.

²³This results from the absolute efficiency calibration via counting coincidences (see section 5.1), and the estimated collection efficiency of unity for this thesis detection system (see section 2.4).

4. Joint Channel Electron Multiplier Detector

In this chapter, the concept of photoionisation detection and the experimental benchmarks for the joint CEM detection system of this thesis are introduced. The CEM detection system is primarily intended to serve as a readout unit for single neutral atoms in an optical dipole trap in the context of a loophole-free Bell test experiment under strict Einstein locality conditions with two remote ^{87}Rb -atoms [18, 21]. For the implementation of the photoionisation detection scheme into the actual single atom trap configuration, the experimental setup of the CEM detection system is explicitly described and theoretically examined. By means of scan measurements using photoionisation, the imaging of the ionisation fragments in the CEM detection system is calibrated and investigated for a stable and reproducible operation of the CEM detection system over several months.

In section 4.1, a brief introduction is given which illustrates the potential of photoionisation detection with CEM detectors in comparison to alternative detection approaches. It further highlights the conceptional design and basic operation criteria of the joint CEM detection system of this thesis work. Accordingly, the experimental realisation of the system is described in section 4.2. Here, the vacuum system, the glass cell setup for the single atom trap, and the integrated CEM detection system are individually characterized. Additionally, initial design criteria and construction considerations are discussed which are required for the specific application of the CEM detection system as single atom readout unit in the actual single atom trap environment [45].

A simulation of the electric potentials of the integrated CEM detection system is performed in section 4.3 by means of numerically solving the corresponding differential equations on basis of the finite element method. The simulation of the potential distribution allows to model the expected flight times $t_{i,e}$ of the generated photoionisation fragments until their impact in the corresponding CEM detector (see section 4.4). It further enables to compare the calculated values with experimentally obtained flight times out of the correlation measurements in chapter 5. Together with the transit time t_{transit} of the secondary electron avalanche in the CEM (see section 3.2), this permits to calculate the detection time t_{det} of the two ionisation fragments with the joint CEM detection system, and thus the detection time to detect a single neutral atom.

The calculated flight times $t_{i,e}$ of section 4.4 will further yield an estimate of the impact position of the photoionisation fragments in the CEM. In combination with the correlation measurements and the measured flight time difference Δt of chapter 5, this will enable to experimentally determine the explicit impact position of the incident primary ^{87}Rb -ions in a CEM detector (see section 5.3). The impact position of the incident primary particles is particularly important in the aspect of obtaining a high quantum yield η_{detector} with a given CEM detector (see section 2.4). The knowledge of the explicit impact position thus permits to evaluate the associated impact parameters E_{kin} and θ , enabling to relate the corresponding parameters to secondary electron emission yield values δ_0 at isolated CEM surfaces. It therefore allows a general comparison of the observed CEM detector quantum yield η_{detector} with cascaded dynode detector theory as introduced in chapter 2.

The potential simulations of section 4.3 additionally show that the influence of the internal CEM potential on the incident primary particle becomes macroscopic for small kinetic particle energies $E_{\text{kin}} < 1$ keV at CEM cone entrance for *any* CEM detection system. This is particularly interesting as the kinetic particle energy at CEM cone entrance is usually stated as reference parameter for efficiency calibration curves $\eta_{\text{detector}}(E_{\text{kin}})$ of CEM detectors in the literature (see section 2.4). However, the kinetic energy at primary particle impact in relation to the kinetic energy at CEM cone entrance is significantly different as for low kinetic particle energies. This generally leaves different efficiency calibrations in the literature difficult to compare with each other even for identical CEM models if the impact positions of the primary particles in the CEM are not additionally stated [48].

The potential simulations and the flight time model also allow to evaluate an eventual particle loss during imaging of the photoionisation fragments into the CEMs. This effectively provides a theoretical estimation of the collection efficiency η_{col} of the joint CEM system of this thesis. The calculations show that the collection efficiency of the joint CEM detection system for the generated photoionisation fragments approaches unity. In contrast to any conventional particle detection system, this enables to observe the raw quantum yield η_{detector} of a single CEM detector with the current CEM detection system. As a remarkable property of this detection system, this leaves the efficiency calibration of this thesis work unencumbered by any eventual particle loss associated with non-detector related properties or counting errors (see section 3.4).

In section 4.5, the imaging of the photoionisation fragments in the CEMs is experimentally calibrated using 2D-scan measurements at a fixed z -position between the CEM detectors. For this, the photoionisation of neutral atoms in a defined ionisation volume as correlated particle pair source is employed. The simultaneous imaging of both photoionisation fragments in the CEMs allows to observe coincidences of the correlated charged particle pair. The counting of these coincidences enables to calibrate the CEM detectors to absolute efficiencies (see section 5.1). In additional measurements, the temporal and spatial performance stability of the CEM detection system is investigated. The calibration measurements indicate a stable and reproducible operation of the CEM detection system for several months of detector use. The joint CEM detection system thus fulfills the basic operation requirements as an atomic readout unit for a future loophole-free Bell test experiment under strict Einstein locality conditions [18, 21]. The beam overlap measurements of section 4.5 further experimentally demonstrate the spectroscopic and the spatial selectivity of the photoionisation detection scheme as introduced in section 4.1. This leaves photoionisation in a defined volume as the unique realization of a correlated particle pair source for the calibration of charged particle detectors (see section 5.1).

Conceptually, the particular design and configuration of the joint CEM detection system enables a large optical access to investigate and optically manipulate the particles to be detected with external laser sources. In contrast to common charged particle detection systems integrated in bulk metal systems, the large optical access due to the glass cell environment thus opens the opportunity for a wide range of, e.g., spectroscopic applications with the CEM detection unit in future experiments, particularly in combination with cold atom beam or trap systems. For an experimental implementation of the detection scheme however, the spatial limitations of the current single atom trap setup imposes significant experimental challenges for the design and integration of the charged particle detection system in the actual UHV

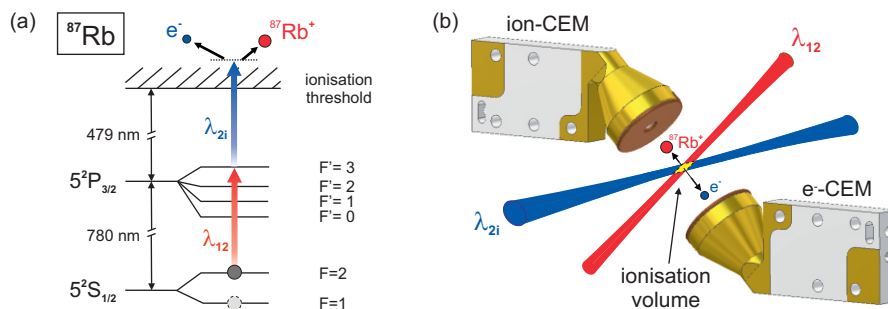


Figure 4.1: Concept of photoionisation detection. (a) Neutral atoms are photoionised hyperfine-state selectively within the spatial overlap volume of two laser beams via the application of a resonant two-step, two-colour photoionisation transition scheme. (b) The correlated pair of charged photoionisation fragments is dissociated by an applied electric field, and the individual fragments are registered by two charged particle detectors.

glass cell environment¹. The successful implementation of the joint CEM detection system in this particular environment thus represents one of the experimental achievements of this thesis.

4.1. Concept of photoionisation detection

The joint CEM detector introduced in this thesis uses photoionisation detection of single neutral atoms (fig. 4.1). The concept of photoionisation detection is generally characterised by two parts. First, a neutral particle is photoionised hyperfine-state selectively within the spatial overlap volume of two laser beams. By photoionisation, the initially neutral particle is subsequently converted into two or more charged photoionisation scattering fragments (fig. 4.1(a)). Second, the pair of oppositely charged ionisation fragments is dissociated by an applied electric field, and individually collected into two charged particle detectors (ion-CEM, e⁻-CEM; fig. 4.1(b)). In the detectors, each ionisation fragment is converted, amplified, and subsequently registered. For the photoionisation, a resonant two-step, two-colour photoionisation transition scheme² is chosen (fig. 4.1(a)). By application of this particular scheme, the photoionisation process is highly selective in the aspect of spectroscopic selectivity [171, 172], and also spatially highly selective for the corresponding beam intensities used in this work.

The spectroscopic selectivity of the photoionisation scheme results from the application of a resonant two-step, two-colour photoionisation transition. This follows as only atoms driven by *both* laser fields (ω_{12}, ω_{2i}) are subsequently photoionised (fig. 4.1). The use of narrow-band, single frequency laser sources further enables to address single hyperfine transitions of a selected atomic or molecular species, where an individual hyperfine state will be resonantly driven with a few saturation intensities only (fig. 4.1(a)). This allows the subsequent photoionisation of single atoms or molecules with a resolution down to single hyperfine states.

¹The inner dimensions of the glass cell are only 120 × 35 × 15 mm (fig. 4.6). This comparably tight confinement with adjacent non-conducting glass surfaces inflicts severe implications for the design and construction of the charged particle detection system.

²In the following, the first transition is denoted as the excitation transition (λ_{12}) while the second is called the ionisation transition (λ_{2i}).

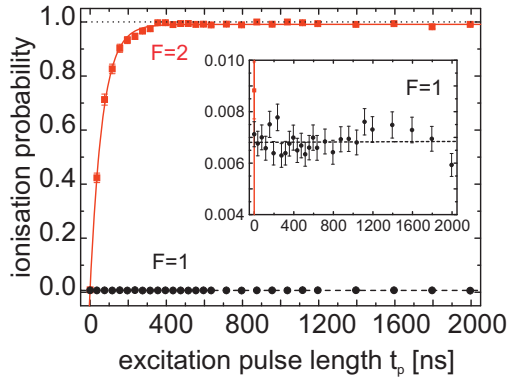


Figure 4.2: Hyperfine-state selective photoionisation of a single neutral ^{87}Rb -atom in an optical dipole trap [24]. Only atoms in the $F = 2$ hyperfine state driven by both laser fields (ω_{12}, ω_{2i}) are subsequently photoionised (fig. 4.1(a)). Depicted is the photoionisation probability p_{ion} for different laser pulse lengths t_p of the excitation laser (λ_{12}). To demonstrate the hyperfine-state selectivity of the resonant photoionisation process, the trapped ^{87}Rb -atom is initially prepared either in the $5^2S_{1/2}, F = 2$ or $F = 1$ hyperfine state (fig. 4.1(a)). Inset: Zoom of the photoionisation probability for the atom prepared in the $F = 1$ state.

Accordingly, the hyperfine-state selective photoionisation of a single neutral ^{87}Rb -atom in an optical dipole trap is depicted in fig. 4.2. The corresponding measurements are performed with the current single atom trap [45], in which the joint CEM detection system of this thesis is designed to be integrated as future single atom readout unit. To experimentally demonstrate the hyperfine-state selectivity, the detection speed, and the photoionisation probability of the chosen photoionisation scheme, the single neutral ^{87}Rb -atom in the optical dipole trap is initially prepared either in the $5^2S_{1/2}, F = 2$ or $F = 1$ hyperfine state (fig. 4.1(a)). Only ^{87}Rb -atoms in the $F = 2$ hyperfine state driven by the resonant³ excitation transition λ_{12} are transferred to the intermediate $5^2P_{3/2}, F' = 3$ -level, and are subsequently photoionised. This hyperfine-state selective photoionisation occurs within a photoionisation time of $t_{\text{ion}} = 386$ ns and with an ionisation probability of $p_{\text{ion}} = 0.991 \pm 0.001$ [24]. However, the detailed analysis of the photoionisation of optically trapped, single ^{87}Rb -atom and the corresponding single atom trap setup will be covered in depth in the PhD thesis of Michael Krug [46]. Therefore, at this stage the reader is recommended to the relating publication [24].

The spatial selectivity of the photoionisation scheme follows as the ionisation via single-step transitions or two-step, single-colour transitions are either not possible (single-step), or extremely unlikely at the laser beam intensities used in the experiment (two-step, single-colour). In the first case this results as the individual single photon energy ($E_{12} = 1.59$ eV, $E_{2i} = 2.62$ eV) of both laser transitions is not sufficient to excite the neutral atom beyond the ionisation threshold by a one-photon transition ($E_{\text{thres}} = 4.18$ eV; fig. 4.1(a)). In the second case, the calculated⁴ transition rate W_2 for any single-colour, two-photon process is negligible at the

³The scattering cross section for a *resonant* transition in the $D2$ -line of ^{87}Rb is $\sigma_{12} \approx 10^{-9}$ cm², while the non-resonant scattering cross section is typically in the range of $\sigma_1 \approx 10^{-17}$ cm² [173].

⁴Non-resonant multi-photon absorption from the ground state to the continuum occurs through laser-induced virtual states which are not eigenstates of the atom [174]. According to perturbation theory of non-resonant multiphoton ionisation, the N -photon ionisation rate W_N is given by $W_N = \sigma_N \Phi^N$, where σ_N is the generalized N -photon ionisation cross section (in units of cm^{2N}), $\Phi = I/E$ is the photon flux, I denotes laser intensity, and $E = \hbar\omega$ represents the energy of the single photon. For non-resonant, two-photon

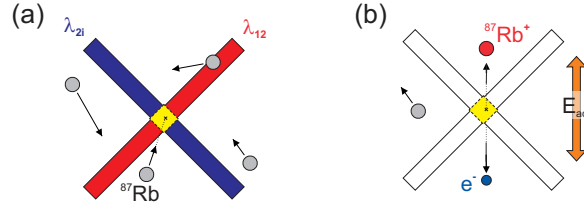


Figure 4.3: Spectroscopic and spatial selectivity of the photoionisation detection. (a) As the narrow excitation transition (λ_{12}) allows to address single hyperfine states in a single species, only ^{87}Rb -atoms resonant to the corresponding transition are subsequently photoionised (fig. 4.1(a)). (b) The photoionisation occurs only within the spatial overlap volume of the two laser beams. This results as any single-colour, multiple-step photoionisation transitions can be neglected at the beam intensities used in the context of this thesis.

laser beam intensities used in the context of this thesis ($W_2 \approx 5.6 \times 10^{-6} \text{ s}^{-1}$). As a result, the photoionisation of neutral atoms therefore occurs only in the spatial overlap of the two laser beams. Consequently, the spatial extension of the beam overlap explicitly defines the dimension of the photoionisation volume (see section 4.5). Moreover, the photoionisation of neutral atoms in a spatially defined ionisation volume yields the perfect calibration source for charged particle detectors (see subsection 5.1.3), providing correlated charged particle pairs for an absolute efficiency calibration of the CEM detectors (see section 5.4).

In the aspect of an experimental realization of photoionisation detection as future readout unit in the current single atom trap setup [45], the joint CEM detector system of this chapter has to be entirely implemented into the extremely shallow glass cell environment (fig. 4.6; glass cell, inner dimensions: $120 \times 35 \times 15 \text{ mm}$). One criterion is therefore to create a detection system for charged particles with as few particle optics elements as possible, and almost no shielding elements. A further restriction is the additionally limited space of the joint CEM system within the glass cell. This results from the particular spatial positions of the optical beams of the future magneto-optical trap (MOT) setup (fig. 4.6; MOT beam access). Moreover, an even tighter constriction is the spatial position of the future single atom trap. It will be situated in the MOT region, i.e., the central spatial overlap of the corresponding MOT beams. The position of the single atom trap defines the origin of the generated photoionisation fragments which thus resembles the future position of the ionisation center (fig. 4.6; atom trap position).

As both photoionisation fragments are to be detected quasi-simultaneously in coincidence, the CEM detectors have to be positioned around the ionisation center accordingly. The detectors are therefore arranged oppositely with a comparably short distance to each other in a 'face-to-face' configuration (fig. 4.1(b)). This particular arrangement will create a free line of sight in between both CEM detectors on which both generated photoionisation fragments will propagate unhindered into the corresponding detector. Moreover, due to the symmetry of the two CEM detector arrangement, also the ability to interchange both CEM detectors is

photoionisation, as a rough approximation the second photon has to be absorbed within the lifetime of the virtual intermediate atomic level which is of the order of ω^{-1} , i.e., 10^{-15} s . Assuming that the ionisation cross section of the second event is comparable to a non-resonant, single-photon transition ($\sigma_1 \approx 10^{-17} \text{ cm}^2$), the overall two-photon ionisation rate will be $W_2 = \sigma_2 \Phi^2 = \sigma_1^2 \Phi^2 \omega^{-1}$, where $\sigma_2 = \sigma_1 \omega^{-1} \sigma_1 = 10^{-49} \text{ cm}^4 \text{ s}$ [175, 176]. For the calibration measurements of this thesis, this results in a two-photon transition rate of $W_2 \approx 5.6 \times 10^{-6} \text{ s}^{-1}$, using an intensity equivalent of $I_{21} = 6.3 \text{ kW} \cdot \text{cm}^{-2}$ at the center of the ionisation volume (see section 4.5), and $E_{21} = 2.62 \text{ eV}$.

given by adjusting the electric potentials of the cone entrances of both CEM detectors accordingly. This allows to operate either CEM as ion (electron) and corresponding electron (ion) detector. Note that the ability to deliberately address a particular CEM detector potential (see subsection 4.2.4) represents one of the distinguished features of the joint CEM detection system.

In the aspect of an experimental realisation of the CEM detection system, a glass cell UHV environment is generally rather unsuited for the integration of a charged particle detector with corresponding charged particle optics and electrical shielding. Moreover, the intended use of high-power laser beams for photoionisation in combination with high voltage potentials in an ultra-high vacuum environment complicates an experimental realization even further due to the increasing influence of stray charges (see section 4.2). The implementation of the joint CEM detection system into the particular glass cell environment therefore resembles probably one of the substantial experimental challenges and achievements of this thesis work. To our knowledge, there is no second system in the literature which combines the coincident detection of charged particle pairs via two CEM or MCP detectors at such small spatial distances, and in a glass cell environment. However, to some extent related systems in bulk metal UHV setups with an opposing two detector arrangement are mentioned by [177–182].

4.1.1. Alternative charged particle detection systems

In this thesis, channel electron multipliers (CEMs) are exclusively used as charged particle detectors. However, possible alternatives to channel electron multipliers as particle detectors are briefly investigated in the following subsection. The particular choice of CEM detectors as particle detectors is primarily guided by the future integration of the CEM detection system as an atomic readout unit for a loophole-free Bell test experiment based on two remote, entangled single ^{87}Rb -atoms [18, 21]. Moreover, although individual properties of some of the alternative detection units seem to be additionally beneficial for the detection system in a more general context (e.g., the spatial resolution of MCPs), the unique prerequisites of the future detector use in the single atom trap experiment reduce the possible choice of detectors down to channel electron multipliers.

Multichannel plates, thermionic diode detectors, and carbon nanotubes

In general, there is only a small range of different particle detectors for the efficient detection of single neutral atoms. As the detector has to be integrated into the particular UHV-glass cell MOT-system of the current single atom trap experiment [45, 183–185], compactness, simplicity, and robustness of the chosen detector unit are prime requisites for a possible implementation. Moreover, the future detection system has also to provide a high detection efficiency for single particle incidences, and an overall detection time under a microsecond as fast and efficient neutral atom readout unit [18, 21]. As a result, only a few alternatives to CEM detectors remain which are worth being considered for this particular application. These alternatives are multichannel plates (MCPs, excellent review by, e.g., [186] and articles by [123, 187–192]), thermionic diode detectors [193], and, to some extent in aspect of efficient ionisation of neutral atoms, carbon nanotubes [194].

Multichannel plates (MCPs) offer two general advantages over single channel detectors, as they additionally preserve the spatial information of an incoming particle and display outstandingly short timing properties due to their compact geometry. Even for stacked MCP

assemblies, the individual length of a single MCP channel is small compared to conventional discrete or continuous dynode multipliers. Accordingly, the transit time of the electron avalanche in the channel is remarkably short, usually in the 100 – 800 ps range⁵ [195]. Moreover, due to the planar detector geometry of the multichannel structure, the spatial information of incoming particles can be preserved and reconstructed for two-dimensional imaging of incident particles [181, 196]. However, the sensitive detection area of an MCP-detector is severely reduced in space due to the interchannel distances (pitches) in between the active microchannels owing to the spatial geometry of the detector face. Thus, primary particles striking the pitches will fail to start a secondary electron cascade. This effectively reduces the sensitive detection area of any MCP detector, yielding typical open area ratios (OAR) of about 60%. As the maximum detection efficiency of an MCP is approximately equal to the value corresponding to the fraction of the active surface that is occupied by the channels [123, 190, 191], the highest attainable detection efficiency will reach only $\eta_{\text{MCP}} = 0.6$. Further, the single channel dead time (time until the channel wall charge has recovered after 'firing') of an individual microchannel within the microchannel plate is on the order of $t = 10^{-3}$ s [186]. Assuming that the same channel is eventually hit repetitively, this will yield a maximum duty cycle of only up to 1000 particle detections per second. Together, these parameters rule out MCPs as possible candidates for efficient particle detection if absolute detection efficiencies over 80 % and detection times in the microsecond range are intended.

Thermionic diode detectors are compact, rugged, and simple in their application [193, 197–199]. Their operation is based on Ohmic heating of an activated cathode filament where the thermionic emission of electrons forms an electron cloud around the cathode wire. In space charge saturation mode, the presence of ionised atoms next to the cathode filament lowers the space charge potential barrier of the cathode resulting in a sudden release of additional, thermionic electrons in burst. This burst results in an observable increase in the electron current ΔJ in the cathode wire related to the given, saturated Richardson-Dushman current J_s as $J_c = J_s \exp[-e_0(\phi_{el} + \Delta\phi_{el})/(k_B T)]$ (where J_c is the diode current through the filament, ϕ_{el} the space charge potential, and T the temperature of the filament). Although thermionic diodes are linear over several orders of magnitude and down to count rates of 10 ions s⁻¹ [193], they are presumably not suited for single particle resolution as the expected detector currents will be too low to be properly discriminated against thermal, flicker, or shot noise of the cathode wire. Additionally, the presence of a hot filament and thus of a thermal electron emission source next to a sample of cold atoms excludes these kind of detectors for the application in the glass cell setup. This results as a thermionic diode will therefore be a possible source for, e.g., radiative heating, or increased thermal collisions with the ultracold sample.

In the aspect of ionisation, as an alternative to laser-induced photoionisation of neutral atoms, carbon nanotubes [194, 200, 201] seem to be a promising candidate for efficient atomic ionisation even in the ground state. Here, neutral atoms via their polarisability are attracted to high electric fields of the wall of a carbon nanotube and are rapidly ionised next to the wall, generating charged ions which can be extracted and subsequently detected [194]. Although, as the ionisation probability of the carbon nanotube system seems to approach almost one, the authors additionally claim a high detection efficiency for the *overall* system. However, the actual detection and counting of the generated ions is still implemented by single CEMs.

⁵<http://sales.hamamatsu.com/en/products/electron-tube-division/detectors/microchannel-plates-mcps.php>

Therefore, at present the ultimate detection efficiency for these systems will still be limited by the absolute detector efficiencies of the used CEMs. Furthermore, as the ionisation next to a carbon nanowire is initiated by the advent and orbiting of the neutral atom around the wire within a considerable time far greater than the timescales of photoionisation, this approach yields for our application no intrinsic advantage to the photoionisation detection scheme described in the thesis.

In summary, CEMs are still the most promising candidate for the highly efficient detection of single neutral atoms in small, compact UHV glass cell setups. Moreover, these detectors still seem to be the only single particle detectors with the potential to achieve a sufficient high quantum yield η_{detector} which will provide the intended, absolute detection efficiencies exceeding 80% within estimated detection times in the sub-microsecond regime.

4.2. Joint CEM detector

The following section describes the vacuum system and the integrated CEM detection system. The CEM detection system is designed and built with the focus on the future use of the setup as a substitute of the entire vacuum system in the actual single atom trap setup. Accordingly, the individual requirements of the particular single atom setup have to be considered in detail. For the integration of the detector in the glass cell UHV environment, selected vacuum materials, different vacuum techniques⁶ and an individual design/treatment of all substantial detector components have to be applied in addition to the 'standard' single atom trap requirements. Moreover, the construction of the CEM detection system demands additional effort especially with respect to stray light, stray particles, and stray charges in the UHV. In contrast to the current single atom trap setup [45], the influence of these ambient stray particles will macroscopically affect the overall readout performance of the future CEM detection system. As a solution, a spatially close configuration of the CEM system in combination with a floating electric potential for the operation of each single CEM detector is introduced. This particular configuration allows to detect the different charged particles originating from photoionisation in between the CEMs in quasi-coincidence within sub-microsecond detection time and high detection efficiency.

4.2.1. Channel electron multipliers

As CEM detectors represent the key element of the joint CEM detector of this thesis, a general introduction in the history, basic operation, and common usage of CEMs is briefly given in the following subsection. However, excellent reviews in the literature are provided by [47, 139, 140], or in common CEM supplier handbooks of, e.g., [85]. The particular operation and performance of these detectors is introduced and extensively discussed in chapter 3. For the application of CEMs in the context of this thesis, only the main, important parameters for the operation of the detector are therefore briefly highlighted.

Channel electron multipliers (CEMs) are an indispensable tool for the detection of single charged particles or charged particle currents where the incident currents involved are low ($I < 10^{-15} \text{ C s}^{-1}$). They are also sensitive to photons and neutral particles (see subsection 2.4.2). Due to their sensitivity to extremely low particle currents, CEMs are heavily

⁶Particularly cleaning techniques of the individual detector components as, e.g., the entire glass cell from adhesive dust particles prior to evacuation, are crucial for the stable operation of the future detector.

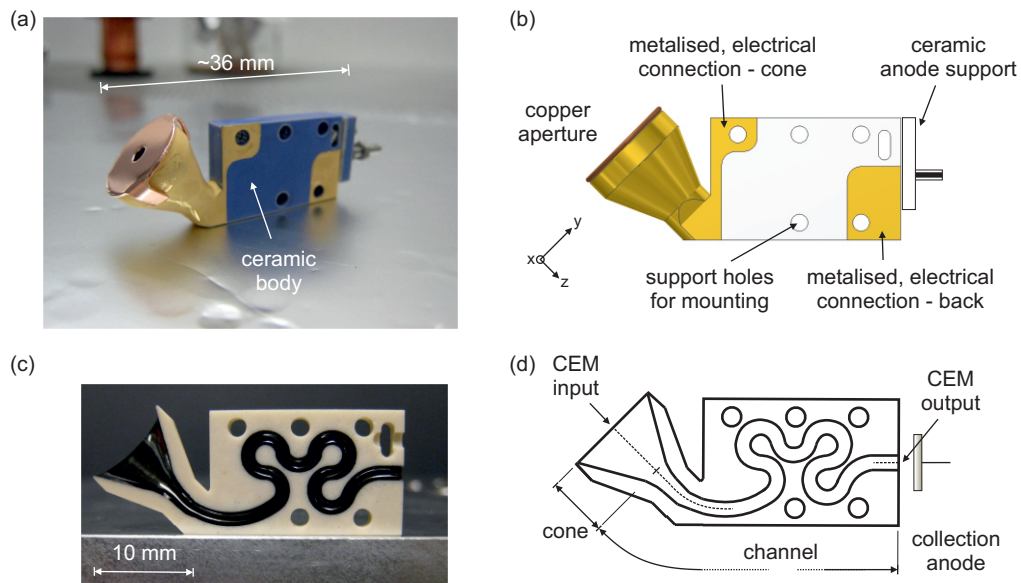


Figure 4.4: (a) Photography of an assembled CEM detector with mounted entrance copper aperture. (b) Schematic view corresponding to (a). The metallised cone and back connections are contacted to the input and output end of the channel tube. This enables the application of a high voltage over the internal, continuous dynode tube. (c) Photography of the ceramic CEM body cut in half, displaying the internal, curved channel dynode structure. (d) Half section view scheme corresponding to (c), showing the cone and channel section.

incorporated in a whole range of detector applications as, e.g., mass spectrometers, scanning electron microscopes, or in ultraviolet/x-ray spectroscopy. Concerning conventional vacuum systems, CEM detectors are relatively simple, rugged, and compact in aspect of handling and integration into an existing setup. Being further comparably inert to the ambient environment, they exhibit a good tolerance for exposure to atmospheric air, to repetitive evacuation, and to bake-out in ultrahigh vacuum systems (see subsection 3.1.2). Moreover, CEMs are commercially available in a variety of shapes, sizes, and models. Over the last decades, mainly two different body versions of single channel electron multipliers have been developed and manufactured, with the historically earlier version based on a lead glass tube (standard CEM or Channeltron™, [59, 202–204]), and a later version based on a ceramic body (ceramic CEM or Ceratron™, [205–209]). For the latter type, the secondary electron emitting lead glass tube is integrated into a solid ceramic body. Due to the ceramic body, this type is to a considerable extent easier in handling, operation, and incorporation into rugged systems as, e.g., space applications [210].

There are generally two modes of operation for channel electron multipliers - the analogue mode and the pulse counting mode (see section 3.1). In analogue mode, the incoming particle flux is linearly amplified without resolving single incidences. This results in a correspondingly enhanced secondary electron current at the detector anode. In pulse counting mode, single particle incidences are individually resolved, amplified, and subsequently counted. In the context of this thesis, as *single* charged particles are to be detected, only the pulse counting mode is therefore of major interest.

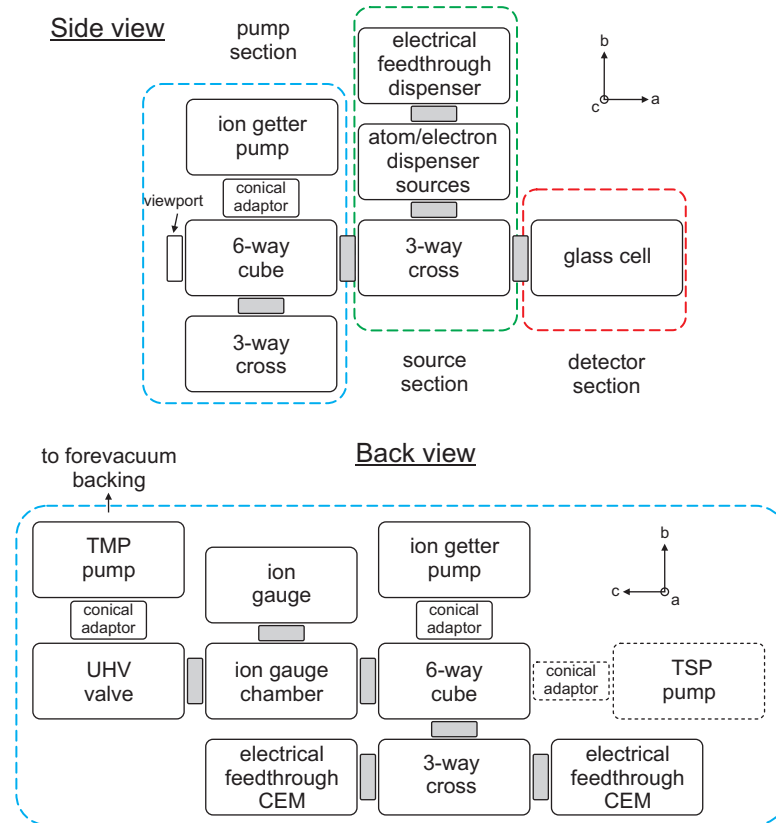


Figure 4.5: Schematic view of the single atom trap vacuum system with the integrated joint CEM detection system. (a) Side view in $a - b$ plane. The entire vacuum system is segmented into three parts; the detector section (red), the atom source section (green), and the pump section (blue). (b) Back view of the vacuum system in $b - c$ plane. Closeup of the pump section with ion getter pump, turbo-molecular pump and ion gauge mounted upside-down. The eventual adaption of a titanium sublimation pump system is indicated by the two dashed elements.

4.2.2. Vacuum system setup

The scheme of the vacuum system for the future integration of the joint CEM detector in the single atom trap setup is illustrated in fig. 4.5. The vacuum system is segmented into three main parts (fig. 4.5(a)). The detector section (red) consists of a quartz glass cell (Suprasil) wherein the joint CEM system and the future single atom trap are situated. The source section (green) consists of the atom sources, an additional electron source and the electric feedthrough for the individual sources. In the pump section (blue), the pump systems, the electrical feedthroughs of the CEM cables, and the ion pressure gauge are set. For future single atom precision experiments, the entire UHV chamber is made of steel with a low magnetic permeability (316LN steel). All individual vacuum elements in the three sections are sized and connected by standard CF-40 flange tubing and consist mainly of commercially available components. For improved pumping of the individual vacuum pump systems, conical adaptor flanges⁷ are used matching the different flange sizes and larger tube diameter of the

⁷Conical adaptor flanges yield improved pumping compared to their zero-length counterpart. Note however that the *calculated* conductance value predicts a reduced performance.

corresponding pump entrance. To shield the CEM detector system from any parasitary stray light or emitted stray charges originating from the ambient vacuum system itself, all active vacuum components are mounted at least around one corner turn (fig. 4.5). Such active components are either the atom/electron sources, the ion gauge, or the ion pump system.

The entire vacuum chamber is pumped through the CF-40 six-way cross cube by a $501 \cdot \text{s}^{-1}$ ion pump (Varian, VacIon Plus 55 StarCell). An attached all metal angle valve at the ion gauge chamber allows to connect a roughing pump system for initial pump down and bakeout of the entire vacuum chamber. To prevent the pumps from macroscopic particle intrusion during rough pumping at initial pump down, the ion getter pump, the turbo-molecular pump and also the ion gauge are mounted upside-down. The vacuum pressure of the entire chamber can be monitored down to levels below 10^{-10} mbar with a high sensitivity ion gauge (Varian, UHV-24p). The ion pressure gauge is mounted in an attached, separate gauge chamber. The separate mounting prevents the operating gauge from measurement deviations induced by magnetic stray fields of the nearby ion getter pump. The spatial dimensions of the ion gauge chamber are designed to be sufficiently large to inhibit ambient wall degassing due to heating by the hot gauge filament. For the eventual adaption of a titanium sublimation pump system (Varian, TSP cartridge source integrated into a water-cooled TSP cryopanel), an additional port at the six-way cube is blindflanged. Such a TSP system will particularly enhance the pumping speed⁸ for reactive, getterable gases like hydrogen and nitrogen. Moreover, at considerable low pressures it allows to switch off the entire ion getter pump system. By dismounting the external magnets of the ion getter pump, the TSP system will then solely pump the whole vacuum system. This will result in a significantly reduced magnetic perturbation of the entire single atom trap setup caused by the ion getter pump magnets.

The source section (fig. 4.5, green) holds three ^{87}Rb -atom sources (atomic vapor dispensers; Alvatec and SAES getters) mounted upside-down in an upright, standard CF-40 tube attached to the three-way cross. An additionally mounted tungsten wire extracted from a commercial light bulb serves as electron emitting source for test purposes. During dispenser operation, the wire is held on a constant positive potential of +300 V which deflects/attracts emitted ions and electrons out of the thermal dispenser source. This effectively creates a charged particle trap, preventing stray charge bombardment of the overall CEM detection system and its associated cables. To further shield the corresponding cables from stray charges or induced cable noise from the atom sources, in the source section all CEM cables are additionally guided within a straight copper tube (Oxygen-free high thermal conductivity (OFHC) copper, inner diameter ~ 10 mm) for the whole length of the section. For neutral atom release, the atomic vapor dispensers are operated by ohmic heating.

Initially, the entire vacuum system is baked out at 240°C for one week. A bakeout at such high temperatures will ensure that most bulk impurities out of the metal walls will be driven out of the material and subsequently be pumped. Prior to the initial bakeout, the glass cell with the joint CEM detector system is dismantled and the open CF-40 port at the source section of the main chamber is blindflanged. For pumping during bakeout, a roughing pump system and a $551 \cdot \text{s}^{-1}$ turbo-molecular pump (Leybold, Turbovac 50) are attached to the main chamber via the all metal angle valve (fig. 4.5). During the baking procedure, the atomic vapour dispensers are initialised, and then constantly heated with a low current ($I = 2.5 - 3.0$ A). After cooling the apparatus down, the main chamber is opened again and

⁸Water-cooled TSP cryopanel pumping speed (at 20°C): $\text{N}_2 \sim 5151 \cdot \text{s}^{-1}$, $\text{H}_2 \sim 12001 \cdot \text{s}^{-1}$, and $\text{H}_2\text{O} \sim 5751 \cdot \text{s}^{-1}$.

the glass cell is reattached to the main chamber. In a second, consecutive bake-out stage, the whole system is then baked again for another one and a half weeks at 110°C. This comparably low bake-out temperature is owed to the low melting point of the glass-to-metal sealing of the glass cell made from indium (melting point: $\sim 157^\circ\text{C}$). After the whole bakeout, a total pressure of the order of 10^{-10} mbar is achieved.

4.2.3. Glass cell setup

The actual detector section of the vacuum system consists of the glass cell and the internal CEM detection system. The entire joint CEM detection system is incorporated in the glass cell as illustrated and pictured in fig. 4.6. The joint CEM detection system and the glass cell are both connected to the atom source section of the main steel chamber by two CF-40 flange mounts (fig. 4.5, red). The glass cell (Helma) is produced from optical high-quality quartz glass (Suprasil) and coated with a broad-band AR-coating on the outer surfaces (reflectivity smaller 0.5% for 473 nm and 780 – 850 nm at normal incidence). The cell exhibits a shallow, rectangular shape with outer dimensions of $120 \times 41 \times 21$ mm, and a wall thickness of 3 mm (fig. 4.6). For a future integration in the actual retro-MOT system [45], two highly reflecting mirror substrates are coated on one of the two large surfaces of the cell (reflectivity greater 98% for 780 nm at incident angles of $45^\circ - 55^\circ$). The glass cell is attached to the source section of the main vacuum chamber by an aluminum clamp that presses the entire cell onto a highly-grade polished CF-40 flange. The pressure on the clamp is applied with only four sealing screws, while careful adjustment of each individual screw ensures that the mechanical stress on the glass cell is distributed evenly. In between the cell and the CF-40 glass cell flange mount, a rod of pure indium metal (GoodFellow, diameter: 2 mm; purity $> 99.999\%$) formed to match the shape of the cell opening provides a leak-tight glass-to-metal sealing. Due to the particular arrangement of the four guiding rods of the clamping, the optical access to the glass cell is excellent along all main optical axes. To prevent the operating high-voltage system from voltage arcing and dielectric breakdown at any elevated tips or corners, the pointed edges of all copper vacuum elements are consequently filed off, trimmed and mechanically high-polished. Moreover, a design avoiding pointed edges at any detector component is generally chosen. For spatial homogeneity of the generated electric fields, also all surfaces are additionally flattened and high-polished.

The entire joint CEM detector system in the glass cell (fig. 4.6) is mounted and suspended on a highly-polished copper frame (OFHC copper, purity $> 99.99\%$). In the actual setup, the copper frame itself is attached to a second frame, the mounting frame, by copper screws. Non-conducting screws and nuts (Macor[®], glass-ceramic or Vespel[®], polyimide) connecting the frames will yield the option to isolate the copper frame potential from the electric ground potential of the mounting frame. As the CEM detectors and compensation electrodes are mounted galvanically decoupled from the copper frame too, this will allow to put the frame on a different electric potential to the other detector components if required.

As the future MOT is intended to be operated with switchable magnetic fields, the copper frame and the compensation electrodes are designed not to form a closed loop. Consequently, a small slit with a connecting non-conducting screw (Vespel[®], DuPont) will inhibit the induction of currents into the frame by switching off the magnetic fields of the future MOT coils. Moreover, with the copper frame being conductive, no isolated patch charges or charge islands will be accumulated on the frame during operation of the CEM detection system (for patch charge potentials and accumulation, [211–214]). From the experience of previous

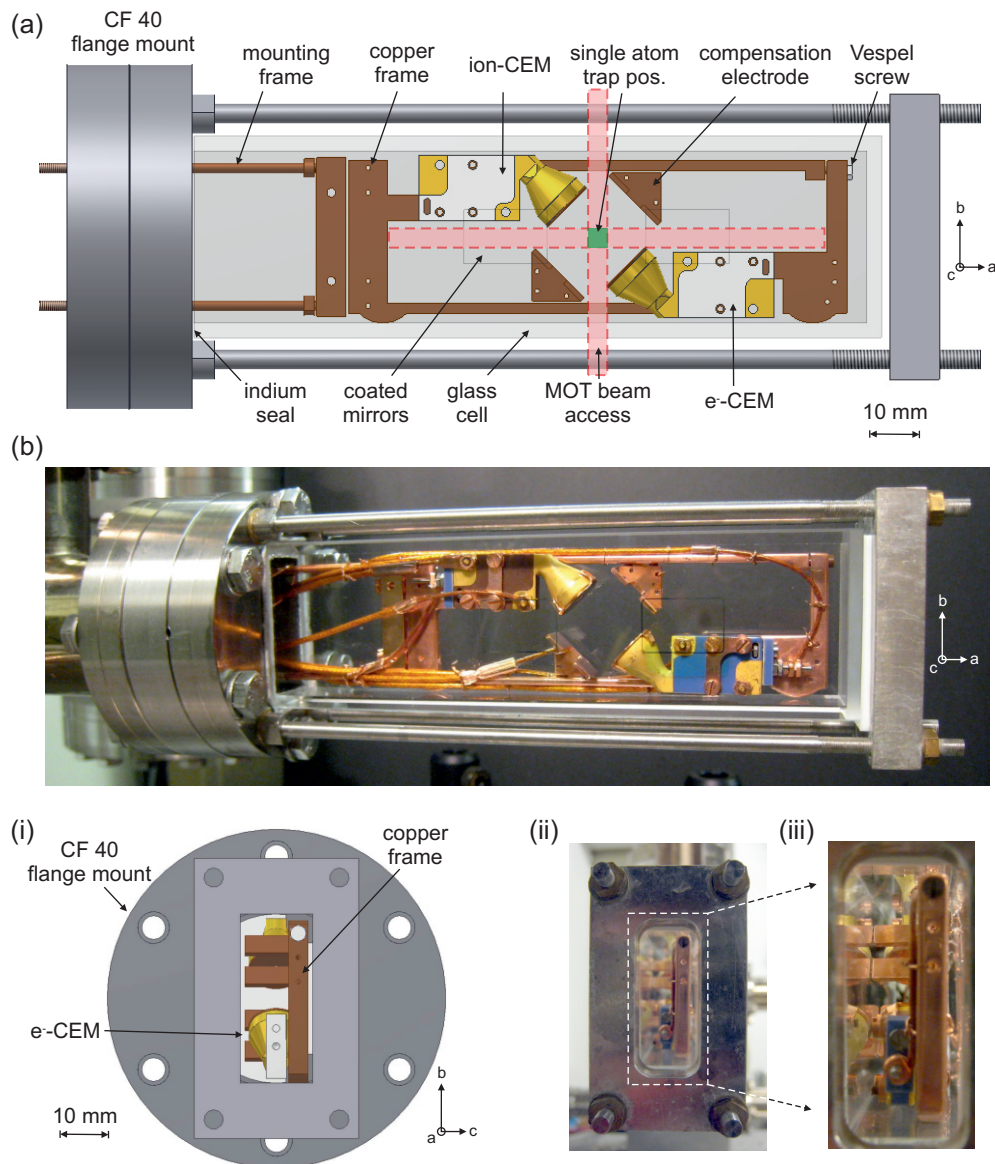


Figure 4.6: Technical drawing (a) and experimental realization (b) of the glass cell holding the joint CEM detection system (detector section; fig. 4.5). The particular design of the CEM detection system is owed to the future integration of the calibrated detector in the actual dipole trap setup. In the technical drawing, the optical access for the MOT beams and the position of the single atom trap are illustrated (dashed areas). In the experimental realization, also the individual CEM electrical wiring is shown. In (i-iii), the corresponding view in a -direction from the right side of fig. 4.5 is depicted.

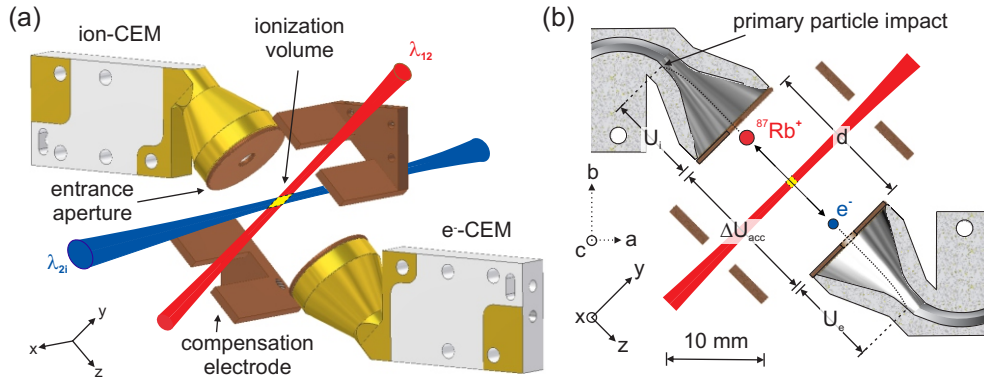


Figure 4.7: Joint CEM detection system. (a) CEM detector arrangement with two compensation electrodes in y -direction (schematic zoom of fig. 4.6). Neutral ^{87}Rb -atoms are photoionised within the overlap of two mutually perpendicular laser beams. (b) CEM detector arrangement in the $y - z$ plane in section view.

frame setups made from glass-ceramics (Macor[®]), such accumulated charges seem to create significant stray charge potentials which also change with time. As observed in the previous detector system designs, the influence of these stray charge potentials macroscopically affect and distort the imaging of the photoionisation fragments in the CEM, eventually leaving a coincident detection of both particles from a common spatial position of the photoionisation center impossible.

In the second of the two CF-40 mounting flanges, the mounting frame is attached to an inner flange structure and thus to the main body of the vacuum chamber by metal screws. By design, the glass cell is only connected with the first of the two CF-40 flange mounts, while the mounting frame with the entire CEM detection system is only attached to the second of the two. This segmented mounting on two independent flanges allows to disassemble the glass cell from the mounted CEM detection system on the copper frame by only untightening the six flange screws of the first CF-40 mounting flanges. This modular arrangement is particularly convenient for the assembly, as the entire internal CEM detector can be preassembled separately on the copper frame under a dust-free flow box environment. For the final assembly of the vacuum system, the preassembled CEM detection system is then simply attached to the glass cell, and to the main vacuum chamber. This modular design assures an easy, dust-free⁹ final assembly of the whole vacuum system.

4.2.4. Joint CEM detection system

The joint CEM detector system consists of two channel electron multipliers whose cone entrances are separated by $d = 15.7$ mm. The channel electron multipliers are custom-made, ceramic CEM detectors (Sjuts, KBL10RS45-V2) with a circular cone inclined at 45° to the detector body. The two detectors are arranged with the open cone entrances facing each other. They are further positioned with their central axis z under an angle of 45° to the MOT beam axes in the $a - b$ plane (see fig. 4.7(b) and fig. 4.6(a)). For floating potential operation of the CEM detectors, each individual CEM detector is mounted electrically isolated on the copper

⁹Internal dust particles adhesive to the glass cell walls will scatter light from the incident laser beams, creating extensive background counts in the photoionisation measurements (fig. 4.20(iii), section 4.5).

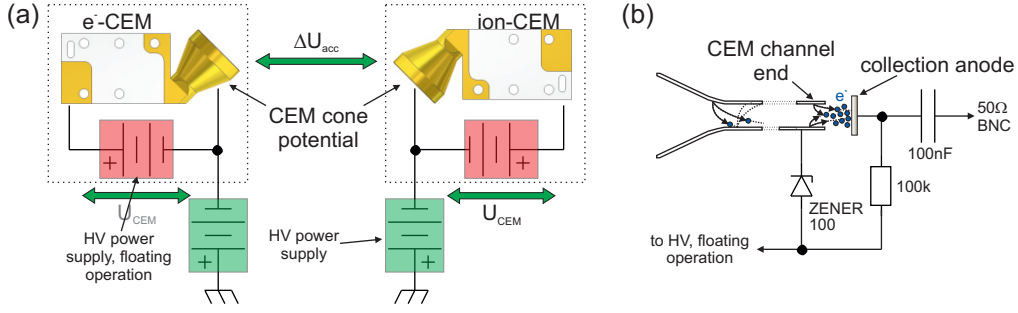


Figure 4.8: Schematic illustration of the CEM power supply circuitry and CEM collection anode decoupling. (a) HV power supply configuration for the joint CEM system. The floating operation of both CEMs allows to deliberately shift the CEM cone potentials ($U_{\text{cone},i}, U_{\text{cone},e}$) of both CEMs to the positive or negative. The difference of both cone potentials defines the acceleration voltage difference ΔU_{acc} in between the CEMs. (b) The CEM signal cable at the respective CEM collection anode is capacitively decoupled from the HV environment.

frame by non-conducting screws (Vespel[®], DuPont). Due to the particular arrangement of the CEM detectors, the integration of the future MOT beams and the single atom trap is assured (fig. 4.6). The corresponding spatial dimensions allow a MOT beam diameter of 4 mm and a theoretical position displacement of the single atom trap of up to $z = \pm 2$ mm along the z -axis in the MOT region. The diameter of the CEM cone entrances is 10 mm. To protect the CEM cones against stray light and stray particles, the entrances are covered by custom-made, electro-polished copper plates. The plates have a circular diameter of 11.2 mm, a thickness of $500 \mu\text{m}$, and an open aperture of 2 mm. The application of the copper plates on the CEM entrances also tailor the electric fields inside the CEM cones [126], ensuring a high homogeneity of the internal fields in the particular CEM (fig. 4.10; see section 4.3). In contrast to commonly applied metal grid structures, they further physically block stray light and stray particles from the UHV background, thereby effectively reducing background noise [164]. In addition to that two isolated, highly-polished copper electrodes next to the CEMs compensate eventual electric stray fields in the y -direction (see fig. 4.7).

The particular arrangement of the CEM detectors in the glass cell ensures a large solid angle for optical access to the central section where the future MOT and single atom trapping region will be situated. For the single atom trap, the high optical access together with the flatness of the glass cell allows to approach the high numerical lens system (Mitutoyo, G-Plan Apo 50x, working distance: 13.89 mm) close to the glass cell surface (fig. 4.6). Moreover, due to the particular configuration of the CEM detectors in the glass cell, the generated photoionisation fragments at $z = d/2$ will almost freely propagate from the ionisation center to the respective CEM cone entrance under the influence of the potential difference ΔU_{acc} in between the CEMs. Additionally, the copper plate apertures in front of the CEM channel cones will deflect the incident primary particles onto the wall of the CEM channel section, not in the CEM cone (fig. 4.7(b)). By this, a primary particle impact under grazing incidences $\theta > 80^\circ$ will be achieved for both photoionisation fragments (^{87}Rb -ion, e^-), yielding an elevated quantum yield η_{detector} with the corresponding CEM detector (see subsection 2.4.3).

HV power supplies and wiring

For high-voltage operation of the entire CEM detector system, a total of six high voltage power supplies is used. For CEM detector operation in particular, each single CEM detector is initially connected to a single high-voltage power supply (green HV supply, fig. 4.8(a)). The corresponding power supply sustains the individual CEM cone potential ($U_{\text{cone},i}$ and $U_{\text{cone},e}$) of each detector compared to the ground potential (ion-CEM: FuG, HCN 36-6500, and e^- -CEM: FuG, HCN 14-3500). A second, additional high-voltage power supply ('gain power supplies'; FuG, HCP 5-5000-MOD, insulated for ± 12.5 kV in DC operation) is connected to the electrodes at the CEM cone and at the back of the CEM, respectively (red HV supply, floating operation; fig. 4.8(a)). The two power supplies are both galvanically decoupled from the absolute ground and provide the relative potential difference U_{CEM} over the CEM channel of both CEMs, respectively (fig. 4.8(a)). Moreover, the two compensation electrodes next to the CEMs (fig. 4.7) are supplied by another two high-voltage power supplies (FuG, HCP 14-12500) which yield the individual compensation electrode potential U_{comp} .

Due to the galvanic decoupling, the HV power supplies for the CEM gain can be operated on floating potential relative to the absolute ground potential (dashed box, fig. 4.8(a)). As a consequence of this particular configuration, the absolute cone potential of both CEMs can be deliberately shifted to an absolute negative or positive potential value (e.g., $U_{\text{cone},i} = -4.2$ kV and $U_{\text{cone},e} = -0.4$ kV, resulting in $\Delta U_{\text{acc}} = 3.8$ kV), even online during measurement with of the CEM detectors. More specific, the floating potential configuration of the CEMs thus allows to shift the relative potential difference ΔU_{acc} of the joint CEM detector system to an absolute negative or positive potential value with respect to the absolute ground potential of, e.g., the UHV chamber walls. As a result, ambient stray charges in the UHV will be deflected and thus shielded from the ionisation center region due the repulsive, absolute negative or positive potential of both CEM cone entrances.

For the high-voltage wiring of the CEM detectors in the UHV, custom-made coaxial HV-cables are employed (Coaxial Capton®wires; Allectra or Caburn). The outer conductor of coaxial cables provides a predefined, fixed electric potential which is usually ground potential (0 V) if the cable itself is not held on a floating potential. In contrast to that, 'naked' wires (non-coaxial cables) will lack this fixed outer potential, exhibiting the electric potential depending on the actual potential they conduct. As an additional benefit of coaxial cables, the outer conductive shielding of especially the CEM signal cables also cancel out the influence of ambient stray charges or induced stray currents from the various emissive sources in the UHV. Moreover, in the case of the CEM detector design, the particular knowledge of the absolute potential of all CEM detector cable wiring to a predefined, set value (e.g., 0 V) is particularly advantageous. This results as a fixed potential value of these elements rather simplifies the calculation and simulation of eventual electric stray fields in the estimated CEM detector setup introduced by the cable potentials (see section 4.3). In the comparably close spatial dimensions of the CEM detection system setup (fig. 4.9), such additional fields will influence the linear potential gradient in between the CEMs, possibly distorting the imaging of the photoionisation fragments into the CEMs significantly.

The galvanic isolation of the whole CEM detection system and its corresponding cables to the surrounding vacuum environment allows a theoretical adjustment of the individual CEM detector cone potential of approximately up to ± 10 kV to the absolute ground potential. Two high-voltage electrical feedthrough flanges (Allectra, Coaxial SHV-20) with four HV-coaxial pins each ensure a safe operation up to this theoretical limit. However, the actual experimen-

tally observed limit lies well below the theoretical limit with values in the region of ± 4.5 kV for the current setup. For higher values, an eventual dielectric breakdown of some of the CEM detector components occurs. The experimental limit is presumably constrained by spontaneous high-voltage arcing induced by the close dimensions of some of the detector components to the ambient glass cell. It may also be limited by spontaneous current breakthroughs in the vacuum-sided, coaxial high-voltage CEM cables themselves.

Concerning the experimental realization of the joint CEM detector as the future single atom trap readout, one should note that the combination of ambient high-voltage potentials, high-power lasers, charged particle optics and the UHV environment are generally difficult to handle. In an UHV environment, especially the accidental generation of free charges in the vacuum chamber and on non-conducting surfaces in the vacuum will introduce substantial problems for the imaging and electrostatic stability of the charged particle detection system. In particular, the accumulation of accidentally generated charges on non-conducting substrates in the UHV will create isolated patch charges or even charge islands [212–214]. In the vacuum, such charge accumulations will not be subject to charge diffusion or to electrostatic discharge as, e.g., free charges under atmospheric air. As a result, the ion or electron optics of any charged particle detection system will be substantially influenced and distorted by the additionally introduced stray potentials from these charge accumulations. To prevent the eventual creation of free charges and to shield the CEM detection system from the influence of any stray potentials, extensive care in the design and the construction of the entire vacuum system has therefore to be taken. Moreover, appropriate shielding of the glass cell environment and the CEM detectors from *any* spurious particle flux in the UHV will additionally reduce the ion/electron background detected by the CEMs [164, 200].

4.3. Charged particle optics

In this section, FemLab¹⁰ simulations of the electric potential distribution of the integrated CEM detection system are performed. From the numerical solution of the simulated model, key parameters for the particular design and the successful operation of the CEM detection system can be extracted. However, the estimated potential distribution from the FemLab simulation will also allow to model the expected flight time (t_i , t_e) of the generated photoionisation fragments until their primary impact in the active surface of the corresponding CEM detector (see section 4.4). Moreover, the potential simulations show that for the determination of the kinetic energy E_{kin} at particle impact in the CEM, the corresponding values have to be corrected compared to the kinetic energy at cone entrance.

The kinetic energy at primary particle impact becomes especially important for any efficiency calibration measurements $\eta_{\text{detector}}(E_{\text{kin}})$ of CEM detectors. In combination with the flight time measurements of chapter 5, the simulation will allow to obtain the impact position of the particles in the corresponding CEMs from the observed flight time difference (see section 5.3). Likewise, this permits to derive the kinetic energy E_{kin} of the incident particles at primary impact in the corresponding CEM detector and to recalibrate the efficiency measurements according to the potential difference ΔU_{acc} between the CEMs (see subsection 5.4.3). In contrast to any conventional calibration attempt stated in the literature, the kinetic energy at impact will thus enable to relate the CEM quantum yield calibrations of chapter 5 with measured secondary emission yield values δ_0 at isolated layer samples of active CEM surfaces

¹⁰FemLab 3.1; Comsol Multiphysics.

(see section 2.3). Even more, this allows to directly compare the measured efficiencies with the dynode multiplier efficiency model of section 2.4, and to the cascaded dynode detector theory of chapter 2.

Additionally, by simulating the electrical potentials and the associated electric field, possible sources for construction errors of the CEM detector system can be identified prior to any experimental realisation. Such construction errors will arise, e.g., due to large potential differences at adjacent surfaces in the CEM detector setup which promote an early dielectric breakdown of the system. Moreover, the influence of possible stray charges or stray potentials on the potential distribution in between the CEM detectors can be studied. During operation of the CEM detection systems, such stray potentials will significantly affect, e.g., the imaging of the photoionisation fragments into the corresponding CEM.

4.3.1. Numerical simulation of the electric field configuration

For the simulation of the electric potentials of the integrated CEM detector setup, the simulation software FemLab is used. Conceptionally, FemLab is an interactive environment for modeling and solving scientific/engineering problems based on partial differential equations. For the numerical solution of a particular problem, an individual physical model is first parametrized and thus implemented. Then, the finite element method is applied on the resulting partial differential equations of the parametrized model. The numerical solution yields a two-dimensional (2D) or even three-dimensional (3D) simulation of a corresponding physical quantity to be deduced out of the model. Such a physical quantity is, e.g., the spatial configuration of the electric potentials $U(x, y, z)$ of the integrated CEM detector system according to the applied electric potentials on the detector surfaces.

In the following, the basic field configuration is investigated for the integrated CEM detection system with the corresponding experimental parameters of the measurements in section 5.4. From the model, the resulting electric potentials can be deduced which suggest the linear approximation of the time-of-flight model of section 4.4. In a second modelling, the importance of using copper apertures on the CEM detector cones is highlighted, similar to conventionally applied metal grid structures (e.g. [85, 87, 88]). Especially in the ion-CEM (fig. 4.10), the application of solid apertures significantly affects the internal CEM fields, allowing a more efficient detection of incident primary ions [126]. In a third evaluation, the electric potential along the central, common line-of-sight axis of the two CEM detectors is simulated (fig. 4.11). The simulation displays the particular influence of the internal CEM fields on each of the two photoionisation fragments. The influence of the internal CEM field will result in modified flight times (t_i , t_e), and in different kinetic energies at primary particle impact (see subsection 4.3.4). Finally, the electric potential along the common, central line-of-sight axis of the two CEM detectors is examined in more detail. The simulation shows that the initially linear time-of-flight model of section 4.4 is only the approximation of a more refined model with an individual accelerating potential for each of the two photoionisation fragments. Consequently, the kinetic energy of both photoionisation fragment at primary particle impact in the corresponding CEM can be estimated more accurately from the refined potentials.

Although the solution of the FemLab model reveals even details of the particular field configuration of CEM detection system, the simulation of the electric potentials in the glass cell will always remain only an approximation. This follows as eventual stray potentials due to accumulated stray charges in the UHV will influence the electric potential distribution

of the integrated CEM detection system [211–214]. These stray potentials are difficult to measure and cannot be properly estimated as they may fluctuate and move in a random-walk pattern on an isolated surface, and thus shift in time. As a consequence, the influence of such potentials cannot be covered adequately by the current simulations without deeper knowledge of the specific experimental situation.

4.3.2. Basic FemLab model for $\Delta U_{\text{acc}} = 3800 \text{ V}$

Figure 4.9 shows a 2D FemLab model of the integrated CEM detection system. As an illustrating example, sample experimental potential parameters from the corresponding efficiency measurements of section 5.4 are chosen for the model. Consequently, the potentials of the cone entrances of the CEM detectors are $U_{\text{cone},i} = -4.2 \text{ kV}$ and $U_{\text{cone},e} = -0.4 \text{ kV}$ (fig. 4.9). The cone aperture potentials result in a relative potential difference of $\Delta U_{\text{acc}} = 3.8 \text{ kV}$ between both CEMs. The two compensation electrodes are held on the same electric potential as the e^- -CEM, with a potential of $U_{\text{comp}} = -0.4 \text{ kV}$ each. The copper frame in this simulation is set to ground potential ($U_{\text{frame}} = 0 \text{ V}$).

Figure 4.9(a) shows the basic geometric model used for the simulations. The displayed 2D-model geometry corresponds to a cut in $y - z$ direction of the integrated CEM detection system (fig. 4.6 and fig. 4.7). The chosen two-dimensional geometry originates from modelling simplification, with the x component of the initial three-dimensional, spatial representation of the CEM detection system being extended to infinity. Figure 4.9(b) shows the resulting, simulated isoline plot of the electric potential in between the two CEMs. The experimentally applied potentials are displayed by their corresponding values. In the model, the potential difference between two adjacent isolines is approximately $\Delta U = 110 \text{ V}$. The spatial distribution of the isolines in between the CEMs and the compensation electrodes further indicates that negative stray charges (spurious electrons or negatively charged ions) in the glass cell are repelled and thus shielded from the center region in between the CEMs. This is a result as the absolute electrical potentials of both CEM cone entrances are shifted to the negative due to the floating operation of the CEM detectors (fig. 4.8). Figure 4.9(c) shows the corresponding current streamline plot according to the electric isoline potentials in fig. 4.9(b). Note, however, that the electric field lines ('streamlines') only indicate the derived spatial orientation of the local electric field in between the CEMs, and do *not* describe eventual trajectories¹¹ of the charged particles.

From the model of fig. 4.9(b), an approximately constant potential gradient can be deduced at the common, central line-of-sight axis in between the two CEMs, being in conceptual correspondence to the constant electric field between two capacitor electrodes. In the CEM cones, a similar constant gradient is observed owed to the application of the copper apertures on the CEM cone entrances. Therefore, the corresponding electric fields in the time-of-flight model of section 4.4 are reasonably represented by a constant approximation of these three gradients.

4.3.3. Effect of CEM cone apertures

In common CEM applications, the purpose of an open grid structure in front of the CEM cone entrance is to prevent external electric potentials from penetrating the CEM cone potential

¹¹For the calculation of particle trajectories, more sophisticated simulation software like, e.g., Simion has to be used.

4. Joint Channel Electron Multiplier Detector

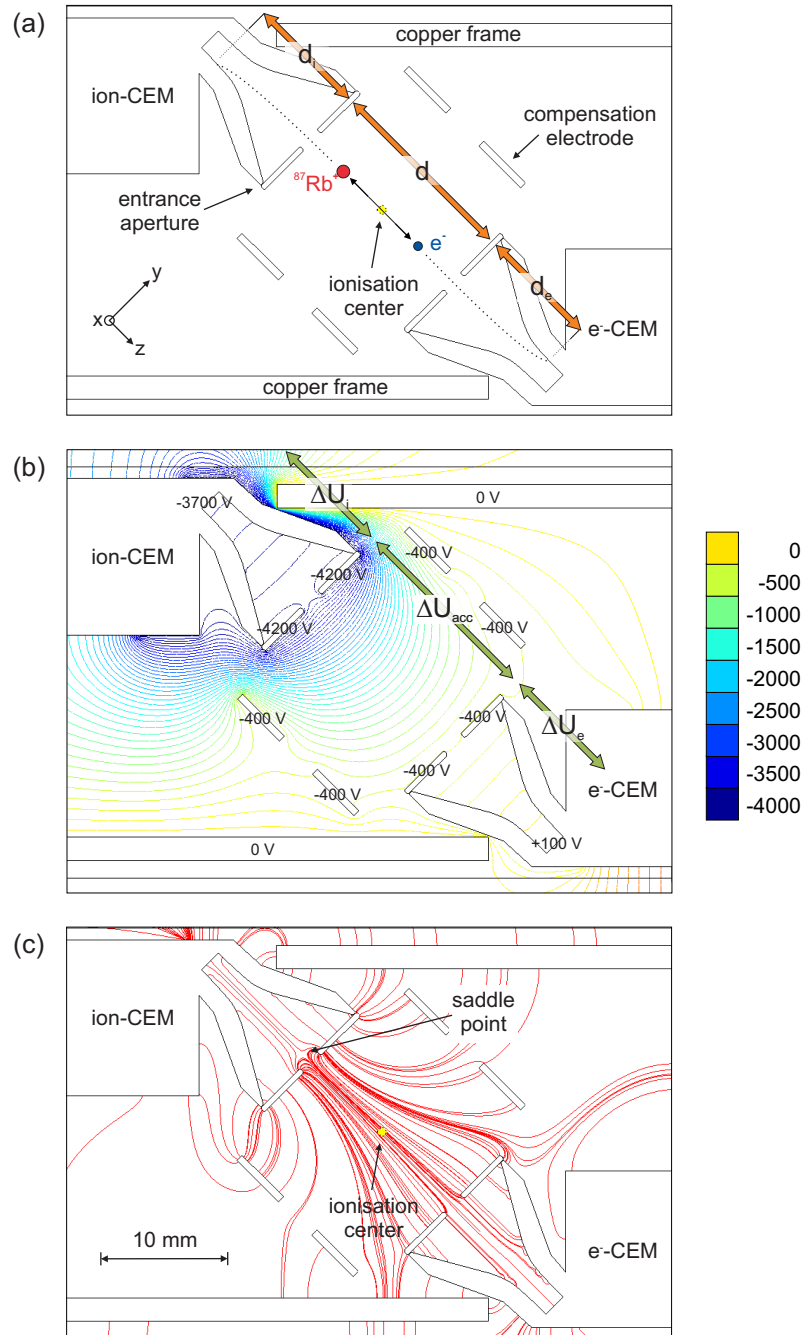


Figure 4.9: Simulated 2D-model of the electric potential isolines and their associated electrical field (current streamlines), using FemLab. (a) Geometric model corresponding to fig. 4.6 and fig. 4.7, with a cut in $y - z$ direction. (b) Isoline plot, showing the applied potentials for the maximum acceleration voltage $\Delta U_{acc} = 3.8$ kV in the measurements (fig. 5.11). The applied potentials are displayed by their corresponding values. The potential difference between two adjacent isolines is approximately $\Delta U = 110$ V. (c) Current streamline plot, illustrating the local spatial orientation of the electric field lines between the two CEMs.

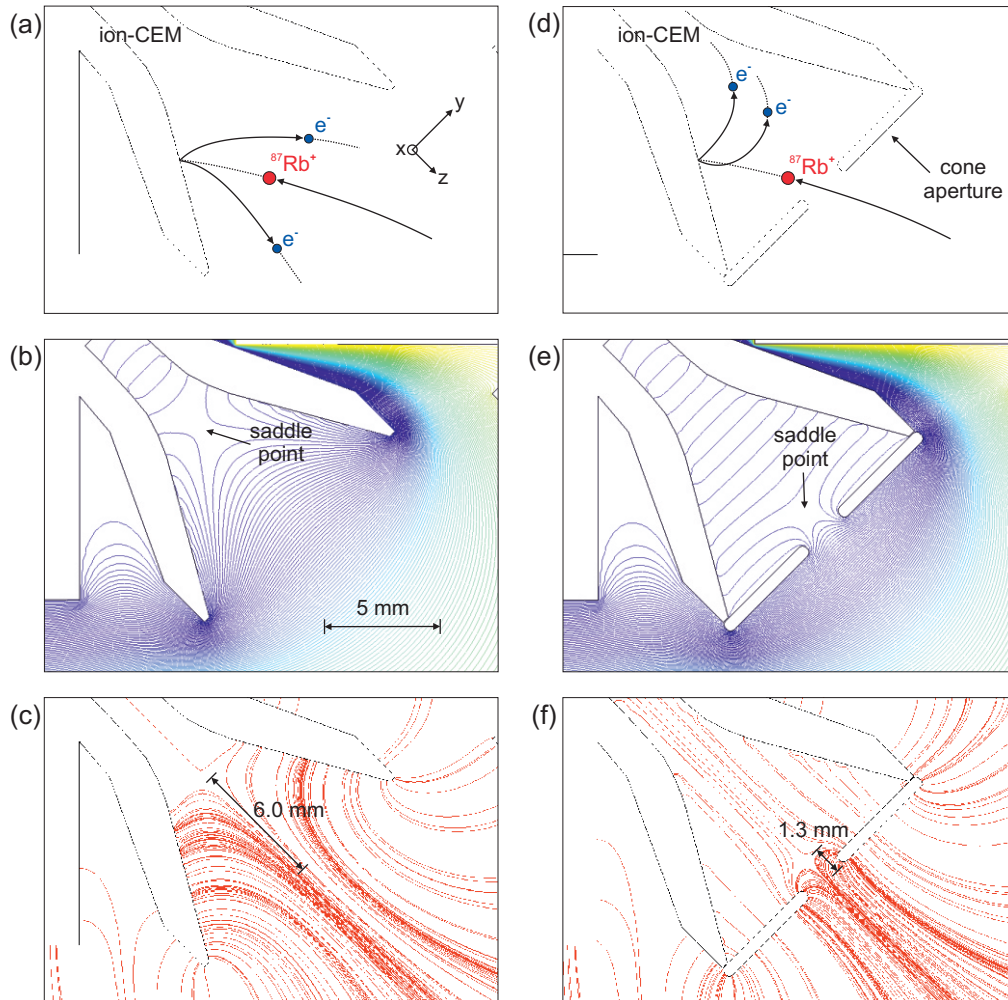


Figure 4.10: Modeled CEM cone for the detection of positively charged primary particles. The potential distributions and streamline plots are simulated without (a,b,c), and with an attached CEM cone aperture (d,e,f) on the CEM detector entrance (fig. 4.9). (a) Illustration of an incident primary $^{87}\text{Rb}^+$ -ion at primary particle impact. Secondary electrons will eventually escape the detector cone as the external field penetrates into the CEM cone section, significantly distorting the electric cone potential. (b) Simulated contour plot of the electric potential isolines, showing the saddle point of the cone potential which lies deep in the CEM cone. (c) According electric field streamline plot. Some secondary electrons emitted at the outer section of the CEM cone will leave the detector without initiating any consecutive secondary electron avalanche. (d) Scheme of an incident primary $^{87}\text{Rb}^+$ -ion with attached aperture at the CEM cone entrance. (e) Contour plot of the isolines. The entrance apertures tailor the internal CEM fields and shield the CEM cone potential against external penetrating fields. Due to the shifted position of the saddle point near to the cone entrance, all emitted secondary electrons are now accelerated down the cone into the channel of the CEM. (f) Electric field streamline plot, accordingly.

[85, 126]. In addition to that, incident stray charges are electrostatically shielded from entering the cone. Due to the fixed grid potential in front of the CEM cone, the internal CEM fields are further efficiently tailored [87, 88, 139, 215]. Moreover, the grid structure thereby also limits the effects of the cone potential on other nearby electrodes, simplifying the simulation and calculation of incident ion or electron trajectories.

In addition to the properties of a grid structure, the application of solid CEM cone apertures *physically* blocks ambient stray light and stray particles, i.e., especially neutral particles from intrusion in the cone. Therefore, the counting background of the CEMs in pulse counting mode will be further reduced, effectively lowering background noise [164]. The cone apertures additionally serve as electrostatic lens, focusing the photoionisation fragments onto the channel wall of the CEM in the channel section (fig. 4.4). The resulting grazing incidence of the primary particle at the channel wall will thus yield a higher detection efficiency due to an increased secondary electron emission yield δ_0 at primary particle impact (see subsection 2.4.3).

Particularly in the ion-CEM, the application of a cone aperture shifts the saddle point of the internal CEM potential from the back of the CEM cone near to the CEM cone entrance (fig. 4.10). The saddle point exists due to the particular potential configuration when detecting positively charged particles with a CEM. This results as incident positively charged particles have to be initially converted into negatively charged secondary electrons for further amplification by a secondary electron avalanche in the CEM detector. Therefore, the potential configuration is usually more negative outside the CEM cone to accelerate the positively charged particles in the CEM cone. In contrast to that, for the subsequent evolution of a secondary electron avalanche in the CEM, the potential gradient in the ion-CEM cone has to be positive, further accelerating the generated secondary electrons down the CEM channel tube. In consequence, the accelerating potential ΔU_{acc} in between the CEMs and of the ion-CEM cone ΔU_i has an opposite sign (fig. 4.11(b)). If the saddle point of the ion-CEM is situated 'deep' in the cone section (fig. 4.10(b)), the particular potential in the untailed CEM cone will allow generated secondary electrons to eventually escape the CEM cone rather than to create subsequent secondary avalanche events down the channel tube (fig. 4.10(a)). With an applied cone aperture, the corresponding repulsive potential configuration will deflect these secondary electrons back in the CEM (fig. 4.10(d)), presumably enhancing the sensitivity and thus the quantum yield η_{detector} of the particular CEM detector [85, 87, 126].

In contrast to that, the overall potential configuration of the e^- -CEM cone and in between the CEMs does not yield a saddle point structure. This results as the corresponding accelerating potentials exhibit the same sign (fig. 4.11(b)). Negatively charged, incident particles are therefore accelerated further in the CEM cone by the internal CEM gain field ΔU_e until their primary particle impact.

4.3.4. Determination of the kinetic energy at primary particle impact

In the literature, the kinetic energy E_{kin} of the primary particle in the CEM is usually stated by the kinetic energy of the incident primary particle at CEM cone entrance (fig. 4.11). However, in many cases this particular definition is comparably vague and deviates significantly from the actual kinetic energy E_{kin} of the incident particle at the primary particle impact in the active surface of the CEM (stage g_1 ; fig. 2.1). Especially for small kinetic energy values $E_{\text{kin}} < 1 \text{ keV}$, the specific impact position of the primary particle in the CEM detector and therefore the correction of the impact energy of the incident particle due to the internal CEM

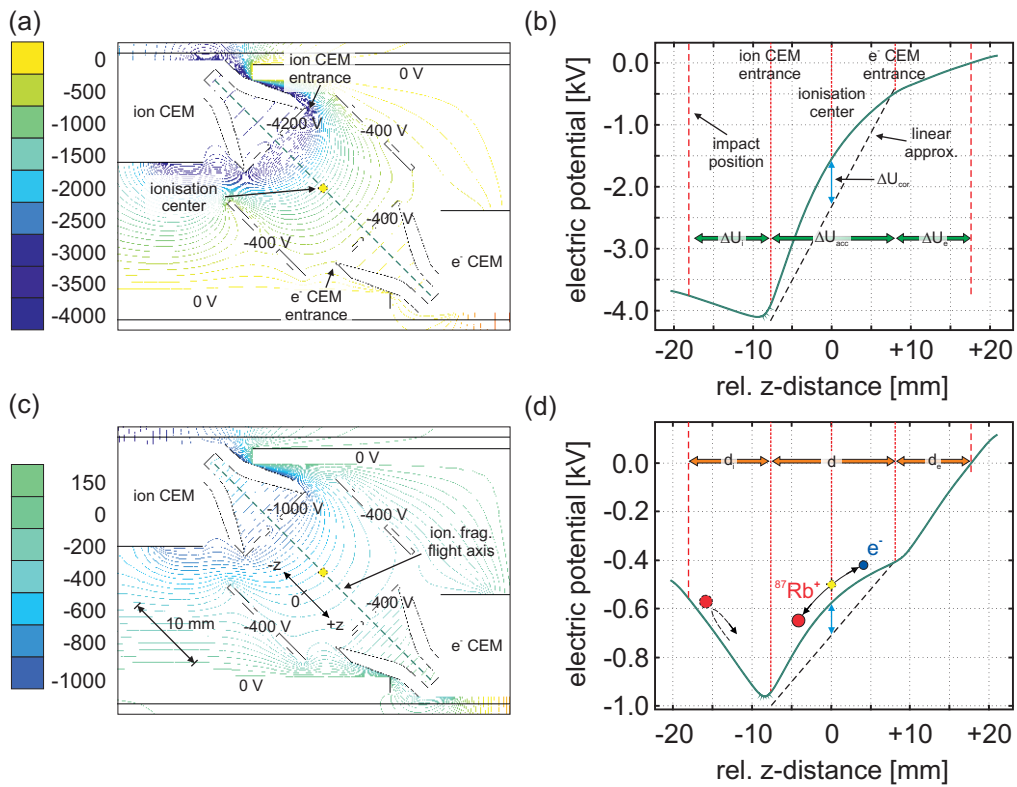


Figure 4.11: Particle accelerating potentials at the central flight axis of the photoionisation fragments in between the CEMs for two different potential differences ΔU_{acc} . (a) Isoline plot as fig. 4.9 with a potential difference of $\Delta U_{acc} = 3800$ V between the two CEMs. (b) Illustration of the electric potential along the dashed line in (a), corresponding to the central flight axis of the photoionisation fragments into the respective CEM. (c) Isoline plot similar to (a), but with a potential difference of $\Delta U_{acc} = 600$ V in between the CEMs only. (d) Corresponding electric potential along the dashed line in (c).

gain potential has to be considered in more detail. In particular, for low kinetic energies (i.e., $E_{\text{kin}} < 1 \text{ keV}$) and a primary impact position deep in the CEM cone, the modification of the kinetic energy E_{kin} due to the internal CEM potential will become macroscopic. This results as the internal gain field in the CEM becomes comparable to the external acceleration fields of the primary particles up to the CEM cone (fig. 4.11(d)). For comparison to the literature, the knowledge of the exact impact energy is especially important in relation to observed isolated values of the primary particle emission yield δ_0 , which will likewise affect the measured CEM detector quantum yield values η_{detector} (see section 2.3). At low kinetic energies at the CEM cone entrance, the influence of the spatial position on the actual kinetic energy E_{kin} of the incident particle at impact and therefore on the detection efficiency of the particular CEM detector can be observed in the measurements of, e.g., [87, 88, 101]. In the following, the individual energy correction for incident ^{87}Rb -ions and electrons in the joint CEM detection system is thus investigated.

Correction of the kinetic impact energy due to the internal CEM field

Figure 4.11 shows the influence of the respective internal CEM field on both photoionisation fragments, individually. In both cases, the influence of the internal gain field explicitly depends on the spatial impact position of the primary particle in the CEM. Specifically, it is directly proportional to the distance d_i (d_e for the electron) the particle has to travel from the cone entrance until primary particle impact at the active CEM surface. Notably, the particular distances in the CEM will be in the order of $d_{i,e} \approx 10 \text{ mm}$ for an impact position at the CEM channel wall (fig. 4.11(b,d), at $z = \mp 18 \text{ mm}$) in contrast to an average cone hit with a distance of $d_{i,e} \approx 4.5 \text{ mm}$ ($z \approx \mp 12.5 \text{ mm}$). The individual potential difference in the corresponding CEM from the cone entrance up to the impact position of the primary particle is defined as

$$\Delta U_{i,e} = E_{i,e} \cdot d_{i,e}. \quad (4.1)$$

Here, the electric field in the CEM is defined as $E_{i,e} = \mp U_{\text{CEM}}/l$, where U_{CEM} represents the individual CEM gain detector voltage (see section 3.3), and l is the entire CEM channel length (see appendix A.3). Note that for incident primary ions, the internal CEM field up to primary particle impact is repulsive, for primary electrons it is further accelerating (see subsection 4.3.3).

In the joint CEM detection system, the actual impact energy E_{kin} at primary particle hit will remain comparably unaffected for large acceleration voltages ΔU_{acc} in between the CEMs (fig. 4.11(b)). However, for small acceleration voltages $\Delta U_{\text{acc}} < 1 \text{ kV}$ especially the ^{87}Rb -ion is significantly affected. Eventually, it will not even have sufficient kinetic energy for a primary particle impact at the CEM surface at the CEM channel wall. As illustrated in fig. 4.11(d), the ^{87}Rb -ion will therefore be repelled before reaching the active secondary emitting surface due to the repulsive internal potential in the ion-CEM ($-\Delta U_i$). In contrast to that, incident electrons in the e^- -CEM are even further accelerated by the internal potential ($+\Delta U_e$). Correspondingly, the kinetic energies E_{kin} of the primary particles (^{87}Rb -ion, e^-) at primary particle impact are individually corrected in accordance with the linear time-of-flight model of subsection 4.4 by

$$E_{\text{kin}}(d_{i,e}) = e_0(\Delta U_{\text{acc}}/2 \mp \Delta U_{i,e}). \quad (4.2)$$

At low kinetic energies at the CEM cone entrance ($E_{\text{kin}} < 1 \text{ keV}$), this leads to a significant modification of the actual kinetic energy $E_{\text{kin}}(d_{i,e})$ at primary particle impact compared to

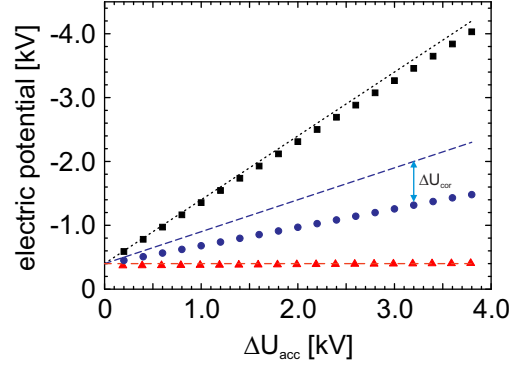


Figure 4.12: Electric potential of the ion-CEM entrance (black), the position of the ionisation center at $d/2$ between the CEMs (blue), and the e^- -CEM entrance (red) as illustrated in fig. 4.11(a). The dashed lines indicate the potentials corresponding to the constant approximation of the electric field along the central flight axis. The scattered points show the electric potentials derived from similar simulations as displayed in fig. 4.11.

the kinetic energy at cone entrance as frequently stated in the literature. For the current setup of this thesis, the latter value would only correspond to $E_{\text{kin}} \approx \Delta U_{\text{acc}} e_0 / 2$, in contrast to the expression of eq. 4.2. Note that for the modified relative potentials of the refined time-of-flight model, the ion flight distance d_i in the ion-CEM has to be substituted to $d_{i\text{CEM}} = d_i - d_{\text{saddle}}$ (fig. 4.13(b)).

Influence of the compensation electrodes

In a more refined version of the potential simulations, the linear scaling of the accelerating potential ΔU_{acc} in fig. 4.11 is only an approximation. In this approximation, each of the two photoionisation fragments being ionised at $d/2$ experiences an identical accelerating potential difference of $\Delta U_{\text{acc}}/2$ until CEM cone entrance. However, in contrast to the constant approximation of the electric field between the two CEMs, the particular electric potential of the compensation electrodes modifies the accelerating potential gradient between the CEMs. In fig. 4.11, this particular situation is illustrated when the electrodes are held at the same potential as the cone entrance aperture of the e^- -CEM.

Figure 4.12 shows the deviation of the electric potential from the linear approximation at three selected positions along the central flight axis (red lines; fig. 4.11(a)). The three positions are the electric potential at the ion-CEM entrance, the potential of the ionisation center at $d/2$ between the CEMs, and of the e^- -CEM entrance as illustrated by the solid lines in fig. 4.11(a,b). From the electric potentials at the two CEM entrance positions, the relative accelerating potential difference of ΔU_{acc} between the two CEMs is derived. In fig. 4.12, the dashed lines show the electric potential corresponding to the linear approximation according to the time-of-flight model introduced in section 4.4. The scattered points illustrate the electric potential as derived from the simulation displayed in fig. 4.11, respectively. At the ionisation region $z = d/2$, the center potential is significantly shifted to the cone potential of the e^- -CEM (ΔU_{cor}) compared to the linear approximation, resulting in a relatively smaller potential difference up to the e^- -CEM and a larger difference up to the ion-CEM. As a result, instead of $\Delta U_{\text{acc}}/2$ each, the ^{87}Rb -ion experiences 72% of the overall accelerating potential difference ΔU_{acc} and the electron only 28%, correspondingly. This discrepancy will affect

the time-of-flight model of subsection 5.4, altering the individual flight times (t_i , t_e) of both generated photoionisation fragments starting at $d/2$.

Corrections of the kinetic energy at CEM cone entrance due to particle impact position

For the joint CEM detection system of this thesis, the actual kinetic energy E_{kin} at primary particle impact can be determined from the estimated impact position of the incident particle in the corresponding CEM detector. Using the modified potentials of the refined model with $\Delta U_{\text{mod},i} = 0.715 \cdot \Delta U_{\text{acc}}/2$ and $\Delta U_{\text{mod},e} = 0.285 \cdot \Delta U_{\text{acc}}/2$ as obtained from the potential simulations (fig. 4.12), the correction of the kinetic energies at particle impact according to the applied acceleration voltage difference ΔU_{acc} between the CEMs is

$$E_{\text{kin},i}(\Delta U_{\text{acc}}, E_i, d_{i\text{CEM}}) = 0.715 \cdot \Delta U_{\text{acc}} e_0/2 - e_0 E_i d_{i\text{CEM}}, \quad (4.3)$$

for the ion-CEM, and

$$E_{\text{kin},e}(\Delta U_{\text{acc}}, E_e, d_e) = 0.285 \cdot \Delta U_{\text{acc}} e_0/2 + e_0 E_e d_e, \quad (4.4)$$

for the e^- -CEM, accordingly. In the previous equations, the covered path length $d_{i\text{CEM}}$ and d_e of the primary particles in the CEMs are obtained from the observed flight times t_i and t_e of the photoionisation fragments (see section 5.3), in accordance with the flight time model of section 4.4. Correspondingly, the parameters $d_{i\text{CEM}}$ and d_e in turn determine the kinetic energy correction by the internal CEM potential $\Delta U_{i,e}$.

4.3.5. Cone entrance energy versus particle impact energy

Although repetitively disregarded in the literature, the correction in the kinetic energy of the incident particle corresponding to the impact position of the primary particle in the CEM becomes macroscopic for most CEM efficiency calibration measurements in the low kinetic energy regime ($E_{\text{kin}} < 10$ keV; see subsection 2.4.2). For example, at an acceleration voltage of $\Delta U_{\text{acc}} = 3.8$ kV for the CEMs used in this thesis, the calculated kinetic energy at primary particle impact in the CEM channel is $E_{\text{kin}}(^{87}\text{Rb}) = 2.044$ keV for the ^{87}Rb -ion, and $E_{\text{kin}}(e^-) = 1.633$ keV for the electron, respectively. The values are obtained from eq. 4.3 and eq. 4.4, using a CEM gain voltage of $U_{\text{CEM}} = 2.8$ kV and covered path lengths of $d_{i\text{CEM}} = 12.22$ mm and $d_e = 10$ mm as experimentally determined in subsection 5.3.1.

In contrast to that, the kinetic energy E_{kin} at cone entrance, which is conventionally used in common efficiency calibration measurements, substantially varies from the calculated impact energies $E_{\text{kin}}(^{87}\text{Rb})$ and $E_{\text{kin}}(e^-)$. Referring to subsection 4.3.4, the kinetic energy for the particles at cone entrance corresponds to energies of $E_{\text{kin}}(^{87}\text{Rb})_{\text{cone}} = 2.717$ keV for the ^{87}Rb -ion, and $E_{\text{kin}}(e^-)_{\text{cone}} = 1.083$ keV for the electron, accordingly. In comparison, the cone entrance to impact energies therefore differ by a factor of $E_{\text{kin}}(^{87}\text{Rb})/E_{\text{kin}}(^{87}\text{Rb})_{\text{cone}} = 0.752$ and $E_{\text{kin}}(e^-)/E_{\text{kin}}(e^-)_{\text{cone}} = 1.508$ for a CEM channel hit. This discrepancy in kinetic energy makes a comparison of observed efficiency values η_{detector} according to the kinetic energy E_{kin} of the primary particle unreasonable, if cone entrance energies are used. For acceleration voltage differences of $\Delta U_{\text{acc}} < 3.8$ kV, the kinetic energy corrections will become even greater. For example, at voltage differences of $\Delta U_{\text{acc}} < 0.8$ kV, the ^{87}Rb -ion will not even reach the estimated impact position at the CEM channel of the ion-CEM (fig. 4.11(d)), as the calculated kinetic energy $E_{\text{kin},i}$ according to eq. 4.3 will become negative at this position.

In reference to the literature, this generally leaves different calibration measurements at low kinetic particle energies ($E_{\text{kin}} < 10 \text{ keV}$) being difficult to compare, if the particular impact position of the primary particles in the CEM or of the calibrating particle beam is not additionally stated (see subsection 2.4.2). This results as the kinetic energy at particle impact is generally not identical to the kinetic energy of the corresponding particle at cone entrance. Moreover, as many particle calibrations in the literature state the detector efficiency η_{detector} according to the kinetic energy at cone entrance, these calibration attempts are generally ill defined. Consequently, all these attempts will not allow a reasonable relation of the observed efficiency values $\eta_{\text{detector}}(E_{\text{kin}})$ to, e.g., obtained secondary emission yield values δ_0 at isolated layer samples of active CEM surfaces (see section 2.3). As a result, if cone entrance energies are used, this will not permit a reasonable comparison of the experimentally observed quantum yield $\eta_{\text{detector}}(E_{\text{kin}})$ to the general cascaded dynode detector theory of chapter 2. However, for the quantum yield measurements $\eta_{\text{detector}}(E_{\text{kin}})$ of the CEM detectors of this thesis (see section 5.4), the corresponding energy corrections according to the measured impact position of the primary particles in the CEMs are therefore included in the efficiency calibrations (see subsection 5.4.3).

4.4. Photoionisation fragment flight time model

In this section, the expected flight times t_i and t_e of the generated photoionisation fragments until their primary particle impact in the active surface of the corresponding CEM detector are theoretically modeled. Together with the transit time t_{transit} in each CEM (see subsection 3.2.1), this will allow to calculate the detection time t_{det} of the two ionisation fragments for a given potential difference ΔU_{acc} in between the CEMs. As a key parameter for the photoionisation detection, the flight time t_i of the ion fragment will almost exclusively influence the detection time t_{det} of the CEM detection system due to the much larger mass of the ^{87}Rb -ion compared to the photoelectron. Moreover, the measured ion flight time t_i will allow to allocate the position of the primary particle impact in the ion-CEM. Finally, an eventual particle loss during imaging of the two photoionisation fragments into the corresponding CEM detectors is investigated. The calculation of the eventual losses allows to estimate the collection efficiency η_{col} of the CEM detection system.

4.4.1. Time-of-flight capacitor model

The simulation of the potential distribution between the CEMs of section 4.3 permits to approximate the acceleration field $E_{\text{acc}}(z)$ along the common line-of-sight of both CEM detector entrances, and the electric gain fields $E_{i,e}(z)$ in the corresponding CEM detector. By means of this approximation, the expected flight times t_i and t_e for the photoionisation fragments in the integrated CEM detection system can be modeled. More specific, the model simulates the acceleration of the ^{87}Rb -ion and the corresponding photoelectron after photoionisation at $z = 0$ in the homogeneous electric field $E_{\text{acc}}(z)$ up to the CEM cone entrance and further deceleration (acceleration) within the respective CEM until primary particle impact (fig. 4.13). It further allows to compare the calculated flight times t_i and t_e to the experimentally accessible parameter in the CEM system which is the time-of-flight difference $\Delta t = t_i - t_e$ of the two ionisation fragments.

The time-of-flight model conceptionally corresponds to the acceleration of a charged particle within two subsequent parallel plate capacitors. The model thus enables to define equations of

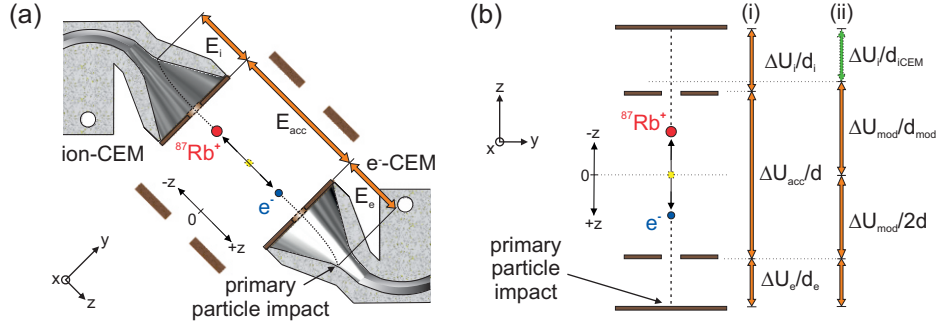


Figure 4.13: Scheme showing all relevant parameters for the time-of-flight model of the ^{87}Rb -ion and its photoelectron. (a) Linear approximation, displaying the accelerating field $E_{\text{acc}}(z)$ and the internal ion/ e^- -CEM gain voltage fields $E_i(z)$ and $E_e(z)$, respectively. (b) Schematic view of the capacitor model, showing the individual TOF-model parameters in linear approximation (i) and with the modified potential approximation (ii).

motion for the two ionisation fragments succeeding the photoionisation of a neutral ^{87}Rb -atom in between the CEMs (fig. 4.13). From the initial equations, the respective flight times (t_i, t_e) are then deduced. In the model, first the acceleration of the photoionisation fragments at $t = 0$ from the ionisation center at $z = 0$ in between the CEMs up to the CEM cone entrance after a distance of $d/2$ is considered ($d = 15.73$ mm). To the latter distance, a distance of 1 mm is added in the model (fig. 4.13(b)) for the propagation of the particles through the respective copper apertures ($z_{\text{aperture}} = 0.5$ mm). After this time t_A , the subsequent deceleration or acceleration (^{87}Rb -ion, photoelectron) in the respective CEM from the cone entrance at $z = d/2$ up to the impact position of the primary particle in the CEM at $z = d/2 + d_{i,e}$ is calculated (fig. 4.13), which yields the corresponding time t_B until impact. The addition of both flight times t_A and t_B will thus result in the corresponding flight time $t_{i,e}$ of the individual particle ($^{87}\text{Rb}^+, e^-$). For the equations of motion, both photoionisation fragments at $z = 0$ are regarded to be initially at rest. This follows as the kinetic energy¹² of the neutral ^{87}Rb -atom prior to photoionisation as well as the kinetic energy of the ionisation fragments gained from the excess energy¹³ E_{excess} of the photoionisation process can be disregarded compared to the acceleration of the charged particles in the electric field.

According to the TOF-model, the flight times of the photoionisation fragments are

$$t_i = t_A + t_B = d \sqrt{\frac{m_{\text{Rb}}}{e_0 \Delta U_{\text{acc}}}} + \frac{\sqrt{-2d_i^2 e_0 m_{\text{Rb}} \Delta U_i + (d_i m_{\text{Rb}} v_i)^2} + d_i m_{\text{Rb}} v_i}{e_0 \Delta U_i} \quad (4.5)$$

and,

$$t_e = d \sqrt{\frac{m_e}{e_0 \Delta U_{\text{acc}}}} + \frac{\sqrt{2d_e^2 e_0 m_e \Delta U_e + (d_e m_e v_e)^2} - d_e m_e v_e}{e_0 \Delta U_e}, \quad (4.6)$$

¹²For the neutral ^{87}Rb -atoms out of the background vapour, an average kinetic energy of $E_{\text{therm}} = 25.7$ meV is calculated, corresponding to the most probable atom velocity of $v_{\text{therm}}^* = \sqrt{2k_B T / m_{\text{Rb}}} = 239$ m/s at room temperature ($T = 25^\circ\text{C}$).

¹³The excess energy E_{excess} contributes with $E_{\text{excess}} = (\hbar\omega_{12} + \hbar\omega_{2i}) - E_{\text{thres}} \approx 33$ meV. Note, the value E_{thres} is the ionisation threshold of the neutral ^{87}Rb -atom, and $\hbar\omega_{12}, \hbar\omega_{2i}$ are the corresponding photon energies of the applied two-photon photoionisation transition (fig. 4.1).

respectively. In the equations¹⁴, the time t_A denotes the flight time of the fragment until CEM cone entrance at $z = d/2$. Accordingly, the flight time t_B yields the time from cone entrance until primary particle hit in the CEM detector corresponding to $z = d/2 + d_{i,e}$. The velocity $v_{i,e} = \sqrt{e_0 \Delta U_{\text{acc}} / m_{\text{Rb},e}}$ represents the velocity of the two ionisation fragments at CEM cone entrance ($z = d/2$) after acceleration of the respective fragment in the field E_{acc} . Note that for an experimental fit of observed flight times $t_{i,e}(\Delta U_{\text{acc}})$ according to the model (see section 5.3), the electric fields E_{acc} and $E_{i,e}$ are predefined by the particular measurement configuration at the CEMs. Therefore, the distances d_i and d_e remain as the only free parameters (see subsection 5.3.1).

Influence of the compensation electrodes and modified relative potentials

For a more accurate description of the electric potential along the central flight axis z of the ionisation fragments (fig. 4.13), the above TOF-model has to be altered to some extent. In a refined model, each ionisation fragment experiences a different, however constant acceleration as extracted from the potential simulation depicted in fig. 4.12. In contrast to the linear flight time model introduced in the previous subsection, the ionisation fragments start at a different relative potential value at $z = 0$ (indicated by ΔU_{cor} , fig. 4.11(b,d)). For example, the value $\Delta U_{\text{acc}} = 3.8 \text{ kV}$ (as used for both particles in the linear approximation model) will be individually¹⁵ changed $\Delta U_{\text{mod},i} = 2717 \text{ V}$ and $\Delta U_{\text{mod},e} = 1083 \text{ V}$, correspondingly. Further, the parameter $d/2$ will be altered to $d_{\text{mod}} = d/2 + d_{\text{saddle}}$ with $d_{\text{saddle}} = 1.3 \text{ mm}$ (fig. 4.10(f)) to compensate for the displaced saddle point in the ion-CEM compared to the linear¹⁶ model. For the e^- -CEM, the parameter remains $d/2$. The parameter d still includes the additional distance the ionisation fragment has to cover while propagating through the copper apertures due to the thickness of the apertures of the actual CEM configuration ($z_{\text{aperture}} = 0.5 \text{ mm}$). In the case of the kinetic energy of the ionisation fragment at primary particle impact, the impact energy E_{kin} of each fragment has to be altered according to the energy gained from the modified potentials (see subsection 4.3.4).

With the refined model, the calculated flight times (eq. 4.5 and eq. 4.6) for typical CEM detection system parameters at, e.g. $\Delta U_{\text{acc}} = 3.8 \text{ kV}$ and $U_{\text{CEM}} = 3.0 \text{ kV}$, are $t_i \sim 399 \text{ ns}$ for the ^{87}Rb -ion and $t_e \sim 1.5 \text{ ns}$ for the photoelectron, respectively. In comparison, the electric field strength values for the detection system are $E_{\text{acc}} = 2416 \text{ V cm}^{-1}$, and an internal CEM gain field strength of $E_{i\text{CEM},e\text{CEM}} = 556 \text{ V cm}^{-1}$ at CEM gain voltage of $U_{\text{CEM}} = 3.0 \text{ kV}$. For the calculation of the previous flight times t_i and t_e , an impact position of $d_{i,e} = d_{i\text{CEM}} + d_{\text{saddle}} = 12.3 \text{ mm}$ in the CEM is assumed for both particles. A different impact position in the corresponding CEM at, lets say, $d_{i,e} = d_{i\text{CEM}} + d_{\text{saddle}} = 7.3 \text{ mm}$ will yield values of $t_i \sim 329 \text{ ns}$ and $t_e \sim 1.3 \text{ ns}$.

In principle, such a difference in flight time allows in accordance with the covered distance $d_{i,e}$ in the CEM at least for the ion to explicitly allocate the spatial impact position of the ^{87}Rb -ion in the ion-CEM detector. Measured from the CEM cone entrance, the distance $d_{i,e}$

¹⁴Note that for calculations, $\Delta U_{i,e} = |E_{i\text{CEM},e\text{CEM}}| \cdot d_{i,e}$. In the equations, the relative polarities of the electric fields ($E_{\text{acc}}, E_e, -E_i$) have already been incorporated, accordingly (see subsection 4.3.4).

¹⁵The modified potential for each fragment individually corresponds to $\Delta U_{\text{mod}} = k \cdot \Delta U_{\text{acc}}/2$. For the linear TOF-model, k will correspond to $k = k_{i,e} = 0.5$ (fig. 4.13(b),i). For the refined model according to the FemLab simulation (see subsection 4.3.4), k corresponds to $k_e = 0.285$ for the photoelectron and to $k_i = 0.715$ for the ^{87}Rb -ion (fig. 4.13(b),ii).

¹⁶In the linear model, the saddle point of the ion-CEM potential is assumed to be at the entrance of the copper aperture (fig. 4.13).

reflects the path length that the particle covers in the CEM until primary particle impact. The derived impact position will thus indicate a CEM cone or channel hit (fig. 4.4), with the channel impact yielding an enhanced quantum yield η_{detector} for the CEM detector (see section 2.4). Further note that to our knowledge, an explicit determination of the particular impact position of any incident particles in the CEM detector has not been reported in the literature before (see section 5.3).

4.4.2. Detection time

The duration t_{tot} of the photoionisation detection of neutral atoms is composed of two parts. The first one is represented by the time t_{ion} of the photoionisation of the neutral atom itself (fig. 4.2), while the second is determined by the neutral atom detection time t_{det} of the generated ionisation fragments with the corresponding CEM detectors (see subsection 4.4.1). Both components simply add up to the overall detection time $t_{\text{tot}} = t_{\text{ion}} + t_{\text{det}}$ of the entire photoionisation detection scheme.

In order to determine the duration t_{det} of the detection process of the photoionisation fragments, the time from the photoionisation event in between the CEMs to the detection of the macroscopic electrical pulse at the anode of the CEMs is calculated. It is composed of the respective flight times (t_i, t_e) of the two ionisation fragments until the primary particle impact of each fragment in the corresponding detector and the transit time t_{transit} of the electron avalanche inside the CEM channels. Nevertheless, in the experiment only the time-of-flight difference $\Delta t = t_i - t_e$ of the two photoionisation fragments is accessible. The detection time of the neutral atom is therefore defined as

$$t_{\text{det}} = t_e + \Delta t + t_{\text{transit}} \quad (4.7)$$

It is approximated to $t_{\text{det}} \approx \Delta t + t_{\text{transit}}$ as the flight time t_e of the photoelectron fragment is much shorter¹⁷ than the flight time t_i of the ^{87}Rb -ion fragment, and the transit time t_{transit} (see subsection 3.2.1).

4.4.3. Collection efficiency

In the following, an eventual particle loss during imaging of the two photoionisation fragments into the corresponding CEM detectors is investigated. From this, the collection efficiency η_{col} of the CEM detection system is estimated (see section 2.4). In order to quantify η_{col} (eq. 2.8; subsection 2.4.1), three possible contributions of an eventual particle loss after photoionisation until primary particle impact in the CEM are analysed.

First, after photoionisation, there is a nonvanishing probability in the ionisation volume for charge recombination of the photoionisation fragments with adjacent atoms and molecules, or with simultaneously generated charged particles. However, due to the diluteness of the background vapour at typical background pressures of $p \sim 10^{-9}$ mbar, the probability of, e.g., a simultaneous second photoionisation event is very low due to the low particle density of the background (typically $n_{\text{back}} \sim 10^6$ atoms cm^{-3}) in the photoionisation volume. Even in a more dense MOT environment, any significant charge recombination of ionisation fragments after photoionisation due to interaction of the particles with the surrounding MOT environment has not been observed [216]. Note, however, that also a mutual charge recapture of the

¹⁷The actual flight times scale by a factor of $t_e/t_i \sim \sqrt{m_e/m_{\text{Rb}}}$ due to the much larger mass of the ^{87}Rb -ion compared to its photoelectron.

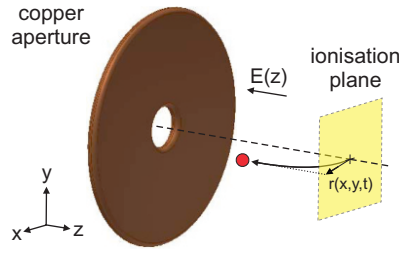


Figure 4.14: Schematic illustration of the propagation of the ionisation fragment through the CEM copper aperture.

two generated fragments immediately after photoionisation can be excluded due to the considerable excess energy E_{excess} for the photoionisation transition scheme used in the context of this thesis.

Second, homonuclear or heteronuclear collisions with the vacuum background are a probable source of particle loss. The mean free path of a particle in a thermal ensemble is $l = k_B T / (\sqrt{2} \pi d_{\text{Rb}}^2 p)$. For thermal atoms ($T = 25^\circ\text{C}$) with a diameter of $d_{\text{Rb}} \sim 235$ pm at an UHV background of $p \approx 10^{-9}$ mbar, the mean free path length is $l = 167$ km. This comparable huge distance leaves a collision of an ionisation fragment with the vacuum background very unlikely if one considers a covered path length of only $l_z \approx 20$ mm up to the primary particle impact in the active surface of the CEM detector. Moreover, this will also hold for the single atom trap immersed in a cloud of trapped atoms of a MOT environment. Even the enhanced atom density in the MOT region with typical particle densities of $n_{\text{Rb}} = 10^9 - 10^{10}$ atoms cm^{-3} will still yield a negligible collision probability at these densities ($n_{\text{Rb}} \sim p \approx 4 \times 10^{-7}$ mbar, with $l \approx 400$ m).

Consequently, the main contribution of an eventual particle loss will occur due to the imaging of the particles into the corresponding CEM detector. In fig. 4.14, the imaging of an ionisation fragments out of the ionisation volume at $z = 0$ until propagation through the CEM aperture is illustrated. In particular, the lateral translation $\vec{r} = \vec{r}(x, y, t)$ of the fragments in the $x - y$ plane perpendicular to the z -axis is investigated while the fragment is accelerated up to the CEM cone entrance at $z = d/2$. If the accumulated lateral deflection $\vec{r}(x, y, t = t_A)$ at the entrance is too large, the ionisation fragment will hit the bulk copper instead of propagating through the entrance of the CEM aperture (fig. 4.14). As the aperture diameter is $d_{\text{aperture}} = 2$ mm, the maximum lateral deflection $\vec{r}(x, y, t_A)$ at aperture entrance should thus not exceed 1 mm for both ionisation fragments.

To calculate the lateral deflection after a particle propagation for a time t_A , the initial velocity components perpendicular to the z -axis are considered in accordance with the linear field approximation $\vec{\mathcal{E}}_{\text{acc}}(x, y, z) = E_{\text{acc}}(z)$. Moreover, the vector of the initial particle velocity is chosen to be situated entirely in the radial $x - y$ plane in order to obtain the maximum attainable deflection of the particles (fig. 4.14). For the calculation, a cylindrical symmetry ($\rho^2 = x^2 + y^2$; z) is chosen. Therefore, the z -axis is situated in the center of the CEM aperture ($\vec{r}(x, y, t) = r(\rho, t)$) and represents the origin of the radial displacement.

The initial velocity $v_{\text{ion,ele}}$ of the fragments is composed of the kinetic energy E_{therm} of the neutral ^{87}Rb -atom prior to photoionisation as well as the excess energy E_{excess} from the photoionisation process. In the first case, the kinetic energy will correspond to $E_{\text{therm}} = 25.7$ meV for photoionisation of neutral ^{87}Rb -atoms out of the background vapour at room

temperature ($T = 25^\circ\text{C}$). In the second case, the individual particle velocity $v_{\text{ion,ele}}^*$ follows from the excess energy E_{excess} of the photoionisation process¹⁸. As energy and momentum are conserved during photoionisation corresponding to an elastic collision, the generated ^{87}Rb -ion and its photoelectron gain a velocity component in the center-of-mass frame of the neutral ^{87}Rb -atom of

$$v_{\text{ion}}^* = \sqrt{\frac{2E_{\text{excess}}}{m_{\text{Rb}} \left(\frac{m_{\text{Rb}}}{m_e} + 1 \right)}} \quad (4.8)$$

and $v_{\text{ele}}^* = m_{\text{Rb}} v_{\text{ion}}^* / m_e$. For an excess energy of $E_{\text{excess}} = 33 \text{ meV}$, the actual velocities are $v_{\text{ion}}^* = 0.68 \text{ m s}^{-1}$ and $v_{\text{ele}}^* = 1.08 \times 10^5 \text{ m s}^{-1}$, respectively. In the moving frame of the ^{87}Rb -atom, this velocity adds linearly to the thermal velocity¹⁹ of the neutral atom for maximum deflection, yielding an initial particle velocity of $v_{\text{ion,ele}} = v_{\text{ele}}^* + v_{\text{therm}}$ after photoionisation. Therefore, the maximum attainable deflection in the $x - y$ plane at $z = d/2$ is

$$r_{i,e}(\rho, t) = r_{i,e}(t) = v_{\text{ion,ele}} \cdot t. \quad (4.9)$$

For acceleration voltages of $\Delta U_{\text{acc}} = 3.8 \text{ kV}$, the calculated maximum displacement for ^{87}Rb -ions in the $x - y$ plane from the central z -axis is $r_i(t_A) \approx 61 \mu\text{m}$ (using a CEM entrance arrival time of $t_A = 256 \text{ ns}$ as calculated in eq. 4.5). Due to the small mass of the photoelectron compared to the ^{87}Rb -ion, the electron takes away almost all the excess energy E_{excess} from the photoionisation, yielding a comparably large initial velocity of $v_{\text{ele}} \approx v_{\text{ele}}^* = 1.08 \times 10^5 \text{ m s}^{-1}$. Thus the thermal component of the velocity v_{therm} based on the motion of the former neutral ^{87}Rb -atom becomes insignificant compared to the gained velocity out of the photoionisation. The corresponding displacement for the photoelectron is $r_e(t_A = 0.85 \text{ ns}) \approx 92 \mu\text{m}$ with an estimated flight time of $t_A \approx 0.85 \text{ ns}$ until entrance into the detector through the copper aperture.

Even for neutral atoms photoionised at the edges of the photoionisation volume corresponding to an initial radial position of $\rho \approx 100 \mu\text{m}$ in the $x - y$ plane (see subsection 4.5.2), the overall displacement of the ionisation fragments will still be smaller²⁰ than $200 \mu\text{m}$. As this value is by a factor of ten smaller than the diameter of the entrance of the aperture, *all* incident ionisation fragments should be properly imaged into the CEMs and subsequently detected.

However, for the future application of a trapped atom in an optical dipole trap, the lateral displacement of the ^{87}Rb -ion will become entirely insignificant due to the ultra-cold temperature of the atom. The thermal component of v_{ion} will only contribute with $v_{\text{therm}} = 0.12 \text{ m s}^{-1}$, considering a measured trapped atom temperature of $T = 70 \mu\text{K}$ [45]. With the full initial particle velocity v_{ion} , the ion²¹ will experience only a lateral displacement of $r_i(t_A = 256 \text{ ns}) \approx 205 \text{ nm}$. Interestingly, from a kinetic energy point of view, already the

¹⁸In this thesis, a two-step process is employed (fig. 4.1(a)), with $^{87}\text{Rb} + (\hbar\omega_{12} + \hbar\omega_{2i}) \longrightarrow ^{87}\text{Rb}^+ + e^-$, and $\lambda_{12} = 780.241 \text{ nm}$ and $\lambda_{2i} = 473 \text{ nm}$, correspondingly.

¹⁹The corresponding most probable velocity for a thermal neutral ^{87}Rb -atom is $v_{\text{therm}} = 239 \text{ m s}^{-1}$, where thermal denotes room temperature of the ensemble (25°C).

²⁰The displacement is $r_{i,e}(\rho, t_A) = \rho + r_{i,e}(t_A)$, with values of $r_i(256 \text{ ns}) \approx 161 \mu\text{m}$ and $r_e(0.85 \text{ ns}) \approx 192 \mu\text{m}$, respectively.

²¹For the photoelectron, the situation is identical to the initial thermal example due to the huge gain in kinetic energy from the excess energy out of photoionisation.

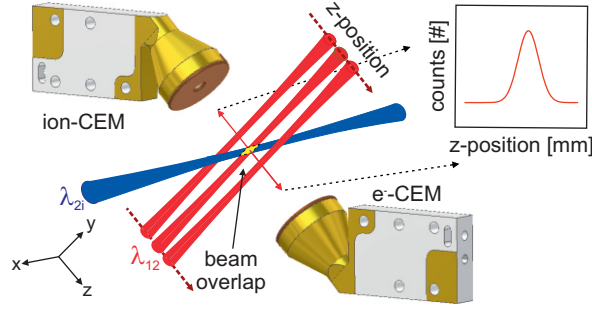


Figure 4.15: Illustration of the spatial overlap of the two laser beams yielding the ionisation volume of the photoionisation scheme. To determine the spatial overlap of the two beams, the red laser beam (λ_{12}) is translated in z -direction through the fixed blue laser beam (λ_{2i}).

corresponding energy of the photoionisation recoil on the ^{87}Rb -ion will still be sufficient to remove²² the ion out of the trap.

As a final result of the above considerations, the collection efficiency of the CEM detection system is assumed to approach unity as stated in subsection 2.4.1.

4.5. Beam overlap and photoionisation fragment imaging

The following section describes the main calibration steps to experimentally determine the sensitive detection area A_c of the CEM detection system at a particular z -position in between the CEMs. The corresponding correlation measurements allow to observe electron-ion coincidences with both CEM detectors from photoionisation of single neutral atoms within the area $A_c(x, y; z)$. As a result, the observation of coincidences in the CEMs enables the calibration of each CEM detector to absolute efficiency values $\eta_{\text{det}} = \eta_{i,e}$ as illustrated in chapter 5.

Moreover, the overlap measurements of this section explicitly reveal the spectroscopic and spatial selectivity of the chosen photoionisation transition (section 4.1). In particular the latter property leaves the photoionisation in a defined ionisation volume as the experimental realisation of a unique calibration source for charged particle pairs, which allows an absolute efficiency calibration of any charged particle detector system (see subsection 5.1.3). The 2D-scan measurements of this section further illustrate the spatial and temporal long term stability of the actual CEM detection system. As a consecutive measurement duration of up to two weeks is estimated for the final Bell test [18], the long term stability of the detection system is a prime requisite of such an experiment.

4.5.1. Calibration measurement setup

For the calibration measurements of the CEM detection system, neutral ^{87}Rb -atoms from the thermal background vapour are photoionised within the spatial overlap of two mutually perpendicular laser beams (fig. 4.15) in the glass cell described in section 4.2. In order to experimentally realise the 2D-scan calibration measurements, two fiber outcoupler cage systems are mounted on motorized translation stages on an optical table outside the vacuum

²²The initial kinetic energy $E_{\text{Rbion}} = \frac{1}{2}m_{\text{Rb}}v_{\text{ion}}^2 \approx 2 \times 10^{-7}$ eV of the photoionised ion in the trap corresponds to a temperature of $T_{\text{Rb}} = E_{\text{Rbion}}/k_{\text{B}} = 2.4$ mK, compared to a typical dipole trap depth of $T_{\text{dipole}} = 1.5$ mK [45].

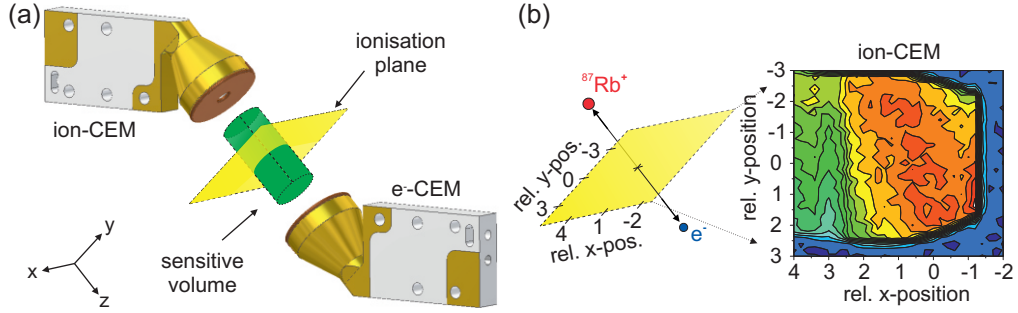


Figure 4.16: 2D-scan measurements in $x - y$ plane at $d/2$. (a) Schematic illustration of the sensitive volume (green) and the spatial orientation of the 2D-scan ionisation plane. (b) Spatial orientation of the relative position coordinates in between the CEMs according to the measurement sample as displayed in fig. 4.19.

chamber. Step motors (MMS 19-25-xxxx, Owis) on the translation stages enable an interface-controlled, spatial displacement of the outcouplers of down to $1 \mu\text{m}$ precision. Attached cage systems on the fiber couplers further provide all subsequent beam optics and the corresponding beam alignment for the two focused laser beams of the calibration measurements. To prevent the glass cell from ambient stray light from the laboratory environment, the whole cell and beam optics are integrated into a black, stray-light save box. For resonant stray light from the two photoionisation beams, especially the ionizing blue laser beam ($\lambda_{2i} = 473 \text{ nm}$) is additionally guided in blackened aluminum tubing extending up to both sides of the glass cell. By this, resonant stray light diffused from the optical elements in the beam path as, e.g. polarisers or focusing lenses, is substantially reduced.

For alignment in the UHV glass cell, the laser beams are oriented perpendicular to the z -axis (fig. 4.15). Further, the single beams are individually aligned²³ parallel to the x -axis (λ_{2i}), and to the y -axis (λ_{12}), respectively. Due to motorised translation stages at the beam mounts (see subsection 4.2.3), both laser beams are moved with respect to each other in the $x - y$ plane in between the CEMs. By this, the center of the beam overlap and thus the photoionisation volume can be positioned deliberately in the $x - y$ plane at different z -positions of the CEM detection system. This spatial displacement of the overlap enables 2D-scan measurements in the $x - y$ plane at any z -position in between the CEMs, using the ionisation volume as efficient source of correlated, charged particle pairs. In the experiment, various 2D-scan measurements are performed at different z -positions in order to calibrate the CEM detection system and to investigate the spatial dependence of the detection efficiency $\eta(x, y)$. Preferably, the position of $z = d/2$ in between the CEMs is chosen as it represents the future position of the integrated optical dipole trap in the UHV glass cell.

The photoionisation process itself is highly selective as a resonant two-step, two-colour photoionisation scheme is employed (see section 4.1). The photoionisation therefore occurs hyperfine-state selectively in the spatial overlap volume of the two laser beams only (fig. 4.15). In consequence, the spatial extension of the beam overlap defines the dimension of the photoionisation volume (see subsection 4.5.2). In addition to that the size of the ionisation volume can actually be altered by choosing different beam waists (w_{12}, w_{2i}).

²³For initial alignment, the spatial extension of the copper frame and the CEM detectors represent useful 'landmarks' in the UHV (fig. 4.6).

Uniform photoionization conditions over the entire $x - y$ scan region of up to $10 \times 10 \text{ mm}^2$ are provided by only weakly focusing the beams ($w_{12}(780 \text{ nm}) = 26 \mu\text{m}$, $P_{12} = 155 \mu\text{W}$; $w_{2i}(473 \text{ nm}) = 43 \mu\text{m}$, $P_{2i} = 164 \text{ mW}$). The uniform conditions result from the large Rayleigh-length of both laser beams compared to the average scan distances, ensuring a negligible spatial beam divergence at these distances. By alignment, the relative positions of the foci of both laser beams are situated to coincide in the common optical axis of both CEMs. Here, the common optical axis is defined by the center of both CEM cone apertures (fig. 4.14). During all calibration measurements, the accelerating voltage difference ΔU_{acc} in between the CEMs is kept constant.

Sensitive detection area and sensitive volume

The sensitive area $A_{i,e}$ of a single CEM detector is defined by the relative positions (x, y) in the ionisation plane out of which particles are imaged into the corresponding detector and subsequently counted (fig. 4.16). By definition, coincidences are only observed in the common overlap area A_c of both detectors sensitive areas. Consequently, the sensitive detection area of the joint CEM detection system is defined as $A_c = A_i \cap A_e$. The sensitive volume V_c of the detection system is then represented by the extension of the sensitive detection area $A_c(x, y)$ in the z -direction. Accordingly, from photoionisation at each position in the sensitive volume $V_c = V_c(x, y, z)$ the two ionisation fragments are detected in coincidence (fig. 4.16).

4.5.2. Spatial beam overlap and ionisation volume

In the experiment, the observed particle counts $N'_{i,e}$ from photoionisation at the CEM detectors represent the overlap of the two laser beams. To the first order, the overlap is resembled by the radial intensity profile of the ionising blue laser beam at a particular relative x -position. As the excitation transition ω_{12} of the photoionisation scheme (fig. 4.1(a)) is saturated with multiple saturation intensities ($I_{12} \gg I_{\text{sat}}$), the population ρ_{ee} of the population of the excited $5^2P_{3/2}$ level is uniform and constant²⁴ over the entire spatial extension of the ionising blue laser beam (fig. 4.15). The transition rate W_{2i} to the continuum is approximately linear [176] to the intensity $W_{2i} \sim \rho_{ee}\sigma_{2i}I_{2i}$ for the small beam intensities I_{2i} as applied here in the calibration measurements (for explicit measurement of the linearity; fig. 5.2, section 5.1). As a result, the spatial distribution of the measured counts $N'_{i,e}(z)$ in fig. 4.17 thus simply represents the spatial intensity distribution of the ionising blue laser beam.

As illustrated in fig. 4.15, in fig. 4.17 a sample overlap scan is displayed at one particular position ($x = 1.0 \text{ mm}$, $y = -0.4 \text{ mm}$; fig. 4.19) at $z = d/2$ in between the CEMs. Figure 4.17(a-c) shows the measured, background corrected counts for ions N'_i , electrons N'_e , and coincidences N'_c according to the relative z -position of both beams with respect to each other. From the determined counts $N'_{i,e} = N'_{i,e}(z_c)$, the spatial dependent absolute detection efficiencies $\eta_{i,e}(z)$ can be derived (fig. 4.17(d); the detection efficiencies are determined from eq. 5.5; see subsection 5.1.2). In order to obtain the optimum spatial overlap of both laser beams according to the observed counts, a Gaussian fit of the spatial variation of the single counts $N'_{i,e}(z)$ is applied. The fit exhibits an almost perfect Gaussian shape of the beam overlap. Consequently, the center position z_c of the Gaussian fit yields the optimum posi-

²⁴However, for excitation of thermal atoms out of the background vapour, the spatial distribution of the excited level population ρ_{ee} in a resonant laser beam is generally difficult to determine (see, e.g., [217])

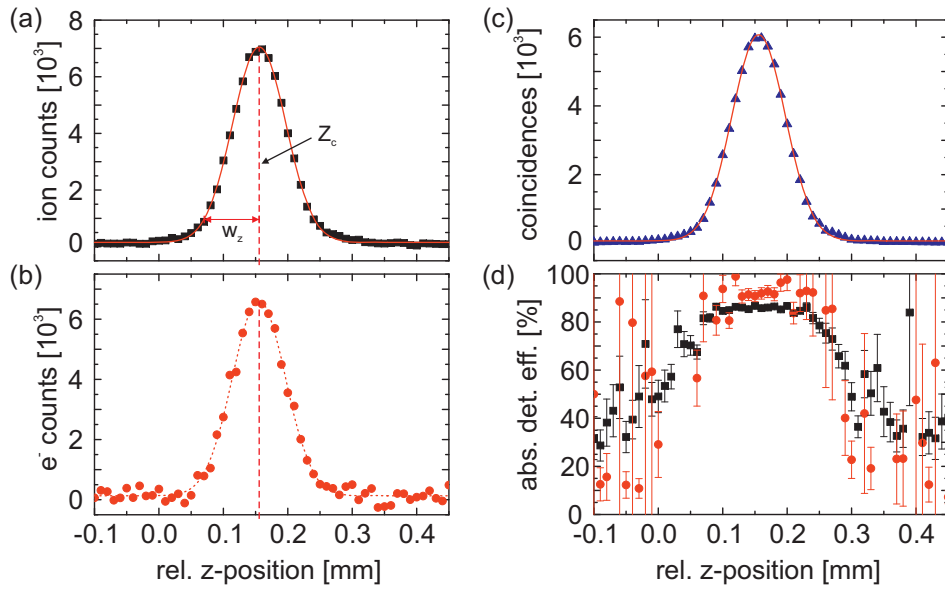


Figure 4.17: Sample overlap scan of the two laser beams according to fig. 4.15 at $(x = 1.0 \text{ mm}, y = -0.4 \text{ mm})$; fig 4.18). (a-c) Measured, background corrected counts for ions, electrons, and coincidences. The solid lines (red line) show a Gaussian fit of the variation of the count rate corresponding to the relative spatial overlap of the two laser beams. The center z_c of the Gaussian fit yields the optimum position for the overlap. The measurement duration for each sample point is $t = 5 \text{ s}$. (d) For comparison of the beam overlap calibration with measurements of chapter 5, additionally the derived absolute detection efficiencies $\eta_{i,e}(z)$ from the observed counts of (a-c) are displayed (for $\eta_{i,e}(z)$; eq. 5.5, subsection 5.1.2).

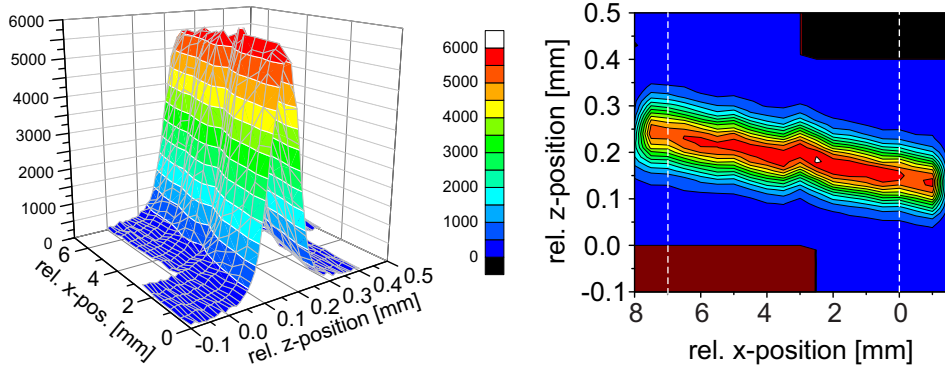


Figure 4.18: Sample one dimensional line scan $N'_i(x; z)$ of the two beam overlap in x -direction at a fixed y -position of $y = -0.4$ mm (fig. 4.19). Over an x -scan distance of up to 9.5 mm in between the CEMs, the detected ^{87}Rb -ion counts exhibit a perfect Gaussian profile. The dashed lines in the contour plot indicate the boundaries of the surface plot.

tion for the overlap (fig. 4.17, red line) and therefore the maximum attainable single counts $N'_{i,e} = N'_{i,e}(z_c)$ from photoionisation, accordingly.

If the two laser beams do not overlap, no resonant photoionisation occurs. This is illustrated by the single counts $N'_{i,e}(z)$ and coincidences $N_c(z)$ for z -positions far from the ionisation center at z_c (e.g., $z = -0.1$ mm or $z = 0.45$ mm; fig. 4.17). This property explicitly demonstrates the *spatial* selectivity of the photoionisation transition scheme as only in the overlap volume of the two corresponding laser beams neutral ^{87}Rb -atoms are ionised (see section 4.1). With a measured beam waist of $w_c \sim 43$ μm determined from the Gaussian fit in fig. 4.17(a,b), the typical $1/e^2$ -ionisation volume of the two beams is only $V_{\text{ion}} = (86 \mu\text{m})^3$ for the chosen beam configuration ($V_{\text{ion}} \sim d_c^3 = (2w_c)^3$). Interestingly, the overlap measurement also exhibits an identical shape ($w_c(N'_i) = (w_c(N'_e))$) of the overlap of both ionisation fragments (fig. 4.17(a,b)), and an identical z -position ($z(N'_i) = (z(N'_e))$) for single traces of the ion or electron counts.

In fig. 4.18, a one dimensional line scan of the beam overlap in x -direction is shown, displaying the background corrected ^{87}Rb -ion counts $N'_i(x; z)$. For the measurement, the blue laser beam is fixed at a relative position of $y = -0.4$ mm (fig. 4.19). The red laser beam is translated in z -direction through the blue laser beam (fig. 4.15), but for various relative x -positions from $x = -1.5$ mm to $x = 8.0$ mm in steps of $\Delta x = 0.5$ mm. Over the entire x -scan distance of 9.5 mm in between the CEMs, the detected ^{87}Rb -ion count rates exhibit a perfect Gaussian profile similar to the measurement in fig. 4.15. From a Gaussian fit of the individual measurements, the relative position $z_c = z_c(x)$ of the center of the overlap is determined. The ionisation center, being the center position of the ionisation volume, is thus given by the center position z_c of the Gaussian fit of the beam overlap.

In the aspect of the 2D-scan measurements, reduced ion or electron counts $N'_{i,e}$ due to a slight relative displacement of the beam overlap during scanning in the $x - y$ plane are observed. Beam overlap measurements as illustrated in fig. 4.18 show that the center position z_c of the beam overlap relatively moves only ~ 11 $\mu\text{m}/\text{mm}$ for a translation in the x -position and ~ 5 $\mu\text{m}/\text{mm}$ in the y -position during a 2D-scan measurement. Therefore, the obtained count rates $N'_{i,e}$ are assumed to be constant for *typical* scan distances of only up to 2 mm in the $x - y$ plane (fig. 4.19). In principle, for the 2D-scan measurements the maximum²⁵

²⁵The maximum attainable count rates result for optimum overlap z_c (fig. 4.17).

attainable counts $N'_{i,e}(z_c)$ at *each* scan position in the $x - y$ plane can be reconstructed from the displacement values in x and y -direction and a single beam overlap measurement. Such a reconstruction will yield the calibrated, maximum counts $N'_{i,e}(x, y)$ at each position even for wide 2D-scan measurements with an area of $6 \times 6 \text{ mm}^2$ (fig. 4.19).

Note that from the one dimensional scan of the overlap of the two laser beams as illustrated in fig. 4.18, the beam waist $w = w_{473}(x)$ along the optical axis of the blue beam can be determined. Further, the relative x -position x_F of the focus of the blue laser beam, and the corresponding beam waist $w(x_F)$ in the focus can be estimated. For the current blue laser beam used in the calibration, the determined waist parameter $w(x_F) = 43 \mu\text{m}$ from the overlap measurement coincides with the calculated value for the chosen set of focusing lenses and the initial beam waist at the exit of the optical fiber ($w_{\text{exit}}(473 \text{ nm}) = 876 \mu\text{m}$, $f_{\text{lens}} = 250 \text{ mm}$). Interestingly, such a measurement will also allow to determine the beam parameters and the relative focal position of the overlapped laser beams in the optical dipole trap in the future integrated CEM detection setup. The spatial calibration of the trap will enable to maximize the corresponding dipole trap parameters for optimum photoionisation of the single atom (e.g., the overlap of the beams) and allow to optimize the spatial overlap of an eventually used, additional fluorescence detection with the dipole trap.

In summary, the beam overlap measurements predict uniform photoionisation beam properties for the upcoming 2D-scan measurements. Local variations in the count rates are thus seemingly caused solely by other factors, i.e., different spatial imaging of the fragments into the CEMs, or variations in the neutral particle flux at a particular spatial position due to, e.g., shading elements in the vacuum.

4.5.3. Photoionisation fragment imaging

A prerequisite for the coincident detection of both ionisation fragments as described in chapter 5 is the mutual imaging of the fragments from one common ionisation center in between the CEMs into the respective detector. To experimentally quantify the spatial imaging of the fragments from the position of the photoionisation origin into the corresponding detector, 2D-scan measurements in the $x - y$ plane at different z -positions in between the CEMs are performed. For these measurements, the position of the photoionisation center is deliberately displaced in the $x - y$ plane (ionisation plane) at a fixed z -position (e.g., $z = d/2$; fig. 4.16)

The main purpose of the 2D-scan measurements is to determine the sensitive detection area $A_c(x, y)$ of the CEM detection system at $z = d/2$. This determination is essential for the coincident detection of the correlated, charged particle pairs and the resulting absolute calibration of detection efficiency of the CEM detectors. The further purpose of the 2D-scan measurements is to investigate the temporal and spatial long term stability of the imaging. Measurements on previous setups show that the influence of fluctuating, ambient stray fields in the UHV can become rather critical, distorting the simultaneous imaging of the two ionisation fragments into the CEMs. In the worst case, this will result in no common overlap of both sensitive areas $A_{i,e}$ of the CEM detectors, not allowing any coincidences to be observed.

Note that 2D-scan measurements in the $x - y$ plane at different z -positions other than $z = d/2$ in between the CEMs have also been performed in the context of this thesis. However, in this case the kinetic particle energy at cone entrance varies from the estimation given in subsection 4.3.4 for $z = d/2$, but explicitly depends on the relative z -distance each charged particle has to travel up to the cone entrance from the z -position of the photoionisation center in the accelerating potential $\Delta U_{\text{acc}}(z)$ (see subsection 4.3.4).

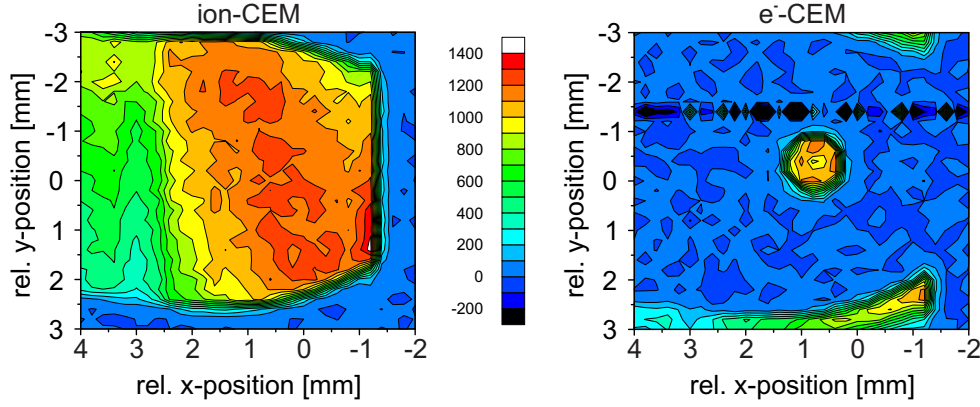


Figure 4.19: Contour plot of a sample 2D-scan measurement in $x - y$ plane at $d/2$. Depicted are the background corrected counts $N'_{i,e}$ at the ion-CEM and the e^- -CEM according to the relative spatial position of the ionisation volume in between the CEMs.

Ionisation area scans in $x - y$ plane

In fig. 4.19, the contour plot of a sample 2D-scan measurement in $x - y$ plane at $z = d/2$ is depicted. For joint CEM detector calibration, similar measurements are frequently performed to probe the spatial and temporal stability of the imaging. Figure 4.19 shows the background corrected counts N'_i , N'_e at the respective CEM detectors (ion-CEM, e^- -CEM). For this, the ion/electron counts $N_{i,e}$ and background counts $N_{ib,eb}$ are measured at each 2D-scan position (x, y) for a fixed time interval ($t = 5$ s), and with a spatial 2D-scan resolution corresponding to the step size of $\Delta x, y = 200 \mu\text{m}$. Note that particularly for the ions, a distinct but varying count rate topography is observed according to the spatial position of the 2D-scan. This results as for large 2D-scan distances, reduced count rates at different spatial positions are attained as the two laser beams are slightly displaced at these positions which leads in a reduced beam overlap of the two beams and correspondingly reduced count rates (fig. 4.18). In the scan measurements, the observed counts therefore reflect to some extent also the quality of the spatial beam overlap (see subsection 4.5.2).

As displayed in fig. 4.19, at a relative x -position of $x \leq -1.5$ mm the copper frame of the CEM detection system prevents any further photoionisation. Here, the spatial extensions of the frame physically block the red laser beam (fig. 4.19(a)). At a relative y -position of $y = -1.4$ mm, the electron background value N_{eb} strongly deviates from the average electron background in the measurement. The deviation is caused by increased stray light from the blue laser beam due to a macroscopic dust particle situated at the wall surface of the UHV glass cell at this position²⁶. The dust particle partly diffuses some of the laser beam light, significantly enhancing the e^- -CEM background counts at this particular scan position.

In fig. 4.19, the sensitive area $A_i(x, y)$ of the ion-CEM extends approximately from the relative positions ($x = -1.4$ mm \rightarrow 4.0 mm, $y = -2.8$ mm \rightarrow 2.5 mm; fig. 4.19). The sensitive area $A_e(x, y)$ of the e^- -CEM only covers a circular shape from the relative positions ($x = 0.4$ mm \rightarrow 1.3 mm, $y = -0.9$ mm \rightarrow 0.0 mm). Consequently, the sensitive detection area $A_c(x, y)$ of the joint CEM detection system is identical to the circular shape A_e of the e^- -

²⁶As a result, a dust-free assembly of the integrated CEM detection system into the glass cell is essential (subsection 4.2.3) to prevent any contamination of the UHV glass cell walls with dust particles. On the other hand, also dust-free conditions outside the glass cell are generally beneficial.

CEM for photoionisation at $z = d/2$ in between the CEMs (for the corresponding absolute detection efficiencies $\eta_{i,e}(x, y)$; see section 5.5, fig. 5.13). Remarkably in fig. 4.19, there is a steep increase in the observed counts $N_{i,e}$ compared to the background $N_{ib,eb}$ once the sensitive area $A_{i,e}$ of the corresponding CEM detector is hit. Further note that for an optimised partial pressure of the neutral Rb-atom vapour background in the UHV, the signal to background ratio of the ion counts increase to more than $N_i/N_{ib} \sim 10^4$.

In fig. 4.19, the observed counts $N'_{i,e}(x, y)$ reflect the spatial imaging of photoionisation fragments out of the ionisation volume of the beam overlap into the respective CEM (fig. 4.15). The ionisation volume $V_{ion} \sim (86 \mu\text{m})^3$ and the calculated, radial displacement²⁷ of the fragments are small compared to the dimensions of the CEM aperture ($d_{aperture} = 2 \text{ mm}$). Compared to the spatial dimensions of the CEM detection system, the ionisation volume therefore approximately serves as a quasi point-like, electric field probe.

By spatial shape, in fig. 4.19 the photoelectrons are rather defocused during imaging in the e^- -CEM, if one compares the observed radius of the sensitive area A_e and the diameter $d_{aperture}$ of the aperture entrance. In contrast to that the collection angle for the photoions in the ion-CEM is significantly enhanced (fig. 4.19(b)), allowing to collect ^{87}Rb -ions from a large spatial area in the ionisation plane. By altering the potential $U_{comp} = -0.4 \text{ kV}$ of the compensation electrodes (fig. 4.9), the collection angle of the photoions or photoelectrons is subsequently reduced or further enhanced. Similar measurements to fig. 4.19 for different compensation electrode potentials U_{comp} show a reduced diameter of the photoion image of $d_{img} \approx 2.5 \text{ mm}$ in y -direction at a potential voltage of $U_{comp} = -1.0 \text{ kV}$ (compared to $d_{img} \approx 5.5 \text{ mm}$ at $U_{comp} = -0.4 \text{ kV}$, fig. 4.19). By adjusting each electrode on an individual potential, further measurements suggest that the relative position of the sensitive areas $A_{i,e}(x, y)$ in the CEMs can also be spatially altered to some extent. In principle, this allows the full spatial control of the 2D-imaging of the photoionisation fragments in the y - direction by adjusting the compensation electrodes accordingly.

Interestingly, in all 2D-scan measurements of the sensitive area A_e of the e^- -CEM, a 'corona' like structure is observed (e.g., see positions $x = -1.0 \text{ mm} \rightarrow 4.0 \text{ mm}, y = \pm 3.0 \text{ mm}$; fig. 4.20(i-iv)). The shape of the structure almost perfectly matches the fringe of the sensitive area $A_i(x, y)$ of the ion-CEM, even for differently chosen compensation electrode potentials. Consequently, the characteristic structure might not originate from primary electrons of the ionisation fragment imaging, but from secondary electron emission out of the aperture edges of the copper aperture of the ion-CEM. This occurs as imaged ^{87}Rb -ions will hit the copper surface at the aperture edge instead of propagating through the aperture entrance (fig. 4.14) at the particular fringe positions in the sensitive area $A_i(x, y)$ of the ion-CEM. As the primary ion will produce secondary electrons with its impact at the surface, some of the generated electrons will be deflected and collected into the opposite e^- -CEM, resulting in the characteristic 'corona' structure observed in the 2D-scan measurements in the e^- -CEM.

Performance stability

In the future, a continuous operation of the CEM detection system for a measurement duration of over two weeks is estimated for the final Bell test [18]. Thus, the spatial and temporal long term stability of the imaging are prime requisites for continuous operation of the detection

²⁷The radial displacement $r_{i,e}(t)$ of the individual fragment during acceleration in the electric field $E_{acc}(z)$ is of the same order of magnitude as the diameter $d_c = 2w_c = 86 \mu\text{m}$ of the ionisation volume (subsection 4.4)

system. A stable imaging will provide the essential high detection efficiencies $\eta_{i,e}$ over the full measurement period for the final Bell test. Particularly in the close dimensions of the glass cell environment, temporal stability of the electric field configuration and its corresponding potentials is not intrinsically given. Measurements at previous²⁸ test setups of the CEM detection system show that especially the influence of slowly accumulated stray charges at non-conducting surfaces in the UHV significantly affects the spatial distribution of the electrical potentials in the glass cell. In such a case, the generated stray fields will change the imaging properties of the system, eventually distorting the imaging of the ionisation fragments in a macroscopic way. In the worst case, this will lead to no common overlap A_c of both CEMs sensitive areas $A_{i,e}$, disallowing to observe any coincidences.

In analogy to related problems in ion trap experiments [211, 212, 214, 218, 219], the exclusive use of conductive surfaces in the UHV prevents the isolated accumulation of stray charges. As a solution, conductive shielding of all components in our experiment is chosen and compensation electrodes in the CEM detection system setup are introduced (fig. 4.6). By use of the electrodes, a distinct electric potential at a particular spatial position of the detection system is defined. Thereby, the compensation electrodes enable the control of the imaging fields in between the CEMs and shield the imaging region of the CEM detection system against the influence of stray potentials situated outside the compensation electrodes (fig. 4.9).

To investigate the spatial and temporal performance of the actual CEM detection setup, in fig. 4.20 contour plots of different sample 2D-measurements similar to fig. 4.19 are shown. The scans display the sensitive areas $A_{i,e}(x, y)$ of both CEM detectors over a measurement period of six months (fig. 4.20(i-vi)). The colour scale of the different contour plots is chosen individually for each plot, reflecting the relative scale of the counts $N'_{i,e}(x, y)$ in each scan. Deviating count rates in single x -traces in the scans result from adhesive dust particles on the glass cell surface (e.g., fig. 4.20(iii)). During the time in between the sample scan measurements at the beginning of each month (i,ii,..,vi), various different CEM detector calibration measurements at alternating positions in all three dimensions (x, y, z) were performed. Nevertheless, the sample scan measurements prove the stability of the particle imaging in the CEM detection system despite the extensive operation of the detection system during that time. In fact, over the full duration of six months no significant drift ($< 80 \mu\text{m}$) in the position of the sensitive areas $A_{i,e}(x, y)$ is observed (fig. 4.20(i-vi)). In addition, also the spatial shape of the areas is almost entirely conserved, leaving the spatial imaging of the photoionisation fragments stable for several months.

²⁸In previous test setups, mounting frames structures made out of Macor[®] were used instead of a copper frame (fig. 4.6). Here, isolated charges continuously accumulate on the frame, entirely distorting the imaging of the fragments into the CEMs resulting in no common coincident overlap of the detection system.

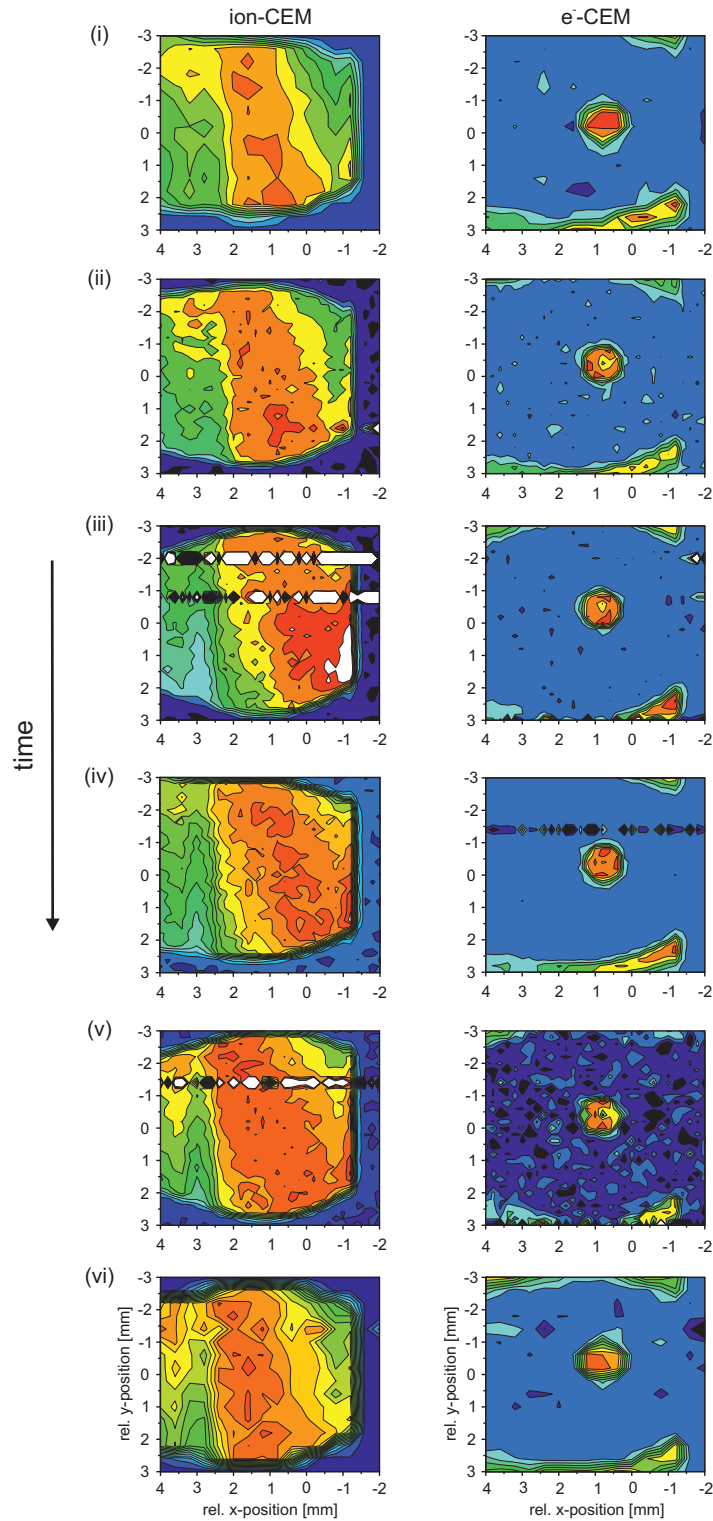


Figure 4.20: Contour plots of different 2D-measurements for identical 2D-scan positions in the $x-y$ plane similar to fig. 4.19. The scans illustrate the imaging performance of the CEM detection system over a measurement period of six months (i-vi). The colour scale of the different contour plots reflects the relative counts $N'_{i,e}(x, y)$ in each scan.

5. Fast and Efficient Photoionisation Detection of Single Atoms

In the following chapter, the experimental calibration of the joint CEM detection system to absolute efficiencies $\eta_{i,e}$ is described. In addition to that, also the flight time $t_{i,e}$ of the individual photoionisation fragments and thus the detection time t_{det} for single neutral atoms with the CEM detection system is experimentally determined. Although the CEM detection system is primarily intended to operate as a hyperfine-state selective readout unit for single neutral atoms in an optical dipole trap [18, 24], the particular detector specifications¹ leave the CEM detection system as a unique experimental solution for a broad range of spectroscopic applications where a sub-microsecond, highly efficient, and hyperfine-state selective detection of single neutral atoms is required. Moreover, as absolute detection efficiencies are determined, the obtained values allow a direct comparison of the CEM detection system with other detection systems in the literature.

In section 5.1, the concept of detector calibration to absolute values is introduced and compared to the conventional, relative detector calibration method. The correlated particle pairs required for the absolute calibration are generated from photoionisation of neutral atoms in a defined ionisation volume (see section 4.5). By using the absolute calibration measurement, all limiting factors of the detection efficiency in the detection system as, e.g., a reduced collection efficiency $\eta_{\text{col}} < 1$ and any system specific parameters are already included in the calibration. In contrast to the relative calibration method, the determined absolute detector efficiencies therefore admit a comparison of different detection systems with each other, and even of individual particle detectors in different detection systems.

The photoionisation of neutral atoms in a defined ionisation volume further represents the experimental implementation of an efficient pair source for differently charged particles. In relation to any conventional particle beam sources, this allows the calibration of charged particle detectors down to single particle efficiencies. In addition to that, it exclusively permits the coincident counting of correlated pairs required for absolute calibration measurements. To our knowledge, a detector calibration source based on photoionisation which yields correlated, differently charged particle pairs has not been reported before.

The counting of the correlated electron-ion events from photoionisation with the CEM detection system is demonstrated in section 5.2. Accordingly, the photoionisation of neutral atoms in a defined ionisation volume in between the CEMs enables to observe correlated particle incidences at the two CEM detectors. From the measurement of the individual electron and ion arrivals at the single CEMs, electron-ion correlation histograms are generated which yield a distinct correlation peak from photoionisation in the relative ion arrival time Δt . The correlation histograms allow to determine the number of coincidences N_c , and thus permit to obtain the absolute detection efficiency of both CEMs from the single counts $N'_{i,e}$ and the coincidences N_c at the two detectors (see section 5.1).

¹For a future loophole-free Bell test with two remote entangled ⁸⁷Rb atoms [18, 21], an overall detection efficiency of $\eta > 95\%$ and an overall detection time of $t_{\text{tot}} < 1\ \mu\text{s}$ for the hyperfine-state selective readout of a single atom via photoionisation are intended (see chapter 6).

Based on the the acceleration potential simulations and the flight time model of chapter 4, the measured arrival time differences Δt in section 5.3 yield the flight times $t_{i,e}$ of the individual ionisation fragments until impact in the corresponding CEM. From the flight times $t_{i,e}$, the neutral atom detection time t_{det} with the joint CEM detection system can be calculated. The measurement of the flight time further allows the discrimination of different isotopic species in accordance with the calculations of section 4.4. This thus enables to selectively detect different isotopic species according to their relative arrival time in the CEM, identical to a highly sensitive mass spectrometer. This property becomes particularly interesting, if a highly efficient, isotope or species selective readout of several atoms or molecules is required in any future experiments (see chapter 6). Moreover, the observed values of Δt at different acceleration voltage differences ΔU_{acc} additionally provide the particular impact position of the primary ^{87}Rb -ion in the ion-CEM (see section 5.5). In contrast to conventional calibration measurements, this property together with an absolute efficiency calibration is explicitly measured.

The measurements in section 5.4 describe the calibration of the CEM detection system to absolute efficiencies. From the two single efficiencies $\eta_{i,e}$ of the two CEM detectors, the neutral atom detection efficiency η_{atom} is determined. The efficiency measurements further allow to observe the raw quantum yield η_{detector} of a CEM detector (see section 2.4), as the estimated collection efficiency of the CEM detection system exceeds unity (see section 4.4) and any counting errors based on the subsequent pulse processing electronics can be excluded (see section 3.4). The measurement of the raw quantum yield $\eta_{i,e}$ of the ion-CEM and the e^- -CEM at different acceleration voltages ΔU_{acc} permits a comparison of the observed efficiencies with the theoretical efficiency response of a CEM detector as introduced in chapter 2, and to the literature. In combination with the determined impact position of section 5.5, it further admits to recalibrate the measured efficiencies $\eta_{i,e}(\Delta U_{\text{acc}})$ according to the kinetic energy E_{kin} of the incident particle at primary impact in the CEM surface. Consequently, this allows an explicit comparison of the observed efficiencies $\eta_{i,e}(E_{\text{kin}})$ with the reduced yield curve model of section 2.4.

In section 5.5, the spatial dependency of the detection efficiency $\eta_{i,e}(x, y)$ and the relative flight time differences $\Delta t(x, y)$ in the $x - y$ plane at a particular z -position in between the CEMs is investigated. From the efficiency response $\eta_{i,e}(x, y)$ at different z -positions, the sensitive volume $V_c(x, y; z)$ of the detection system out of which particles can efficiently be detected by both CEMs is estimated. The simultaneous observation of the flight time differences $\Delta t(x, y)$ from the individual correlation peaks at each scan position further admit to determine the particular impact position of the ^{87}Rb -ions in the ion-CEM detector. From this, the explicit properties at primary particle impact $\delta_0(E_{\text{kin}}, \theta)$ can be derived, allowing a direct comparison with obtained secondary emission yield values δ_0 at isolated CEM surface samples in the literature (see section 5.4). The small temporal spread of the relative flight time differences $\Delta t(x, y)$ from the correlation peaks additionally indicate that almost the same impact position in the CEM is hit repetitively, leaving the imaging of the ionisation fragments with the CEM detection system remarkably stable, accurate, and reproducible.

Consequently, the CEM detection system of this thesis resembles a robust testing ground for the application of the cascaded dynode detector model of chapter 2 onto continuous channel electron multipliers. In particular the latter finding is not only important for the actual optimisation of the quantum yield η_{detector} of a particular CEM detector according to the key parameters E_{kin} and θ (see section 2.4). From a more general point of view, the

calibration measurements and the cascaded dynode detector theory will also allow to estimate² the detection efficiency $\eta_{\text{det}}(E_{\text{kin}}, \theta)$ for future CEM detectors, and for any detection systems based on such detectors.

Parts of this chapter are published in: “Highly efficient state-selective submicrosecond photoionization detection of single atoms”, F. Henkel, M. Krug, J. Hofmann, W. Rosenfeld, M. Weber, and H. Weinfurter, *Physical Review Letters* **105**, 253001 (2010).

5.1. Detector efficiency calibration and absolute detection efficiency

The crucial parameter for many applications of charged particle detectors as CEMs is a high detection efficiency. In particular, the calibration of these detectors to absolute values becomes important if single particle resolution and the efficient subsequent detection of the single particles are required [18, 21, 220, 221]. In contrast to detection efficiencies of *relative* calibration measurements, absolute detection efficiencies are determined by coincident detection of correlated³ particle pairs (or more). The correlation of the particles introduces an additional degree of freedom in the calibration of a detection system which allows to derive the absolute detection efficiency η_{det} of the system (see subsection 2.4.1). Remarkably, the absolute calibration of two detectors via correlated pairs therefore provides an efficiency measurement method that is not encumbered by errors commonly associated with conventional relative calibration techniques. In this calibration method, the accuracy also depends on individual system-specific parameters as the intensity of the charged particle beam source (i.e., an electron/ion beam), the particular collection efficiency η_{col} of the calibration system, or the specific quantum yield of the reference detector (fig. 5.1(a)). The calibration of a detection system to absolute values is therefore superior to any conventional relative efficiency calibration. Moreover, it even enables a continuous on-line monitoring of the efficiency in the system [220]. Even more, the efficiency calibration of CEM detectors to absolute values represents an important criterion for the future usage of the joint CEM detection system as an atomic readout in the context of a loophole-free Bell test [18]. Accordingly, this leaves the implementation of an absolute calibration method via correlated particle pairs a key ingredient for the particle detection system of this thesis.

In the context of this thesis, the calibration of the corresponding detectors to absolute detection efficiencies is strongly embedded in the concept of photoionisation detection of single neutral atoms introduced in chapter 4. Here, the required correlated particle pairs are generated by photoionisation of single neutral atoms within the overlap of two laser beams (fig. 5.1(b)). The generated pair of oppositely charged photoionisation fragments ($^{87}\text{Rb}^+, e^-$) is then separated and subsequently counted in coincidence with two individual CEM detectors (see section 4.5). From the obtained single counts $N_{i,e}$ and the coincident counts N_c , the CEM detectors are calibrated to absolute values. Such a calibration is in perfect conceptual correspondence to $4\pi\beta\gamma$ -coincidence counting in nuclear physics [222, 223], or to absolute photodetector calibration via correlated photon pairs [224–228].

²Assuming that the primary particle impact position and the corresponding parameters (E_{kin}, θ) at impact can be to some extent derived from, e.g., the spatial geometry and the imaging properties of the specific imaging system.

³Correlated in the sense that the particles share a common initial incidence or property (e.g., radioactive decay of a parent particle or correlated photon pairs from a downconversion process).

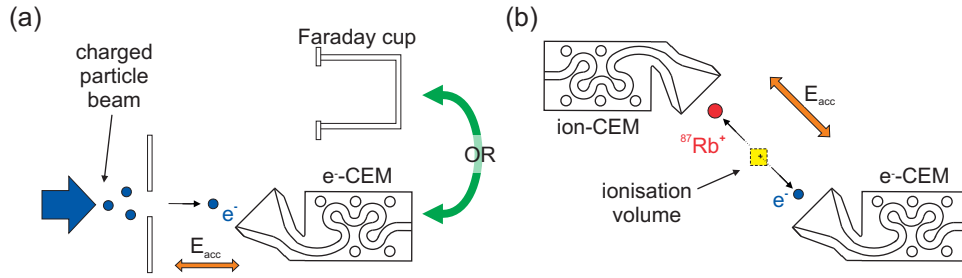


Figure 5.1: Concept of determining absolute detector efficiencies η_{det} via coincident detection of correlated particle pairs. (a) Conventional relative calibration of a CEM detector using a pre-calibrated beam source and a reference detector. (b) Absolute detector calibration via coincident counting of correlated particle pairs with two CEM detectors. The correlated pairs are generated by photoionisation of neutral atoms in a spatially defined ionisation volume.

Historically, the concept of counting coincident events from a common initial incidence is mentioned comparably early in the literature of the last century [222, 229]. In fact, coincident counting of correlated particle pairs has been performed already before and at the beginning of CEM usage as charged particle detectors (electron pairs; [230]). Nevertheless, from a detector efficiency point of view, even until today an *in-situ* calibration of charged particle detectors to absolute values using correlations is only sparsely mentioned in the literature [179, 180, 182, 231–233]. Astonishingly, the absolute calibration method still seems to lack a reliable, deterministic, spatially defined source for correlated charged particles, although several source approaches have been studied (thin foil [230], photoionisation of neutral atoms out of thermal beam [177, 180, 181], by synchrotron radiation [231, 232], out of the background vapour in an optical cavity [182], or breakup of diatomic molecular ions [233]). As a possible experimental solution, the photoionisation of neutral atoms within the overlap volume of two laser beams turns out to provide all the integral properties and prerequisites for such a source (see subsection 5.1.3).

In the following section, first the conventional relative efficiency calibration of an unknown detector is summarised. Further, some disadvantages of the relative calibration method itself are highlighted, in particular those relevant for the calibration of a detector to a few or even single particle efficiencies as required in the context of this thesis. Then, the absolute calibration method of the CEM detection efficiency via counting coincidences of correlated particle pairs is introduced. From the two absolute detection efficiencies $\eta_{\text{det}} = \eta_{i,e}$ of the single photoionisation fragments in the respective CEM detectors (see section 5.4), the total detection efficiency η_{atom} is derived to detect a single neutral atom by means of photoionisation detection (see section 4.1). Finally, the photoionisation process itself is further investigated in the aspect of providing a reliable source of correlated charged particle pairs for the calibration of any charged particle detectors with low particle flux ($n_0 \sim 1 - 1000 \text{ s}^{-1}$).

5.1.1. Conventional, relative detection efficiency

The detection efficiency η_{rel} of charged particle detectors is conventionally determined with a collimated beam of charged particles and using a second precalibrated detector as reference device [161]. In the experiments, commonly used reference devices are Faraday cups or similar particle/current detectors (fig. 5.1(a)). In pulse counting mode, the detection efficiency η_{cal}

for the precalibrated reference detector is defined by the corresponding measured counts as

$$\eta_{\text{cal}} = N_{\text{cal}}/N_0 \quad (5.1)$$

where N_0 is the actual number⁴ of particles (ions, electrons) in the calibration beam, and N_{cal} is the number of particles measured by the reference detector. The detection efficiency η_{rel} of the unknown device to be calibrated is then defined, accordingly,

$$\eta_{\text{rel}} = N_{\text{rel}}/N_0 \quad (5.2)$$

where N_{rel} is the detected number of incident particles with the uncalibrated detector. In the calibration measurement, the detection efficiency η_{rel} is obtained by a relative comparison of the measured counts N_{rel} at the uncalibrated detector to the counts N_{cal} of the precalibrated detector (fig. 5.1(a)). The detection efficiency from a *relative* calibration therefore reads:

$$\eta_{\text{rel}} = \eta_{\text{cal}} N_{\text{rel}}/N_{\text{cal}}. \quad (5.3)$$

According to eq. 5.3, the obtained detection efficiency η_{rel} is thus still dependent on the individual detection efficiency η_{cal} of the precalibrated reference detector. As the used reference detector has generally assumed to be imperfect ($\eta_{\text{cal}} < 1$), this calibration technique intrinsically yields only a *relative* detection efficiency of the unknown detector to the precalibrated one. It thus does not yield an absolute detection efficiency. Moreover, the calibrated detection efficiencies η_{rel} and η_{cal} will additionally include systematic errors of the individual detection system. Such possible error sources are, for example, the explicit spatial geometry of the calibration system which likewise affects the collection efficiency η_{col} of the particular system. Moreover, these factors will additionally vary between different calibration setups. From a calibration point of view therefore, especially the influence of the particular system geometry seems to be responsible for the partially huge discrepancies measured by many different calibration attempts for identical detectors (see subsection 2.4.2).

Efficiency calibration for few particle detections

For the detection efficiency of single particle incidences, usually the determined efficiencies obtained for macroscopic pulse rates ($n_0 > 10^4 \text{ s}^{-1}$) are scaled down to single particle efficiencies [47, 96, 161, 180]. However, from a sensitivity point of view, the simple downscaling of the detection efficiency of a calibrated detector is conceptionally difficult. This follows as the efficiency response of a detector obtained from the calibration measurements for high count rates ($n_{i,e} > 10^4 - 10^5 \text{ s}^{-1}$) is *not* identical to the response of the detector for low count rates ($n_{i,e} = 1 - 10 \text{ s}^{-1}$). For example, in the case of CEMs a different detector gain G_0 is observed for high count rates compared to low count rates (see subsection 3.2.2), significantly affecting the subsequent pulse discrimination for a fixed discriminator level, the subsequent pulse counting and thus the obtained efficiency response of the CEM.

Although the relative detector calibration method illustrated in eq. 5.3 appears to be straightforward, it is not perfectly appropriate to determine few or single particle detection efficiencies of a given detector. In fact, already the precalibration of the number of particles N_0 in the calibrated beam (eq. 5.1) with the reference detector will become difficult for low

⁴The particle current $I_{\text{beam}} = \vec{j} \cdot \vec{A}$ in the beam at the detector entrance is generally assumed to be constant for the duration of the calibration measurements.

count rates. This is a result of the required low intensities of the particle beam yielding the intended, few particle incidences per second. In analogue mode⁵, the lowest ion currents detectable by an electrometer are in the range of $I_{\text{beam}} < 10^{-12}$ A with particle rates of $n_0 \sim 10^4 \text{ s}^{-1}$ [161, 180]. However, an *accurate* current calibration⁶ of an incident particle beam with a Faraday cup usually demands beam current values corresponding to count rates of $n_0 > 10^6 \text{ s}^{-1}$ [105]. This follows as for the measurement of low currents, the influence of electronic noise, parasitary cable induction, or leak currents in the measurement setup becomes macroscopic at low values [161]. In contrast to that, typical count rates for single particle detection applications are in the range of 1 – 1000 counts s^{-1} , being up to six orders of magnitude lower than the lowest detectable current limit. Therefore, for a particle beam with such a low intensity, already the precalibration of the incident beam will introduce a significant error in the detection efficiency due to the uncertainty of the number of particles N_0 in the beam. In consequence, detection efficiencies for a few particle detections or even single particle efficiencies are generally difficult to determine with conventional beam sources and calibration methods. As a result, an absolute detector calibration method has to be employed (fig. 5.1).

5.1.2. Absolute detection efficiency via counting coincidences

For an absolute detection efficiency calibration, the CEM detectors of this thesis are calibrated with correlated particle pairs from photoionisation of neutral atoms in a defined overlap volume in between the CEMs (fig. 5.1(b)). The absolute efficiencies $\eta_{\text{det}} = \eta_{i,e}$ of the ion and e^- -CEM detector, as defined in section 2.4, are given by the single detector counts $N_{i,e}$ and the coincident counts N_c . Note that the single counts for each CEM detector still correspond to eq. 5.2

$$\eta_{i,e} = N_{i,e}/N_0,$$

whereas in this context, the value N_0 actually denotes the number of neutral atoms being photoionised, η_i and η_e are the detection efficiencies of the ion-CEM and the e^- -CEM, respectively, and $N_{i,e}$ is the number of ions (electrons) counted with the ion-CEM (e^- -CEM). The coincidences observed at both CEM detectors are defined as

$$N_c = \eta_i \eta_e N_0, \quad (5.4)$$

where N_c is the number of coincident events of the correlated photoelectron-photoion pairs within the coincidence time window Δt_c counted with both CEMs (see subsection 5.2.2). Accordingly, the CEM ion and e^- -detection efficiencies are given by [220, 223]

$$\eta_i = \frac{N'_c}{N'_e} = \frac{N_c - N_{\text{ac}}}{N_e - N_{\text{be}}}; \quad \eta_e = \frac{N'_c}{N'_i} = \frac{N_c - N_{\text{ac}}}{N_i - N_{\text{bi}}}, \quad (5.5)$$

where the corresponding single counts $N'_{i,e}$ are already represented by their background corrected values $N'_{i,e} = N_{i,e} - N_{\text{bi,be}}$. Similarly, accidental coincidences N_{ac} from uncor-

⁵Although eq. 5.1 states the explicit reference calibration in pulse counting mode, in most cases only the current equivalent I_{beam} of the particle number N_0 in a beam is measured.

⁶Specified for an observed current I_{beam} corresponding to a relative error in the particle number smaller than 0.2%.

related events in the chosen coincidence time window Δt_c are subtracted to gain the corrected⁷ coincident counts $N'_c = N_c - N_{ac}$. The errors of the detection efficiencies in eq. 5.5 are given by a single standard deviation $\Delta\eta_{i,e} = \sqrt{\sigma_{\eta_{i,e}}^2}$, with the corresponding variances $\sigma_{\eta_{i,e}}^2 = (N_c/N'_{e,i})^2(1/N_c - 1/N'_{e,i} + 2N_{be,bi}/N'^2_{e,i})$. Note that in the determination of the variances also the covariant dependency of the single counts $N'_{i,e}$ to the observed number of coincidences is included [221, 226, 234, 235] as the coincidences intrinsically depend on both single counts (i.e., $N_c = N_c(N'_i, N'_e)$).

Remarkably, the detector efficiencies in eq. 5.5 only depend on the two single counts $N'_{i,e}$ and the number of coincidences N'_c . In contrast to the relative calibration of eq. 5.3, neither the total number of photoionisation events N_0 nor any other observable (i.e., the detection efficiency $\eta_{i,e}$ of the second CEM detector in the system) enter the calibration of the single detector. Moreover, the method is also independent of the actual number of initial photoionisation events N_0 as long as at least some of the ionisation incidences are detected. As the method already includes both the collection efficiency η_{col} and the quantum yield $\eta_{detector}$ of the particular detector, absolute efficiency values for each CEM detector can be stated explicitly ($\eta_{det} = \eta_{i,e}$; see subsection 2.4.1).

Neutral atom detection efficiency

From the single CEM detector efficiencies η_i and η_e , a total efficiency can be determined for the detection of the initially neutral atom prior to photoionisation. As it is sufficient to detect either the photoion or the photoelectron of the ionised neutral atom [220], the neutral atom detection efficiency η_{atom} of the joint CEM detection system is

$$\eta_{atom} = 1 - (1 - \eta_i)(1 - \eta_e) = \eta_i + \eta_e - \eta_i\eta_e. \quad (5.6)$$

Note that the previous equation denotes only the total efficiency of the detection process and does not include the probability p_{ion} to photoionise the neutral atom prior to the detection [24].

5.1.3. Photoionisation as unique calibration pair source

Conceptually, the photoionisation of single neutral atoms out of the background vapour represents the experimental implementation of a defined charged particle pair source for detector calibration down to single particle efficiencies. This follows as the unique properties of the photoionisation enable genuine pair source operation compared to any conventional particle beam sources commonly used in calibration measurements. By using a resonant multiple-step, multiple-colour photoionisation scheme, the photoionisation process itself is highly selective in the aspect of spectroscopic selectivity and spatial resolution (see section 4.1). Moreover, assuming sufficient optical access, the ability to move and adjust the ionisation volume of the two laser beams yields an almost deliberate positioning and size⁸ of the photoionisation source in the calibration system. In contrast to conventional beam sources of a single particle

⁷However, within the chosen coincidence time window $\Delta t_c = 100$ ns of this thesis, accidental coincidences play an insignificant role (see section 5.2) and can therefore be neglected.

⁸As the ionisation volume is to the first order given by the $1/e^2$ -diameter of the ionising laser beam (see subsection 4.5.2), only the ionising beam diameter has to be adjusted in size accordingly.

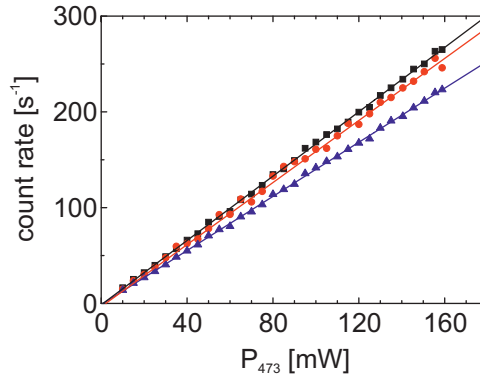


Figure 5.2: Background corrected count rates for ion and electron detections (black; red scatter), and coincidences (blue). The corresponding count rates n'_i, n'_e , and n'_c show the linearity of the photoionisation process at small laser powers P_{473} of the ionising transition ω_{2i} (see subsection 4.5.2) in the low particle flux regime ($n'_{i,e} = 10 - 300 \text{ s}^{-1}$). The straight lines yield linear fits of the count rates $n'_{i,e,c}(P_{473})$, accordingly.

type only, photoionisation further allows the simultaneous creation of single correlated particle pairs with opposite charge ($^{87}\text{Rb}^+, e^-$). For calibration measurements, either charged particle of the created pair can be used to determine the efficiency of the particle detector. In a two detector configuration, the subsequent detection of the correlated fragments allows to observe coincidences which will yield absolute detector efficiencies (see section 5.4).

Explicitly, there are two additional advantageous properties of a photoionisation particle pair source compared to conventional beam sources (e.g., collimated electron or ion beam out of an electron/ion gun [87, 88]). As a first advantage, the photoionisation source allows to create differently charged ionisation fragments with extremely small, well-defined kinetic energies within the ionisation volume of the two laser beams (fig. 4.1). More specific, the initial velocity and the corresponding velocity spread of the particle pair is insignificantly small compared to the kinetic energies and the velocity spread for charged particles out of a conventional particle beam source. This results as for a photoionisation of neutral atoms out of the residual vacuum background, the initial kinetic energy of the generated photoionised fragments are in the range of $E_{\text{kin}} = E_{\text{therm}} + E_{\text{excess}} \approx 60 \text{ meV}$ only (see subsection 4.4.3). In contrast to that, typical beam sources operate⁹ at minimum particle beam energies of $E_{\text{kin}} \sim 1 \text{ keV}$, even if the beam is precollimated and sufficiently calibrated. Conventional calibration beam sources therefore provide particles with an associated velocity spread which is four orders of magnitude larger than for a photoionisation source. From a calibration point of view, the generated photoionisation fragments can therefore be assumed to be approximately at rest. Consequently, the initial small kinetic energy together with its corresponding negligible *transversal* velocity spread will dramatically increase, e.g., the spatial resolution and accuracy for 2D-scan calibration measurements of the sensitive detection area and the spatial response of a charged particle detection system (see section 5.5).

The second main advantage of a photoionisation source is the generation of a linear, low particle flux down to single charged particles per second. This property is particularly important for the detector calibration down to few particle efficiencies (see subsection 5.1.1). In the

⁹See data sheets of common electron/ion gun suppliers, e.g., <http://www.kimballphysics.com/electron-gun-systems/comparison-charts>.

aspect of the stable generation of only a few charged particles per second, such an extremely low particle flux of $n_0 = 1 - 1000 \text{ s}^{-1}$ is generally difficult to obtain with any conventional beam sources (see subsection 5.1.1). In fig. 5.2, the detection of correlated particle pairs generated from photoionisation of neutral atoms out of the background vapour is shown (see section 4.5). In particular at small laser beam powers P_{473} of the ionising transition ω_{2i} (fig. 4.1) corresponding to observed count rates of $n'_{i,e} = 10 - 300 \text{ s}^{-1}$, the linearity of the particle generation according to the beam power is given (fig. 5.2). This leaves photoionisation as an exceptional alternative to conventional beam sources which are usually unable to provide reproducible count rates from $n_0 = 1 - 1000 \text{ s}^{-1}$.

In a more general context, the ability of a photoionisation source to generate single charged particles at a specific spatial position with a negligible initial kinetic energy allows to probe the electric field configuration $\vec{E}(x, y, z)$ of a given charged particle detection system with experimentally created, single test charges. This specifically enables, e.g., to test the imaging properties of the detection system via 2D or 3D-scan calibration measurements of the detector surface/entrance with single charged particles (see subsection 4.5.3). In the future, the use of pulsed laser sources with high pulse intensities will further enable to produce single charged particle pairs in the ionisation volume within a certain time window quasi on demand. However, for this triggered application, appropriate laser sources and corresponding beam powers have to be provided. Moreover, from a general spectroscopic and calibration point of view, the perfect future calibration source is represented by the integrated CEM detection system combined with the single atom dipole trap setup. This combined system will allow to deterministically create *one* charged particle pair at a deliberate point in time and at a particular spatial position by triggered photoionisation of the neutral atom in the single atom dipole trap.

5.2. Electron-ion correlation measurements

The photoionisation of neutral atoms in between the CEMs in a defined ionisation volume allows to observe correlated particle incidences at the two CEM detectors of the joint CEM detection system. This temporal correlation of the generated photoelectron-photoion pair results as the two ionisation fragments are generated from a common event, the photoionisation of a neutral atom in between the CEMs. On one hand, the photoelectron-ion correlation permits to observe the relative arrival time difference Δt of the two ionisation fragments in the corresponding CEM. On the other hand, the counting of these coincidences allows to calibrate both CEM detectors to absolute detection efficiencies by only measuring the corresponding number of single counts $N'_{i,e}$ and coincidences N_c at the two CEMs (see subsection 5.1.2).

The temporal correlation Δt of the two photoionisation fragments ($^{87}\text{Rb}^+, e^-$) therefore adds an additional degree of freedom to the calibration measurements of the CEM detectors compared to any conventional detector calibration methods. The measured arrival time difference Δt further allows to derive the flight times $t_{i,e}$ of the individual ionisation fragments in combination with the acceleration potential simulations and the flight time model of chapter 4. Moreover, the observed values of Δt at different acceleration potential differences ΔU_{acc} do not only enable a comparison to calculated flight times $t_{i,e}$ (see section 4.4), but also yield the particular impact position of the primary ^{87}Rb -ion in the ion-CEM (see section 5.5).

To experimentally observe coincidences from photoionisation with the CEMs, an adequate imaging of the photoionisation fragments in the corresponding CEMs has to be obtained

as a first step (see section 4.5). Once a sufficient sensitive detection area $A_c(x, y)$ for both CEM detectors is established, coincidence measurements can be performed. The calibration of a sufficient detection area for the joint CEM detection system of this thesis is described in section 4.5. Accordingly, in the following section the counting of the obtained coincident events with the CEM detection system is presented. To illustrate the characteristic temporal signature of the correlated photoion-electron pair, two sample single coincidence traces are shown as typically observed in a coincidence measurement. Outgoing from this, the observed incidences $N_{i,e}$ at the two CEMs of a measurement series are then arranged in an electron-ion correlation histogram. The correlation histogram enables to reveal the strong temporal correlation of the photoion-electron pairs according to their characteristic relative arrival time difference Δt in the corresponding CEMs. The characteristic signature of the photoionisation fragments becomes evident by a distinct correlation peak in the corresponding electron-ion correlation histogram at a particular relative arrival time difference Δt . Consequently, the integrated number of counts within the coincidence window Δt_c in the correlation histogram at the correlation peak yields the number of coincidences N_c for the CEM detector calibrations (see section 5.4). The number of accidental coincidences N_{ac} is obtained from the observed singles background count rates $n_{bi,be}$ of the respective background measurement without photoionisation, accordingly. In typical measurements, the accidental to true coincidence ratio is determined to be smaller than $N_{ac}/N_c < 10^{-5}$.

Finally, the increased background count rates n_{bi}, n_{be} caused by the incident laser radiation in the calibration measurements are investigated. The background counts in relation to the photoionisation counts (N_{bi}/N_i and N_{be}/N_e ; see subsection 5.1.2) become particularly important for the accuracy and the measurement duration of the efficiency calibration of the CEM detectors (see section 5.4), especially if scan measurements of the sensitive detection area $A_c(x, y)$ of the joint CEM detection system are intended (see section 5.5). For the elevated electron background of the e^- -CEM during laser operation, the photoeffect at adsorbed Rubidium on the UHV surfaces seems to be primarily responsible.

5.2.1. Single coincidence pulse trace

The temporal correlation of both ionisation fragments at the two CEMs represents one characteristic property of the photoionisation of neutral atoms in between the CEMs, allowing to temporally discriminate correlated photoionisation events (coincidences) from any accidental coincidences at the CEM detectors. In fig. 5.3, two sample oscilloscope traces of a typical photoionisation coincidence are displayed. For the acquisition of the traces in this sample, the oscilloscope is triggered on electron pulses in the e^- -CEM at $t = 0$ (red trace). As the characteristic temporal signature of a photoionisation coincidence in the CEMs, first the photoelectron is observed at the e^- -CEM. This results due to the much shorter flight time t_e of the photoelectron compared to the flight time t_i of the corresponding photoion (see section 4.4). Due to the much larger mass of the ion fragment, the subsequent ^{87}Rb -ion pulse follows significantly after the photoelectron pulse, but within a defined relative time difference Δt (fig. 5.3(b)). In correspondence to that, fig. 5.3(b) shows the definition of the experimentally observed photoion¹⁰ and photoelectron flight times t_i and t_e . Note that for the overall detection time of each individual ionisation fragment with the CEMs, the transit

¹⁰For illustration purposes, the ion-trace in fig. 5.3 is artificially shifted down by an offset of -20 mV.

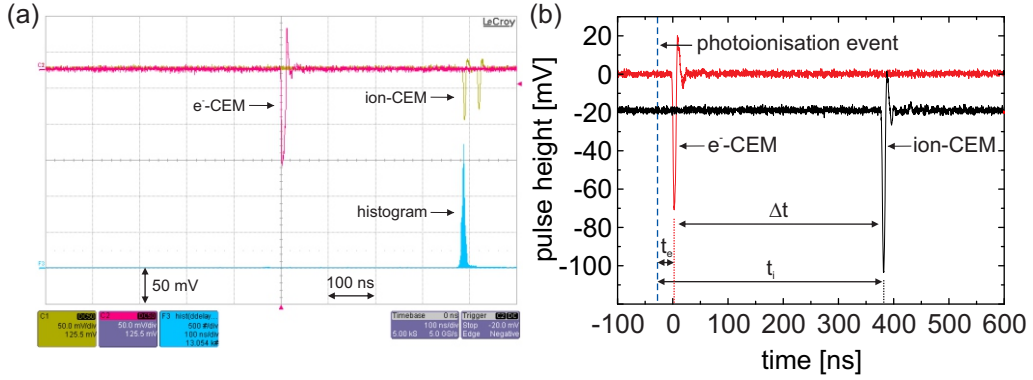


Figure 5.3: Sample traces of photoionisation coincidences at the CEM-detectors. (a) Single oscilloscope trace with the photoelectron incidence in the e^- -CEM (red trace) at $t = 0$ as trigger. The subsequent ion pulse in the ion-CEM (yellow trace) is observed after a defined time-of-flight difference Δt . The accumulated histogram of relative time-of-flight differences Δt from several electron-ion incidences is displayed by the blue trace. (b) Definition of the photoion and photoelectron flight times t_i and t_e . In the experiment, only the relative time difference Δt of the arrival times of both photoionisation fragments is accessible.

time t_{transit} of the electron avalanche in the corresponding CEM has to be added to the flight time (see subsection 4.4.2).

In the calibration measurements, only the relative arrival time difference $\Delta t = t_i - t_e$ of the two ionisation fragments is accessible. This results as the photoionisation depends on the presence of neutral atoms in the ionisation volume and on the individual power of the corresponding laser beams. For the calibration measurements of this chapter, the explicit point in time of a photoionisation event in the ionisation volume is thus random¹¹. However, the arrival time difference Δt of the two ionisation fragments for photoionisation coincidences in the CEMs is comparably well-defined and temporally narrow (see section 4.4). Out of the individual temporal arrivals of electrons and ions at the single CEM detectors, electron-ion correlation histograms can be generated (fig. 5.4). These histograms particularly enable to reveal the characteristic temporal signature of photoionisation coincidences.

5.2.2. Electron-ion correlation histograms

The electron-ion correlation histogram displays the relative time difference Δt until a subsequent ion pulse is detected in the opposite ion-CEM after observing an electron pulse in the e^- -CEM (fig. 5.3(b)). In fig. 5.4, a sample electron-ion correlation histogram of measured time differences Δt for an accelerating voltage of $\Delta U_{\text{acc}} = 3.8 \text{ kV}$ is shown¹². In the histogram, all electron arrivals are arranged to be situated at $t = 0$. The strong temporal correlation of the photoelectron-ion pair from the photoionisation of neutral atoms is displayed by the pronounced correlation peak at $\Delta t = 388.5 \text{ ns}$ in the correlation histogram. The correlation peak

¹¹ Assuming sufficient laser power for the ionisation transition ω_{2i} , the trapped neutral atom in the future combined setup will be photoionised within nanoseconds. Due to this triggered photoionisation of a quasi-resting single atom target, also the individual flight times $t_{i,e}$ can be observed.

¹² The single measurement in fig. 5.4 corresponds to a relative position of $(x = 1.2 \text{ mm}, y = -0.4 \text{ mm})$ in fig. 5.13 (see section 5.4).

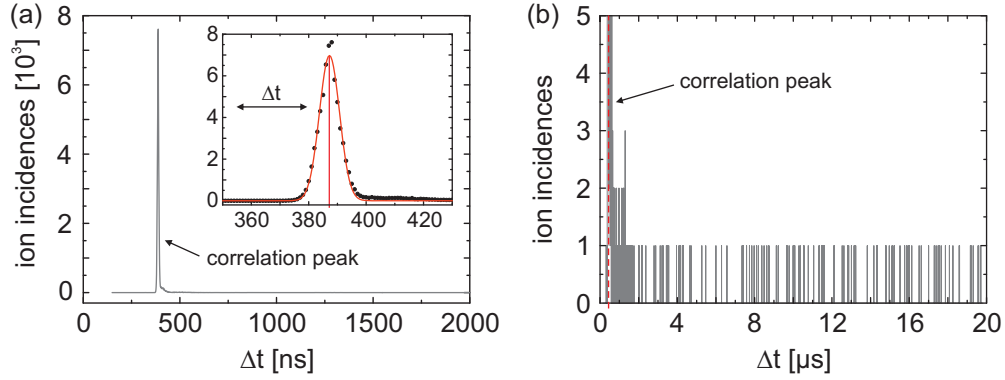


Figure 5.4: (a) Sample electron-ion correlation histogram of measured time differences Δt between electron and ^{87}Rb -ion detections (fig. 5.3(b)) for an accelerating voltage of $\Delta U_{\text{acc}} = 3.8 \text{ kV}$. The histogram displays a pronounced correlation peak from photoionisation at $\Delta t = 388.5 \text{ ns}$. Inset: Zoom of the correlation peak with Gaussian fit (red curve). (b) Baseline zoom of the histogram in (a), showing correlated ion counts from 0 – 5 and for relative arrival time differences Δt from 0 up to $20 \mu\text{s}$. Apart the correlation peak at $\Delta t = 388.5 \text{ ns}$ from photoionisation, no second correlation peak can be identified.

exhibits a Gaussian shape with a narrow temporal spread¹³ of $\Delta t_{\text{fwhm}} = 8.5 \text{ ns}$ (fig. 5.4(a), inset). The prominent correlation peak in the electron-ion correlation histogram represents a clear signature of the photoionisation of neutral atoms in the ionisation volume in between the CEMs. In contrast to that, without photoionisation¹⁴ only a flat baseline plateau of ion incidences without any correlation peak is observed in the corresponding correlation histogram. In this case, the electron-ion correlations are merely random distributed in the histogram, similar to the distribution of arrival times as depicted in fig. 5.4(b) for values of $\Delta t > 1 \mu\text{s}$.

Coincidence time window

The number of coincidences N_c from photoionisation of neutral atoms can be deduced from the electron-ion correlation histograms. Particularly, it is derived from the specific temporal position and shape of the correlation peak in the histograms. To determine the exact number of coincidences in contrast to any uncorrelated events (accidental coincidences, N_{ac}), first a fixed coincidence time window Δt_c has to be chosen. The integrated number of electron-ion correlations in the chosen window Δt_c reflects the total number of coincidences N_c (fig. 5.5). This number will be used to determine the absolute efficiency of the CEM detectors in the efficiency calibration measurements (see section 5.4).

For the photoionisation calibration measurements of this thesis, the coincidence time window Δt_c starts 20 ns before the center of the Gaussian correlation peak and ends 80 ns after it (fig. 5.5). The length of the coincidence time window is explicitly chosen to be $\Delta t_c = 100 \text{ ns}$. By temporal width, the time window thus encloses the entire photoionisation correlation peak together with an additional dead time window following the peak. This follows as the dead time of the discriminator unit of $t_{\text{wmt}} = 80 \text{ ns}$ prevents the CEMs from possible multiple

¹³The full width at half maximum Δt_{fwhm} of the Gaussian peak corresponds to a single standard deviation of $1\sigma = 3.6 \text{ ns}$.

¹⁴For example, photoionisation does not occur if only one of the two laser beam sources or even no laser beam is present in the glass cell (fig. 4.1), or with the dispenser sources turned off (see section 4.2).

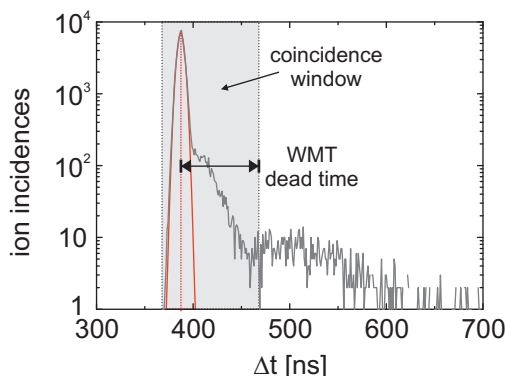


Figure 5.5: Zoom of the histogram in fig. 5.4(a), in logarithmic representation. Despite the fitted Gaussian correlation peak, some late ^{87}Rb -ion arrivals occur within the chosen coincidence window of $\Delta t_c = 100$ ns (shaded area). In comparison, the integral dead time (80 ns) of the used discriminator unit for single pulse counting is shown.

counting of single physical incidences in pulse counting mode caused by cable ringing or ion feedback at the end of the CEM detector (see section 3.4). The particular choice of the asymmetric, extended coincidence window Δt_c thus results from the presence of a few late ion detections (fig. 5.5; values from 400 – 600 ns) compared to the entirely random distributed background of accidental incidences (fig. 5.4(b); $\Delta t > 1 \mu\text{s}$). Independent measurements with *different* pulse processing circuitry show that these late ion detections are indeed physical incidences, and are not an artifact of any subsequent pulse processing electronics. Consequently, the coincidence time window has also to include some of these late ion counts¹⁵.

Measurement of correlated photoelectron-ion incidences and data acquisition

In the experiment, the single counts $N_{i,e}$ and the background counts $N_{\text{bi,be}}$ at the CEMs are measured alternating with 100 Hz. The single counts $N_{i,e}$ include the correlated events from photoionisation while the additional measurement of the background counts $N_{\text{bi,be}}$ without photoionisation allows a refined background correction. Experimentally, the measurement of the single and background counts is performed by switching¹⁶ the laser beam of the excitation transition ($\lambda_{12} = 780$ nm; fig. 4.1(a)) on and off by means of an acousto-optical modulator (AOM). In contrast to that, the laser beam of the ionising transition ($\lambda_{2i} = 473$ nm) is continuously operated during an entire measurement series.

For the pulse processing and data acquisition, the single ion and electron incidences at the CEMs are postprocessed in a custom-made timestamp unit [236], or with a digital storage oscilloscope¹⁷. Electron-ion correlation histograms are then generated from the data sets by cross-correlating the temporal arrivals of the individual electron and ion incidences. The

¹⁵Additionally, the independent measurements suggest that also the late ion detections *after* the coincidence window end at $\Delta t > 468.5$ ns are physical incidences (fig. 5.5). Theoretically, the chosen coincidence time window may therefore be extended even further, counting the full contribution of observed late ion arrivals (up to $\Delta t = 600$ ns). However, these physical incidences are not covered by the dead time $t_{\text{wmt}} = 80$ ns of the comparator unit anymore. As a conservative estimation therefore, only a coincidence time window of $\Delta t_c = 100$ ns up to $\Delta t = 468.5$ ns is chosen.

¹⁶The duration of a single measurement cycle is 10 ms. The red laser beam is thus turned on/off for an equal time period of 5 ms each per single cycle (fig. 5.6(a), inset).

¹⁷LeCroy, Waverunner 204Xi.

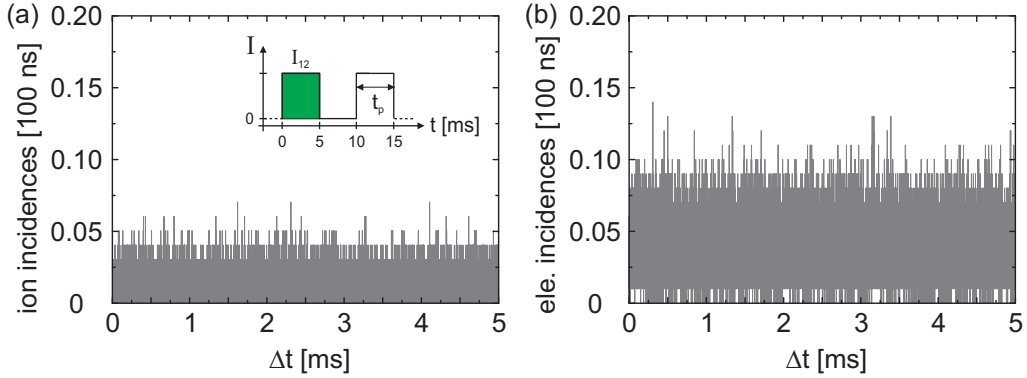


Figure 5.6: Trigger-ion correlations (a) and trigger-electron correlations (b) per 100 ns time bin. The histograms correlate the relative arrival time of ion and electron incidences relative to the trigger of the photoionisation pulse at $t = 0$ (inset, (a)). Within the entire photoionisation sequence ($\Delta t = 5$ ms; green box, inset), the arrival of the electron and ion incidences are merely stochastic at the respective CEM. Consequently, the photoionisation of neutral atoms out of the thermal background of the UHV occurs random during a photoionisation sequence.

number of coincidences N_c for the calibration measurements is thus subsequently determined from the correlation histograms generated with these devices. For the data acquisition however, in particular the timestamp unit represents an outstanding alternative as it additionally allows to assign each single electron or ion incidence an individual timetag corresponding to its arrival time at the respective CEM. This enables not only to cross-correlate individual electron-ion incidences, but to reconstruct the full temporal evolution of the observed counts $N_{i,e}$ and $N_{bi,be}$ during the entire measurement.

One should further note that the photoionisation of neutral atoms itself out of the thermal background in the UHV occurs completely stochastic within the photoionisation sequence of $t_p = 5$ ms during a single measurement cycle of 10 ms (fig. 5.6, inset). In fig. 5.6, the relative temporal arrival of ion and electron incidences for the photoionisation sequence ($\Delta t = t_p = 5$ ms; green box, inset) is depicted after switching the red laser on for photoionisation. The histograms of the relative arrivals for ions and electrons are shown for several accumulated photoionisation sequences of t_p . Neither for the ion or the electron incidences, any preferred relative arrival time for the incidences according to the switching on of the red laser beam (trigger at $\Delta t = 0$) can be identified. This leaves the photoionisation of neutral atoms out of the thermal background of the UHV temporally random during a photoionisation sequence.

5.2.3. Accidental coincidences

For the detector calibration to absolute efficiencies (eq. 5.5; subsection 5.1.2), the rate of accidental coincidences n_{ac} is obtained from the observed singles background count rates $n_{bi,be}$. Assuming Poissonian statistics of the background counts, the probability of a single background event to lie within the chosen coincidence time window of $\Delta t_c = 100$ ns is $p(n_{bi,be}) = \Delta t_c \cdot n_{bi,be}$. Accidental coincidences within this time window will therefore occur with a rate of $n_{ac} \sim \Delta t_c \cdot n_{bi} \cdot n_{be}$ (see, e.g., [18, 235]). Accordingly, for a typical coincidence measurement the rate of accidental coincidences from the background counts of the single CEM detectors is calculated to $n_{ac} = 0.0092 \text{ s}^{-1}$ (e.g., $\Delta U_{acc} = 3.8 \text{ kV}$, fig. 5.4; where $n_{bi} = 38 \text{ s}^{-1}$ and $n_{be} = 2464 \text{ s}^{-1}$), with single probabilities of $p(n_{bi}) = 3.7 \times 10^{-6}$ and

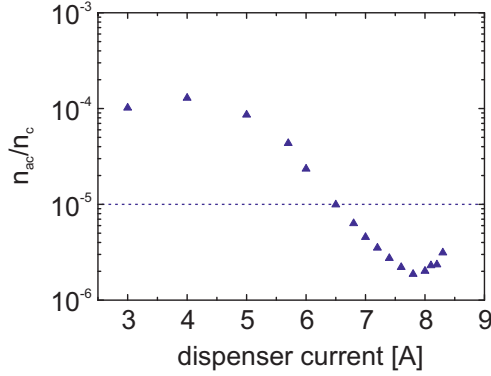


Figure 5.7: Relative ratio of accidental n_{ac} to true coincidences count rate n_c within the chosen coincidence time window of $\Delta t_c = 100$ ns. In the experiment, typical coincidence measurements as illustrated in fig. 5.8 yield a relative ratio of n_{ac}/n_c well below 10^{-5} (dashed line).

$p(n_{be}) = 2.5 \times 10^{-4}$. The observed rate of coincidences is $n_c = 752 \text{ s}^{-1}$. Consequently, the measured accidental to true coincidence ratio out of photoionisation within the coincidence time window of $\Delta t_c = 100$ ns is $n_{ac}/n_c = 1.22 \times 10^{-5}$. This order of magnitude is a commonly observed ratio for the joint CEM detection system (fig. 5.7). The number of accidental coincidences N_{ac} can thus generally be neglected for the CEM detector calibration of this thesis work (see section 5.4), yielding $N'_c = N_c$ (eq. 5.5; see subsection 5.1.2).

5.2.4. Analysis of background counts

The accuracy of the calibration of the CEM detectors to absolute efficiencies from the measured single counts $N_{i,e}$ and $N_{bi,be}$ at the corresponding detectors depends mainly on the single count to background ratios N_i/N_{bi} and N_e/N_{be} (see subsection 5.1.2). This follows as an elevated background $N_{bi,be}$ compared to a small signal $N_{i,e}$ will significantly affect the single counts $N'_{i,e}$ for detector calibration (eq. 5.5), and its associated errors $\Delta\eta_{i,e}$. In the following therefore, possible sources of an enhanced background in the CEM detectors albeit from intrinsic CEM detector based dark counts (see subsection 3.2.3) are analysed and discussed. This follows as particularly for a long term operation of the joint CEM detection system for a future loophole-free Bell test [18, 21], stable and reproducible background rates are an important criterion.

Typical background rates for the joint CEM detector

In the calibration measurements, a significant increase in the background counts of the CEM detectors is almost entirely caused by the blue laser radiation of the ionising laser beam (fig. 4.1). The single application of the red laser beam ($\lambda_{12} = 780$ nm) only with corresponding laser powers (see section 4.5) does not contribute to any increased background¹⁸. In contrast to that, already the sole presence of the blue laser beam ($\lambda_{2i} = 473$ nm) only significantly increases the background count rates, particularly the electron background rate. Accordingly, the rate n_{be} rises proportionally to an increase in laser intensity ($n_{be} \sim I_{2i}$) for the ionising transition. This effect is generally observed in several different calibration measurements.

¹⁸For an explicit definition of background counts $N_{bi,be}$ and dark counts $N_{di,de}$ at a CEM detector, see subsection 3.2.3.

For a typical coincidence measurement as illustrated in fig. 5.4 ($\Delta U_{\text{acc}} = 3.8 \text{ kV}$), the CEM detector based¹⁹ dark count rates $n_{\text{di,de}}$ are in the range of $n_{\text{di}} = 20 - 30 \text{ s}^{-1}$ for the ion-CEM, and $n_{\text{de}} = 250 - 350 \text{ s}^{-1}$ for the e^- -CEM. In contrast to that, the laser induced electron background rates n_{be} exceed the electron dark count rates n_{de} by more than an order of magnitude (i.e., $n_{\text{be}} = 2464 \text{ s}^{-1}$ compared to $n_{\text{de}} = 250 \text{ s}^{-1}$ in fig. 5.4). However, in relation to that the ion background rate n_{bi} compared to the ion-CEM dark count rate n_{di} remains almost unaffected ($n_{\text{bi}} = 38 \text{ s}^{-1}$ compared to $n_{\text{di}} = 35 \text{ s}^{-1}$).

Possible sources for background counts at the CEMs

For the detector efficiency calibration measurements, the continuous operation of the laser beams will become unfavourable, if the background count rates $n_{\text{bi,be}}$ induced by the ionising laser radiation ($\lambda_{2i} = 473 \text{ nm}$) are too high. Enhanced background rates result in prolonged measurement times for the system, and even in an eventual electrical breakdown of the detection system caused by the elevated charge background. Therefore in the following, some possible sources of background enhancement in the CEM detectors are discussed. However, an elevated detector background in the calibration efficiency measurements will not constrain the future application of the joint CEM system as single atom readout in the single atom trap. This results as the neutral ^{87}Rb -atom in the optical dipole trap will be photoionised by a pulsed readout scheme with both laser beams being blocked for most of the time during the experiment.

Primarily, an obvious source for enhanced background counts $N_{\text{bi,be}}$ in the CEM detectors will originate from photonic stray particles entering the CEMs. As the detectors have a non-vanishing detection efficiency for any photons in the visible and infrared spectrum (see subsection 2.4.2), additional background counts induced by stray light of the two laser beams ($\lambda_{12}, \lambda_{2i}$) will be observed. However, this possible source can mainly be excluded as possible source for the enhanced detector background. This follows as if one interchanges both CEM detectors, using the previously used ion-CEM as e^- -CEM and vice versa, again only the electron background rate N_{be} now at the 'new' e^- -CEM significantly increases, while the ion-CEM shows comparable rates to the previous CEM detector configuration.

A second source of background will possibly stem from photoelectric emission of ambient surfaces next to the CEM detectors in the UHV induced by stray photons from the two laser beams. Even more, the photoelectric emission will further particularly explain the increased electron background for the ionising laser light (λ_{2i}) in contrast to the non-significant increase in the ion-CEM background. Generally, photoelectric emission sets in at a threshold energy $E_{\text{th}} \sim \Phi$ of the specific surface, with Φ being the electron work function of the corresponding bulk material. However, only the work function of alkali²⁰ metals exceed the single photon energy ($E_{12} = \hbar\omega_{12} = 1.59 \text{ eV}$, $E_{2i} = \hbar\omega_{2i} = 2.62 \text{ eV}$) of the two laser transitions used in the calibration experiments of this thesis (e.g., Rubidium: $\Phi_{\text{Rb}} \sim 2.26 \text{ eV}$). The work function of all other elements lies significantly beyond the single photon energy (e.g., Copper: $\Phi_{\text{Cu}} \sim 4.53 - 5.10 \text{ eV}$). Consequently, photoelectrons will thus only be emitted from Rubidium²¹ doped or coated surfaces in the UHV, caused by the increased Rubidium background vapour from the dispenser sources (see section 4.2).

¹⁹Assuming all laser beams are blocked with no light in the glass cell setup.

²⁰The values for the electron work function of alkali metals range from $\Phi_{\text{Cs}} \sim 2.14 \text{ eV}$ to $\Phi_{\text{Li}} \sim 2.93 \text{ eV}$ [237].

²¹Other alkali metals are not macroscopically present in the UHV of the glass cell system.

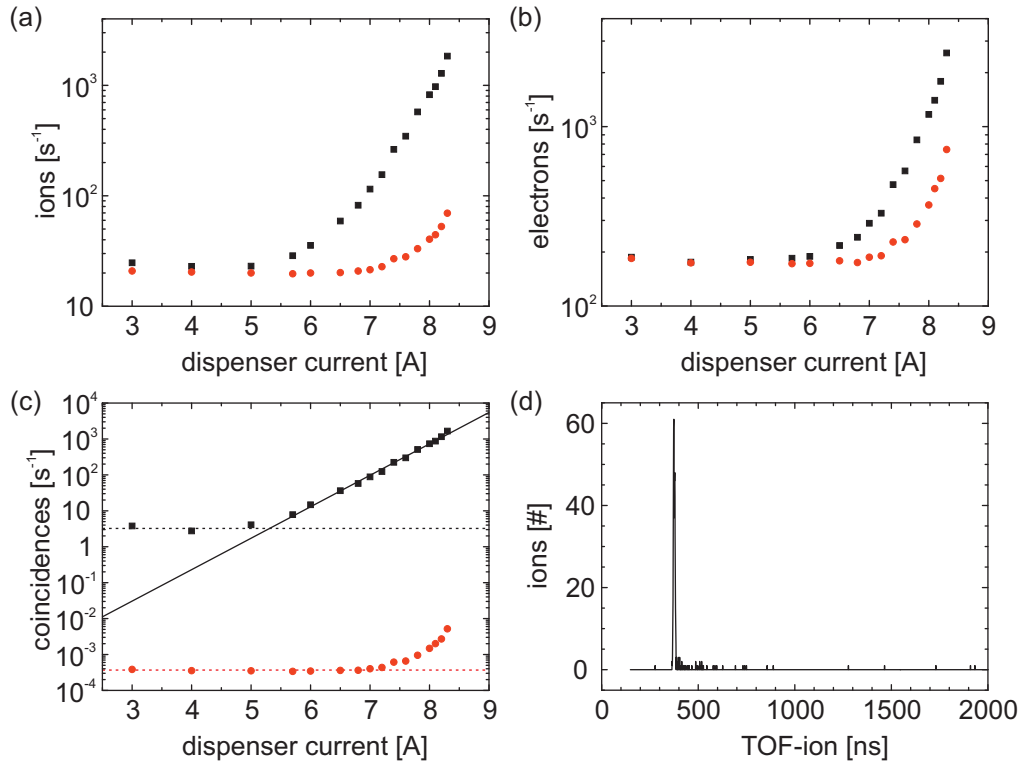


Figure 5.8: Measured count rates per second for various dispenser currents at one particular relative position ($x = 1.2$ mm, $y = -0.4$ mm; fig. 5.13). In the figures (a-c), the values are displayed for measurements with the count rates n_i (black scatter) and background count rates n_{bi} (red) for ions (a), for electrons (n_e, n_{be} ; (b)), and true/accidental coincidences (n_c, n_{ac} ; (c)). (d) Correlation histogram of measured time differences Δt similar to fig. 5.4(a), but at a dispenser current of $I = 3$ A (see values in (a-c)). Although the partial ^{87}Rb -background pressure is vanishingly low at these currents ($< 10^{-10}$ mbar), still a distinct photoelectron-ion correlation peak can be identified in the correlation histogram, demonstrating the spectroscopic sensitivity of the photoionisation detection method [176].

A third source for an increased CEM background is certainly related to outgassed volatile impurities out of the dispenser source which are emitted during dispenser operation. These outgassed impurities will either already be charged due to the thermal emission or will be subsequently photoionised in combination with the two laser beams of the calibration measurements, producing an enhanced charged particle background in the UHV. Referring to outgassed impurities without the presence of any laser radiation in the UHV, an increase in the background count rate of a CEM detector by enhanced degassing of impurities out of a dispenser source is experimentally observed by [164]. Nevertheless, the measurements show that a relevant increase in CEM detector background only starts at considerable higher pressures of $p > 10^{-6}$ mbar. In the aspect of photoionisation of outgassed dispenser impurities in the UHV, in fig. 5.8 the count rates and background rates for ^{87}Rb -ions (n_i (black), n_{bi} (red); fig. 5.8(a)), electrons (n_e , n_{be} ; fig. 5.8(b)), and the coincidences to accidental coincidences (n_c , n_{ac} ; fig. 5.8(c)) for various applied dispenser currents I are depicted. The measurements are performed at one particular relative position ($x = 1.2$ mm, $y = -0.4$ mm; fig. 5.13) with identical CEM operation parameters as used in fig. 5.4, while only altering the current I of the dispenser source. For high currents, an increased background is observed, although the residual background pressure in the UHV chamber remains still low ($p < 7.8 \times 10^{-9}$ mbar at $I = 8.3$ A). However, the background increase occurs simultaneously in both background count rates n_{bi} , n_{be} (red traces; fig. 5.8(a,b)), also excluding this as possible source for an enhanced CEM detector background in the e^- -CEM only.

For the particular detection scheme of this thesis (see section 4.1), photoionisation of atoms or molecules from the residual vapour background of the UHV is in general comparably unlikely as possible source for an increased stray charge background in the CEMs. For single photon transitions to the continuum, the ionisation threshold of any neutral atom²² is too large compared to the single photon energy ($\hbar\omega_{12} = 1.59$ eV, $\hbar\omega_{2i} = 2.62$ eV) of the used laser transitions. Moreover, also the photoionisation due to multi-photon transitions is extremely unlikely at the laser beam intensities used in the experiments (see section 4.1). Furthermore, photoionisation will always affect both background count rates in the CEMs, the ion *and* the electron background, as it generates charged particle pairs. Therefore, atomic/molecular photoionisation out of the residual background is also not responsible for an enhanced electron background in the e^- -CEM, too. This leaves the photoelectric emission from ambient surfaces in the UHV coated or doped with ^{87}Rb -atoms as possible source of the increased background count rate. However, an additional bakeout of the entire UHV system (see section 4.2) should in this case substantially reduce the elevated CEM detector background.

5.3. Photoionisation fragment detection time

In the following section, the measured arrival time differences Δt of ^{87}Rb -ions to their corresponding photoelectrons are investigated. The observed time differences are compared to the theoretical flight time model introduced in subsection 4.4. The model shows a good agreement with the measured data for acceleration voltage differences $\Delta U_{\text{acc}} > 1.6$ kV. It further allows to calculate individual detection times $t_{i,e}$ for the two photoionisation fragments. From the individual flight times $t_{i,e}$, the neutral atom detection time t_{det} of the CEM detection system is derived. In particular this detection time t_{det} is important for the application of the system

²²Rubidium yields the third lowest ionisation threshold of all elements; below that are only Francium ($E_{\text{thres}}[\text{Fr}] = 4.0727$ eV), and Cesium ($E_{\text{thres}}[\text{Cs}] = 3.8939$ eV).

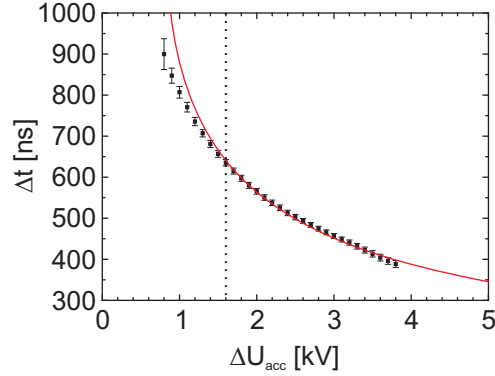


Figure 5.9: Measured relative arrival time differences Δt of ^{87}Rb -ions to their corresponding photoelectrons for different acceleration voltage differences ΔU_{acc} between the CEMs. The individual time difference Δt at a particular value of ΔU_{acc} is derived from a Gaussian fit of the correlation peak from photoionisation in the corresponding correlation histogram (e.g., $\Delta U_{\text{acc}} = 3.8$ kV; fig. 5.4). The error bars represent the full width at half maximum value Δt_{fwhm} from each Gaussian fit (fig. 5.4(a), inset). For acceleration voltage values $\Delta U_{\text{acc}} > 1.6$ kV, a least-squared fit with the model of subsection 4.4.1 is employed (red line).

as a fast and efficient neutral atom detector. Moreover, it turns out that the obtained detection time t_{det} with the CEM detection system is remarkably fast compared to any competing single atom readout system, if one assumes similar detection efficiencies for these systems.

5.3.1. Photoelectron-ion arrival time difference Δt

In fig. 5.9, the measured time differences Δt of generated ^{87}Rb -ions to their corresponding photoelectrons for different acceleration voltage differences ΔU_{acc} are displayed (see section 4.3). The measurements are performed at one particular point of the sensitive detection area $A_c(x, y)$, at a relative position of $(x = 1.2 \text{ mm}, y = -0.4 \text{ mm})$ in fig. 5.13 (see section 5.5). The individual time differences Δt at each value of ΔU_{acc} in fig. 5.9 are derived from a Gaussian fit of the corresponding time difference histogram²³. The error bars represent the full width at half maximum value Δt_{fwhm} from each Gaussian fit (fig. 5.4(a), inset). The associated single standard deviation (1σ) of the Gaussian fit is thus smaller by a factor of $2\sqrt{2\ln 2} \sim 2.3548$. The temporal spread of the individual correlation peaks (Gaussian histogram fits) remains extremely narrow for a wide range of acceleration voltages ΔU_{acc} , with a fitted full width at half maximum of $t_{\text{fwhm}} < 8.5$ ns for values of $\Delta U_{\text{acc}} > 1.6$ kV. Note that the center position Δt of the Gaussian fit in all these measurements can be determined with a relative accuracy of smaller than 10^{-5} (e.g., $\Delta t = 388.5 \pm 0.01$ ns for $\Delta U_{\text{acc}} = 3.8$ kV as in fig. 5.4(a), inset).

The time-of-flight model from subsection 4.4.1 holds for acceleration voltage differences $U_{\text{acc}} > 1.6$ kV (red line, fig. 5.9), below this value the actual field configurations between and inside the CEMs have to be taken into account in more detail (see subsection 4.3.4). In fig. 5.9, the boarder between the two ranges is marked by a dashed line. In particular, the imaging of the particle in the CEM until primary particle impact will substantially vary as the internal CEM fields become comparable to the external applied acceleration voltages.

²³For example, the respective electron-ion correlation histogram at $\Delta U_{\text{acc}} = 3.8$ kV is explicitly displayed in fig. 5.4.

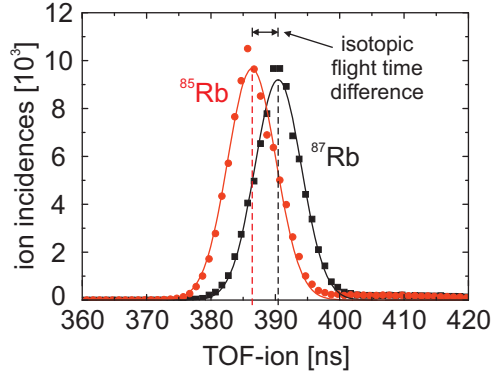


Figure 5.10: Observed relative arrival time differences Δt for the two isotopes, ^{87}Rb (black square) and ^{85}Rb (red circle). In the measurements, the spatial position of the ionisation center in between the CEMs and the laser beam parameters are identical. The Gaussian fits to the correlation peaks from photoionisation shows a relative difference in ion flight time ($t_i(^{87}\text{Rb}) - t_i(^{85}\text{Rb})$). The difference is caused by the different mass ($m_{85\text{Rb}}, m_{87\text{Rb}}$) of the two isotopes and is in agreement with the calculated values from the time-of-flight model (see subsection 4.4.1).

This results as for small voltage differences ΔU_{acc} and a ^{87}Rb -ion impact deep in the channel section ($d_{i,e} > 10$ mm), the internal CEM fields $E_{i,e} = \Delta U_{i,e}/d_{i,e}$ yield the same magnitude as the external acceleration field $E_{\text{acc}} = \Delta U_{\text{acc}}/d$ (fig. 4.11(d); see subsection 4.3.4).

For acceleration voltage differences $\Delta U_{\text{acc}} > 1.6$ kV, the fitted average distance d_i covered in the CEM is $d_i = 10.92 \pm 0.05$ mm. This average distance is determined from a least-squared fit with eq. 4.5 (see section 4.4), while the uncertainty of the fit translates into the ^{87}Rb -ion impact position uncertainty as stated by the previous expression. Moreover, the fit from the flight time model in section 4.4 and the observed relative flight time differences $\Delta t(\Delta U_{\text{acc}})$ are in good agreement. However, the fit generally assumes that the same impact position in the CEM is hit repetitively for all different acceleration voltages $\Delta U_{\text{acc}} > 1.6$ kV. In contrast to that, the deviations of the flight time model to the observed values for acceleration voltages $\Delta U_{\text{acc}} < 1.6$ kV will be caused by a slightly different impact position of the ^{87}Rb -ions in the ion-CEM. This results as at these acceleration voltages, the repulsive internal CEM gain field E_i will start to significantly decelerate and thus to deflect the incident ^{87}Rb -ions earlier at the CEM channel wall. This will lead to shorter ion flight times t_i , and thus to shorter arrival time differences Δt as observed in fig. 5.9.

Together with the saddle point distance²⁴ of d_{saddle} , the distance $d_{\text{iCEM}} = d_i + d_{\text{saddle}} = 12.22$ mm corresponds to a primary ^{87}Rb -ion impact position deep in the channel section (fig. 4.4) of the CEM detector (compare to subsection 5.5.3). Note that for comparably high acceleration voltage differences $\Delta U_{\text{acc}} > 10$ kV, the relative arrival time difference Δt follows approximately a $\Delta U_{\text{acc}}^{-1/2}$ -dependency ($\Delta t \sim t_i$) as derived from eq. 4.5.

Isotopic time-of-flight difference

To further test the accuracy of the time-of-flight model, flight time measurements similar to section 5.2 are performed, although this time using the ^{85}Rb -isotope²⁵. The different isotope will not only demonstrate the spectroscopic and thus isotopic selectivity of the photoionisation detection scheme (see section 4.1), but also reveal the properties of the joint CEM detection system as fast, selective and efficient mass spectrometer. In fig. 5.10, the measurement of the relative arrival time differences Δt for the two isotopes ^{87}Rb (black square) and ^{85}Rb (red circle) at $\Delta U_{\text{acc}} = 3.8\text{ kV}$ are depicted. In the measurements, all experimental parameters (e.g., relative spatial position of the ionisation center in between the CEMs, laser beam parameters) are identical. Even more, only the resonant excitation transition λ_{12} is detuned (fig. 4.1(b)) to either resonantly excite the ^{87}Rb - or ^{85}Rb -isotope selectively. The Gaussian fits of the both correlation peaks for the ^{87}Rb - and ^{85}Rb -isotope yield a relative difference in ion flight time ($t_i(^{87}\text{Rb}) - t_i(^{85}\text{Rb})$) for the two isotopes (fig. 5.10). The relative isotopic difference of $4.09 \pm 0.01\text{ ns}$ from the center of the Gaussian fits agrees with the calculated values of the time-of-flight model according to eq. 4.5 ($\Delta t_{85-87} = 4.54\text{ ns}$).

To explicitly resolve the single peaks of the different isotopes and therefore of single particle incidences according to their mass, the relative isotopic difference Δt_{85-87} is too small. However, already for species with element masses heavier than 98 amu (i.e., Technetium) and lighter than 76 amu (i.e., Selenium), the respective correlation peaks will be temporally separated by $\Delta t_{87-98,87-76} \approx 25\text{ ns}$. The latter value corresponds to three $t_{\text{fwhm}} = (3 \times 8.5)\text{ ns}$ of the expected full width at half maximum value (fig. 5.9), while the ion flight times are calculated using eq. 4.5.

The high temporal resolution for particles of different mass makes this setup therefore an ideal system to investigate mixtures of samples of different species with high efficiency and even hyperfine-state selectively (see section 5.1), within detection times under a microsecond. Note that the temporal resolution of the individual flight time of any two isotopes or atomic species is of particular interest, if homonuclear or even heteronuclear mixtures are subject of investigation and subsequent detection (e.g., for the site specific readout of ultracold heteronuclear molecules at one particular lattice site in optical lattices [238–240]).

5.3.2. Neutral atom detection time

For the application of a fast and efficient neutral atom detector for a future loophole-free Bell test [18], the detection time of a single neutral atom in the CEM detection system is investigated. At $\Delta U_{\text{acc}} = 3.8\text{ kV}$, we observe a time-of-flight difference of $\Delta t = 388.51 \pm 0.01\text{ ns}$ (fig. 5.4(a), inset). According to the time-of-flight model of subsection 4.4.1, we obtain a calculated photoelectron flight time of $t_e = 0.95\text{ ns}$ for this acceleration voltage. Together with the CEM transit time $t_{\text{transit}} = 26\text{ ns}$ (see appendix A.3), this sums up to a detection time of $t_{\text{det}} = 415.5\text{ ns}$ for the neutral atom (see subsection 4.4.2).

²⁴See subsection 4.4.1 for the definition of the covered distance d_{CEM} until primary impact in the CEM according to the refined model.

²⁵The dispenser source emits Rb-atoms corresponding to the natural abundance of the species ($^{87}\text{Rb} = 27.83\%$; $^{85}\text{Rb} = 72.17\%$).

5.4. Absolute detection efficiencies

The following section describes and analyzes the measurements of the absolute CEM efficiencies of the two CEM detectors in the joint CEM detection system. The absolute efficiencies are obtained from coincident counting of correlated charged particle pairs as introduced in section 5.1. The correlated pairs are generated from photoionisation of neutral atoms within the ionisation volume at $z = d/2$ in between the CEMs (see section 4.5). The absolute detection efficiencies η_i and η_e of the single CEM detectors are subsequently calculated from the accumulated photoionisation counts $N_{i,e}$, the background counts $N_{bi,be}$ and the coincidences N_c in the CEMs as introduced in subsection 5.1.2. As a unique property of this thesis CEM detection system, the counting of coincidences N_c from correlated particle pairs enables to calibrate the CEM detectors to absolute efficiency values in contrast to any relative detection efficiency calibration in the literature (see section 5.1).

In this section, initially the absolute detection efficiencies η_i and η_e of the single CEM detectors and the neutral atom detection efficiency η_{atom} of the joint CEM detection system are determined at one particular position within the sensitive detection area $A_c(x, y)$ (for $A_c(x, y)$; see section 4.5). The single efficiencies $\eta_{i,e}(\Delta U_{\text{acc}})$ are displayed with respect to different acceleration potential differences ΔU_{acc} between the two CEM detector cones. From the absolute detection efficiencies η_i and η_e of the single CEM detectors, the neutral atom detection efficiency η_{atom} is determined.

For a comparison of the observed efficiency values to the cascaded dynode detector theory of chapter 2 and the literature, the absolute detection efficiencies $\eta_{i,e}(\Delta U_{\text{acc}})$ are then rearranged according to their estimated kinetic impact energy E_{kin} at primary particle impact in the corresponding CEM detector. In relation to the theory (see section 2.4), a least-squared fit of the individual CEM efficiency response $\eta_{i,e}(E_{\text{kin}})$ allows to compare the observed values to the cascaded dynode detector theory with respect to the two key parameters E_{kin} and θ . Moreover, the obtained efficiency values further suggest a CEM channel hit for the ions in relation to the literature, in contrast to a common CEM cone hit. This estimation will confirm the statement of a CEM channel impact obtained from the derived ion flight times t_i of section 5.3, and is also in accordance with the 2D-scan measurements of section 5.5.

Moreover, based on the previous analysis of the measured values in comparison to the theory, some general remarks in obtaining a high detection efficiency $\eta_{i,e}(E_{\text{kin}})$ with a given CEM detector are stated. It turns out that grazing incident angles θ of the primary particle and a high kinetic energy E_{kin} at primary particle impact are generally beneficial for enhanced detection efficiencies of any given CEM detector in a CEM detection system.

5.4.1. CEM calibration to absolute detection efficiencies

Figure 5.11 shows the absolute detection efficiencies for ions and electrons at different acceleration voltages ΔU_{acc} . The measurements are performed at $z = d/2$ in between the CEMs at a fixed relative position of $(x = 1.2 \text{ mm}, y = -0.4 \text{ mm})$; fig. 5.13; see section 5.5), using a CEM gain voltage of $U_{\text{CEM}} = 2.8 \text{ kV}$ for both detectors²⁶. The absolute detection efficiencies $\eta_{i,e}(\Delta U_{\text{acc}})$ are calculated from the measured, background corrected single counts $N'_{i,e}$ and

²⁶Note that the comparably high CEM gain voltages U_{CEM} applied at both CEMs in the calibration measurements result from advanced CEM detector degradation due to extensive detector use and considerable detector age (see subsection 3.1.2).

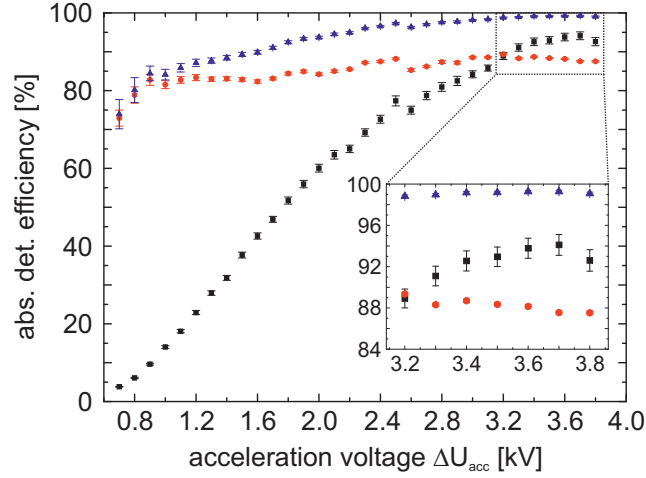


Figure 5.11: Absolute detection efficiency $\eta_{i,e}$ for ^{87}Rb -ions (black square) and electrons (red circle) for different acceleration voltages ΔU_{acc} and the calculated, neutral atom detection efficiency η_{atom} (blue triangle). The measurements are performed at a relative position of $(x = 1.2 \text{ mm}, y = -0.4 \text{ mm})$ in fig. 5.13, using a CEM gain voltage of $U_{\text{CEM}} = 2.8 \text{ kV}$ for both detectors. Inset: Zoom for acceleration voltages from 3.2 kV to 3.8 kV.

the obtained coincidences N_c from the individual²⁷ correlation histograms at each acceleration voltage ΔU_{acc} according to eq. 5.5. In the measurement, the acceleration voltage is increased from $\Delta U_{\text{acc}} = 0.7 \text{ kV}$ up to $\Delta U_{\text{acc}} = 3.8 \text{ kV}$, in relative steps of $\Delta U_{\text{acc}} = 0.1 \text{ kV}$, while the individual CEM gain voltages²⁸ are kept constant during the entire measurement.

As an example, at an acceleration voltage $\Delta U_{\text{acc}} = 3.8 \text{ kV}$ for a measurement time of $t = 60 \text{ s}$, we observe photoionisation and background counts of $N_i = 53762$, $N_{\text{bi}} = 2235$, $N_e = 196547$, $N_{\text{be}} = 147845$, and $N_c = 45099$ (including ion and electron dark counts $N_{\text{di}} \sim 2100$ and $N_{\text{de}} \sim 15000$, respectively). In reference to eq. 5.5, these numbers result in an absolute CEM detection efficiency of $\eta_i = 0.926 \pm 0.010$ and $\eta_e = 0.875 \pm 0.002$ (fig. 5.11). The corresponding errors $\Delta\eta_{i,e}$ of the detection efficiencies are calculated as described in subsection 5.1.2, accordingly.

For acceleration voltages up to 3.8 kV, the ion detection efficiency η_i increases in qualitative agreement with previous studies for different ion species [88, 89, 93, 95, 97, 98, 101, 102, 105, 106, 123, 135]. For $\Delta U_{\text{acc}} > 3.3 \text{ kV}$, ion detection efficiencies of $\eta_i > 0.926$ are achieved. For an acceleration voltage of $\Delta U_{\text{acc}} = 3.7 \text{ kV}$, the ion detection efficiency even reaches $\eta_i = 0.941 \pm 0.010$. In contrast to the observed ion efficiencies, the measured electron detection efficiency η_e remains almost constant in contrast to the usually observed dependency in the literature (see section 2.4). In subsection 5.4.4, this apparent discrepancy is further resolved. In our measurements, the electron detection efficiencies attain $\eta_e > 0.872$ for acceleration voltages of $\Delta U_{\text{acc}} > 2.8 \text{ kV}$ with a peak value of $\eta_e = 0.893 \pm 0.002$ at $\Delta U_{\text{acc}} = 3.2 \text{ kV}$. However, for a detailed analysis and comparison of the measured ion and electron efficiencies with the literature and to the general theory of chapter 2, the observed values have first to be rearranged as a function of the kinetic energy at primary particle impact in the respective CEM. This will be further described in subsection 5.4.3 (fig. 5.12).

²⁷An example for an individual correlation histogram is given by fig. 5.4, for $\Delta U_{\text{acc}} = 3.8 \text{ kV}$.

²⁸See fig. 4.8 in section 4.2 for the explicit definition of ΔU_{acc} and the CEM gain voltage U_{CEM} .

Note that for acceleration voltages greater than 3.8 kV, the joint CEM detection system in the current UHV glass cell setup turns out to be temporarily unstable²⁹ during a measurement series. At these acceleration voltages, spontaneous current breakthroughs via voltage arcing due to temporary shortcuts with the UHV environment are observed from time to time. This seems to be similar to what is reported by, e.g., [165]. Additionally, charged primary particle crosstalk between the two differently charged CEM detectors occurs. This crosstalk results in induced pulselike cascades of spontaneous high currents of primary particles at the corresponding CEM detectors, permanently degrading the active CEM surface and the CEM gain due to their high initial charge at secondary electron multiplication in the CEM [241].

5.4.2. Neutral atom detection efficiency

From the observed single CEM efficiencies in fig. 5.11, a neutral atom detection efficiency according to subsection 5.1.2 is calculated. Using above values of $\eta_i = 0.926 \pm 0.010$ and $\eta_e = 0.875 \pm 0.002$ at an acceleration voltage difference of $\Delta U_{\text{acc}} = 3.8 \text{ kV}$, a neutral atom detection efficiency of $\eta_{\text{atom}} = 0.991 \pm 0.002$ is derived (fig. 5.11; inset). For acceleration values of $\Delta U_{\text{acc}} = 3.4 - 3.6 \text{ kV}$, an even higher efficiency of $\eta_{\text{atom}} = 0.993 \pm 0.001$ is achieved. Correspondingly, the stated uncertainty of η_{atom} is obtained using Gaussian error propagation in eq. 5.6. In comparison, a combined detection efficiency of $\eta_{\text{atom}} = 0.897$ is achieved in a related work using mercury atoms [242], within a detection time of $t_{\text{tot}} = 16.2 \mu\text{s}$.

Fast neutral atom detection with high detection efficiency

To obtain faster detection times than $t_{\text{det}} = 415.5 \text{ ns}$ ($\Delta t \approx t_i = 388.5 \text{ ns}$ and $t_e = 0.95 \text{ ns}$; see section 5.3), the ionisation region can be moved closer towards the ion-CEM if the configuration of the particular experiment allows an ionisation center position different from $z = d/2$. For example, one can translate the ionisation center from $z = d/2$ to a position half-way towards the ion-CEM, corresponding to a distance³⁰ at $z = -3.9 \text{ mm}$ in fig. 4.11. The calculated ion flight time according to eq. 4.5 and eq. 4.6 are then considerably shorter with $t_i = 288.1 \text{ ns}$, and the electron flight time larger with $t_e = 1.77 \text{ ns}$, respectively. This follows as the ^{87}Rb -ion only has to travel a distance of $d_{\text{Rb}} = d/4$, while its photoelectron will cover $d_e = 3d/4$ until CEM cone entrance (fig. 4.11).

Although this configuration allows a much faster detection of the ion, in such a case also the kinetic energy at primary particle impact changes due to the different covered distance of the particle in the accelerating potential difference ΔU_{acc} . Consequently, the particle impact energy will then be considerably smaller for the ^{87}Rb -ion and larger for the photoelectron, in accordance with eq. 5.7 and eq. 5.8 (see subsection 5.4.3). The particle impact energy at an ionisation center position of $z = -3.9 \text{ mm}$ ($d_{\text{Rb}} = d/4$, $d_e = 3d/4$) thus yields calculated values of $E_{\text{kin}} = 0.672 \text{ keV}$ for the ^{87}Rb -ion and $E_{\text{kin}} = 2.175 \text{ keV}$ for the electron (see subsection 5.4.3). However, the calculated CEM efficiencies at these impact energies are smaller for the ion, and larger for the photoelectron (fig. 5.12; $\eta_i(0.672 \text{ keV}) = 0.576$, and $\eta_e(2.175 \text{ keV}) = 0.894$; see subsection 5.4.3). Therefore, the determined neutral atom detection time is only $\eta_{\text{atom}} = 0.955$ (eq. 5.6). Consequently, although t_i and t_e are significantly

²⁹Consequently, the temporal instability of the CEM cone potentials constrains the continuous operation of the particular CEM detector configuration of this thesis to acceleration voltages $\Delta U_{\text{acc}} < 3.9 \text{ kV}$.

³⁰In such a configuration, the ion will only travel for $d_{\text{Rb}} = d/4$ of the distance in between the CEM detectors, while the photoelectron will cover $d_e = 3/4d$ of the overall distance.

shorter for a different ionisation center position than $z = d/2$, to obtain a comparable, neutral atom detection efficiency of $\eta_{\text{atom}} \sim 0.99$, the acceleration voltage ΔU_{acc} in between the CEMs has to be increased in such a configuration, accordingly.

5.4.3. Kinetic energy at primary particle impact

For any comparison of the measured CEM efficiency values $\eta_{i,e}$ with cascaded dynode multiplier theory of chapter 2, the observed efficiency values $\eta_{i,e}(\Delta U_{\text{acc}})$ in fig. 5.11 have to be rearranged as a function of the kinetic energy E_{kin} at primary particle impact in the respective CEM. In the literature, the kinetic energies E_{kin} of the primary particles are commonly stated until the CEM cone entrance as the actual impact position in the CEM detector is usually rather unknown (subsection 4.3.4). However, particularly for low kinetic energies E_{kin} of the incident particles (i.e., $E_{\text{kin}} < 1 \text{ keV}$), the corrections of the kinetic particle energy at the impact due to the accelerating or decelerating fields by the CEM gain potential will become macroscopic (fig. 4.11). Nevertheless, the lack of accuracy of this measurement procedure and corresponding change of the kinetic energy according to the actual impact position in the CEM are still sparsely mentioned in the literature (e.g., [87, 95, 101]). In the following, the obtained efficiencies $\eta_{i,e}(\Delta U_{\text{acc}})$ from the measurements of fig. 5.11 will thus be recalibrated in accordance with the simulated CEM potentials as described in section 4.3. Together with the obtained impact position of the particles in the CEMs (see section 5.3), this allows to determine the kinetic energy E_{kin} of the incident primary particles at particle impact in the corresponding CEM.

In general, the knowledge of the impact position in the CEMs is of particular interest for any comparison of measured quantum yield values η_{detector} with cascaded dynode detector theory (chapter 2). This follows as only the exact kinetic energy E_{kin} at primary particle impact in the CEM allows to relate the derived primary particle emission yield δ_0 from the measured efficiencies $\eta_{i,e}$ with isolated measurements of the primary emission yield $\delta_0(E_{\text{kin}}, \theta)$ of common CEM surfaces and of the secondary emission yield δ in the CEM (see section 2.3 and section 2.4).

Corrections of the kinetic energy at CEM cone entrance due to particle impact position

For the joint CEM detection system of this thesis, the actual kinetic energy E_{kin} at primary particle impact can be determined from the estimated impact position in the corresponding CEM. According to the time-of-flight model of subsection 4.4.1, the actual impact position is derived from the flight times $t_{i,e}$ of the individual particles (eq. 4.5 and eq. 4.6). The corresponding measurements of section 5.3 show excellent agreement with the calculated values. The obtained covered path length d_{CEM} and d_e yields the impact position in the CEM, which in turn determines the energy correction by the internal CEM potential (see subsection 4.3.4).

From eq. 4.3 and eq. 4.4, the correction of the kinetic energies according to the applied acceleration voltage difference ΔU_{acc} at the CEMs is, using an applied CEM gain voltage of $U_{\text{CEM}} = 2.8 \text{ kV}$ for both detectors, determined by

$$E_{\text{kin}}(\Delta U_{\text{acc}}, d_{\text{CEM}}) = 0.715 \cdot \Delta U_{\text{acc}} e_0 / 2 - (55.05 \text{ eV/mm} \cdot d_{\text{CEM}}), \quad (5.7)$$

for the ion-CEM, and

$$E_{\text{kin}}(\Delta U_{\text{acc}}, d_e) = 0.285 \cdot \Delta U_{\text{acc}} e_0 / 2 + (55.05 \text{ eV/mm} \cdot d_e), \quad (5.8)$$

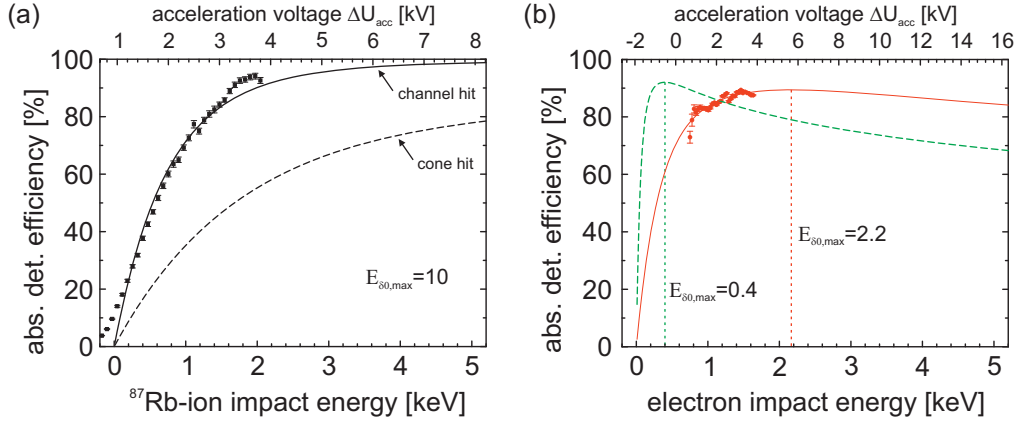


Figure 5.12: Rearranged efficiency values and corresponding least-squared fit according to the estimated kinetic energy at primary particle impact in the CEM. (a) ^{87}Rb -ion efficiency, yielding $\delta_{0, \max} = 6.5$ at $E_{\delta_0, \max} = 10$ keV, and using $\delta = 2$. For comparison, a fictitious cone hit of the primary ion to the observed CEM channel impact is illustrated (dashed line). (b) Electron efficiency, yielding $\delta_{0, \max} = 2.8$ and $E_{\delta_0, \max} = 2.2$ keV at a fixed $\delta = 2$. For comparison, a sample efficiency curve (dashed, green) for incident electrons and cone impacts is shown [48, 66, 87], as displayed in common operating manuals (e.g., [85]).

for the e^- -CEM, accordingly. The resulting kinetic energies at the primary impact for the different acceleration voltages ΔU_{acc} are displayed in fig. 5.12. For direct comparison, an additional axis with the corresponding acceleration voltages ΔU_{acc} is shown (fig. 5.12; upper axis).

5.4.4. Absolute detection efficiency versus impact energy

In fig. 5.12, the measured values displayed in fig. 5.11 are rearranged according to the estimated kinetic energy E_{kin} at primary particle impact referring to eq. 5.7 and eq. 5.8. For the determination of the ^{87}Rb -ion impact energies in fig. 5.12(a), an average value of $d_{\text{CEM}} = 12.22$ mm is chosen in eq. 5.7 as determined from the relative flight time differences in subsection 5.3.1 (fig. 5.9). For the electron impact energies in fig. 5.12(b), a CEM channel hit is assumed at a distance³¹ $d_e = 10$ mm for a typical channel impact in the e^- -CEM. For analysis and comparison of the rearranged efficiency data with the cascaded dynode multiplier efficiency model of section 2.2 and the literature, a least-squared fit according to eq. 2.10 is performed on both data sets as shown in fig. 5.12(a) and (b) (straight and dashed lines).

For the least-square fit, a uniform secondary electron yield of $\delta = 2$ is assumed for the consecutive stages $g_{2..m}$ and both CEM detectors. This choice results from the generalized conditions of the single emission process at the consecutive stages $g_{2..m}$ in the CEM as illustrated in section 2.1 and described by [48]. For the ion-CEM and the corresponding efficiencies $\eta_i(E_{\text{kin}})$, a maximum yield energy of $E_{\delta_0, \max} = 10$ keV is further chosen as fixed value for the least-squared fit of the ^{87}Rb -ion efficiencies. However, the latter choice is to some extent artificial and results as the measured efficiency values $\eta_i(E_{\text{kin}})$ in fig. 5.12(a) do not show a

³¹The minimum possible distance in the CEM until a primary impact in the active CEM surface is $d_e = 4.25$ mm (cone hit), whereas the minimum distance for a channel hit is $d_e \approx 7$ mm and the maximum distance is $d_e \approx 13.1$ mm (see Appendix A.4). Therefore, a distance of $d_e = 10$ mm is chosen for a common channel hit in the CEM.

defined maximum within the observed kinetic energy range as generally expected by eq. 2.10. Nevertheless, the experimental evidence from related experiments of [88, 105, 106, 123, 135] with similar incident ions at comparable impact energies $E_{\text{kin}} < 15$ keV strongly suggests the choice of such a value for the least-squared fit of ion efficiencies [88]. Note further that the ion efficiency data is fitted starting with impact energies $E_{\text{kin}} \geq 0.2$ keV corresponding to acceleration voltage values of $\Delta U_{\text{acc}} > 1.6$ kV in accordance to the considerations of subsection 5.3.1.

Ion efficiencies

The measured ion efficiencies $\eta_i(E_{\text{kin}})$ shown in fig. 5.12(a) depict the quasi-linear increase up to a certain saturation level as observed by various previous efficiency calibration measurements [88, 89, 93, 95, 97, 98, 101, 102, 105, 106, 123, 124, 135]. A similar increase and saturation level is also continuously observed for multi-channel plates³² (MCPs) (e.g., [123, 243]). However, the measured values $\eta_i(E_{\text{kin}})$ depicted in fig. 5.12(a) display a significantly higher efficiency up to a factor of two to three compared to related previous calibration experiments in the literature, using ions with a similar mass-to-charge ratio and within the same energy range (e.g., the krypton isotopes $^{82,83,84}\text{Kr}^+$ in [123] with $\eta_i(E_{\text{kin}}) \sim 30\%$ at $E_{\text{kin}} = 2$ keV; or Ar^+ , Xe^+ for $E_{\text{kin}} \leq 2.5$ keV in [105] and for $E_{\text{kin}} < 10$ keV in [88, 135]). Nevertheless, if one assumes a channel impact for the primary ions as initially intended by the CEM detector design (see subsection 4.2.4) and not a CEM cone hit (dashed curve, fig. 5.12(a)), the observed factor is consistent with generally measured, enhanced efficiencies in the literature for channel impacts compared to cone hits [87, 88, 133, 134].

In more detail, the least-squared fit shown in fig. 5.12(a) yields a primary particle yield of the ^{87}Rb -ion of $\delta_0 = 6.5 \pm 0.1$. By comparison of this value to commonly observed primary yield values δ_0 for related active surfaces and kinetic energies E_{kin} [66, 73, 77, 83, 244], such a high value will only be explained by a ^{87}Rb -ion impact under grazing incidences θ in the CEM. As a common cone hit yields an incident particle angle of $\theta = 60^\circ$ (see subsection 2.4.3), an average incident angle of $\theta \approx 80^\circ$ can be assumed for a typical CEM channel hit (fig. 2.8). Using identical kinetic energies at primary particle impact for both cases, the primary particle yield values $\delta_0(60^\circ)$ and $\delta_0(80^\circ)$ for a cone or a channel hit will differ only by a fixed factor as indicated by eq. 2.12. For an acceleration voltage of $\Delta U_{\text{acc}} = 3.8$ kV, corresponding to an impact energy of $E_{\text{kin}} = 2.044$ keV (fig. 5.12), with $E_{\delta_0, \text{max}} = 10$ keV and $\delta = 2$, this will result, e.g., in a calculated absolute efficiency of $\eta_{\text{det}}(\delta_0(60^\circ)) = 0.559$ compared to $\eta_{\text{det}}(\delta_0(80^\circ)) = 0.905$ according to eq. 2.10.

For a comparison of typical cone to channel impacts, a fictitious curve $\eta_{\text{det}}(\delta_0(60^\circ))$ for a sample cone hit under $\theta = 60^\circ$ with $\delta_0(60^\circ) = 2.3$ is illustrated³³ in fig. 5.12(a). In relation to a CEM channel impact (dashed curve), this reference curve is additionally plotted to the observed data as usually only CEM cone impacts are observed in most CEM detector calibration measurements. Compared to the literature data, the observed values of the measurement thus represent a typical channel hit in the CEM. The latter observation is also consistent with the observed ion flight times t_i in subsection 5.3.1, further suggesting a CEM channel impact and not a cone hit.

³²MCPs generally yield similar active secondary emitting surfaces as CEMs.

³³The data of the fictitious curve yields the identical fit parameters of the channel hit curve, but using $\delta_0(60^\circ) = \delta_0(80^\circ)(\sec(60^\circ)/\sec(80^\circ)) = 2.3$ as deduced from eq. 2.10 instead of $\delta_0(80^\circ) = 6.5$ as obtained from the fit on the experimental data.

Maximum ion detection efficiency The least-squared fit according to eq. 2.10 displays a good agreement with the observed efficiency values (fig. 5.12(a); black line). Extending the theoretical fit curve to higher kinetic energies E_{kin} , the calculated ion efficiency will already raise to $\eta_{i,\text{fit}}(5 \text{ keV}) = 0.989$ at an impact energy of $E_{\text{kin}} = 5 \text{ keV}$. From the fit, a maximum ion detection efficiency of $\eta_{i,\text{fit}}(10 \text{ keV}) = 0.9943$ is expected at an impact energy of $E_{\text{kin}} = 10 \text{ keV}$ for previously stated parameters of δ_0 , $E_{\delta_0,\text{max}}$, and δ (eq. 2.10; see section 2.4). Unfortunately, such kinetic energy values cannot be observed with the current UHV glass cell setup as eventual current breakthroughs contain the system to acceleration voltage differences $\Delta U_{\text{acc}} < 3.9 \text{ kV}$ (see section 4.2).

Note that for a chosen value of $\delta = 3$ in eq. 2.10, the fitted primary ion yield is still $\delta_0 = 5.5$ for the measured ion efficiency values with a chosen $E_{\delta_0,\text{max}} = 10 \text{ keV}$. These values are in accordance with the theoretically obtained yield values of subsection 2.5. However, the secondary avalanche in the CEM will then undergo only $m = 16$ stages of amplification in correspondence to commonly observed gain values of $G_0 = 5 \times 10^7$, using eq. 3.2 and the values $\delta_0 = 5.5$ and $\delta = 3$. As a result, the transit time t_{transit} of the secondary electron avalanche in the CEM will be subsequently altered by the fewer amplification stages, yielding shorter transit times than stated by the manufacturer (see subsection 3.2.1). Therefore, the initial assumption of $\delta = 2$ seems to be generally reasonable for the CEM detectors used in the context of this thesis, and as a reference parameter for any curved CEMs [48].

Electron efficiencies

In contrast to the ion efficiencies, the observed electron detection efficiency η_e displayed in fig. 5.12(b) shows only a low increase, almost remaining constant for the given impact energies E_{kin} . In comparison to the literature (see subsection 2.4.2), the measured efficiencies $\eta_e(E_{\text{kin}})$ lie well within the usually stated range of efficiency values from $E_{\text{kin}} = 0.1 - 5 \text{ keV}$ for incident electrons (see extensive compilation by [48]). However, our measured values indicate a slight increase even for impact energies $E_{\text{kin}} > 1 \text{ keV}$ in contrast to many CEM detector calibrations in the literature.

Maximum electron detection efficiency The least-squared fit of the electron efficiencies $\eta_e(E_{\text{kin}})$ according to eq. 2.10 displays a very good agreement to the measured data (fig. 5.12(b); red line). For comparison, a sample efficiency curve for incident electrons is additionally shown³⁴ (fig. 5.12(b); dashed curve). The sample curve illustrates the observed efficiencies for a common CEM cone impact as reported by [48, 66, 87, 133], and being generally displayed as standard reference of the CEM efficiency response for incident electrons in common CEM operating manuals (e.g., [85]). From the fit as depicted in fig. 5.12(b), a primary electron yield value of $\delta_0 = 2.8 \pm 0.1$ and a fitted impact energy $E_{\delta_0,\text{max}} = 2.2 \pm 0.2 \text{ keV}$ for maximum efficiency is determined. From this, a maximum detection efficiency of $\eta_{e,\text{fit}}(2.2 \text{ keV}) = 0.8940$ at a kinetic energy of $E_{\delta_0,\text{max}} = 2.2 \text{ keV}$ is deduced (eq. 2.10; see section 2.4). The fitted primary electron yield value of $\delta_0 = 2.8$ agrees to extensive studies for the primary electron yield δ_0 and hydrogen reduced lead glass ($\delta_0 = 2.6 - 3.5$; [63, 66]), and for common values assumed for CEM detectors by [48, 87]. However, the position of the maximum efficiency $E_{\delta_0,\text{max}}$ according to the fit is significantly shifted to higher kinetic energies E_{kin} compared to these studies, where the maximum is usually situated at $E_{\delta_0,\text{max}} = 0.35 - 0.4 \text{ keV}$.

³⁴The displayed curve is derived from eq. 2.10, using common parameter values of $\delta_0,\text{max} = 3.6$ and $E_{\delta_0,\text{max}} = 0.4$ for a typical CEM cone impact [63, 66].

The origin of this shift to higher kinetic energy values $E_{\delta_0, \max}$ is difficult to determine. In general, the primary particle yield δ_0 for different emissive surfaces with their corresponding reduced yield curve characteristic is shifted to higher energy values for grazing incident angles θ of the primary particles [62, 127]. Therefore, the shifted maximum $E_{\delta_0, \max}$ of the efficiency towards higher impact energies suggests a channel impact³⁵ of the primary electrons in the CEM detector under a grazing angle ($\theta > 80^\circ$), compared to a CEM cone hit ($\theta \approx 60^\circ$). However, this cannot be specifically proven in our experiments as the actual impact position of the incident primary electrons in the e^- -CEM is rather undefined (see subsection 4.4.1). Nevertheless, the 2D-scan measurements of section 5.5 indicate by the spatial characteristic of the observed efficiencies in the e^- -CEM also a channel impact (fig. 5.14). Moreover, a shifted maximum $E_{\delta_0, \max}$ similar to our observed values for CEM channel to cone hits is explicitly measured for sample CEMs by [87], and for primary electron yield values δ_0 by [63, 66].

5.4.5. Obtaining high CEM efficiencies

In summary, the observed detection efficiencies behave according to $\eta_{i,e} = \eta_{i,e}(\delta_0, \delta)$ as expressed by eq. 2.10, where the parameter $\delta_0(E_{\text{kin}}, \theta)$ depends on the two key quantities E_{kin} and θ . These key parameters can be estimated in most CEM detector setups, allowing in principle to calculate the maximum attainable quantum yield η_{detector} of a given CEM detector in any CEM detection system as stated by eq. 2.10. Based on this estimation, the individual adjustment and optimization of the two key parameters E_{kin} and θ allows to experimentally maximize the detection efficiency of the given CEM detector and thus enables to push the corresponding CEM detector to its limiting extremes.

The calibration measurements in this section show that with respect to the incident angle θ of the primary particle at impact, the efficiencies for CEM channel impacts under grazing incidence θ yield considerably higher detection efficiencies than related CEM cone hits. Moreover, if one compares a CEM cone hit to a channel impact at identical impact energies E_{kin} , the detection efficiencies of the incident primary particles differ by a fixed factor as expressed by eq. 2.12. Therefore, if high detection efficiencies are to be obtained from a CEM detector, a channel hit or a primary particle impact under grazing angle θ to the active CEM surface is generally beneficial.

In the aspect of the impact energy E_{kin} of the primary particle, the individual optimization of the kinetic energy E_{kin} of the incident particle is further advantageous if one wants to obtain an increased detection efficiency with a given CEM detector. Here, in particular a maximized primary particle yield $\delta_0(E_{\text{kin}})$ at primary particle impact is the relevant parameter for a high quantum yield η_{detector} . This follows from the individual characteristic of the CEM efficiency response $\eta_{i,e}(\delta_0, \delta)$ as stated by the reduced yield curve in eq. 2.10. For example, in the case of the joint CEM detection system of this thesis, high ion efficiency values of $\eta_i > 80\%$ are obtained for incident ^{87}Rb -ions and corresponding ion impact energies $E_{\text{kin}} > 1\text{ keV}$ (fig. 5.12(a)). Even higher efficiency values will be observed for considerably larger impact energies of $E_{\text{kin}} \approx 10\text{ keV}$. For incident electrons, the optimum impact energy maximizes at $E_{\text{kin}} = 2.2\text{ keV}$ (fig. 5.12(b)). However, in relation to commonly observed maximum efficiency values in standard CEM detector references (e.g., [85]), an optimum impact energy of $E_{\text{kin}} = 0.4\text{ keV}$ is recommended for incident electrons. Nevertheless, the latter value seems only to be useful with respect to a common CEM cone impact of the

³⁵A common channel hit will generally occur with an impact of the primary electron in the active CEM surface under grazing angles θ (see subsection 2.4.3).

incident primary electrons. Concerning CEM channel impacts under grazing incident angles θ , the larger value as measured in this thesis presumably represents the better estimate. For future applications of the CEM detection system with even higher detection efficiencies $\eta_{i,e}(\delta_0(E_{\text{kin}}))$, the kinetic energies E_{kin} at primary particle impact have thus to be individually optimised in the experiment.

5.5. Spatial efficiency dependence and particle impact position in the CEMs

In the following, the spatial dependency of the CEM detection efficiencies $\eta_{i,e}(x, y)$ for charged particles generated in the $x - y$ plane at a particular z -position in between the CEMs is examined. The topography of the observed CEM detector efficiency determines the sensitive area $A_{i,e}$ of both CEM detectors in the joint CEM detection system. From the single sensitive area $A_{i,e}$ of the individual CEMs, the sensitive detection area A_c of the joint CEM system is obtained (see section 4.5). Using sufficiently high CEM gain voltages at both CEM detectors, single particle detection efficiencies of $\eta_{i,e}(x, y) \sim 90\%$ and a neutral atom detection efficiency η_{atom} exceeding 98.8% within the entire area A_c are achieved. Remarkably, the obtained efficiencies are based on an absolute calibration method (see section 5.1) in contrast to common efficiency calibration experiments of CEM detectors, as they rely on relative measurement methods only. This leaves the determined absolute CEM detector efficiencies of this section unique from a calibration point of view compared to any common calibration experiments in the literature.

Additionally, the sensitive volume V_c of the CEM detection system in the glass cell setup is determined. On the one hand, this will be of particular interest for a future integration³⁶ of the joint CEM detection system as single atom readout unit in a Bell test arrangement with two remote atoms [18]. On the other hand, a large sensitive volume V_c with high detection efficiencies generally represents a key property of the joint CEM detection system for *any* spectroscopic application, demanding single atom detection resolution as, e.g., the site-specific readout of atoms in optical lattices [238–240].

In contrast to conventional CEM detector calibrations, the coincident measurement of the correlated particle pairs in the respective CEM adds an additional degree of freedom to the calibration measurements. Therefore, as introduced in section 4.4, the temporal correlation of the photoionised correlated pair and the determined relative ion arrival time difference Δt allows to allocate the spatial position of the primary ^{87}Rb -ion impact in the ion-CEM. Accordingly, the temporal characteristic of the obtained relative arrival time differences $\Delta t(x, y)$ of the ^{87}Rb -ion in correspondence to the observed sensitive detection area $A_c(x, y)$ is analyzed. The obtained differences $\Delta t(x, y)$ within $A_c(x, y)$ suggest that the ^{87}Rb -ions hit the ion-CEM detector deep in the channel section at the channel wall under grazing incident angles (fig. 2.8; see section 2.4). This grazing incidence in the channel section represents the key property to the observed high detection efficiencies for the joint CEM detection system in this thesis (see section 5.4).

Moreover, the calculated covered distances d_{iCEM} in the ion-CEM and the knowledge of the explicit impact position allow to specifically quantify the relevant impact parameters E_{kin} and

³⁶In a future combined setup, the loading MOT and thus the center of the optical dipole trap can only be placed at a specific position in between the CEMs (see section 4.1). Therefore, a possible large detection volume will generally be advantageous to compensate for eventual position compromises.

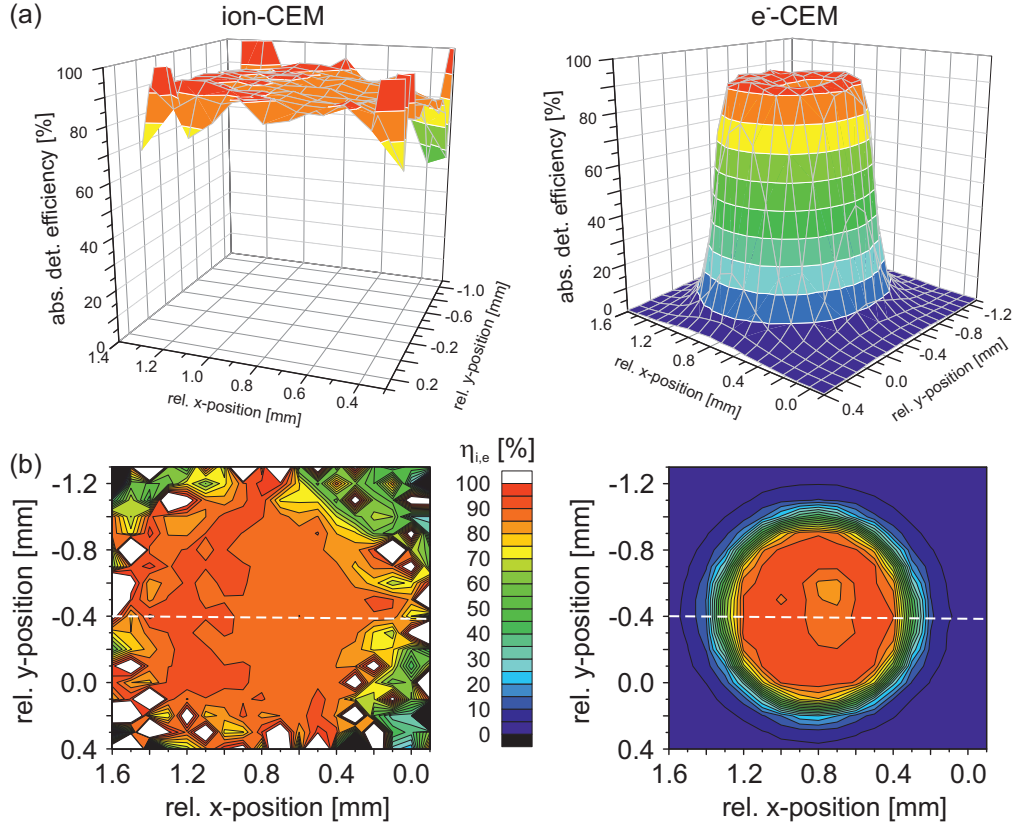


Figure 5.13: 2D-scan of the absolute detection efficiencies $\eta_{i,e}(x, y)$, obtained from the measured single counts $N'_{i,e}(x, y)$ and coincidences $N_c(x, y)$ at $z = d/2$ in the $x - y$ plane in between the CEMs. (a) Surface plot of the 2D-scan, illustrating the topography of the CEM detector efficiencies. (b) Contour plot of the surface plot displayed in (a). The dashed lines at $y = -0.4$ mm indicate the additional line scan measurements of fig. 5.15.

θ of the corresponding primary particle in the CEM (see section 2.4). This thus enables to directly relate the obtained detector quantum yield η_{detector} and the derived primary particle emission yield $\delta_0(E_{\text{kin}}, \theta)$ to the general cascaded dynode detector theory of chapter 2.

5.5.1. Spatial dependence of detection efficiency

In fig. 5.13, a 2D-scan measurement of the absolute detection efficiencies $\eta_{i,e}(x, y)$ at $z = d/2$ in the $x - y$ plane in between the CEMs is displayed. In the measurements, the charged photoionisation fragments ($^{87}\text{Rb}^+$, e^-) out of the ionisation volume are used as correlated particle pair source for detector calibration (see section 5.1). The calculated efficiencies $\eta_{i,e}(x, y)$ are obtained from the measured single counts $N'_{i,e}(x, y)$ and coincidences $N_c(x, y)$, using eq. 4.5 and eq. 4.6. In the 2D-measurements (fig. 4.16; see section 4.5), a relative scan step size of $\Delta x, \Delta y = 100 \mu\text{m}$ in the $x - y$ plane is used. The single counts $N'_{i,e}(x, y)$ are background corrected (see subsection 5.2.2 and subsection 5.2.4). The coincidences $N_c(x, y)$ are deduced from number of correlated ion events within the coincidence time window in the individual correlation histograms at each single scan position (x, y) (see section 5.2). The accidental coincidences N_{ac} can be neglected in these measurements (see subsection 5.2.3). The ge-

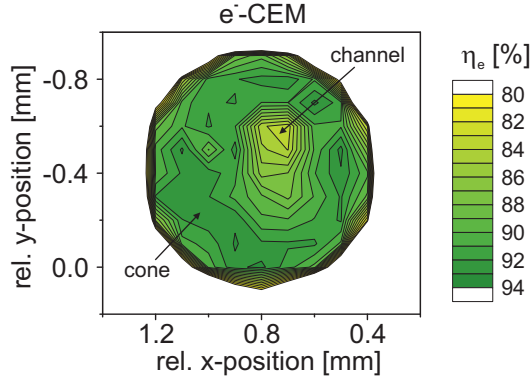


Figure 5.14: Detailed zoom of the electron detection efficiency $\eta_e(x, y)$ in fig. 5.13. The topography of the efficiency resembles the internal CEM geometry according to the impact position of the incident primary electrons.

nerated correlation histograms further yield the option to determine the relative ion flight time difference $\Delta t(x, y)$ at each single scan position (subsection 5.5.3), obtained from the center of the individual photoionisation correlation peak in each correlation histogram (e.g., $\Delta t = 388.5$ ns, fig. 5.4; at $x = 1.2$ mm, $y = -0.4$ mm). During measurements, a gain voltage of $U_{\text{CEM}} = 2.8$ kV at both CEMs and an acceleration voltage difference of $\Delta U_{\text{acc}} = 3.8$ kV in between the CEMs is applied.

The 2D-scan measurements are shown in fig. 5.13 and indicate a plateaulike structure for the ion efficiencies $\eta_i(x, y)$ and a similar structure with a central dip for the electron efficiencies $\eta_e(x, y)$. Further, the topography of the absolute efficiencies $\eta_{i,e}(x, y)$ of both CEM detectors exhibits a roughly circular distribution with a diameter of up to 1.2 mm. The particular radius of the circular structure correlates to a considerable extend to the open aperture of the copper aperture entrances in front of the CEM cones ($d_{\text{aperture}} = 2$ mm; see subsection 4.2.4). However, the particular spatial distribution of the single counts $N'_{i,e}(x, y)$ is generally determined by the specific imaging properties of the entire CEM detection system at the respective electric potential configuration (see subsection 4.5.3). Principally, this does therefore not allow an explicit comparison of the observed spatial topography of the detector efficiencies with any single CEM detector components.

Nevertheless, the circular structure of the single CEM efficiencies can be related to the imaging of the electrons in the e⁻-CEM, and thus to the sensitive detection area $A_c(x, y)$ of the CEM detection system (see section 4.5). This results as the observation of coincident events N_c in *both* CEM detectors is required (i.e., the sensitive detection area $A_c(x, y)$) to determine the absolute detection efficiencies according to eq. 4.5 and eq. 4.6. As a result, the particular spatial distribution of the sensitive area $A_e(x, y)$ of the e⁻-CEM (fig. 4.19) thus evokes the circular shape of the efficiencies in these measurements.

The detailed shape of the dip in the observed electron efficiencies $\eta_e(x, y)$ in fig. 5.14 further suggests a comparison to the particular impact position of the primary electron in the e⁻-CEM (compare, e.g., [131]). Assuming that the observed efficiencies depend only on the incident angle θ of the primary particle at impact (see subsection 2.4.3), the measured efficiency topography maps the spatial extensions of the internal CEM geometry (i.e., the explicit shape and spatial orientation of the CEM channel, fig. 4.4) in correspondence of the incident angle

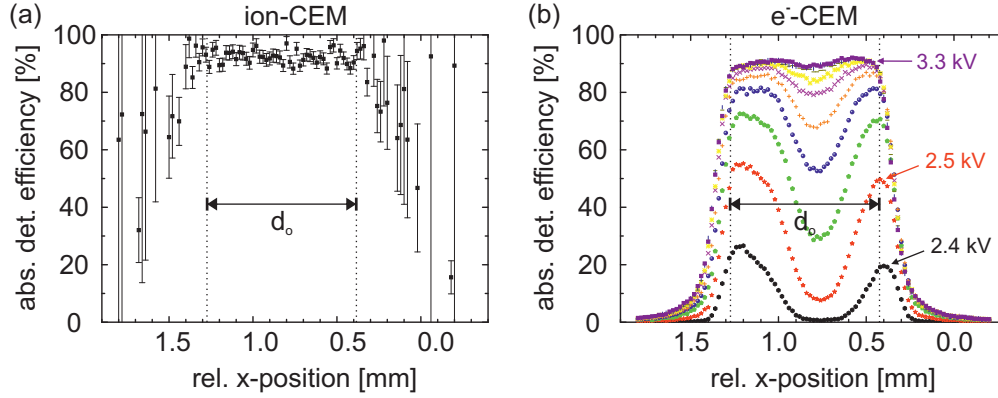


Figure 5.15: Additional line scan of the CEM detection efficiency $\eta_{i,e}(x)$ in relative x -direction at a fixed y -position ($y = -0.4$ mm) as indicated in fig. 5.13. The dotted lines resemble the diameter d_o of the circular shaped sensitive detection area $A_c(x, y)$ of the CEM detection system. The acceleration voltage difference is $\Delta U_{\text{acc}} = 3.8$ kV. (a) ^{87}Rb -ion detection efficiency $\eta_i(x)$ for a CEM gain voltage of $U_{\text{CEM}} = 2.7$ kV. (b) Electron detection efficiencies $\eta_e(x)$ at different CEM gain voltages from $U_{\text{CEM}} = 2.4 - 3.3$ kV, in steps of 0.1 kV.

θ . The channel of the e^- -CEM is thus identified by smaller efficiency values³⁷ ($\eta_e(x, y) < 90\%$) at the applied CEM gain voltage of $U_{\text{CEM}} = 2.8$ kV, in accordance with the line scan measurements in fig. 5.15. Similar observations are reported in the literature by [87, 88, 131].

Increased detection efficiencies and CEM detector gain

In fig. 5.15, a line scan of the CEM detection efficiency $\eta_{i,e}(x)$ in relative x -direction is displayed, measured at a fixed y -position at $y = -0.4$ mm (dashed line; fig. 5.13). The depicted line scan data is obtained in an additional measurement series to fig. 5.13, using a higher spatial resolution (relative scan step size: $\Delta x = 20$ μm). The individual efficiencies $\eta_{i,e}(x)$ are calculated from the corresponding measured single counts $N'_{i,e}(x)$ and coincidences $N_c(x)$, identical to the obtained values in fig. 5.13. During the measurements, the acceleration voltage difference in between the CEMs is $\Delta U_{\text{acc}} = 3.8$ kV. At the e^- -CEM, alternating gain voltages of $U_{\text{CEM}} = 2.4 - 3.3$ kV are applied for the single line scans, in steps of 0.1 kV. The ion-CEM is held constant at a fixed gain voltage of $U_{\text{CEM}} = 2.7$ kV.

The line scan measurements confirm the expected shape in the efficiency response $\eta_{i,e}(x)$ as already observed in the 2D-scan measurements (fig. 5.13). In the e^- -CEM, the suggested channel structure of the CEM detector is identically observed (fig. 5.14). The line scan measurements show that from applied e^- -CEM gain voltages of $U_{\text{CEM}} > 3.0$ kV on (yellow scatter; fig. 5.15(b)), almost uniform high detection efficiencies $\eta_e(x) > 88\%$ are achieved over the full e^- -CEM detection area A_e (i.e., within the diameter d_o). By raising the CEM gain, it appears that especially the CEM channel efficiency experiences an enhanced efficiency increase³⁸ at higher CEM gain voltages. These observations coincide with detailed studies of previous experiments [87, 88, 133].

³⁷Following this argument, this simply corresponds to a smaller incident angle $\theta < 70^\circ$ at primary impact of the incident electrons in the CEM detector.

³⁸The increase corresponds to a higher primary electron yield value δ_0 (see section 2.3).

In fig. 5.15(a), additionally the calculated uncertainty $\Delta\eta_i(x)$ of the ion efficiency $\eta_i(x)$ according to eq. 5.5 is displayed for the ion-CEM. At the fringes of the sensitive area A_i of the ion-CEM (i.e., outside d_o in fig. 5.15(a)), the calculated efficiencies and uncertainties strongly vary due to large statistical fluctuations which result from the very low counts N_e and N_c compared to the large number of background counts N_{be} (eq. 5.5; see subsection 5.1.2). For the e^- -CEM, the calculated uncertainties $\Delta\eta_e(x)$ in fig. 5.15(b) are not shown to retain a better visibility of the spatial characteristic of the individual curves. One has to mention although that the calculated uncertainties $\Delta\eta_e(x)$ are *all* below 0.5%.

Reference experiments of the spatial CEM efficiency response

Generally speaking, in the literature only a few 2D-scan measurements of the sensitive area $A_{i,e}(x, y)$ of CEM detectors are reported as the measurements illustrated in fig. 5.13. Moreover, even 1D-line scans of the CEM detector entrance are rather uncommon (fig. 5.15). Even more, most experiments unfortunately do *not* show the sensitive area $A_{i,e}(x, y)$ of a CEM detector in the sense of an efficiency calibration, but only the relative count rate response $n_{i,e}(x, y)$ of the individual CEM detector. Employing different incident particles, the few scan calibrations are: (a) for EUV photons [114], (b) for incident ions (1D) [88, 97, 101, 107, 134, 135, 215], and (c) for incident electrons (1D) [87, 128, 133], and (2D) [131]. However, all these measurements are based on relative calibration methods only, and do not rely on an absolute calibration of the respective detectors (see section 5.1). Remarkably, this leaves the measurement in fig. 5.13 rather unique from a calibration point of view, and in the aspect of the determined absolute CEM detector efficiencies.

5.5.2. Sensitive detection area and sensitive volume

From the definition of subsection 4.5.1, the sensitive detection area $A_c(x, y)$ of the joint CEM detection system at $z = d/2$ can be derived. The previous observations and the 2D-scan measurements of subsection 4.5.3 show that in our setup the sensitive detection area $A_c(x, y)$ is identical to the sensitive area $A_e(x, y)$ of the e^- -CEM. This results as the sensitive area A_i of the ion-CEM is large compared to A_e due to the particular imaging properties of the joint CEM detection system (see subsection 4.5.3). The sensitive detection area $A_c(x, y)$ of the joint CEM detection system at $z = d/2$ therefore corresponds to the circular shape of the sensitive area $A_e(x, y)$ of the e^- -CEM (fig. 5.13(b)). From the line scan measurements shown in fig. 5.15, the diameter d_o of $A_e(x, y)$ and thus of $A_c(x, y)$ can be determined. Assuming a circular shape of the sensitive detection area $A_c(x, y) = \pi/4 \cdot d_o^2$, the diameter is $d_o = 0.84$ mm (fig. 5.15(a,b)). Within the entire sensitive detection area $A_c(x, y) = 0.55$ mm², neutral atom detection efficiencies $\eta_{\text{atom}}(x, y)$ exceed 98.8% for e^- -CEM gain voltages of $U_{\text{CEM}} > 3.0$ kV. The latter value follows from the enhanced, uniform detection efficiencies $\eta_e(x, y)$ over the entire sensitive area A_e of the e^- -CEM (fig. 5.15(b)).

To characterize the minimum sensitive volume V_c of the joint CEM detection system (see subsection 4.5.1), additional measurements are performed at z -positions different from $z = d/2$ in between the CEMs. The measurements display a similar spatial shape and extension of the sensitive detection area $A_c(x, y; z)$ at the different z -positions, indicating that the sensitive volume $V_c(x, y, z)$ has a longitudinal extension of at least ± 2 mm in z -direction from $z = d/2$ (fig. 4.11; see section 4.3). In general, the comparably large size of this volume and the good

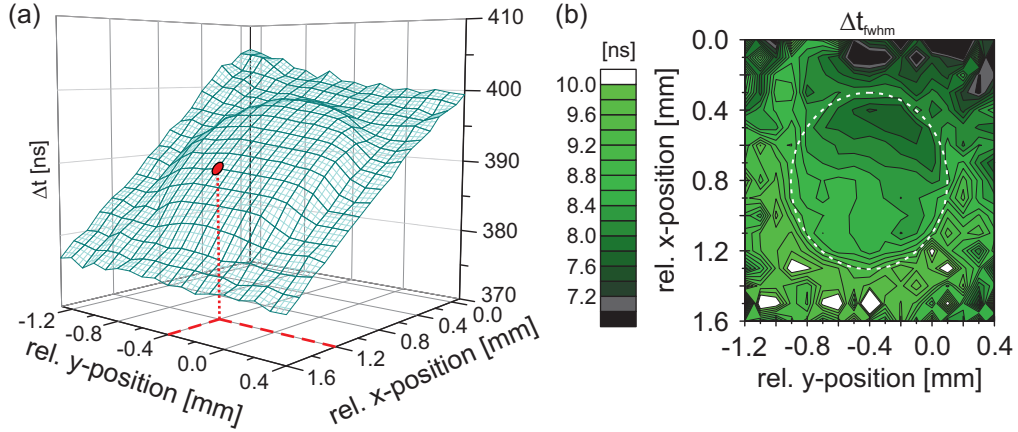


Figure 5.16: (a) Surface plot of the relative arrival time differences $\Delta t(x, y)$ obtained from the 2D-efficiency scan (fig. 5.13). The scan shows a narrow temporal variation of the time differences Δt over the scanned area with $\Delta t(x, y) = 385 - 400$ ns. The red spot indicates the position of the sample histogram of fig. 5.4 with $\Delta t(1.2 \text{ mm}, -0.4 \text{ mm}) = 388.5$ ns. (b) Full width at half maximum Δt_{fwhm} of the individual time differences $\Delta t(x, y)$ from the corresponding Gaussian histogram fits. Within the pronounced structure of (a), all fitted values are within the small range of $\Delta t_{\text{fwhm}} = 7.5 - 9.4$ ns (dashed circle).

optical access³⁹ to this volume in the glass cell make the joint CEM detection system therefore suitable for a wide range of spectroscopic applications, demanding the detection of neutral atoms down to a few or even single atom precision.

5.5.3. ⁸⁷Rb-ion impact position in the ion-CEM

In fig. 5.16, a spatial 2D-area plot with the determined ion arrival time difference $\Delta t(x, y)$ from the 2D-efficiency scan in (fig. 5.13(b)) are depicted. Additionally, also the fitted full width at half maximum values $\Delta t_{\text{fwhm}}(x, y)$ of the corresponding Gaussian histogram fit at each relative position $\Delta t(x, y)$ are shown (fig. 5.16(b)). The individual ion arrival time differences $\Delta t(x, y)$ are obtained from the 2D-area scan of the coincidence counting measurements for the sensitive detection area $A_c(x, y)$ in fig. 5.13. At each scan position⁴⁰ (x, y) in fig. 5.16, an individual Gaussian fit at the measured correlation peak in the correlation histogram⁴¹ is performed. As an example for a single correlation histogram in the 2D-scan measurements, the red spot in fig. 5.16(a) shows the relative position of the sample histogram of fig. 5.4 at a relative position of $(x = 1.2 \text{ mm}, y = -0.4 \text{ mm})$. The center value Δt of the individual Gaussian fits yields the relative ion flight time difference $\Delta t(x, y)$ according to the spatial position in the sensitive detection area $A_c(x, y)$ of both CEMs (e.g., $\Delta t(x = 1.2 \text{ mm}, y = -0.4 \text{ mm}) = 388.5$ ns; (see subsection 5.2.2)).

In the middle of the surface plot of the 2D-scan shown in fig. 5.16(a), a pronounced circular, elevated structure is observed exactly coinciding with the dimensions of the sensitive detection area $A_c(x, y)$ of the CEMs (see subsection 5.5.2). The surface plot further indicates a general

³⁹See subsection 4.2.3 for details.

⁴⁰The relative 2D-scan step size in x - and y -direction is $\Delta x, y = 100 \mu\text{m}$ (see subsection 5.5.1).

⁴¹The area of the peak in the individual correlation histograms (see subsection 5.2.2) is used to derive the number of coincidences N_c and to determine the absolute efficiencies $\eta_{i,e}(x, y)$.

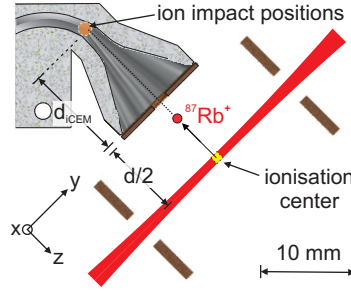


Figure 5.17: Schematic illustration of the position of the ^{87}Rb -ions at primary particle impact in the ion-CEM channel (orange spot). The illustrated size of the spot is not to scale. The particular impact position according to the obtained relative arrival time differences $\Delta t(x, y)$ (fig. 5.16(a)) is determined from the covered distances $d_{i\text{CEM}}$ of the ^{87}Rb -ions in the ion-CEM (eq. 4.5).

linear increase of the flight time differences Δt in x -direction while it remains almost constant in y -direction. Remarkably, the relative arrival time differences $\Delta t(x, y)$ of the 2D-scan only show a narrow time-of-flight window of $\Delta t(x, y) = 385 - 400$ ns for the ^{87}Rb -ions (fig. 5.16(a)). Moreover, in fig. 5.16(b) the full width at half maximum values Δt_{fwhm} of the corresponding Gaussian histogram fits at the individual time differences $\Delta t(x, y)$ are displayed. Within the pronounced structure of fig. 5.16(a), all fitted values are within the small range of $\Delta t_{\text{fwhm}} = 7.5 - 9.4$ ns (dashed circle).

Impact position and enhanced detection efficiencies

Assuming the flight time model of subsection 4.4, the measured arrival time differences $\Delta t(x, y)$ in fig. 5.16(a) from the 2D-efficiency scan (fig. 5.13) allow to estimate the covered distance of the ^{87}Rb -ion in the ion-CEM. They thus enable to determine the particular impact positions of the incident ^{87}Rb -ions in the ion-CEM (fig. 5.17). Using the refined model of subsection 4.4.1, the observed relative arrival time differences $\Delta t(x, y)$ simply transform into different covered distances $d_{i\text{CEM}}$ of the ^{87}Rb -ions in the ion-CEM (fig. 5.17). With the parameter $\Delta t(x, y)$ given by the correlation histograms of the 2D-scan measurements (fig. 5.16), the covered distances $d_{i\text{CEM}}$ in the CEM can thus be calculated (eq. 4.5; see section 4.4). For the calculations, a constant electron flight time of $t_e = 1$ ns is assumed yielding an approximated ion flight time of $t_i \approx \Delta t$ for the model.

The observed values in the pronounced circular structure of fig. 5.16 correspond to calculated impact positions at $d_{i\text{CEM}} = 11.31 - 12.34$ mm in the ion-CEM. Such large covered distances $d_{i\text{CEM}}$ in the ion-CEM generally imply that the ^{87}Rb -ions in the ion-CEM have their primary impact position in the CEM channel at the CEM channel wall, not in the CEM cone (fig. 5.17). This observation is further supported by the high detection efficiencies observed in fig. 5.13, which will therefore occur under grazing incidence θ at primary particle impact in the ion-CEM (CEM channel hit; see subsection 2.4.3). As enhanced detection efficiencies in CEM detectors are mostly caused by a grazing incidence θ of the primary particles at the CEM surface, a CEM channel impact seems therefore reasonable.

The small temporal range from $\Delta t(x, y) = 385 - 400$ ns, and the particular shape of the data ($\Delta t(x, y)$; constant in y -direction, linear in x -direction; fig. 5.16) additionally suggest that by imaging of the joint CEM system, the incident ^{87}Rb -ions are focused and deflected to one

side of the CEM channel wall. The obtained different flight times $\Delta t(x, y)$ in x -direction also correlate in detail to the slightly increased ion efficiencies in fig. 5.13 for relative x -positions from $x = 0.8 \text{ mm} - 1.4 \text{ mm}$, while they remain almost constant in the relative y -direction. This becomes plausible as shorter covered distances d_{iCEM} in the CEM correspond to a slightly increased grazing angle θ at primary particle impact, thus yielding a higher detection efficiency for these values (see subsection 2.4.3). Similar observations for an efficiency variation due to deflecting the incident particles onto one CEM channel wall with increasing grazing angles θ and correspondingly enhanced detection efficiencies are reported in the literature by [131].

Another indication that a CEM channel hit and not a CEM cone hit is observed, is the reduced CEM gain value G_0 at the particular positions of fig. 5.16. According to [87], the gain G_0 for a CEM channel hit will yield a reduced gain value by at least a factor of two to five compared to a primary particle impact in the CEM cone. This results as the generated secondary electron avalanche in the CEM channel misses two to three stages g_m of amplification in the CEM, despite achieving a higher primary particle yield δ_0 at first impact (see subsection 3.1.1). In the literature, such experimentally reduced gain values G_0 for explicit CEM channel impacts are reported by [107, 131]. From gain measurements with our system at the position ($x = 1.2 \text{ mm}, y = -0.4 \text{ mm}$), a reduced gain value G_0 by approximately a factor of five to ten is observed compared to the gain calibration measurements in section 3.3. This further indicates a CEM channel impact as already suggested by the time difference Δt measurements.

Temporal spread and impact position uncertainty in the ion-CEM

In fig. 5.16(b)), the small temporal spread Δt_{fwhm} of the relative arrival times $\Delta t(x, y)$ for the correlated ^{87}Rb -ions over the sensitive detection area $A_c(x, y)$ is extraordinary. By sheer value, it gives a strong evidence that the imaging of the ^{87}Rb -ions from the small photoionisation volume at $z = d/2$ into the CEM detector and onto the CEM channel wall is extremely stable and reproducible. Experimentally, the temporal spread Δt_{fwhm} of the individual Gaussian correlation peaks is caused by three possible contributions. These are on one hand the photoionisation of neutral atoms at a different spatial z -position of the ionisation center in the ionisation volume, and the temporal broadening of the pulse arrival due to ballistic propagation of the secondary electron avalanche in the CEM detector [85, 159]. Additionally, also a slight position uncertainty at primary particle impact in the CEM will contribute to a temporal spread in Δt (fig. 5.17). Of these three contributions, the first two are intrinsically given and remain therefore set for a specific configuration of the joint CEM system. However, the latter contribution allows to some extent to determine the accuracy and stability of the imaging of the ionisation fragments in the corresponding CEMs. This follows from the estimated magnitude in impact position uncertainty in relation to the first two contributions.

The size of the ionisation volume in the calibration measurements is approximately $V_{\text{ion}} = (86 \mu\text{m})^3$ (see subsection 4.5.2). The photoionisation at a different spatial z -position in the volume other than at $z = d/2$ corresponds to a lateral displacement of the ionisation center in the z -direction up to $z_0 = d/2 \pm 43 \mu\text{m}$. As a result, a photoionisation event at the fringe of the overlap volume ($\pm 43 \mu\text{m}$) modifies the relative ion flight time Δt by a calculated value of $\Delta t(z \pm 43 \mu\text{m}) = \pm 1.11 \text{ ns}$ (eq. 4.5; see section 4.4). This corresponds to a full width at half maximum value of $\Delta_{\text{diffz}} = 2\sqrt{2 \ln 2} \times 1.11 \text{ ns} = 2.6 \text{ ns}$.

The temporal spread in the transit time of the developing secondary electron avalanche in the CEM is $t_{\text{spread}} < 2.4 \text{ ns}$ (appendix A.3), where t_{spread} denotes a single standard deviation

(1σ) of the transit time t_{transit} . In the literature, this value agrees well with common measured values t_{spread} in the order of $t_{\text{spread}} = 1\sigma(t_{\text{transit}}) \approx 1 - 3$ ns [153, 230]. In values of the full width at half maximum Δt_{fwhm} , the temporal spread of the secondary avalanche in the CEM of $t_{\text{spread}} < 2.4$ ns corresponds to a value of $\Delta_{\text{spread}} = 2\sqrt{2 \ln 2} t_{\text{spread}} = 5.7$ ns.

In addition, these two uncertainties already yield a calculated temporal spread of $\Delta_{\text{spread}} + \Delta_{\text{diffz}} = 8.3$ ns in comparison to the observed values of $\Delta t_{\text{fwhm}} = 7.5 - 9.4$ ns (dashed circle; fig. 5.16(b)). This leaves a maximum temporal spread for an eventual impact position uncertainty of only $\Delta_{\text{impact}} \approx 2$ ns. Therefore, a significant position uncertainty at impact in the CEM can be excluded as a possible source for any temporal uncertainty in the relative arrival times $\Delta t(x, y)$. Accordingly, the remaining temporal uncertainty will translate into a calculated, relative position uncertainty at particle impact of only $\Delta d_{\text{CEM}} = \pm 0.07$ mm at a single 2D-scan position (fig. 5.16(a)). This implies that almost the same impact position in the CEM is hit repetitively during an entire measurement series at a single 2D-scan position. Therefore, the imaging of the ^{87}Rb -ions in the ion-CEM is extremely stable and reproducible. This further supports the outstanding accuracy and stability of the imaging of the two photoionisation fragments of the joint CEM detection system in the corresponding CEMs.

6. Summary and Outlook

In this thesis, a novel detection scheme for the fast and efficient detection of single atoms is experimentally demonstrated. The detection scheme is based on the hyperfine-state selective photoionisation of single atoms and the subsequent detection of the correlated photoionisation fragments using two channel electron multiplier detectors (CEMs). The scheme is developed to provide a highly-efficient and hyperfine-state selective readout unit for atomic qubits in the current atom-photon entanglement experiments with single neutral ^{87}Rb -atoms in our group. It is expected to detect the atomic qubit state within sub-microsecond time and with high detection efficiency. These two properties are the prime detector requirements for a proposed loophole-free test of a Bell inequality with two entangled ^{87}Rb -atoms at two remote locations [18, 21].

In the actual single atom dipole trap setup [45, 183], photoionisation detection will substitute the comparably slow and inefficient fluorescence detection of the single neutral ^{87}Rb -atom. In order to quantify photoionisation detection, the two main components of the detection scheme were individually investigated. In this work, the focus was on the development and experimental realisation of the CEM detection system, which allows to register the photoionisation fragments with two CEM detectors. Measurements on the CEM detection system show that it enables to detect single ^{87}Rb -atoms by their ionisation fragments with a neutral atom detection efficiency of $\eta_{\text{atom}} = 0.991 \pm 0.002$ within a detection time of $t_{\text{det}} = 415.5$ ns following a photoionisation event (see section 5.4). In a separate experiment, the hyperfine-state selective photoionisation of optically trapped single neutral ^{87}Rb -atoms yields a photoionisation probability of $p_{\text{ion}} = 0.991 \pm 0.001$ and an ionisation time of $t_{\text{ion}} = 386$ ns (see section 4.1). Combining these two components of photoionisation detection in a future single setup, this will allow to detect single ^{87}Rb -atoms in an optical dipole trap with an absolute detection efficiency of $\eta = p_{\text{ion}}\eta_{\text{atom}} = 0.982 \pm 0.002$ within a detection time of $t_{\text{tot}} = t_{\text{ion}} + t_{\text{det}} = 802$ ns [24].

For the experimental realisation, the entire CEM detection system has been designed and built from scratch. A ready-to-implement version of the CEM detection system for the actual single atom trap setup has been completed (see chapter 5). The subsequent calibration of the CEM detectors with the correlated ionisation fragments from photoionisation enables to determine absolute detection efficiencies for the CEM detectors and the CEM detection system (see chapter 5). The characterisation of the CEM detection system further provides measurements on the imaging stability of the entire detection system (see section 4.5), and the single CEM detector performance (see chapter 3). The particular design of the system will admit a comparably fast and easy integration of the novel detection system into the single atom trap setup (see section 4.2), as initially intended.

The characterisation of the CEM detectors allows a direct comparison with the reduced yield model for the CEM efficiency response and with the cascaded dynode detector theory of chapter 2. Additionally, the correlation measurements yield the relative flight time difference $\Delta t = t_i - t_e$ of the two photoionisation fragments up to the CEM detectors after a common photoionisation event (see section 5.3). From the flight time difference and the transit time of the secondary avalanche in the CEM, the detection time t_{det} for a neutral atom after a photo-

ionisation event can be calculated. The flight time difference Δt further allows to determine the impact position of the ^{87}Rb -ions in the ion-CEM detector with the corresponding impact parameters E_{kin} and θ at primary particle impact.

The photoionisation of neutral atoms in a defined ionisation volume out of the background vapour further represents the experimental realisation of a unique calibration source for charged particle detectors. This follows as the photoionisation of neutral atoms in the overlap volume of two laser beams produces correlated charged particle pairs, with the ionisation volume almost deliberately positionable and with variable size (see section 4.5). This is remarkable as a similar pair source for charged particle detector calibration was previously not available (see section 5.1).

Although being inherently destructive and thus a single-shot¹ detection scheme, photoionisation detection will compete with the most sophisticated fluorescence detection readouts for neutral atoms. Moreover, the large optical access (see section 4.2) and the huge sensitive detection area (see section 5.5) leave the CEM detection system generally interesting concerning future detection applications with single atoms or atomic ensembles via their ionisation fragments. The concept of photoionisation detection is further universally applicable to any atomic or molecular species, assuming the corresponding atomic transitions in the particular species can be individually addressed accordingly.

6.1. Short term prospects with the current CEM detection system

In its current state, the CEM detection system represents a highly selective and sensitive single particle detector, allowing to determine partial pressures or concentrations of single isotopes or molecules below the detection limit of any conventional detection system. This results as the ultimate detection limit with the CEM detection system is provided by the ratio of true to accidental coincidences N_c/N_{ac} of the correlation measurement, and not by the ratio of the photoionisation to background counts $N_{i,e}/N_{ib,eb}$ of the single CEM detectors as in conventional systems (see section 5.2). It will thus be able to identify different species due to the different arrival time at the CEM detectors according to the mass-to-charge ratio of the single isotopes or molecules (see section 5.3). However, to resolve the mass of *single* particle incidences in the CEM detection system according to their individual flight time, the species have to be slightly different in their mass-to-charge ratio assuming the current detector configuration (see subsection 5.3.1).

Combined with the single atom trap environment, the CEM detection system further enables highly-efficient precision spectroscopy on single neutral atoms with hyperfine-state selectivity. This will permit to measure, e.g., the photoionisation cross section of a single neutral atom free from any statistical uncertainties usually associated with atomic ensembles [245–247], and down to single hyperfine-state resolution. The combination of the single atom trap with the CEM detection system thus resembles an ideal testing ground for ionisation-based precision spectroscopy on ultracold single atoms.

Minor amendments Better galvanic isolation from the glass cell environment or additional shielding will allow to operate the current CEM detection system at higher acceleration voltages ΔU_{acc} (see section 4.2). In accordance with the CEM efficiency model of section 2.4,

¹Single-shot in the meaning that a definite measurement result is obtained after a single readout operation. Here, the single readout operation is represented by a successful photoionisation of the neutral atom.

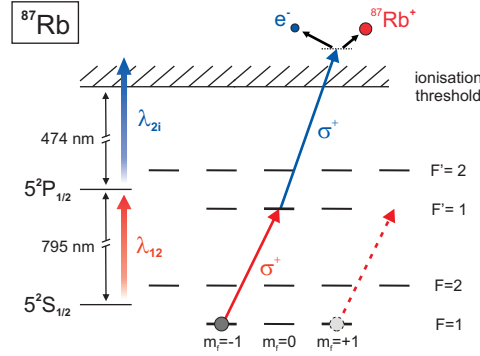


Figure 6.1: Proposed single hyperfine-state selective readout of the ^{87}Rb -atom qubit by polarisation dependent photoionisation via the $D1$ -transition ($\lambda_{12} = 795 \text{ nm}$). Using σ^+ -polarised light for the excitation transition λ_{12} , only the $m_f = -1$ state is subsequently ionised while the $m_f = +1$ state remains in a 'dark' state.

the maximum attainable ^{87}Rb -ion detection efficiency in such a configuration is calculated to $\eta_i = 0.9943$ at an impact energy of $E_{\text{kin}} = 10 \text{ keV}$ (see section 5.4). For the photoelectrons, a maximum detection efficiency of $\eta_e = 0.8940$ at $E_{\text{kin}} = 2.2 \text{ keV}$ is estimated. For such fields, the flight time of the ^{87}Rb -ion will only be $t_i = 170 \text{ ns}$ ($\Delta U_{\text{acc}} = 20 \text{ kV}$; see section 4.4). The previous values will provide a theoretical neutral atom detection efficiency of $\eta_{\text{atom}} = 0.9995$.

Additionally, the use of a slightly modified CEM detector configuration will yield higher detection efficiencies and a larger optical access than in the current system (see Appendix C). In particular the implementation of a single CEM detector unit only with an opposing conversion dynode seems to be a promising alternative as the ionisation fragments will both be detected by the same CEM detector and will therefore be processed by the same pulse processing electronics. This will make a second CEM detection unit with its associated pulse processing electronics and high voltage power supplies obsolete, further simplifying the CEM detection system.

Triggered photoionisation detection In the future, pulsed photoionisation schemes with single laser pulses of high intensity will yield photoionisation times t_{ion} in the nanosecond range and with ionisation probabilities p_{ion} approaching unity² [171, 172, 174, 176, 248]. This will enable a heralded detection of single atoms within a nanosecond time window, triggered by the advent of the ionising laser pulse. The triggered photoionisation will allow, e.g., to explicitly determine the individual flight times t_i and t_e of the photoionisation fragments until impact in the corresponding CEM detectors (see section 5.3). It may also be employed for a gated particle detection at the single CEM detectors within a certain time window after the photoionisation event.

Atom qubit readout protocol without STIRAP transfer The use of pulsed photoionisation and an alternative detection scheme via the $D1$ -transition in ^{87}Rb (fig. 6.1) will make the

²This results as in a resonant two-step photoionisation scheme the spontaneous decay from the resonant intermediate state during the pulsed excitation of the atom can be neglected on such timescales [171, 172, 174].

adiabatic transfer of the atomic qubit state³ via a stimulated Raman adiabatic passage (STIRAP) process [249, 250] in the current atomic qubit readout protocol obsolete [21, 23, 45]. This will be realised by polarisation dependent photoionisation of the single Zeeman sublevels, where the corresponding circular polarisation for the excitation transition (e.g., σ^+ for $\lambda_{12} = 795$ nm) excites the 'bright' state ($|m_f = -1\rangle$), but leaves the 'dark' state ($|m_f = +1\rangle$) unaffected (fig. 6.1). This improved readout scheme will further shorten the detection time of the current readout protocol by 120 ns for the STIRAP transfer [18], and additionally avoid the imperfect state transfer of $\eta_{\text{stirap}} = 0.97$.

6.2. Long term options using photoionisation detection

Photoionisation detection has a potential range of applications in quantum information technologies, quantum communication, and precision spectroscopy of single atoms. In the future, it may be applied as site-selective, conditional readout unit for atomic qubits in cluster states for one-way quantum computation [251, 252], as highly-efficient atomic hyperfine-state detection unit for large-scale atomic clock arrays in optical lattices [253], for real-time probing of neutral atom ensembles with sub-Poissonian accuracy [221, 234, 235], or as detector for a loophole-free test of a Bell inequality with a pair of entangled ^{87}Rb -atoms at remote locations [18, 21].

Site-selective qubit readout of quantum registers The photoionisation detection scheme seems exceptionally suited for future quantum information applications based on single neutral atoms as qubits [254]. In particular the speed and the spatial selectivity of the photoionisation process might become highly versatile as the individual optical addressing of single neutral atom qubits in adjacent optical dipole traps [255–257] and in single lattice sites [240] has been successfully demonstrated. Therefore, photoionisation detection will possibly serve as position-dependent readout for quantum registers made of strings of individually trapped neighboring atoms [255–259], or atomic ensembles in optical lattice structures [238–240, 260, 261]. Here, especially the high optical access to the ionisation region and the large sensitive volume of the CEM detection system may be additionally advantageous in comparison to conventional detection methods.

In the context of quantum computation with single atom qubits, the site-specific qubit readout represents a key ingredient for quantum registers based on atomic qubits [262, 263]. By optical addressing, photoionisation detection will thus enable to read out individual qubit sites without perturbing others, or allow to deliberately ionise specific patterns or entire groups of single atom qubit sites. For the conditional readout of single atom qubits in a cluster state for one-way quantum computing [251, 252], even the destructive nature of the photoionisation process may be advantageous. By physically removing the probed atomic qubit out of the array or lattice, decoherence in the remaining qubits of the cluster state may be reduced.

Moreover, a readout operation time for a single qubit site of 50 ns seems to be feasible with the current CEM detection system (see subsection 3.2.2). As a consequence, this will theoretically allow to probe a macroscopic array of, e.g., up to 100 atom qubits within an

³In the current setup, the atomic qubit is encoded in single Zeeman sublevels of the hyperfine ground state of the ^{87}Rb -atom [21, 23], where the qubit state $|1\rangle$ is represented by the $|m_f = +1\rangle$ sublevel and $|0\rangle$ is denoted by the $|m_f = -1\rangle$ state of the hyperfine ground level $F = 1$ (fig. 6.1).

overall detection time of only a few microseconds and with a high detection efficiency per single qubit site.

Loophole-free test of a Bell inequality with two remote atoms In the future, the combined detection efficiency η and the detection time t_{tot} of the photoionisation detection scheme is expected to exceed the experimentally demanding detector requirements⁴ to close the detection loophole. This will allow a proposed loophole-free test of Bell's inequality under strict Einstein locality conditions with two entangled ^{87}Rb -atoms at remote locations [18, 21]. Assuming an experimental distance of $d = 300$ m between the two single atom trap setups, the sub-microsecond detection time of photoionisation detection will therefore enable to close the locality and the detection loophole simultaneously in one experiment. By estimation, the determined detection efficiency of $\eta = 0.982$ for a single ^{87}Rb -atom qubit readout will require only 611 entangled atom-atom events for the violation of the Bell inequality by three standard deviations [18]. With this, a concise loophole-free test of a Bell inequality with statistical significance should be feasible within 51 hours of continuous measurement.

⁴For a CHSH-type Bell inequality [28] with two entangled ^{87}Rb -atoms [18, 21], the prime requirements for the atomic qubit readout are the selective detection of single hyperfine-states, an absolute detection efficiency of $\eta \geq 2/(1 + \sqrt{2}) \approx 0.8284$ for the entire detection process [15, 25–27], and a sub-microsecond detection time for a spatial separation of the two remote ^{87}Rb -atoms by a distance of $d = 300$ m.

A. Appendix

A.1. Natural constants

The values of the following natural constants correspond to the recommendations of the CODATA commission. For further reference see <http://physics.nist.gov/cuu/Constants/index.html>.

quantity	symbol	value	unit
electron charge	e_0	$1.602\,18 \times 10^{-19}$	C
Boltzmann constant	k_B	$1.380\,650\,4(24) \times 10^{-23}$	J K ⁻¹
Planck constant	$\hbar = h/2\pi$	$1.054\,571\,628(53) \times 10^{-34}$	J s
speed of light	c_0	299 792 458	m s ⁻¹
electron mass	m_e	$9.109\,382\,15(45) \times 10^{-31}$	kg
atomic mass unit	u	$1.660\,538\,782(83) \times 10^{-27}$	kg

A.2. Atomic properties

The following table summarizes the most important atomic properties used in the experiments described in the context of this thesis.

symbol	quantity	⁸⁷ Rb	unit	reference
m_{Rb}	atomic mass	86.909 180 520(15)	u	[264]
E_{thres}	ionisation energy	4.177 127 06(10)	eV	[265, 266]
d_{Rb}	atom radius	235	pm	[267]
I_{sat}	saturation intensity	1.669	mW cm ⁻²	[268]
Φ_{Rb}	electron work function	2.26	eV	[237]

A.3. Channel electron multiplier data

Note that for an explicit illustration of the internal CEM structure, see fig. 4.4.

Dimension	Parameter	Value
typical gain ¹ (at gain 2.3 kV)	G_0	1×10^8
channel resistance ¹ (ion-CEM)	R_{brown}	204 M Ω
channel resistance ¹ (e ⁻ -CEM)	R_{blue}	279 M Ω
dark count rate ¹	n_{dark}	0.02 counts s ⁻¹
transit time ¹ (at gain 2.3 kV)	t_{transit}	26 ns
transit time spread ¹ (at gain 2.3 kV)	t_{spread}	< 2.4 ns
average pulse width ¹ (FWHM, at gain 2.3 kV)	t_{FWHM}	8 ns
channel length	l	54.5 mm
cone length	l_{cone}	8.4 mm
channel tube length	l_{chan}	46.1 mm
channel diameter	d	1.4 mm
estimated Radius of curvature	R_0	~ 1 mm
distances in the cone section	d_{cone}	0 – 6.7 mm
distances in the channel section	d_{channel}	6.8 – 13.1 mm
minimum distance for primary particle impact	$d_{\text{hit,min}}$	4.25 mm (cone hit)
maximum distance for primary particle impact	$d_{\text{hit,max}}$	13.1 mm (channel hit)

¹

A.4. Joint CEM detector data

A detailed overview of the explicit CEM detector configuration is given in chapter 4.

Dimension	Parameter	Value
distance between both CEM apertures	d_z	15.73 mm
cone copper aperture plate thickness	z_{aperture}	0.5 mm
cone copper aperture plate diameter	$d_{\text{ap-full}}$	11.4 mm
cone copper aperture	d_{aperture}	2 mm (hole diameter)

¹Values are provided by the manufacturer (www.sjuts.com) and stated for juvenile detectors immediately after burn-in phase. At increased CEM age/use, some of these values might differ considerably.

B. Compound Poisson distribution

In the following, the source code for the explicit calculation of the compound Poisson distributions in subsection 2.1.2 is given (see fig. 2.2). The calculation strictly follows the Polya model introduced in Ref [53] (explicitly: [53], eq. (5), page 177). For the implementation of the numerical computation, the program *Mathematica7* from Wolfram Research was used. The parameters δ_0, δ, Js , and n_{\max} for the calculation of the individual distributions have to be adjusted, correspondingly.

```

 $\delta_0=4; \delta=2;$ 

 $\mu[1\_]:=Which[l==1,\delta_0,True,\delta];$ 
 $\mu[1];$ 
(*  $\mu[1] == \delta_0, \mu[2..i] == \delta$  *)

 $b[1\_]:=Which[l==1,.0000001,True,.0000001];$ 
 $b[1];$ 
(*  $b[1..i]$  chosen to .0000001, as 0 cannot be computed *)

 $Js = 4;$ 
(*  $Js = m+1$ ;  $m$  is number of amplification stages  $gm$  *)

 $nmax=200;$ 
(* max. range for  $n$ :  $n \rightarrow \{0,nmax\}$  *)

 $P[n_,k_,l_,j_,erglist\_]:=Module[{erg=-1},$ 
   $Which[l>j || k>j || k<0 || l<1,erg=0,$ 
     $k==0\&\&n==1,erg=1,$ 
     $k==0\&\&n\neq 1,erg=0,$ 
     $erglist[[n+1,k+1,l+1]]\geq 0,erg=erglist[[n+1,k+1,l+1]],$ 
     $n==0, erg=(1+b[1]\mu[1](1-P[0,k-1,l+1,j,erglist]))^{(-1/b[1])},$ 
     $True,erg=(\mu[1]/n)(P[0,k,l,j,erglist])^{(b[1])}*$ 
     $Sum[(n+i(b[1]-1))P[i,k,l,j,erglist]P[n-i,k-1,l+1,j,erglist],\{i,0,(n-1)\}]$ 
  ];
   $erg$ 
];

Timing[ $erg = Table[-1,\{n,0,nmax\},\{k,0,Js\},\{l,0,Js\}];$ 
   $For[k=0,k<Length[erg[[1]]]-1,k++,$ 
     $For[l=0,l<Length[erg[[1,l]]]-1,l++,$ 
       $For[n=0,n<=Length[erg]-1,n++,$ 
         $erg[[n+1,k+1,l+1]]= P[n,k,l,Js,erg];$ 
      ]
    ]
  ]
];

 $Liste=Transpose[Table[Drop[erg[[All,i,2]],1],\{i,1,Js\}];$ 
 $%%//MatrixForm;$ 
 $ListPlot[Drop[erg[[All,Js,2]],1],PlotRange->\{\{0,All\},\{0,All\}\},Frame->True]$ 

```


C. Three alternative CEM detector configurations

In the following, three proposals for an alternative CEM detector configuration are given. The alternative configurations will further enhance the detection efficiency and detection time in comparison to the current CEM detection system, and exhibit additional properties compared to the standard system of this thesis.

Universal CEM detector improvements In general, there are three universal improvements for the CEM detection system of which the actual CEM detector configuration and also the three proposed configurations will probably benefit. However, particularly the cryogenic option (c) is extremely challenging to implement in the current experimental system. The improvements are:

(a) Transfer of the entire HV-vacuum wiring of the CEM detectors (fig. 4.6; section 4.2) on printed circuit boards based on SMD elements and CEM detector adaptable substances [269], thereby creating a chip-based HV-wiring architecture¹ for the CEM detection system ('CEM chip'). In this context, already the galvanic decoupling of the HV-signal at the CEM anode via an SMD capacitor in the UHV allows an improved impedance matching of the pulse signal cable (see section 3.4). The printed circuit boards enable a simplified but more accurate simulation of the potential distribution (see section 4.3), and a very easy integration of the 'CEM chip' in any suitable UHV or glass cell environment (see section 4.2).

(b) Additional shielding of the signal cables and the ceramic body of the CEM detectors in a conducting enclosure ('metal box') to suppress dark counts and spurious noise.

(c) Cryogenic cooling of the detectors [270–273] to further reduce thermal noise and thus the dark count rate in the CEM detectors.

C.1. Two CEMs, individual acceleration of the ionisation fragments

In the first alternative configuration, two isolated copper apertures in front of the CEM entrance cone will be additionally introduced (fig. C.1). A different electric potential with respect to the CEM cone entrance potential can be applied on these apertures. In fig. C.1(b), the corresponding electric potential simulation along the central flight axis is shown, similar to the potential simulations of section 4.3. For the simulation, sample electric potentials of $U_{i,aper} = -5\text{ kV}$ and $U_{e,aper} = +5\text{ kV}$ for the additional copper apertures are used. The cone potentials of the CEM detectors at particle entrance are $U_{i,cone} = -10\text{ kV}$ for the ion-CEM and $U_{e,cone} = +0.4\text{ kV}$ for the e^- -CEM. This particular configuration results in kinetic impact energy of the ionisation fragments of $E_{kin,e} = 0.8\text{ keV}$ for the photoelectron and of $E_{kin,e} = 9.6\text{ keV}$ for the ^{87}Rb -ion.

The integration of the two additional copper apertures thus enables an individual acceleration or deceleration of the photoionisation fragments, similar to the configuration of Ref. [95]. It therefore allows to modify the acceleration of the individual ionisation fragment to achieve

¹See http://www.sjuts.com/index_english.html for the successful implementation of such circuits.

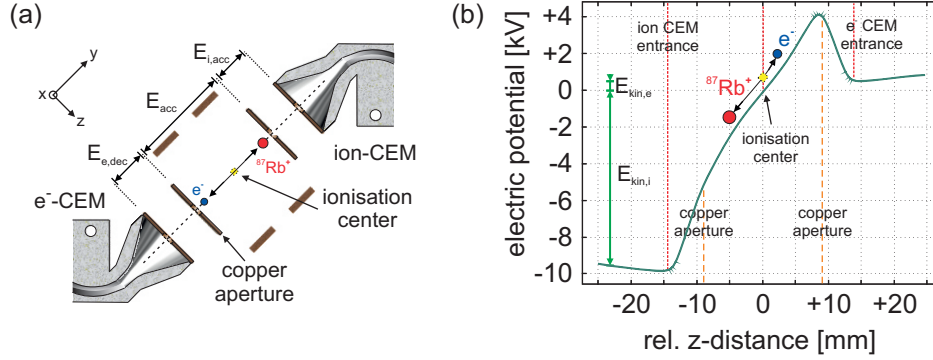


Figure C.1: (a) CEM detection system configuration with two additional isolated copper apertures. An additional electric field ($E_{i,acc}$, $E_{e,dec}$) with respect to the CEM cone potential enables an individual acceleration or deceleration of the photoionisation fragments. (b) Electric potential simulation along the central flight axis of the ionisation fragments. The sample configuration results in a kinetic impact energy in the CEMs of $E_{kin,e} = 0.4$ keV for the photoelectron and of $E_{kin,i} = 9.6$ keV for the ^{87}Rb -ion.

the optimum kinetic energy E_{kin} at primary particle impact in the corresponding CEM detector, resulting in a maximized detection efficiency $\eta_{i,e}(E_{kin})$. In addition to this, the modified system will yield an even larger optical access compared to the current CEM detection system. It will further reduce incident stray light and stray particles in the CEM detectors due to the additional shielding by the apertures.

C.2. Two CEMs, and conversion dynodes

In a further modification, additional conversion dynodes are introduced in the system as illustrated in fig. C.1. The dynodes are mounted under grazing incident angle ($\theta > 80^\circ$) corresponding to the incident primary particle. The use of individual conversion dynodes [53, 72] yields an additionally enhanced optical access and higher detection efficiencies with the CEM detectors due to more efficient conversion of the primary particle (see section 2.3). For alkali ions, detection efficiencies approaching unity have already been reported for Li^+ , Rb^+ , and Cs^+ using a converter plate [106]. Moreover, in this detector configuration the CEM detector entrances are additionally rotated by 90° with respect to the ionisation center. This will further improve the shielding of the detectors against stray light or stray charges from the ionisation center.

C.3. Single CEM detector, and photoion conversion dynode

In fig. C.3, the configuration of a single CEM detector and an opposing photoion conversion dynode is shown. The configuration represents a simplification of the current CEM detector setup, as only one CEM detector (e^- -CEM) is used with its associated detection electronics. The single CEM detector thus serves as a combined detector for the primary photoelectrons and the temporally delayed, secondary electrons originating from the conversion of the primary photoion at the conversion dynode. Figure C.3(c) shows a sample 2D-simulation of the isolines of the electric potential configuration of this setup. For the sample simulation, the cone

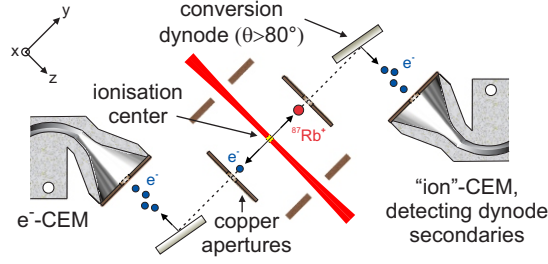


Figure C.2: Similar configuration to fig. C.1, using additional conversion dynodes mounted under grazing incident angle ($\theta > 80^\circ$) corresponding to the incident primary particle. A higher detection efficiency is achieved due to a highly-efficient conversion of the primary particles at the conversion dynode (see section 2.3). Moreover, as the CEMs are situated farther away from the photoionisation interaction region, improved shielding against stray light and stray charges can be implemented.

potential of the e^- -CEM was $U_{e,\text{cone}} = -0.4\text{ kV}$, the copper aperture had $U_{i,\text{aper}} = -5\text{ kV}$, and the dynode potential was $U_{\text{dyn}} = -10\text{ kV}$. Figure C.3(d) illustrates the electric potential of the CEM detector-dynode configuration along the central flight axis (dashed line, fig. C.3(c)) of the ionisation fragments.

The single CEM and conversion dynode detector configuration yields the main advantage that only a single CEM with single subsequent pulse processing electronics is used, providing a rather compact detection setup. From a measurement point of view, it is particularly interesting as both generated pulses from the two initial photoionisation fragments ($^{87}\text{Rb}^+$, e^-) are processed in the *same* pulse processing electronics. Note that the neutral atom detection time t_{det} in the system will be mainly determined by the distance d_{ion} the photoion has to travel until it is converted in the dynode (fig. C.3(b,d)).

At normal incidence ($\theta = 0^\circ$) to the approaching photoions, the secondary emission yield of a common conversion dynode is $\delta_0 = 6$ per primary ^{85}Rb -ion [72]. The use of a conversion dynode thus intrinsically provides a high detection efficiency for the initial photoion by the sheer number of generated secondary electrons after primary particle conversion (see section 2.3). The conversion dynode in the detector configuration is further rotateable (fig. C.3). A rotation to a grazing angle $\theta > 80^\circ$ will result in a huge secondary electron yield $\delta_0 > 20$ for common conversion dynode substrates. Therefore, even if the individual detection efficiency of the back-reflected accelerated secondary electrons in the e^- -CEM is low due to their large kinetic energy at impact in the detector, the overall detection efficiency for the converted photoion will approximate unity (see subsection 2.3.2).

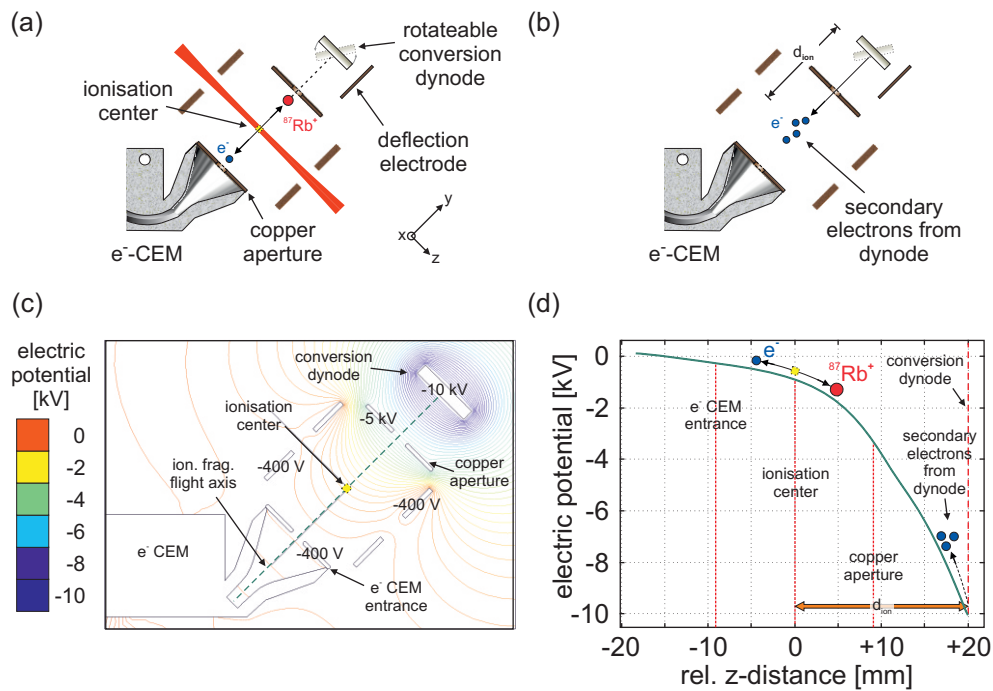


Figure C.3: Single CEM detector and photoion conversion dynode. (a) Neutral ⁸⁷Rb-atoms are photoionised in the overlap volume of two laser beams. The generated photoelectrons are directly detected. The ⁸⁷Rb-ions are accelerated towards the conversion dynode, and are efficiently converted into several secondary electrons. (b) Being oppositely charged, the generated secondary electrons are deflected into the e⁻-CEM, and subsequently counted. (c) Simulated 2D-isoline model of the electric potential for the single CEM-dynode configuration. (d) Illustration of the electric potential along the central flight axis (dashed line, (c)). The relative position of the ionisation center, the copper aperture, and the CEM cone entrance are depicted by dashed lines.

D. Possible CEM detection system applications

In the following, three possible applications for photoionisation detection and the current CEM detection system of this thesis are illustrated.

D.1. Photoionisation as calibration source for charged particle detectors

The resonant photoionisation of single neutral atoms in the overlap volume of two laser beams embodies the physical realisation of a universal calibration source for charged particle detectors. Due to the use of a resonant two-step, two colour photoionisation scheme (see section 4.1), it allows to photoionise a selected isotope of atoms or molecules with unprecedented efficiency and spectroscopic selectivity [171, 172]. The photoionisation is further highly selective in aspect of spatial selectivity (see section 4.5).

As a unique property compared to any conventional calibration source, the photoionisation source provides correlated charged particle pairs (see section 5.1), and with opposite polarity. The ability to deliberately position the photoionisation volume in front of the detector enables 2D-scan measurements (3D-scans) of the sensitive detection area (volume) of the corresponding charged particle detector with unprecedented resolution compared to any conventional beam source (see section 4.5). In a two detector configuration, the generation and subsequent detection of correlated charged particle pairs further admits to calibrate the corresponding detectors to absolute efficiencies (see section 5.1). Such a calibration is in perfect conceptual correspondence to $4\pi\beta\gamma$ -coincidence counting in radiative decay measurements [222, 223, 229] or absolute photodetector calibration via correlated photon pairs from parametric downconversion [225, 226, 235]. To our knowledge, a similar spatially defined and deliberately positionable calibration source producing pairs of correlated charged particles has not been reported in the literature (see section 5.1). This leaves photoionisation of neutral single atoms in a defined overlap volume a unique correlated pair source for the calibration of charged particle detectors.

D.2. Mass spectroscopy below the current detection limit

The CEM detection system represents a highly selective, sensitive, and efficient mass spectrometer, allowing to determine extremely low partial pressures or concentrations of selected isotopes or molecules with unchallenged accuracy. This results as the ultimate detection limit with the CEM detection system is provided by the coincidence signal to accidental coincidence ratio N_c/N_{ac} from the correlation measurements (see section 5.2), and *not* by the signal to background ratio of the single counts $N_{i,e}/N_{ib,eb}$ at the single CEM detectors. For conventional ion gauges and mass spectrometer, the latter property impedes the accurate determination of partial pressures below 10^{-9} mbar as the expected low signal currents in comparison to residual background fluctuations are extremely difficult to measure. Moreover, this technically prevents the measurement of partial pressures of smaller than 10^{-11} mbar

element (ion)	TOF-ion [ns]	element (ion)	TOF-ion [ns]
$^1\text{H}^+$	42	-	-
$^6\text{Li}^+$	102	$^9\text{Be}^+$	125
$^{23}\text{Na}^+$	200	$^{24}\text{Mg}^+$	205
$^{40}\text{K}^+$	261	$^{40}\text{Ca}^+$	264
$^{85}\text{Rb}^+ / ^{87}\text{Rb}^+$	384/389	$^{88}\text{Sr}^+$	390
$^{133}\text{Cs}^+$	480	$^{138}\text{Ba}^+$	488

Table D.1: Calculated ion flight times $t_i \approx \Delta t$ with the CEM detection system from photoionisation detection at $\Delta U_{\text{acc}} = 3.8 \text{ kV}$. The flight times t_i are denoted for different alkali and alkaline earth metal isotopes actually used as atomic qubits or in future atom clock experiments as frequency standard. The difference in flight time is caused by the different mass of the single isotopes.

with such systems. In contrast to that, much lower partial pressures may be measured with the actual CEM detection system and photoionisation detection. By measurement of coincidences within a certain relative time window, the coincidence signal to accidental coincidence ratio determines the accuracy of the measurement and thus the ultimate pressure limit which will be finally resolved by the system (e.g., fig. 5.8(d), section 5.2). This leaves the actual CEM detection system the unique realisation of an atomic detection unit for selected isotopes or molecules with respect to extremely low particle concentrations and with a resolution for partial pressures far below 10^{-10} mbar.

D.3. Readout of neutral atom qubits and of ultracold heteronuclear molecules

Due to the high spatial selectivity and the single atom resolution, the CEM detection system is particularly suited for detection applications in the context of ultracold atom experiments with single atoms or atomic ensembles. Moreover, the CEM detection system enables the simultaneous readout of heteronuclear atoms or molecules in ultracold neutral atom trap systems like, e.g., magneto-optical traps (MOTs), optical dipole traps, or optical lattices. This results as the different mass of the single constituents in the heteronuclear mixture leads to different flight times of the ionic fragments from photoionisation until impact in the ion-CEM. In table D.1, the flight time $t_i \approx \Delta t$ for different alkali and alkaline earth metal isotopes with the joint CEM detection system is shown (e.g., $^{85}\text{Rb}/^{87}\text{Rb}$; fig. 5.10, see section 5.3). Besides the well probed alkali metal isotopes used in various ultracold neutral atom applications, the alkaline earth metal isotopes are additionally listed due to their potential as neutral atom qubits or as frequency standard in atomic clocks. The calculated values in the table D.1 represent the estimated flight times t_i with the current CEM detection system for an acceleration voltage difference of $\Delta U_{\text{acc}} = 3.8 \text{ kV}$ (see section 5.4).

E. Publications

- “Simultaneous magneto-optical trapping of three atomic species”,
M. Taglieber, A.-C. Voigt, F. Henkel, S. Fray, T. W. Hänsch, and K. Dieckmann,
Physical Review A **73**, 011402(R) (2006).
- “Towards Long-Distance Atom-Photon Entanglement”,
W. Rosenfeld, F. Hocke, F. Henkel, M. Krug, J. Volz, M. Weber, and H. Weinfurter,
Physical Review Letters **101**, 260403 (2008).
- “Towards a Loophole-Free Test of Bell’s Inequality with Entangled Pairs of Neutral Atoms”,
W. Rosenfeld, M. Weber, J. Volz, F. Henkel, M. Krug, A. Cabello, M. Zukowski, and H. Weinfurter,
Advanced Science Letters **2**, 469 (2009).
- “Highly efficient state-selective submicrosecond photoionization detection of single atoms”,
F. Henkel, M. Krug, J. Hofmann, W. Rosenfeld, M. Weber, and H. Weinfurter,
Physical Review Letters **105**, 253001 (2010).

Bibliography

- [1] Bell, J. S. *Physics* **1**, 195 (1964).
- [2] Einstein, A., Podolsky, B., and Rosen, N. *Phys. Rev.* **47**(10), 777 May (1935).
- [3] Freedman, S. J. and Clauser, J. F. *Phys. Rev. Lett.* **28**(14), 938 April (1972).
- [4] Laméhi-Rachti, M. and Mittag, W. *Phys. Rev. D* **14**(10), 2543 November (1976).
- [5] Aspect, A., Grangier, P., and Roger, G. *Phys. Rev. Lett.* **47**(7), 460 August (1981).
- [6] Aspect, A., Dalibard, J., and Roger, G. *Phys. Rev. Lett.* **49**(25), 1804 December (1982).
- [7] Weihs, G., Jennewein, T., Simon, C., Weinfurter, H., and Zeilinger, A. *Phys. Rev. Lett.* **81**(23), 5039 December (1998).
- [8] Bramon, A. and Nowakowski, M. *Phys. Rev. Lett.* **83**(1), 1 July (1999).
- [9] Rowe, M. A., Kielpinski, D., Meyer, V., Sackett, C. A., Itano, W. M., Monroe, C., and Wineland, D. J. *Nature* **409**(6822), 791 February (2001).
- [10] Hasegawa, Y., Loidl, R., Badurek, G., Baron, M., and Rauch, H. *Nature* **425**(6953), 45 September (2003).
- [11] Moehring, D. L., Madsen, M. J., Blinov, B. B., and Monroe, C. *Phys. Rev. Lett.* **93**(9), 090410 August (2004).
- [12] Matsukevich, D. N., Chaneliere, T., Bhattacharya, M., Lan, S.-Y., Jenkins, S. D., Kennedy, T. A. B., and Kuzmich, A. *Phys. Rev. Lett.* **95**(4), 040405 July (2005).
- [13] Chou, C.-W., Laurat, J., Deng, H., Choi, K. S., de Riedmatten, H., Felinto, D., and Kimble, H. J. *Science* **316**(5829), 1316 June (2007).
- [14] Matsukevich, D. N., Maunz, P., Moehring, D. L., Olmschenk, S., and Monroe, C. *Phys. Rev. Lett.* **100**(15), 150404 April (2008).
- [15] Pearle, P. M. *Phys. Rev. D* **2**(8), 1418 October (1970).
- [16] Clauser, J. F. and Shimony, A. *Reports on Progress in Physics* **41**(12), 1881 (1978).
- [17] Simon, C. and Irvine, W. T. M. *Phys. Rev. Lett.* **91**(11), 110405 September (2003).
- [18] Rosenfeld, W., Weber, M., Volz, J., Henkel, F., Krug, M., Cabello, A., Zukowski, M., and Weinfurter, H. *Advanced Science Letters* **2**, 469 (2009).
- [19] Zukowski, M., Zeilinger, A., Horne, M. A., and Ekert, A. K. *Phys. Rev. Lett.* **71**(26), 4287 December (1993).

- [20] Weber, M., Volz, J., Saucke, K., Kurtsiefer, C., and Weinfurter, H. *Phys. Rev. A* **73**(4), 043406 April (2006).
- [21] Volz, J., Weber, M., Schlenk, D., Rosenfeld, W., Vrana, J., Saucke, K., Kurtsiefer, C., and Weinfurter, H. *Phys. Rev. Lett.* **96**(3), 030404 January (2006).
- [22] Rosenfeld, W., Berner, S., Volz, J., Weber, M., and Weinfurter, H. *Phys. Rev. Lett.* **98**(5), 050504 February (2007).
- [23] Rosenfeld, W., Hocke, F., Henkel, F., Krug, M., Volz, J., Weber, M., and Weinfurter, H. *Phys. Rev. Lett.* **101**(26), 260403 December (2008).
- [24] Henkel, F., Krug, M., Hofmann, J., Rosenfeld, W., Weber, M., and Weinfurter, H. *Phys. Rev. Lett.* **105**(25), 253001 December (2010).
- [25] Garg, A. and Mermin, N. D. *Phys. Rev. D* **35**(12), 3831 June (1987).
- [26] Fine, A. *Foundations of Physics* **19**(5), 453 (1989).
- [27] Eberhard, P. H. *Phys. Rev. A* **47**(2), R747 February (1993).
- [28] Clauser, J. F., Horne, M. A., Shimony, A., and Holt, R. A. *Phys. Rev. Lett.* **23**(15), 880 October (1969).
- [29] Leibfried, D., Blatt, R., Monroe, C., and Wineland, D. *Rev. Mod. Phys.* **75**(1), 281 March (2003).
- [30] Blatt, R. and Zoller, P. *European Journal of Physics* **9**(4), 250 (1988).
- [31] Blatt, R., Häffner, H., Roos, C. F., Becher, C., and Schmidt-Kaler, F. *Quantum Information Processing* **3**(1), 61 (2004).
- [32] Hume, D. B., Rosenband, T., and Wineland, D. J. *Phys. Rev. Lett.* **99**(12), 120502 September (2007).
- [33] Olmschenk, S., Younge, K. C., Moehring, D. L., Matsukevich, D. N., Maunz, P., and Monroe, C. *Phys. Rev. A* **76**(5), 052314 November (2007).
- [34] Myerson, A. H., Szwer, D. J., Webster, S. C., Allcock, D. T. C., Curtis, M. J., Imreh, G., Sherman, J. A., Stacey, D. N., Steane, A. M., and Lucas, D. M. *Phys. Rev. Lett.* **100**(20), 200502 May (2008).
- [35] Gibbons, M. J., Hamley, C. D., Shih, C.-Y., and Chapman, M. S. *Phys. Rev. Lett.* **106**(13), 133002 March (2011).
- [36] Fuhrmanek, A., Bourgain, R., Sortais, Y. R. P., and Browaeys, A. *Phys. Rev. Lett.* **106**(13), 133003 March (2011).
- [37] Tey, M. K., Chen, Z., Aljunid, S. A., Chng, B., Huber, F., Maslennikov, G., and Kurtsiefer, C. *Nat Phys* **4**(12), 924 December (2008).
- [38] Shu, G., Kurz, N., Dietrich, M. R., and Blinov, B. B. *Phys. Rev. A* **81**(4), 042321 April (2010).

-
- [39] Streed, E. W., Norton, B. G., Jechow, A., Weinhold, T. J., and Kielpinski, D. *Phys. Rev. Lett.* **106**(1), 010502 January (2011).
- [40] Teper, I., Lin, Y.-J., and Vuletic, V. *Phys. Rev. Lett.* **97**(2), 023002 July (2006).
- [41] Bochmann, J., Mücke, M., Guhl, C., Ritter, S., Rempe, G., and Moehring, D. L. *Phys. Rev. Lett.* **104**(20), 203601 May (2010).
- [42] Gehr, R., Volz, J., Dubois, G., Steinmetz, T., Colombe, Y., Lev, B. L., Long, R., Estève, J., and Reichel, J. *Phys. Rev. Lett.* **104**(20), 203602 May (2010).
- [43] Specht, H. P., Nolleke, C., Reiserer, A., Uphoff, M., Figueroa, E., Ritter, S., and Rempe, G. *Nature* **473**(7346), 190 May (2011).
- [44] Terraciano, M. L., Olson Knell, R., Norris, D. G., Jing, J., Fernandez, A., and Orozco, L. A. *Nat Phys* **5**(7), 480 July (2009).
- [45] Ortegel, N. Master's thesis, Ludwig-Maximilians-Universität München, July (2009).
- [46] Krug, M. (*untitled*). PhD thesis, Ludwig Maximilians Universität München, (2012).
- [47] Eschard, G. and Manley, B. W. In *Acta Electronica*, volume 14, 19. Labs. d'Electronique Physique Appliquee, Val-de-Marne, France (1971).
- [48] Seah, M. P. *Journal of Electron Spectroscopy and Related Phenomena* **50**(1), 137 (1990).
- [49] Lombard, F. J. and Martin, F. *Rev. Sci. Instrum.* **32**(2), 200 February (1961).
- [50] Baldwin, G. C. and Friedman, S. I. *Rev. Sci. Instrum.* **36**(1), 16 January (1965).
- [51] Dietz, L. A. *Rev. Sci. Instrum.* **36**(12), 1763 December (1965).
- [52] Prescott, J. *Nuclear Instruments and Methods* **39**(1), 173 January (1966).
- [53] Dietz, L. A., Hanrahan, L. R., and Hance, A. B. *Rev. Sci. Instrum.* **38**(2), 176 February (1967).
- [54] Wright, W. H. *Journal of Physics D: Applied Physics* **2**(6), 895 (1969).
- [55] Eberhardt, E. H. *Appl. Opt.* **18**(9), 1418 May (1979).
- [56] Lundin, L. and Rolander, U. *Applied Surface Science* **67**(1-4), 459 April (1993).
- [57] Funsten, H. O., Suszcynsky, D. M., and Harper, R. W. *Rev. Sci. Instrum.* **67**(10), 3478 October (1996).
- [58] Feller, W. *An Introduction to Probability Theory and Its Applications, Vol. 1, 3rd Edition*. Wiley, January (1968).
- [59] Evans, D. S. *Rev. Sci. Instrum.* **36**(3), 375 March (1965).
- [60] Loubet, D. and Barat, C. *Nuclear Instruments and Methods* **111**(3), 441 September (1973).

- [61] Oba, K. and Maeda, H. *Advances in electronics and electron physics: Photo-electronic image devices : Proceedings of the Sixth Symposium*. Academic Press, September (1974).
- [62] Krebs, K. H. *Fortschritte der Physik* **16**(8), 419 (1968).
- [63] Bouchard, C. and Carette, J. D. *J. Appl. Phys.* **50**(11), 7168 November (1979).
- [64] Dekker, A. *Secondary Electron Emission*, volume Volume 6. Academic Press, (1958).
- [65] Hachenberg, O. and Brauer, W. *Secondary Electron Emission from Solids*, volume Volume 11. Academic Press, (1959).
- [66] Barat, C. and Coutelier, J. *Nuclear Instruments and Methods* **143**(1), 87 May (1977).
- [67] Fijol, J. J., Then, A. M., Tasker, G. W., and Soave, R. J. *Applied Surface Science* **48-49**, 464 (1991).
- [68] Allen, J. S. *Rev. Sci. Instrum.* **18**(10), 739 October (1947).
- [69] Marchand, P., Paquet, C., and Marmet, P. *Rev. Sci. Instrum.* **37**, 1702 (1966).
- [70] Seah, M. P., Lim, C. S., and Tong, K. L. *Journal of Electron Spectroscopy and Related Phenomena* **48**(1), 209 (1989).
- [71] Stein, J. D. and White, F. A. *J. Appl. Phys.* **43**(6), 2617 June (1972).
- [72] Dietz, L. A. and Sheffield, J. C. *Rev. Sci. Instrum.* **44**(2), 183 February (1973).
- [73] Dietz, L. A. and Sheffield, J. C. *J. Appl. Phys.* **46**(10), 4361 October (1975).
- [74] Kirschner, J. and Müller, N. *Applied Physics A: Materials Science & Processing* **11**(2), 179 (1976).
- [75] Manalio, A. A., Burin, K., and Rothberg, G. M. *Rev. Sci. Instrum.* **52**(10), 1490 October (1981).
- [76] Eckart, F. *Ann. Phys.* **446**(4-7), 181 (1953).
- [77] Petzel, B. *Ann. Phys.* **461**(1-2), 55 (1960).
- [78] Pongratz, M. B. *Rev. Sci. Instrum.* **43**(11), 1714 November (1972).
- [79] Lapsen, L. B. and Timothy, J. G. *Appl. Opt.* **12**(2), 388 February (1973).
- [80] Timothy, J. G. and Bybee, R. L. *Rev. Sci. Instrum.* **49**(8), 1192 August (1978).
- [81] Bruining, H. *Physica* **5**(10), 901 December (1938).
- [82] Salow, H. *Ann. Phys.* **440**(6-8), 417 (1950).
- [83] Baragiola, R. A., Alonso, E. V., and Florio, A. O. *Phys. Rev. B* **19**(1), 121 January (1979).
- [84] Brusilovsky, B. A. *Applied Physics A: Materials Science & Processing* **50**(1), 111 January (1990).

-
- [85] BURLE Electro-Optics, Inc. *Channeltron electron multiplier handbook for mass spectrometry applications*, (2008).
- [86] Hill, G. *Secondary Electron Emission and Compositional Studies on Channel Plate Glass Surfaces*, volume Volume 40, Part 1. Academic Press, (1976).
- [87] Seah, M. P. and Smith, G. C. *Rev. Sci. Instrum.* **62**(1), 62 January (1991).
- [88] Gilmore, I. S. and Seah, M. P. *Applied Surface Science* **144-145**, 113 April (1999).
- [89] Egidi, A., Marconero, R., Pizzella, G., and Sperli, F. *Rev. Sci. Instrum.* **40**(1), 88 January (1969).
- [90] Frank, L. A., Henderson, N. K., and Swisher, R. L. *Rev. Sci. Instrum.* **40**(5), 685 May (1969).
- [91] Paschmann, G., Shelley, E. G., Chappell, C. R., Sharp, R. D., and Smith, L. F. *Rev. Sci. Instrum.* **41**(12), 1706 December (1970).
- [92] Bordoni, F. *Nuclear Instruments and Methods* **97**(2), 405 December (1971).
- [93] Archuleta, R. J. and DeForest, S. E. *Rev. Sci. Instrum.* **42**(1), 89 January (1971).
- [94] Olsen, J. O. *Journal of Physics E: Scientific Instruments* **12**(11), 1106 (1979).
- [95] Burrous, C. N., Lieber, A. J., and Zaviantseff, V. T. *Rev. Sci. Instrum.* **38**(10), 1477 October (1967).
- [96] Tatry, B., Bosqued, J., and Reme, H. *Nuclear Instruments and Methods* **69**(2), 254 March (1969).
- [97] Fox, J., Fitzwilson, R. L., and Thomas, E. W. *Journal of Physics E: Scientific Instruments* **3**(1), 36 (1970).
- [98] Iglesias, G. E. and McGarity, J. O. *Rev. Sci. Instrum.* **42**(11), 1728 November (1971).
- [99] Potter, W. E. and Mauersberger, K. *Rev. Sci. Instrum.* **43**(9), 1327 September (1972).
- [100] Meier, K. and Seibl, J. *Journal of Physics E: Scientific Instruments* **6**(2), 133 (1973).
- [101] Crandall, D. H., Ray, J. A., and Cisneros, C. *Rev. Sci. Instrum.* **46**(5), 562 May (1975).
- [102] Fields, S. A., Burch, J. L., and Oran, W. A. *Rev. Sci. Instrum.* **48**(8), 1076 August (1977).
- [103] Rinn, K., Muller, A., Eichenauer, H., and Salzborn, E. *Rev. Sci. Instrum.* **53**(6), 829 June (1982).
- [104] Keller, C. A. and Cooper, B. H. *Rev. Sci. Instrum.* **67**(8), 2760 August (1996).
- [105] Tassotto, M. and Watson, P. R. *Rev. Sci. Instrum.* **71**(7), 2704 July (2000).
- [106] Koizumi, T. and Chihara, Y. *Journal of Physics: Conference Series* **163**, 012114 (2009).
- [107] Hird, B., Suk, H. C., and Guilbaud, A. *Rev. Sci. Instrum.* **47**(1), 138 January (1976).

- [108] Goodings, J. M., Jones, J. M., and Parkes, D. A. *International Journal of Mass Spectrometry and Ion Physics* **9**(4), 417 September (1972).
- [109] Martin, K. and Martelli, G. *Nuclear Instruments and Methods* **56**(1), 173 (1967).
- [110] Johnson, M. C. *Rev. Sci. Instrum.* **40**(2), 311 February (1969).
- [111] Mayer, U., Mozer, M., and v. Reinhrdt, M. *Appl. Opt.* **8**(3), 617 March (1969).
- [112] Pook, H. *Acta Electronica* **14**(1), 135 (1971).
- [113] Bordoni, F., Martinelli, M., Paganini Fioratti, M., and Piermattei, S. R. *Nuclear Instruments and Methods* **116**(1), 193 March (1974).
- [114] Timothy, J. G. and Lapson, L. B. *Appl. Opt.* **13**(6), 1417 June (1974).
- [115] Hibst, R. and Bukow, H. H. *Appl. Opt.* **28**(10), 1806 May (1989).
- [116] Chen, J. N., Shi, M., Tachi, S., and Rabalais, J. W. *Nuclear Instruments and Methods in Physics Research Section B: Beam Interactions with Materials and Atoms* **16**(1), 91 May (1986).
- [117] Kuipers, E. and Boers, A. *Nuclear Instruments and Methods in Physics Research Section B: Beam Interactions with Materials and Atoms* **29**(3), 567 December (1987).
- [118] Bruining, H. *Physica* **3**(9), 1046 November (1936).
- [119] Baroody, E. M. *Phys. Rev.* **78**(6), 780 June (1950).
- [120] Barut, A. O. *Phys. Rev.* **93**(5), 981 March (1954).
- [121] Parilis, E. S. and Kishinevskii, L. M. *Soviet Physics-solid State* **3**(4), 885 (1961).
- [122] Schram, B. L., Boerboom, A. J. H., Kleine, W., and Kistemaker, J. *Physica* **32**(4), 749 April (1966).
- [123] Krems, M., Zirbel, J., Thomason, M., and DuBois, R. D. *Rev. Sci. Instrum.* **76**(9), 093305 September (2005).
- [124] Ravon, J. *Nuclear Instruments and Methods in Physics Research* **211**(1), 7 June (1983).
- [125] Lye, R. G. and Dekker, A. J. *Phys. Rev.* **107**(4), 977 August (1957).
- [126] Seah, M. P. and Holbourn, M. W. *Journal of Electron Spectroscopy and Related Phenomena* **42**(3), 255 (1987).
- [127] Baragiola, R. A. *Nuclear Instruments and Methods in Physics Research Section B: Beam Interactions with Materials and Atoms* **78**(1-4), 223 May (1993).
- [128] Sauter, W., Zimmermann, U., and Baumgartner, W. *Zeitschrift für Angewandte Mathematik und Physik (ZAMP)* **21**(4), 669 (1970).
- [129] Hasselkamp, D., Lang, K. G., Scharmann, A., and Stiller, N. *Nuclear Instruments and Methods* **180**(2-3), 349 April (1981).

-
- [130] Walker, C., El-Gomati, M., Assa'd, A., and Zadrazil, M. *Scanning* **30**(5), 365 (2008).
- [131] Geiger, J. and Huck, F. *Nuclear Instruments and Methods* **164**(3), 501 September (1979).
- [132] Streeter, J. K., Hunt, Jr., W. W., and McGee, K. E. *Rev. Sci. Instrum.* **40**(2), 307 February (1969).
- [133] Arnoldy, R. L., Isaacson, P. O., Gats, D. F., and Choy, L. W. *Rev. Sci. Instrum.* **44**(2), 172 February (1973).
- [134] Mori, C., Sugiyama, T., and Watanabe, T. *Nuclear Instruments and Methods in Physics Research* **211**(2-3), 407 June (1983).
- [135] Shchemelinin, S., Pszona, S., Garty, G., Breskin, A., and Chechik, R. *Nuclear Instruments and Methods in Physics Research Section A: Accelerators, Spectrometers, Detectors and Associated Equipment* **438**(2-3), 447 December (1999).
- [136] Andresen, R. D. and Page, D. E. *Rev. Sci. Instrum.* **42**(3), 371 March (1971).
- [137] Loty, C. In *Acta Electronica*, volume 14, 107. Labs. d'Electronique Physique Appliquee, Val-de-Marne, France (1971).
- [138] Baumgartner, W. and Schmid, J. *Journal of Physics D: Applied Physics* **5**(10), 1769 (1972).
- [139] Baumgartner, W. E. and Huber, W. K. *Journal of Physics E: Scientific Instruments* **9**(5), 321 (1976).
- [140] Kurz, E. A. *American Laboratory* **11**(3), 67 (1979).
- [141] Timothy, J. G. *Rev. Sci. Instrum.* **44**(2), 207 February (1973).
- [142] Young, J. R. *Rev. Sci. Instrum.* **37**(10), 1414 October (1966).
- [143] Wright, W. H. *Rev. Sci. Instrum.* **38**(12), 1802 December (1967).
- [144] Steiner, K., Hafner, P., and Baumgartner, W. *Zeitschrift für Angewandte Mathematik und Physik (ZAMP)* **22**(4), 789 (1971).
- [145] Rager, J. P., Renaud, J. F., and Montcel, V. T. d. *Rev. Sci. Instrum.* **45**(7), 927 July (1974).
- [146] Rager, J. P. and Renaud, J. F. *Rev. Sci. Instrum.* **45**(7), 922 July (1974).
- [147] Gibson, D. K. and Reid, I. D. *Journal of Physics E: Scientific Instruments* **17**(6), 443 (1984).
- [148] Smith, D. G. *Journal of Scientific Instruments* **44**(12), 1053 (1967).
- [149] Timothy, A. F. and Timothy, J. G. *Journal of Physics E: Scientific Instruments* **2**(9), 825 (1969).

- [150] Bennett, F. D. G. and Thorpe, D. G. *Journal of Physics E: Scientific Instruments* **3**(3), 241 (1970).
- [151] Bedo, D. E. *Rev. Sci. Instrum.* **43**(1), 130 January (1972).
- [152] Prince, R. H. and Cross, J. A. *Rev. Sci. Instrum.* **42**(1), 66 January (1971).
- [153] Green, M., Kenealy, P., and Beard, G. *Nuclear Instruments and Methods* **99**(3), 445 March (1972).
- [154] Wolber, W. G., Klettke, B. D., Miller, J. S., and Schmidt, K. C. *Appl. Phys. Lett.* **15**(2), 47 July (1969).
- [155] Fraser, G., Pain, M., Lees, J., and Pearson, J. *Nuclear Instruments and Methods in Physics Research Section A: Accelerators, Spectrometers, Detectors and Associated Equipment* **306**(1-2), 247 August (1991).
- [156] Giudicotti, L., Bassan, M., Pasqualotto, R., and Sardella, A. *Rev. Sci. Instrum.* **65**(1), 247 January (1994).
- [157] Coeck, S., Beck, M., Delauré, B., Golovko, V., Herbane, M., Lindroth, A., Kopecky, S., Kozlov, V., Kraev, I., Phalet, T., and Severijns, N. *Nuclear Instruments and Methods in Physics Research Section A: Accelerators, Spectrometers, Detectors and Associated Equipment* **557**(2), 516 February (2006).
- [158] Pearson, J. F., Fraser, G. W., and Whiteley, M. J. *Nuclear Instruments and Methods in Physics Research Section A: Accelerators, Spectrometers, Detectors and Associated Equipment* **258**(2), 270 August (1987).
- [159] Sjuts, H. *Final test sheet - channel electron multiplier type KBL10RS45-V2*. www.sjuts.com, (2007).
- [160] Andresen, R. and Page, D. *Nuclear Instruments and Methods* **102**(2), 363 July (1972).
- [161] Savin, D. W., Gardner, L. D., Reisenfeld, D. B., Young, A. R., and Kohl, J. L. *Rev. Sci. Instrum.* **66**(1), 67 January (1995).
- [162] Grzeszczak, A., Kaszczyszyn, S., and Klein, S. *Vacuum* **57**(1), 99 April (2000).
- [163] Grzeszczak, A., Kaszczyszyn, S., and Klein, S. *Measurement Science and Technology* **12**(2), L1 (2001).
- [164] Seko, A. *Jpn. J. Appl. Phys.* **12**(5), 647 (1972).
- [165] Pfeffer, W., Kohlmeyer, B., and Schneider, W. *Nuclear Instruments and Methods* **107**(1), 121 February (1973).
- [166] Shikhaliev, P. M. *Nuclear Instruments and Methods in Physics Research Section A: Accelerators, Spectrometers, Detectors and Associated Equipment* **420**(1-2), 202 January (1999).
- [167] Candy, B. H. *Rev. Sci. Instrum.* **56**(2), 183 February (1985).

-
- [168] Candy, B. H. *Rev. Sci. Instrum.* **56**(2), 194 February (1985).
- [169] Mann, W. B. *A Handbook of Radioactivity Measurements Procedures - Report No. 058*. National Council on Radiation Protection and Measurements (NCRP), 2nd edition edition, (1985).
- [170] Knoll, G. F. *Radiation detection and measurement*. Wiley, New York, (1989).
- [171] Letokhov, V. and Mishin, V. *Optics Communications* **29**(2), 168 May (1979).
- [172] Hurst, G. S., Payne, M. G., Kramer, S. D., and Young, J. P. *Rev. Mod. Phys.* **51**(4), 767 October (1979).
- [173] Aymar, M., Robaux, O., and Wane, S. *Journal of Physics B: Atomic and Molecular Physics* **17**(6), 993 (1984).
- [174] Letokhov, V. *Laser photoionization spectroscopy*. Academic Press, (1987).
- [175] Bebb, H. B. *Phys. Rev.* **149**(1), 25 September (1966).
- [176] Letokhov, V., Mishin, V., and Puretzky, A. *Progress in Quantum Electronics* **5**, 139 (1979).
- [177] Minowa, T., Katsuragawa, H., Nishiyama, K., Shimazu, M., and Inamura, T. *J. Appl. Phys.* **61**(1), 436 January (1987).
- [178] Hall, R. I., McConkey, A., Ellis, K., Dawber, G., Avaldi, L., MacDonald, M. A., and King, G. C. *Measurement Science and Technology* **3**(3), 316 (1992).
- [179] Bader, A., Sarkadi, L., Hegyesi, G., Viktor, L., and Palinkas, J. *Measurement Science and Technology* **6**(7), 959 (1995).
- [180] Brehm, B., Grosser, J., Ruscheinski, T., and Zimmer, M. *Measurement Science and Technology* **6**(7), 953 (1995).
- [181] Ullrich, J., Moshhammer, R., Dorner, R., Jagutzki, O., Mergel, V., Schmidt-Bocking, H., and Spielberger, L. *Journal of Physics B: Atomic, Molecular and Optical Physics* **30**(13), 2917 (1997).
- [182] Stibor, A., Kraft, S., Campey, T., Komma, D., Gunther, A., Fortagh, J., Vale, C. J., Rubinsztein-Dunlop, H., and Zimmermann, C. *Phys. Rev. A* **76**(3), 033614 September (2007).
- [183] Krug, M. Master's thesis, Ludwig-Maximilians-Universität München, May (2007).
- [184] Jakob, C. Master's thesis, Ludwig-Maximilians-Universität München, April (2008).
- [185] Deeg, A. Master's thesis, Ludwig-Maximilians-Universität München, July (2008).
- [186] Wiza, J. L. *Nuclear Instruments and Methods* **162**(1-3), 587 June (1979).
- [187] Parkes, W. and Gott, R. *Nuclear Instruments and Methods* **95**(3), 487 September (1971).

- [188] Colson, W. B., McPherson, J., and King, F. T. *Rev. Sci. Instrum.* **44**(12), 1694 December (1973).
- [189] Taylor, R. C., Hettrick, M. C., and Malina, R. F. *Rev. Sci. Instrum.* **54**(2), 171 February (1983).
- [190] Gao, R. S., Gibner, P. S., Newman, J. H., Smith, K. A., and Stebbings, R. F. *Rev. Sci. Instrum.* **55**(11), 1756 November (1984).
- [191] Straub, H. C., Mangan, M. A., Lindsay, B. G., Smith, K. A., and Stebbings, R. F. *Rev. Sci. Instrum.* **70**(11), 4238 November (1999).
- [192] Stephen, T. M. and Peko, B. L. *Rev. Sci. Instrum.* **71**(3), 1355 March (2000).
- [193] Niemax, K. *Applied Physics B: Lasers and Optics* **38**(3), 147 November (1985).
- [194] Ristroph, T., Goodsell, A., Golovchenko, J. A., and Hau, L. V. *Phys. Rev. Lett.* **94**(6), 066102 February (2005).
- [195] Fraser, G. *Nuclear Instruments and Methods in Physics Research Section A: Accelerators, Spectrometers, Detectors and Associated Equipment* **291**(3), 595 June (1990).
- [196] Robert, A., Sirjean, O., Browaeys, A., Poupard, J., Nowak, S., Boiron, D., Westbrook, C. I., and Aspect, A. *Science* **292**(5516), 461 April (2001).
- [197] Harvey, K. C. *Rev. Sci. Instrum.* **52**(2), 204 February (1981).
- [198] Herrmann, P. P., Schlumpf, N., Telegdi, V. L., and Weis, A. *Rev. Sci. Instrum.* **62**(3), 609 March (1991).
- [199] Bhatti, S. A., Farooqi, S. M., Ahmad, N., Akram, M., and Baig, M. *Measurement Science and Technology* **7**(7), 1038 (1996).
- [200] Grüner, B., Jag, M., Stibor, A., Visanescu, G., Häffner, M., Kern, D., Günther, A., and Fortágh, J. *Phys. Rev. A* **80**(6), 063422 December (2009).
- [201] Goodsell, A., Ristroph, T., Golovchenko, J. A., and Hau, L. V. *Phys. Rev. Lett.* **104**(13), 133002 March (2010).
- [202] Heroux, L. and Hinteregger, H. E. *Rev. Sci. Instrum.* **31**(3), 280 March (1960).
- [203] Goodrich, G. W. and Wiley, W. C. *Rev. Sci. Instrum.* **32**(7), 846 July (1961).
- [204] Goodrich, G. W. and Wiley, W. C. *Rev. Sci. Instrum.* **33**(7), 761 July (1962).
- [205] Masuoka, T. *Rev. Sci. Instrum.* **48**(10), 1284 October (1977).
- [206] Sueoka, O. *Jpn. J. Appl. Phys.* **21**(Part 1, No. 5), 702 (1982).
- [207] Takagi, S., Kawasumi, Y., Noda, N., and Fujita, J. *Jpn. J. Appl. Phys.* **22**(Part 1, No. 9), 1453 September (1983).
- [208] Takagi, S., Iwai, T., Kaneko, Y., Kimura, M., Kobayashi, N., Matsumoto, A., Ohtani, S., Okuno, K., Tawara, H., and Tsurubuchi, S. *Nuclear Instruments and Methods in Physics Research* **215**(1-2), 207 September (1983).

-
- [209] Suzuki, I. H. and Saito, N. *Appl. Opt.* **24**(24), 4432 December (1985).
- [210] Smith, P. H., Tamppari, L. K., Arvidson, R. E., Bass, D., Blaney, D., Boynton, W. V., Carswell, A., Catling, D. C., Clark, B. C., Duck, T., DeJong, E., Fisher, D., Goetz, W., Gunlaugsson, H. P., Hecht, M. H., Hipkin, V., Hoffman, J., Hviid, S. F., Keller, H. U., Kounaves, S. P., Lange, C. F., Lemmon, M. T., Madsen, M. B., Markiewicz, W. J., Marshall, J., McKay, C. P., Mellon, M. T., Ming, D. W., Morris, R. V., Pike, W. T., Renno, N., Stauffer, U., Stoker, C., Taylor, P., Whiteway, J. A., and Zent, A. P. *Science* **325**(5936), 58 July (2009).
- [211] Henkel, C., Pötting, S., and Wilkens, M. *Applied Physics B: Lasers and Optics* **69**(5), 379 (1999).
- [212] Turchette, Q. A., Kielpinski, King, B. E., Leibfried, D., Meekhof, D. M., Myatt, C. J., Rowe, M. A., Sackett, C. A., Wood, C. S., Itano, W. M., Monroe, C., and Wineland, D. J. *Phys. Rev. A* **61**(6), 063418 May (2000).
- [213] Madsen, M., Hensinger, W., Stick, D., Rabchuk, J., and Monroe, C. *Applied Physics B: Lasers and Optics* **78**(5), 639 March (2004).
- [214] Harlander, M., Brownutt, M., Hänsel, W., and Blatt, R. *New Journal of Physics* **12**(9), 093035 (2010).
- [215] Fricke, J., Müller, A., and Salzborn, E. *Nuclear Instruments and Methods* **175**(2-3), 379 September (1980).
- [216] Fuso, F., Ciampini, D., Arimondo, E., and Gabbanini, C. *Optics Communications* **173**(1-6), 223 January (2000).
- [217] Sagle, E., Namiotka, R. K., and Huennekens, J. *Journal of Physics B: Atomic, Molecular and Optical Physics* **29**(12), 2629 (1996).
- [218] Labaziewicz, J., Ge, Y., Leibbrandt, D. R., Wang, S. X., Shewmon, R., and Chuang, I. L. *Phys. Rev. Lett.* **101**(18), 180602 October (2008).
- [219] Dubessy, R., Coudreau, T., and Guidoni, L. *Phys. Rev. A* **80**(3), 031402 September (2009).
- [220] Fry, E. S., Walther, T., and Li, S. *Phys. Rev. A* **52**(6), 4381 December (1995).
- [221] Campey, T., Vale, C. J., Davis, M. J., Heckenberg, N. R., Rubinsztein-Dunlop, H., Kraft, S., Zimmermann, C., and Fortagh, J. *Phys. Rev. A* **74**(4), 043612 October (2006).
- [222] Dunworth, J. V. *Rev. Sci. Instrum.* **11**(5), 167 May (1940).
- [223] Debertain, K. *Applied Radiation and Isotopes* **47**(4), 423 April (1996).
- [224] Klyshko, D. N. *Soviet Journal of Quantum Electronics* **10**(9), 1112 (1980).
- [225] Kwiat, P. G., Steinberg, A. M., Chiao, R. Y., Eberhard, P. H., and Petroff, M. D. *Phys. Rev. A* **48**(2), R867 August (1993).

- [226] Kwiat, P. G., Steinberg, A. M., Chiao, R. Y., Eberhard, P. H., and Petroff, M. D. *Appl. Opt.* **33**(10), 1844 April (1994).
- [227] Migdall, A., Datla, R., Sergienko, A., Orszak, J., and Shih, Y. *Metrologia* **32**(6), 479 (1995).
- [228] Ware, M. and Migdall, A. *Journal of Modern Optics* **51**(9/10), 1549 June (2004).
- [229] Geiger, H. and Werner, A. *Zeitschrift für Physik A Hadrons and Nuclei* **21**(1), 187 December (1924).
- [230] Amaldi, Jr., U., Egidi, A., Marconero, R., and Pizzella, G. *Rev. Sci. Instrum.* **40**(8), 1001 August (1969).
- [231] Luhmann, T. *Rev. Sci. Instrum.* **68**(6), 2347 June (1997).
- [232] Luhmann, T., Gerth, C., Groen, M., Martins, M., Obst, B., Richter, M., and Zimmermann, P. *Phys. Rev. A* **57**(1), 282 January (1998).
- [233] Gaire, B., Saylor, A. M., Wang, P. Q., Johnson, N. G., Leonard, M., Parke, E., Carnes, K. D., and Ben-Itzhak, I. *Rev. Sci. Instrum.* **78**(2), 024503 February (2007).
- [234] Jakeman, E. and Rarity, J. *Optics Communications* **59**(3), 219 September (1986).
- [235] Rarity, J. G., Ridley, K. D., and Tapster, P. R. *Appl. Opt.* **26**(21), 4616 November (1987).
- [236] Schmitt-Manderbach, T. *Long distance free-space quantum key distribution*. PhD thesis, Ludwig Maximilians Universität München, (2007).
- [237] Haynes, W. *CRC Handbook of Chemistry and Physics*. Taylor and Francis, (2011).
- [238] Bakr, W. S., Gillen, J. I., Peng, A., Fölling, S., and Greiner, M. *Nature* **462**(7269), 74 November (2009).
- [239] Sherson, J. F., Weitenberg, C., Endres, M., Cheneau, M., Bloch, I., and Kuhr, S. *Nature* **467**(7311), 68 September (2010).
- [240] Weitenberg, C., Endres, M., Sherson, J. F., Cheneau, M., Schausz, P., Fukuhara, T., Bloch, I., and Kuhr, S. *Nature* **471**(7338), 319 March (2011).
- [241] Kurz, E. A. *Rev. Sci. Instrum.* **50**(11), 1492 November (1979).
- [242] Bertz, A. *Resonant PEPICO-spectroscopy of Hg for a new Bell experiment*. PhD thesis, Technische Universität Darmstadt, Germany, (2010).
- [243] Fraser, G. W. *International Journal of Mass Spectrometry* **215**(1-3), 13 April (2002).
- [244] Mayer, R. and Weiss, A. *Phys. Rev. B* **38**(16), 11927 December (1988).
- [245] Dinneen, T. P., Wallace, C. D., Tan, K.-Y. N., and Gould, P. L. *Opt. Lett.* **17**(23), 1706 December (1992).

-
- [246] Gabbanini, C., Gozzini, S., and Lucchesini, A. *Optics Communications* **141**(1-2), 25 August (1997).
- [247] Ciampini, D., Anderlini, M., Müller, J. H., Fuso, F., Morsch, O., Thomsen, J. W., and Arimondo, E. *Phys. Rev. A* **66**(4), 043409 October (2002).
- [248] Hurst, G. S., Payne, M. G., Kramer, S. D., Chen, C. H., Phillips, R. C., Allman, S. L., Alton, G. D., Dabbs, J. W. T., Willis, R. D., and Lehmann, B. E. *Reports on Progress in Physics* **48**(10), 1333 (1985).
- [249] Unanyan, R., Fleischhauer, M., Shore, B. W., and Bergmann, K. *Optics Communications* **155**(1-3), 144 October (1998).
- [250] Vewinger, F., Heinz, M., Garcia Fernandez, R., Vitanov, N. V., and Bergmann, K. *Phys. Rev. Lett.* **91**(21), 213001 November (2003).
- [251] Raussendorf, R. and Briegel, H. J. *Phys. Rev. Lett.* **86**(22), 5188 May (2001).
- [252] Mandel, O., Greiner, M., Widera, A., Rom, T., Hansch, T. W., and Bloch, I. *Nature* **425**(6961), 937 October (2003).
- [253] Derevianko, A. and Katori, H. *Rev. Mod. Phys.* **83**(2), 331 May (2011).
- [254] Monroe, C. *Nature* **416**(6877), 238 March (2002).
- [255] Urban, E., Johnson, T. A., Henage, T., Isenhower, L., Yavuz, D. D., Walker, T. G., and Saffman, M. *Nat Phys* **5**(2), 110 February (2009).
- [256] Isenhower, L., Urban, E., Zhang, X. L., Gill, A. T., Henage, T., Johnson, T. A., Walker, T. G., and Saffman, M. *Phys. Rev. Lett.* **104**(1), 010503 January (2010).
- [257] Wilk, T., Gaetan, A., Evellin, C., Wolters, J., Miroshnychenko, Y., Grangier, P., and Browaeys, A. *Phys. Rev. Lett.* **104**(1), 010502 January (2010).
- [258] Schrader, D., Dotsenko, I., Khudaverdyan, M., Miroshnychenko, Y., Rauschenbeutel, A., and Meschede, D. *Phys. Rev. Lett.* **93**(15), 150501 October (2004).
- [259] Miroshnychenko, Y., Alt, W., Dotsenko, I., Förster, L., Khudaverdyan, M., Meschede, D., Schrader, D., and Rauschenbeutel, A. *Nature* **442**(7099), 151 July (2006).
- [260] Bloch, I. *Nature* **453**(7198), 1016 June (2008).
- [261] Bakr, W. S., Peng, A., Tai, M. E., Ma, R., Simon, J., Gillen, J. I., Fölling, S., Pollet, L., and Greiner, M. *Science* **329**(5991), 547 July (2010).
- [262] DiVincenzo, D. P. *Fortschr. Phys.* **48**(9-11), 771 (2000).
- [263] Hughes, R. *Technical Report No. LA-UR-04-1778* (2004).
- [264] Bradley, M. P., Porto, J. V., Rainville, S., Thompson, J. K., and Pritchard, D. E. *Phys. Rev. Lett.* **83**(22), 4510 November (1999).
- [265] Lee, S. A., Helmcke, J., Hall, J. L., and Stoicheff, B. P. *Opt. Lett.* **3**(4), 141 October (1978).

- [266] Lorenzen, C.-J. and Niemax, K. *Physica Scripta* **27**(4), 300 (1983).
- [267] Slater, J. C. *J. Chem. Phys.* **41**(10), 3199 November (1964).
- [268] Steck, D. A. available online at <http://steck.us/alkalidata> (revision 2.1.4, 23 December 2010), (2010).
- [269] McComas, D. J. and Bame, S. J. *Rev. Sci. Instrum.* **55**(4), 463 April (1984).
- [270] Smith, D. *Nuclear Instruments and Methods* **71**(2), 137 June (1969).
- [271] Sawicki, J. *Nuclear Instruments and Methods in Physics Research Section B: Beam Interactions with Materials and Atoms* **16**(6), 483 July (1986).
- [272] Roth, P. and Fraser, G. W. *Nuclear Instruments and Methods in Physics Research Section A: Accelerators, Spectrometers, Detectors and Associated Equipment* **439**(1), 134 January (2000).
- [273] Shibata, M., Tada, M., Kishimoto, Y., Kominato, K., Haseyama, T., Ogawa, I., Matsuki, S., Yamada, S., Funahashi, H., and Yamamoto, K. *Rev. Sci. Instrum.* **74**(7), 3317 July (2003).